The final publication is available at

Coupling methodology of 1D finite difference and 3D finite volume CFD codes based on the Method of Characteristics

4 AUTHORS:

José Galindo
Universitat Politècnica de València
71 PUBLICATIONS **614** CITATIONS

SEE PROFILE

Andrés Omar Tiseira
Universitat Politècnica de València
24 PUBLICATIONS **230** CITATIONS

SEE PROFILE

Pablo Fajardo
University Carlos III de Madrid
25 PUBLICATIONS **115** CITATIONS

SEE PROFILE

Roberto Navarro
Universitat Politècnica de València
11 PUBLICATIONS **54** CITATIONS

SEE PROFILE

MODELLING FOR ADDICTIVE BEHAVIOUR, MEDICINE AND ENGINEERING 2010

Instituto de Matemática Multidisciplinar

Edited by: L. Jódar, Instituto de Matemática Multidisciplinar

im²

Instituto de Matemática Multidisciplinar

UNIVERSIDAD POLITECNICA DE VALENCIA

GENERALITAT VALENCIANA

MODELLING FOR ADDICTIVE BEHAVIOUR,
BEHAVIOUR,
MEDICINE AND ENGINEERING 2010

Instituto de Matemática Multidisciplinar

Universidad Politécnica de Valencia

Valencia 46022, SPAIN

CONTENTS

Seasonal Respiratory Syncytial Virus Epidemic in a Random Social Network

L. Acedo*, J.-A. Moraño*, R.-J. Villanueva*,
J. Villanueva-Oller† and J. Díez-Domingo‡

(*) Instituto de Matemática Multidisciplinar,

Universidad Politécnica de Valencia,

Edificio 8G, Piso 2, 46022 Valencia, España.

(†) CES Felipe II,

Universidad Complutense de Madrid,

Aranjuez, Madrid, España.

(‡) Centro Superior de Investigación en Salud Pública (CSISP),

Valencia, España.

October 10, 2010

1   Introduction

The main characteristic of RSV and influenza pandemics is their seasonality, i.e., their incidence on the human population fluctuates broadly and regularly year after year with large peaks of infections occurring at the same time of the year in the same country. However, depending on the country, the time at which the largest peak is reached varies from midwinter to early spring [1]. Seasonality is also found in climatic conditions as different as those of Gambia, Singapore, Florida or Finland [2]. In the case of tropical countries a connection with the rainy season has been suggested. Following the idea of the influence of climatic conditions, whatever they should be, on the infection probability the seasonal behavior is forced into standard models by proposing a cosine variation in the form

$$b = b_0 + b_1 \cos(2\pi t), \tag{1}$$

where t is measured in years. However, the explanation of the seasonal outbreaks of these diseases remains poorly understood. Many statistical studies have been carried out in order

*e-mail: luiacrod@imm.upv.es

to provide a correlation of the outbreaks with climatic or social factors without achiev-
ing a definitive conclusion [3]. The complexities of the interactions among the human
host, the pathogen and the exogenous factors obscure the problem and the elucidation of
causal pathways leading to the emergence of the seasonal pattern. To go beyond this im-
passe, some authors have suggested that the variations on the infection probability could
be undetectable but sufficient to cause the seasonal fluctuations by dynamical resonance
amplification [4]. Traditional models for the epidemic propagation are based upon contin-
uous differential equations but this approach suffers from many inconveniences because we
cannot monitor the evolution of individuals separately. Here we show that, in a random
social network, self-sustained seasonal epidemics emerge as a process modulated by the
infection probability and the immunity period after recovering from the infection. This is
a purely endogenous phenomenon that does not require any exogenous forcing. Assuming
that this is the dominant mechanism for seasonal epidemics, many implications for public
health policies in infectious respiratory diseases could be drawn.

2   The Social Random Network Model

Person-to-person propagation of infectious diseases is now more and more frequently sim-
ulated by means of complex networks [5]. This provides a more realistic scenario in which
we can follow the clinical history of every individual and tag them with relevant variables:
age, sex, susceptibility to the viral infection or social connections with other individuals.

The emergent science of networks provides several standard alternatives of implemen-
tation of the network substrate. The most traditional is based upon the pioneer work of
Erdös and Rényi [6], the so-called "random graphs", where connections among the pairs
of subjects are created with the same probability. Alternative models are the scale-free
networks [7] or the small-world networks of Watts and Strogatz [8] . These social networks
have been ascertained from real data and used to study the social pandemics of smoking
[9] and obesity [10].

For these reasons, we have chosen the random network model as the most appropriate
modeling of the transmission of RSV and infectious diseases in general. The detailed
monitoring of people's activities in order to ascertain possible contagion contacts is too
complicated to be considered, although it has been attempted for the city of Portland [11].

3   Epidemic Behaviour in a Random Network

We have considered a random network with $N =$1,000,000 nodes and an average degree
of the node, k. Consequently, the number of links in the network is given by Nk. These
links are randomly assigned to pairs of individuals with the obvious rule that, at most,
only a link can connect two individuals. The epidemic is propagated through this network
following the standard rules of the SIR model: (i) Infected nodes transmit the disease
through the links to susceptible nodes with probability α. Infected individuals recover
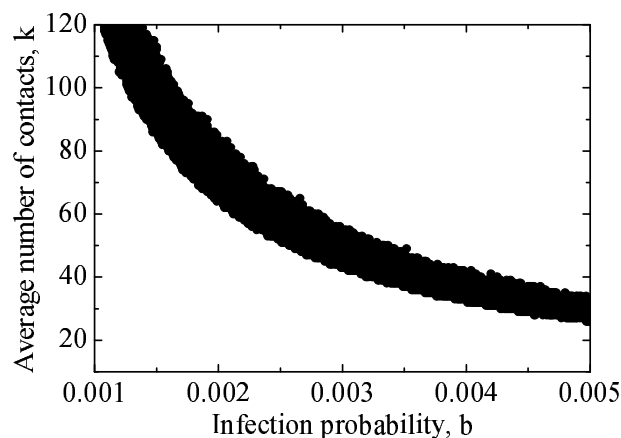
Figure 1: Phase diagram for the epidemic behaviour of the random network model. The region in which the epidemic does not fade away is plotted in black.

with probabitily ν ($\nu = 1/10$ days^{-1} in the case of RSV) and recovered individuals become susceptibles again after an average of 200 days [2].

In order to obtain a global perspective of the propagation behavior in the random network we tested 60,000 combinations of k (in the range 5-124) and the transmission probability in a person-to-person contact ($0 = b = 0.005$ with 0.00001 jumps). For most of these combinations the epidemic disappears after the first outbreak. This happens for two reasons: (a) for low probabilities of contagion the epidemic cannot spread to a sufficient number of individuals and the virus disappears when the small number of individuals affected by the disease recover from it; (b) for large probabilities of contagion a very high outbreak peak develop but the epidemic fades away afterwards because most of the population becomes recovered and there is no reservoir of susceptibles to maintain the virus waiting for the immunity loss of the rest of the population.

For intermediate values of the infection probability b, there are endemic situations and, for some of them, a seasonal epidemic appears. The corresponding region is plotted in Figure 1.

An important consequence of this behavior is that a small variation in the parameters (infection probability, b or average degree of connectivity, k) could lead to the disappearing or emergence of an endemic situation or a seasonal epidemic if the initial situation is close to the border between the black and white regions. In this situation a campaign to make the population conscious of taking prophylactic measures, as those spoiled by the recent Influenza H1N1 menace, could be highly effective.

Acknowledgements

References

[1] P. Glezen and F. W. Denny, Epidemiology of acute lower respiratory disease in children. *N. Engl. J. Med.*, 288:498–505, 1973.

[2] A. Weber, M. Weber, and P. Milligan. Modeling epidemics caused by respiratory syncytial virus (RSV). *Math. Biosc.*, 172:95–113, 2001.

[3] E. N. Naumova. Mystery of Seasonality: Getting the Rhythm of Nature. *J. Public Health Policy*, 27(1):2–12, 2006.

[4] J. Dushoff, J. B. Plotkin, S. A. Levin, and D. J. D. Earn. Dynamical resonance can account for seasonality of influenza epidemics. *Proc. Natl. Acad. Sci.*, 101(48):16915–16916, 2004.

[5] M. E. Halloran, I. M. Longini Jr., A. Nizam, and Y. Yang. Containing Bioterrorist Smallpox. *Science* 298:1428–1432, 2002.

[6] B. Bollobás. Random Graphs, 2º Ed, Cambridge University Press, 2001.

[7] R. Albert and A. L. Barabási. Emergence of scaling in random networks. *Science* 286:509–512, 1999.

[8] D. J. Watts. Small Worlds: The Dynamics of Networks Between Order and Randomness, Princeton University Press, 1999.

[9] N. A. Christakis and J. H. Fowler. The Collective Dynamics of Smoking in a Large Social Network. *N. Engl. J. Med.* 358:2249–2258, 2008.

[10] N. A. Christakis and J. H. Fowler. The spread of obesity in a large social network over 32 years. *N. Engl. J. Med.* 357:370–379, 2007.

[11] S. Eubank, V. S. Anil Kumar, M. V. Marathe, A. Srinivasan and W. Nan. Structure of Social Contact Networks and Their Impact on Epidemics. *DIMACS Series in Discrete Mathematics and Theoretical Computer Science* 70:181–214, 2006.

Analysis of the electroencephalogram as a random walk

L. Acedo*and D. F. Aranda†

(*) Instituto de Matemática Multidisciplinar,

Universidad Politécnica de Valencia,

Edificio 8G, Piso 2, 46022 Valencia, España.

(†) Laboratorio de Salud Pública,

Secretaría de Salud Pública de Bogotá D. C.,

Kra 32, No 12-81, Building LSP, 3º Floor, Bogotá, Colombia.

October 10, 2010

1   Introduction

Human brain is the most complex system in the Universe we know to exist. Support to this statement can be given from the psychological capacities displayed by human beings and the modern neurological and anatomical descriptions of it: a set of 10^{10}-10^{11} neuron cells projecting as many as 10^4 to 10^5 synapses to other neurons. Moreover, neurons and their interaction among them are very complex: chemical communication among neurons is modulated by more than 50 neurotransmitters including aminoacids, peptides and monoamines. On a level below we found the cytoskeletal network of microtubules with a very intricate filament structure.

Consequently, in the brain we observe complexity at many levels:

(i) The mental-psychological, including memory,language, perception, attention and consciousness.

(ii) The anatomical corresponding to the subdivided structures: prefontal cortex, Broca's and Wernicke's areas, visual cortex, motor cortex, cerebelum, lymbic system and its substructures and the large fiber's bundles connecting them.

(iii) The cell level where we find neuron and synaptic connections.

(iv) The cytoskeletal network at the nanometer scale.

---

*e-mail: luiacrod@imm.upv.es

Understanding how these complexities relate to each other is the main problem of neuroscience. The scientific study of the brain can be retraced to the work of Thomas Willis, an English doctor which at 1664 published the first systematic treatise of neuroanatomy and developed the idea of functional neuroanatomy by describing the distinctive functions of certain areas of the brain. Work at the XIXth century follow Willis's trail when Broca's and Wernicke's studies of aphasic patients allow to localize the brain areas involved in speech production and comprehension, respectively. Much of the work today in neurology is based upon these ideas of functional localization of higher mental functions but, despite many advances, the very complicate nature of connections, even at this macroscopic level, makes the elucidation of the involvement of the different structures in brain processes very difficult.

At the turn of the XIXth century, Ramón y Cajal observed the detailed microscopic structure of the nervous system thanks to the staining method developed by Golgi. These breakthroughs settled the foundations of modern neuronscience after the proposal of the so-called neuron doctrine by von Waldeyer-Hartz in 1891, i. e., the fundamental notion that the nervous system is composed by individual cells. Later on, Cajal proved the directionality of synaptic contacts among neurons and showed that these contacts are contiguous but not continuous as Golgi defended.

Among all the mental abilities exhibited by organisms with neural tissue, memory stands as the one for which more theories, scientific or philosophical, have been proposed. It is well-known that Plato, at the Theaetetus dialogue, recalled Socrate's analogy of memory function as the imprinting of bodies in wax.

Hopfield Networks are an example of a Cellular Automata capable of explaining certain complex functions of the brain (including memory) and, moreover, soundly founded on neurophysiological discoveries [2]. These models make predictions about the maximum storage capacity of the neural network, the emergence of spurious memories near overload and the way in which memories are store and retrieved in the brain as orchestrated firings of neuron assemblies [3] that could be useful to guide research of applied neuroscientist searching for neurological basis of memory.

Finally, we should mention the largely controversial, difficult to categorize and theoretically elusive phenomenon of consciousness [4]. Considered as a physical system, human beings know that they are such a system and, moreover, we know that we know it. Every perception elicits a qualitative and introspective feeling about it called 'qualia'. This phenomenon is now the central subject of a broad philosopical debate in neuroscience and, perhaps, more than any other process convince us of the sheer complexity of the brain. An inspired 'toy model' for this problem should be surely very useful for this cross-disciplinary topic. Cellular automata neural networks have been also proposed as an starting point for comprehension of consciousness, individuality as the highest information processes of human brains.
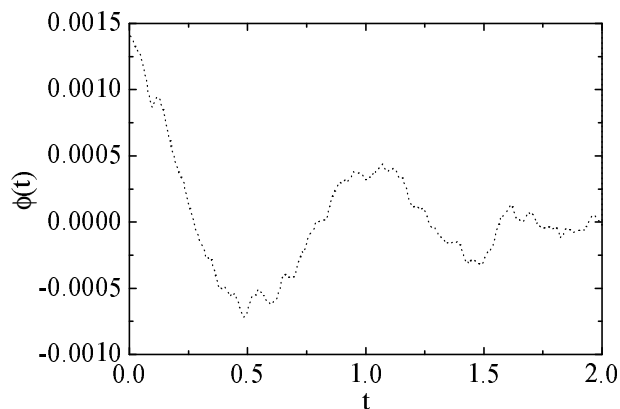
Figure 1: The autocorrelation function for the delta wave. Time is measured in seconds.

2 EEG as a random walk

Hans Berger, a german medical doctor, discovered in 1929 that between electrodes attached to the human scalp a potential difference in the mV range could be detected by means of a precision galvanometer. He observed that a rhythmic pattern with a frequency of 8-12 Hz was recorded from subjects with their eyes closed (Alpha rhythm or Berger's wave). After opening their eyes the frequency increased to 12-30 Hz (Beta rhythm).

In his work, Berger's was inspired by the findings of the surgeon Richard Caton who in 1875 measured electrical potentials on the cortex of laboratory animals. The discovery of intracranial measures of electrical activity preceded by half a century the epoch-making Berger's discovery. The importance of Berger's method is that, being an extracraneal and non-invasive technique, could develop into a very useful monitoring and diagnosing tool for neurologist and psychiatrists.

In a pioneer work N. Wiener studied brain waves from the point of view of random theory [5] by defining the autocorrelation function and the power spectrum of the wave. The last tool is still much used in statistical analysis of EEG [6] but the autocorrelation function is largely forgotten.

In this work we have analyzed the relaxation of correlations in EEG. In order to obtain independent records from a continuous signal we have divided EEG records corresponding to the same state and (with a total length that varies from 30 minutes to 1 hour) in portions of 10 seconds. This portions are then considered as independent records because autocorrelations are supposed to vanish after a few seconds. This is confirmed in the subsequent analysis. The self-correlation function, $\phi(t)$, is the calculated as follows:

$$\phi(t) = \langle V(t)V(t=0)\rangle - \langle V(t)\rangle^2 \,, \tag{1}$$

where $V(t)$ is the potential difference measured by two typical electrodes attached to the scalp of the patient. The records were obtained from the on-line Physionet database [7]. Results for the autocorrelation function of the delta wave are plotted in Figure 1.

We observe a damped oscillatory relaxation. A general pattern present in many physical systems. An interpretation of this result in terms of a recently proposed cellular automata model of the brain is possible. This model can be understood as a stochastic cellular automata with a population of individual automata placed upon the nodes of a complete graph. An interpretation of the SIS model in terms of neural physiology has been proposed: firing neurons are corresponded with the infected sites while quiescent neurons are mimicked by susceptible sites. In several previous papers [8, 9] this model was investigated in connection with a proposal to understand EEG as a statistical epiphenomenon, i. e., EEG is simulated as the fluctuations in the number of firing (infected) sites in a finite-size complete network evolving according to the SIS model's rules.

The damped oscillatory behaviour is also found in the SIS and SIRS models [10] and could explain the autocorrelation of EEG records.

Acknowledgements

References

[1] S. Ramón y Cajal, The Croonian Lecture: La Fine Structure des Centres Nerveux, *Proceedings of the Royal Society of London.* 55:444–468, 1894.

[2] J. J. Hopfield, Neural networks and physical systems with emergent collective computational abilities, *Proceedings of the National Academy of Sciences of the USA.* 79(8):2554–2558, 1982.

[3] Y. Bar-Yam, Dynamics of Complex Systems, Addison-Wesley, Reading, MA, 1997.

[4] M. Bennett, D. Dennet, P. Hacker and J. Searle, Neuroscience & Philosophy. Brain, Mind & Language, Columbia University Press, 2007.

[5] N. Wiener, Nonlinear problems in random theory, John Wiley & Sons, Inc., New York, 1958.

[6] A. Krakovska and S. Štolc Jr., Spectral decay versus correlation dimension of EEG, *Neurocomputing*, 71:2978–2985, 2008.

[7] A. L. Goldberger, L. A. N. Amaral, L. Glass, J. M. Hausdorff, P. Ch. Ivanov, R. G. Mark, J. E. Mietus, G. B. Moody, C.-K. Peng and H. E. Stanley, PhysioBank, PhysioToolkit, and PhysioNet: Components of a New Research Resource for Complex Physiologic Signals, *Circulation*, 101(23): e215–e220, 2000. (Circulation Electronic Pages:http://circ.ahajournals.org/cgi/content/full/101/23/e215).

[8] L. Acedo, A second-order phase transition in the complete graph stochastic epidemic model, *Physica A*, 370: 613–624, 2006.

[9] L. Acedo, A cellular automaton model for collective neural dynamics, *Mathematical and Computer Modelling*, 50: 717–725, 2009.

[10] L. Acedo, G. González-Parra and A. J. Arenas, An exact global solution for the classical SIRS epidemic model, *Nonlinear Analysis: Real World Applications*, 11: 1819-1825, 2010.

Use of machine learning techniques to analyse the risk associated with mine lode deposits

M. Araújo* ; T. Rivas*, E. Giráldez* and J. Taboada*

(*) Universidad de Vigo

Dpto. de Ingeniería de los Recursos Naturales y Medio Ambiente

Lagoas Marcosende 36310, Vigo, Spain

October 10, 2010

1   Introduction

Intensive mining in the Autonomous Community of Galicia in northwest Spain has a significant environmental impact on the area in the vicinity of the mines. The environmental risk frequently arises from sludge deposits, which could overflow or whose retaining walls could erode or break. Therefore, sludge deposits, an inevitable consequence of mining and transformation activities, require risk associated with the accumulated sludge to be evaluated, measured and quantified.

In recent years, a number of institutions and environmental agencies [1] and also researchers [2, 3] have developed methodologies to evaluate environmental risk in various fields. Traditional methodologies have calculated environmental risk by estimating and rigidly weighting each of the factors conditioning the risk.

In our article we propose a more flexible approach to constructing a risk index from the criteria of an expert familiar with each studied deposit and capable of assigning, on the basis of technical criteria, a hazard rating to each deposit that indicates the potential impact on the environment were the retention walls to fail. Once expert criteria were defined, with a view to implementing automated simulation, different machine learning techniques were implemented and compared by analysing and processing a set of input variables that condition the probability of a retaining wall failure in terms of the vulnerability of the population, the vulnerability of the infrastructure, the vulnerability of the environment and the intrinsic and extrinsic hazards associated with an event.

Thus, 3 classification algorithms were implemented: classification and regression trees (CARTs) [4], multilayer perceptron (MLP) [5] and support vector machines (SVMs) [6].

---

*e-mail:maraujo@uvigo.es

2 Construction of a risk index for sludge deposits with machine learning techniques

2.1 Sources and variable definition

A total of 25 state variables representative of factors conditioning environmental risk were considered in the following terms: (1) the probability of a failure occurring in the structure; (2) the vulnerability of the persons and objects exposed to the risk; and (3) the hazard or intensity of the risk.

Once the factors affecting the risk index were defined, they were evaluated and measured by an expert in106 sludge deposits in situ, with the expert scoring each variable according to an ordinal scale of 1 to 10 that indicated a gradual increase in environmental risk.

2.2 Construction of the expert system

Once each of the state variables was evaluated and quantified according to technical criteria, the expert qualitatively assessed and evaluated risk for each of the sludge deposits in terms of risk to the environment as minimal, moderate or severe.

The expert system takes the following form:

$$y = f(x_1, ..., x_d) \tag{1}$$

where x_i, $i = 1, ..., d$ are the $d = 25$ state variables, y is the risk index for each studied sludge deposit and f represents the expert knowledge reflecting the influence of the above-mentioned variables on the environmental risk index for the sludge deposits. Risk incidence for the state variables x_i, $i = 1, ..., 25$ was scored between 1 and 10, whereas the risk index was graduated from 1 to 3 (minimal, moderate or severe risk). The 2 ordinal scales represented gradual increases in the environmental risk implied by the sludge deposits.

The available sample $\{(\mathbf{x}_i, y_i)\}_{i=1}^{N}$, of size $N = 106$, where $\mathbf{x}_i \in \mathbb{R}^{25}$ represented all the parameters referring to the sludge deposits and the environment—as quantified in the field—that affect the potential environmental risk, with $y_i \in \{1, 2, 3\}$ identifying the risk index for each of the studied deposits.

Given the above scoring system, the estimation of the model (1) can be viewed as a classification problem supervised by an expert. Three supervised learning algorithms were implemented to resolve the problem: CARTs, MLP networks and SVMs.

In order to construct, compare and select the optimal algorithm for the risk data, a cross-validation process was implemented. The cross-validation process enabled us to determine the optimal depth of the CART, the optimal values for the σ in the Gaussian kernel $k(\mathbf{x}, \mathbf{x}') = \exp\left(-\frac{\|\mathbf{x} - \mathbf{x}'\|^2}{2\sigma^2}\right)$ used to build the SVM, the regularization constant C for the SVM model, and the optimal number of neurons in the hidden layer of the MLP network, which was trained using a backpropagation algorithm and with sigmoid logarithm transfer functions in the input layer and linear transfer functions in the output layer.

2.3 Results and discussion

The mean error rate (ER) values resulting from the validation process revealed that the MLP network was most successful (ER=4.80%), followed by the SVM (ER=8.20%) and CART (ER=18.60%), in resolving our specific classification problem. In this particular case, the greater capacity for interpretation of the CART did not mitigate its imprecision in simulating the expert criteria. Consequently, given that the MLP network demonstrated a superior prediction capacity and a greater capacity for eliminating noise, we ruled out CART and SVM for the resolution of the classification problem.

3 Conclusions

Our results point to the success of the MLP neuronal networks in simulating an expert's criteria regarding the estimation of the level of risk in sludge deposits associated with mining activities in Galicia. The great accuracy of the network in assimilating the expert's criteria, along with its good generalization and updating capacities, make it a useful model for predicting the risk index for the sludge deposits, while assuring objectivity and coherence in the expert's criteria.

The development of a specific and objective protocol for quantitative data collection in the field, combined with the database developed in this research—provided it was suitably updated and improved on the basis of feedback—would preempt the need for an expert to supervise future risk evaluations of sludge deposits.

References

[1] US EPA, Risk Characterization Handbook. Science Policy Council, US Environmental Protection Agency, Washington DC., 2000.

[2] Colomer Mendoza F.J. and Gallardo Izquierdo A. Design of a model to assess the environmental risk of leachate dams *Waste Management*, 28:2122–2133, 2008.

[3] Senese V., Boriani E., Baderna D., Mariani A., Lodi M., Finizio A., Testa S. and Benfenati E. Assessing the environmental risks associated with contaminated sites: Definition of an Ecotoxicological Classification index for landfill areas (ECRIS) *Chemosphere*, 80:60–66, 2010.

[4] L. Breiman, J. Friedman, R. Olshen and C. Stone, Classification and Regression Trees. Monterey, CA, Wadsworth, 1984.

[5] Pinkus A. Approximation theory of the MLP model in neural networks *Acta Numerica* 8: 143-195, 1999 .

[6] B. Scholkopf and A.J. Smola, Learning with Kernels. Cambridge, MIT Press, 2002.

Optimal iterative methods to calculate artificial satellites preliminary orbits [*]

Víctor Arroyo[*] , Alicia Cordero[*] [†] and Juan R. Torregrosa[*]

(*) Instituto de Matemática Multidisciplinar,

Universidad Politécnica de Valencia,

Camino de Vera, s/n, 46022

Valencia, Spain

October 10, 2010

In recent years, high-order methods have shown to be very useful in many practical applications, in which nonlinear equations $f(x) = 0$ or nonlinear systems $F(x) = 0$ arise. In this context, the optimal order methods are the most efficient, because of the number of functional evaluations per step involved in the iterative expression is minimum. The efficiency index (see [8]), gives a measure of the balance between those quantities, according to the formula $p^{1/d}$, where p is the order of the method and d the number of functional evaluations per step. Kung and Traub [7] conjecture that the order of convergence of any multipoint method, for solving nonlinear equations, without memory cannot exceed the bound 2^{d-1}, (called the *optimal order*).

Thus, the optimal order for a method with 2 functional evaluations is 2, so Newton is an optimal method to solve the nonlinear equation $f(x) = 0$. In the case of 3 functional evaluations per step, the optimal order would be 4, as for example in Owstroski's method [8] and in Jarrattt's method [6]. If the number of functional evaluations is 4, then the optimal order is 8; we will use the MOP8 method, described in [1].

Nevertheless, when nonlinear systems are considered, the number of functional evaluations per step depends of the size n of the system; even more, the computational cost of a functional evaluation depends on the object that is evaluated (the nonlinear function, n functional evaluations, or its associated jacobian matrix, n^2 functional evaluations). So, we have adapted the definition of optimal order of convergence to the case of iterative methods to solve nonlinear systems. The extension to several variables of the conjecture of Kung and Traub could be done in the following way:

Conjecture 1 *Given a multipoint iterative method to solve nonlinear systems of equations which requires* $d = k_1 + k_2$ *functional evaluations per step such that* k_1 *of them correspond to the*

[†]e-mail: acordero@mat.upv.es

13

number of evaluations of the jacobian matrix and k_2 to the evaluations of the nonlinear function. We conjecture that the optimal order for this method is $2^{k_1+k_2-1}$ if $k_1 \leq k_2$.

Under this premise, when iterative methods are taken into account in order to solve nonlinear systems, only Newton's method can be considered as a optimal method. When we look at fourth-order methods, we find that $k_2 = 2 > k_1 = 1$, as in Jarratt's method, or $k_1 + k_2 > 3$, as in HMT method, where $k_1 = 1$ and $k_2 = 3$ (see [5]). It should be necessary to design fourth-order methods with one functional evaluation of the jacobian matrix and only two evaluations of the nonlinear function. As far as we know, this methods does not exist yet. So, further effort must be made in the future to get optimal methods to solve nonlinear systems. In this paper we propose a new method that, not being optimal, has the best efficiency index of the methods we know till now.

We propose a new iterative method, called M5, that uses the same number of functional evaluations and operations as in HMT, but the order of convergence is higher. Its iterative expression is:

$$
\begin{aligned}
z^{(k)} &= y^{(k)} - 5[F'(x^{(k)})]^{-1}F(y^{(k)}), \\
x^{(k+1)} &= z^{(k)} - \tfrac{1}{5}[F'(x^{(k)})]^{-1}\left[-16F(y^{(k)}) + F(z^{(k)})\right],
\end{aligned}
\tag{1}
$$

where $y^{(k)}$ is the kth iteration of Newton's method and $F'(x)$ denotes the jacobian matrix of F. We are able to prove that the order of convergence of this method is 5, specifically

Theorem 1 *Let $F : D \subseteq \mathbb{R}^n \longrightarrow \mathbb{R}^n$ be sufficiently differentiable at each point of an open neighborhood D of $\bar{x} \in \mathbb{R}^n$, that is a solution of the system $F(x) = 0$. Let us suppose that $F'(x)$ is continuous and nonsingular in $\bar{x}$. Then, the sequence $\{x^{(k)}\}_{k \geq 0}$ obtained using the iterative expression (1) converges to $\bar{x}$ with order 5.*

So, the efficiency index of the method M5 is $I_{M5} = 5^{\frac{1}{n^2+3n}}$, meanwhile the corresponding indices of Newton' and Jarrat's methods are, respectively, $I_N = 2^{\frac{1}{n^2+n}}$ and $I_J = 4^{\frac{1}{2n^2+n}}$. In Figure 1 we can see that the index of M5 is plainly higher than the rest of methods.

However, in the n-dimensional case, it is also important to take into account the number of operations performed, since for each iteration a number of linear systems must be solved. For this reason we defined in [2] the *Computational Efficiency Index* as

$$
CI = p^{1/(d+op)},
\tag{2}
$$

where op is the number of products/quotients per iteration. We consider that this index is complementary to the classical one, as allows us to compare the different methods taking into account the computational effort dud, not only to the functional evaluations, but also to the operations made. In Figure 2 we can see the computational efficiency indices of the mentioned methods: it is clear that, under the computational point of view, the new method M5 is also the best one.

Applying these methods to preliminary orbit determination is expected to increase the order of convergence of the process. Preliminary orbit determination consists in determining the orbital elements $(a, e, i, \omega, \Omega, T_0)$, from position coordinates of a satellite (or another celestial body) for two given times, being necessary to calculate the velocity vector corresponding to one of the
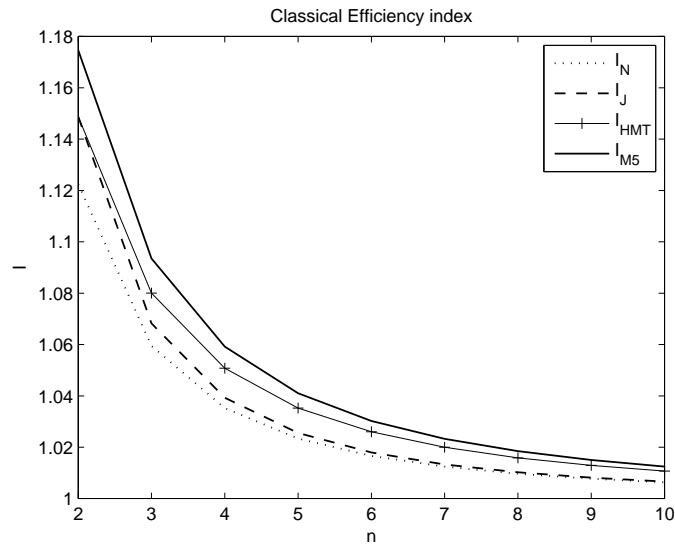
Figure 1: Classical efficiency indices.

known instants. To compute the velocity vector from both position vectors and respective times, it is necessary to calculate first the semi-major axis a and the difference in eccentric anomalies $E_2 - E_1$, which relates the positions with the perigee and the center of the elliptical orbit. The classical Gauss method calculates these values solving a reduced nonlinear equation with the fixed point method (see [3]). This reduced equation comes from both First and Second Gauss equations, which can form a system of nonlinear equations. We aim at introducing more efficient higher order methods to solve this nonlinear equation and system, in order to reduce the number of steps and the computational cost of the process.

For that purpose, we have developed a graphical application with Matlab GUIDE to be able to make graphical and numerical comparison of different methods and test orbits from Escobal [4]. Using Variable Precision Arithmetics, with 500 digits of mantissa, we set a stopping criterion of

$$\left\|x^{(k+1)} - x^{(k)}\right\| + \left\|F\left(x^{(k+1)}\right)\right\| < 10^{-250}.$$

Testing the classical Gauss method, the number of iterations grows as the spreads between observations or more restrictive tolerances do. In the test of these variants of the Gauss method, it is observed that they strongly reduce the number of iterations and the elapsed time, making the process faster even when limiting tolerances are used. Moreover, 2-dimensional methods show to be more stable when higher spreads in the observations of the satellites are involved. Nevertheless, the small size of the system and the near-singularity of its jacobian matrix avoid a better behavior of the new fifth-order method.
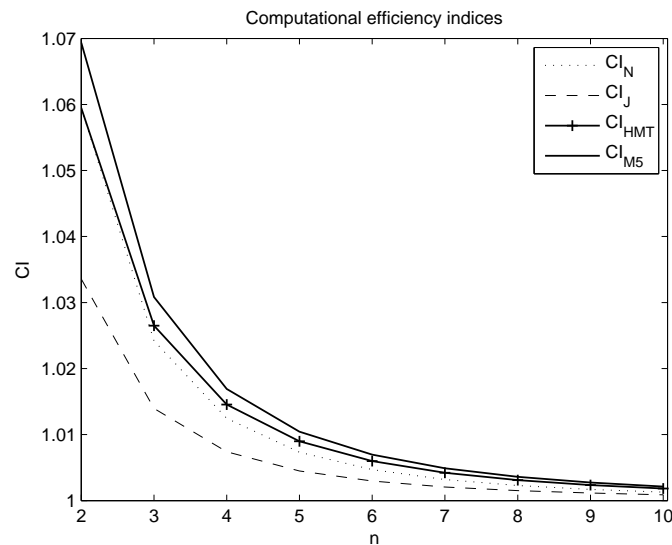
Figure 2: Computational efficiency indices.

References

[1] Cordero, A., Hueso, J.L., Martínez, E. and Torregrosa, J.R. New modifications of Potra-Pták's method with optimal fourth and eighth order of convergence, *Journal of Computational and Applied Mathematics*, 234: 2969–2976, 2010.

[2] Cordero, A. , Hueso, J.L., Martínez, E. and Torregrosa, J.R. A modified Newton-Jarrattt's composition, *Numerical Algorithms*, 55: 87–99, 2010.

[3] Danby, J.M.A. Fundamentals of Celestial Mechanics. The MacMillan Company, 1962.

[4] Escobal, P.R. Methods of Orbit Determination. Robert E. Krieger Publishing Company, 1975.

[5] Hueso, J.L., Martínez, E. and Torregrosa, J.R. Third and fourth order iterative methods free from second derivative for nonlinear systems, *Applied Mathematics and Computation*, 211: 190–197, 2009.

[6] Jarratt, P. Some fourth order multipoint iterative methods for solving equations, *Mathematical Computation*, 20: 434-437, 1966.

[7] Kung, H.T. and Traub, J.F. Optimal order of one-point and multi-point iteration, *Applied Mathematics and Computation*, 21: 643–651, 1974.

[8] Ostrowski, A.M. Solutions of equations and systems of equations, New York-London, Academic Press, 1966.

Towards the visualization of water supply system components with GPR images*

D. Ayala–Cabrera[‡†], M. Herrera[‡], J. Izquierdo[‡]
and R. Pérez–García[‡]

([‡]) FluIng-IMM, Universidad Politécnica de Valencia,

C. de Vera s/n, 46022 Valencia, Spain.

October 10, 2010

1   Introduction

Water supply systems (WSS) are mainly composed of pipes, valves, reservoirs, and other ancillary elements. Knowledge of these components and any changes suffered are necessary to control and productively manage the system. The aims of this approach include: detect illegal connections; estimate lost water volumes; simulate system scenarios; study pollutant evolution in the network; and examine rehabilitation strategies. This work proposes a first step towards developing a tool for identifying unknown component characteristics in urban WSS. It is based on the use of ground penetrating radar (GPR) as a non-invasive technique enabling buried objects to be detected without altering the environment [2].

The aim of this paper is to generate a tool to help recognize WSS components with GPR images. To this end, we have studied the wave amplitude parameter for buried pipes. In laboratory tests we have analyzed the effect of different environment conditions on GPR signal propagation [1].

2   An approach to GPR

GPR prospection is based on the emission of electromagnetic pulses from the surface which are propagated and reflected by the discontinuities encountered underground. This technique can reveal interfaces between the different materials, provided there is sufficient contrast between the dielectric properties of the materials. The energy of the reflected

---

[†]contact e-mail: daaycab@upv.es

pulse is measured on the surface by receiving devices. The time needed for the pulse to travel from the surface and return provides a measurement of the depth of a given reflector, given the positions of the source and receiver and the propagation speed of the pulses in a given soil type. Secondly, a comparison between amplitudes of emitted and received pulses provides additional information about the composition of the subsoil.

GPR is a technique that has the advantage of great resolution and an ability to detect non-magnetic objects through environmental signals. These signals, called traces, are captured at fixed times and contain electromagnetic characteristics of the traversed medium. The subsequent accumulation of traces leads to what is known as radargrams, which are generally displayed using color or grey scales to generate images. This last aspect is of interest because our analysis is based on GPR images.

3 Methodology

The method we propose is based on the wave amplitude parameter, which is taken as input and divided into ranges of values to be rebuilt into new matrices. This process gathers various characteristics of the sought anomalies and produces clean images. The aim is to generate tools based on intelligent training systems to efficiently apply GPR technology to WSS. Thus, the process takes raw data as input and follows two procedures: a) a matrix-visualization process; and b) the construction of a classifier. The first procedure builds the so-called $T14$ and $T15$ matrices [1] and comprises four phases: WAV classification, WAV extraction, WAV accumulation, and WAV rebuilding. The second procedure takes as inputs the $T14$ (or $T15$) of generated matrices and uses multi-agent methods to locate the pipes within the images.

4 Results

The GPR images without post-processing (raw matrices) are compared with the $T14$ and $T15$ matrices resulting from the applied procedures on raw data (see an instance of $T14$ application in Figure 1). To generate the possibility of making a visual contrast between the pipe images and a reference image we performed a reference test without a pipe, under the same environmental conditions.

We can see how the color intensity due to material contrast (resulting from the signal passage through soil-pipe-soil) reveals the non-plastic pipes when compared with the raw results (Figure 1). Note the intensity of the color images representing asbestos cement and cast iron pipes, the intensity being weaker for the plastic tested pipes (PVC, PE). However, while PVC and PE pipes are visible in Figure 1, the contrast of the boundaries is not strong enough for them to be seen at a glance.

Based on $T14$ (or $T15$) images we want to be able to detect the presence of pipes and their location. To achieve this we carried out a multi-agent based process with the GPR images of the PVC pipes. The multi-agent location algorithm is implemented in the
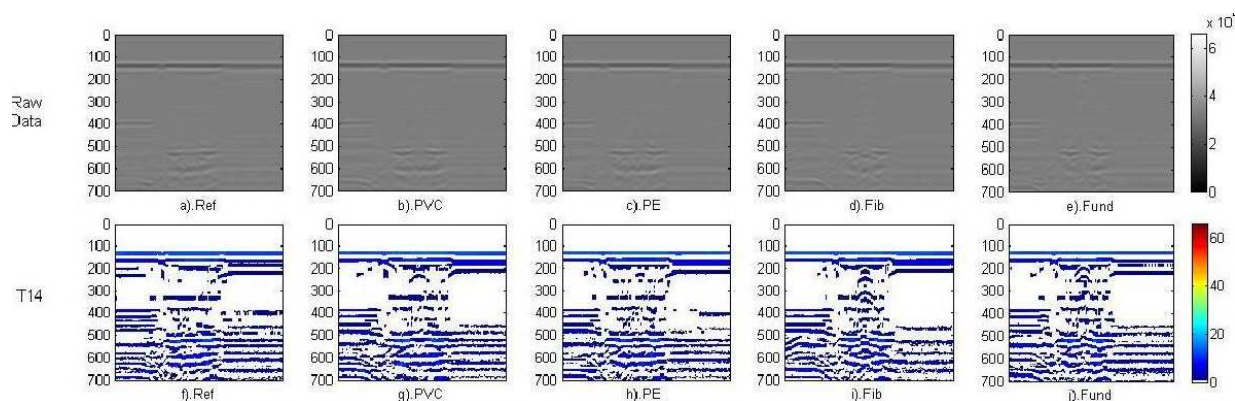
Figure 1: Raw image and $T14$ images obtained with GPR.

NetLogo platform [3] and the developed software is customizable by users. We tested this multi-agent location process on 40 $T14$ and 40 $T15$ images of PVC pipes. In more than 95% of the instances the process successfully detected the pipes with both matrices. The final output with this multi-agent process should be the pipe alone (perhaps with some surrounding noise). These pixels are shown as red and placed over the original image (see Figure 2).
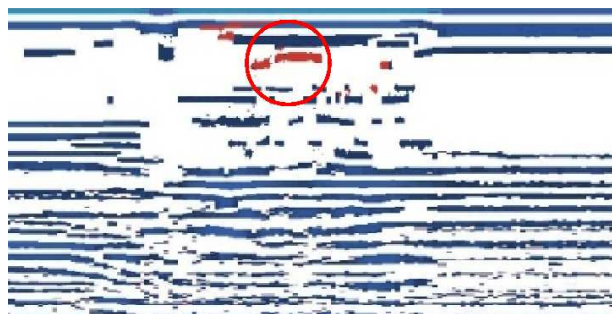
Figure 2: An instance of $T14$ PVC image and multi-agent location output.

5 Conclusions

The transformation of raw data based on the $T14$ and $T15$ matrices improves the visualization of plastic pipe images by producing a better representation of the signal characteristics. In addition, we propose an automatic pipe location method that uses multi-agent systems. This takes advantage of the facilities offered by the $T14$ and $T15$ image representations. The developed methodology is efficient with computational resources and accurate in its results (even in the complex case of plastic pipes).

Finally, it should be noted that this is a simple process that does not depend on specialist skills (being a non-subjective process) and is repeatable. Also, with appropriate

adjustments, the radargrams enable the parameterization of supply pipe systems and this can serve as a basis for intelligent training systems.

References

[1] D. Ayala-Cabrera, Caracterización de tuberías enterradas para redes de abastecimiento en servicio mediante el análisis de imágenes obtenidas con radar de subsuelo (Ground Penentrating Radar - GPR). Master Thesis - Polytechnic University of Valencia, Valencia Spain, 2009

[2] Pasolli, E., Melgani, F., Donelli, M. A pattern recognition system for extracting buried object characteristics in GPR images. *Geoscience and Remote Sensing Symposium*, 430–433, 2009.

[3] A. Wilensky, NetLogo. http://ccl.northwestern.edu/netlogo/, Northwestern University - Evanston, 1999

Low-Rank Update of Preconditioners for the Inexact Newton Method with SPD Jacobian

L. Bergamaschi[†], R. Bru,[*‡] and A. Martínez[†]

October 20, 2010

1   Introduction

In this note we are mainly concerned with the efficient preconditioning of the linear system arising in the Newton iteration for the solution of a general system of nonlinear equations: $\boldsymbol{F}(\boldsymbol{x}) = 0$, which is usually written as

$$\begin{cases} J(\boldsymbol{x}_k)\boldsymbol{s}_k & = & -\boldsymbol{F}(\boldsymbol{x}_k) \\ \boldsymbol{x}_{k+1} & = & \boldsymbol{x}_k + \boldsymbol{s}_k \end{cases}. \tag{1}$$

In a number of applications such as e. g., unconstrained optimization, or discretization of nonlinear PDEs with Picard linearization, J is symmetric positive definite (SPD). When in addition J is large and sparse, the preconditioned Conjugate Gradient (PCG) method can be employed for the solution of the linear system, so that two nested iterative procedures need to be implemented, the outer iteration formed by the Newton steps and the inner iterations of the PCG method. Since in each Newton step a new system has solved, we are dealing with the construction of a sequence of preconditioners P_k which are "optimal" in the sense that they would minimize the constant C of:

$$\|I - P_k J(\boldsymbol{x}_k)\| \le C. \tag{2}$$

One would like C to be as small as possible or even to tend to zero as $k \to \infty$. This requires that information from the nonlinear iterative scheme be taken into account in the evaluation

---

of P_k. In particular, the secant condition should be satisfied by those preconditioners. Then, instead to construct a new preconditioner of the corresponding Jacobian in each outer iteration we propose to update an initial preconditioner using information of the Newton method. The approach proposed in this note follows the line of a previous work [1] where the authors have shown to accelerate the Inexact Newton method by a Broyden-type rank-one of a preconditioner of choice. It is worth to mention that this technique can be considered in the framework of e.g. the paper [7] by J. M. Martínez. In this note our aim is to solve the SPD system (1) with the PCG method, starting with an initial preconditioner, in our case either IC(0)or AINV preconditioners, computed from the initial Jacobian, and to update this preconditioner using low-rank matrices. A sequence of SPD preconditioners P_k can thus be defined by imposing the secant condition, as used in the implementation of quasi-Newton methods [4]. We choose to work with the BFGS update as described for instance in [5], and analyze the theoretical properties of the preconditionerand the numerical behavior of the resulting scheme. The idea is to start with a preconditioner $P_0 = B_0^{-1} \approx J_0^{-1}$. If the preconditioner is under the form of a sparse approximate inverse P_0 is known explicitly, otherwise, if $B_0 = \tilde{L}\tilde{U}$ is an incomplete LU factorization, we only can compute P_0 times a vector by solving two triangular sparse linear systems. Let us define $\boldsymbol{y}_k = \boldsymbol{F}(\boldsymbol{x}_{k+1}) - \boldsymbol{F}(\boldsymbol{x}_k)$ and recall that $\boldsymbol{s}_k$ is the solution of the kth Newton system. Following [6] we can develop a similar recurrence formula for the preconditioner as

$$P_{k+1} = P_k + \frac{\boldsymbol{y}_k \boldsymbol{y}_k^T}{\boldsymbol{s}_k^T \boldsymbol{y}_k} - \frac{P_k \boldsymbol{s}_k \boldsymbol{s}_k^T P_k}{\boldsymbol{s}_k^T P_k \boldsymbol{s}_k} P_{k+1} = \left(I - \frac{\boldsymbol{s}_k \boldsymbol{y}_k^T}{\boldsymbol{s}_k^T \boldsymbol{y}_k}\right) P_k \left(I - \frac{\boldsymbol{y}_k \boldsymbol{s}_k^T}{\boldsymbol{s}_k^T \boldsymbol{y}_k}\right) + \frac{\boldsymbol{s}_k \boldsymbol{s}_k^T}{\boldsymbol{s}_k^T \boldsymbol{y}_k}. \quad (3)$$

If the Jacobian matrices are SPD and P_0 is so, thenalso P_k is SPD under the condition $\boldsymbol{s}_k^T \boldsymbol{y}_k > 0$ (see Lemma 4.1.1 in [6]).It can also be easily proved that the sequence of matrices just defined satisfy the secant condition

$$P_{k+1} \boldsymbol{y}_k = \boldsymbol{s}_k$$

In the next section we will prove that $\|I - P_k J(\boldsymbol{x}_k)\|$ can be made as small as possible by suitable choices of the initial guess $\boldsymbol{x}_0$ and the initial preconditioner P_0. Note that this makes our preconditioner almost ideal in the sense of (2).

2   Convergence results

From now on we will also denote the preconditioner matrix and its inverse by B_k^{-1} and B_k, respectively and use the *standard assumptions* on $\boldsymbol{F}$ as e.g. in [5].

Moreover, we assume in the sequel that our preconditioner accelerates the Newton systems in the framework of the Inexact Newton methods [3]. We therefore stop the linear iteration as soon as the following test is satisfied

$$\|J(\boldsymbol{x}_k)\boldsymbol{s}_k + \boldsymbol{F}(\boldsymbol{x}_k)\| \le \eta_k \|\boldsymbol{F}(\boldsymbol{x}_k)\|. \quad (4)$$

The sequence $\{\eta\}$ will be chosen such that $\eta_k = O(\|\boldsymbol{F}(\boldsymbol{x}_k)\|)$. This will guarantee quadratic convergence of the Inexact Newton method and as a consequence, the following result.

Proposition 2.1 *Let the standard assumptions hold, and define $\boldsymbol{e}_k = \boldsymbol{x}^* - \boldsymbol{x}_k$. There exist $\delta > 0$ and $r < 1$ such that if $\|\boldsymbol{e}_0\| < \delta$ then $\|\boldsymbol{e}_{k+1}\| \leq r\|\boldsymbol{e}_k\|$ for every k.*

It is now convenient to indicatewith the subscript c every vector or matrix referring to the current iterate and with the subscript $+$ every quantity referring to the new iterate $k+1$. We can define the error vectors as $\boldsymbol{e}_+ = x^* - x_+, \quad \boldsymbol{e}_c = x^* - x_c$. Now we state the main convergence results:

Lemma 2.2 *Let the standard assumptions hold and $\|\boldsymbol{e}_c\| \leq \delta$. Then setting*

$$E'_+ = B_+^{-1} - J_+^{-1}, \quad and \quad E'_c = B_c^{-1} - J_c^{-1}$$

we have, for some $K_1 > 0$,

$$\|E'_+\| \leq \|E'_c\| + K_1\|\boldsymbol{e}_c\|$$

The following theorem establish that $\|I - B_+^{-1}J_+\|$ can be made arbitrarily small provided that $\|\boldsymbol{e}_0\|$ and $\|E'_0\|$ are sufficiently small.

Theorem 2.3 *Let the standard assumptions hold. Fixed $\varepsilon_1 > 0$, then thereare δ_0, δ_B such that if $\|\boldsymbol{e}_0\| < \delta_0$ and $\|E'_0\| < \delta_B$ then*

$$\|I - B_+^{-1}J_+\| < \varepsilon_1.$$

3 The Newton-BFGS Algorithm

Following [3], the implementation of the Inexact Newton method requires the definition of a stopping criterion for the linear solver (4) based on the nonlinear residual. More precisely, we stop the linear iteration using the following test

$$\|J(\boldsymbol{x}_k)\boldsymbol{s}_k + \boldsymbol{F}(\boldsymbol{x}_k)\| \leq \eta_k\|\boldsymbol{F}(\boldsymbol{x}_k)\|. \tag{5}$$

Superlinear or even quadratic convergence of the Inexact Newton method can be achieved by properly setting the sequence $\{\eta_k\}$. We can now write the Newton-BFGS Algorithm as follows: If the number of nonlinear iterations is high (e.g. more than ten iterations),the application of BFGS preconditioner may be too heavy to be counterbalanced by a reduction in the iteration number. To this aim we define $k_{\max}$ the maximum number of rank two corrections we allow. When the nonlinear iteration counter k is larger than $k_{\max}$, the vectors $\boldsymbol{s}_i, \boldsymbol{y}_i, \ i = k - k_{\max}$ are substituted with the last computed $\boldsymbol{s}_k, \boldsymbol{y}_k$ and a new preconditioner B_0^{-1} is computed.

NEWTON-BFGS (NBFGS) ALGORITHM
Input: $\boldsymbol{x}_0, \boldsymbol{F}, nlmax$, toll

- WHILE $\|\boldsymbol{F}(\boldsymbol{x}_k)\| > \text{toll} \|\boldsymbol{F}(\boldsymbol{x}_0)\|$ AND $k < nlmax$ DO

  1. Compute $B_0(B_0^{-1})$ approximating $J_0(J_0^{-1})$; $k = 0$
  2. IF $k > 0$ THEN update B_k^{-1} from B_{k-1}^{-1}.
  3. Solve $J(\boldsymbol{x}_k)\boldsymbol{s}_k = -\boldsymbol{F}(\boldsymbol{x}_k)$ by a Krylov method (CG) with preconditioner B_k^{-1} and tolerance η_k.
  4. $\boldsymbol{x}_{k+1} := \boldsymbol{x}_k + \boldsymbol{s}_k$
  5. $k := k + 1$

- END WHILE

4   Summary of Results

Our first numerical experiments onto unconstrained minimization problems show that this algorithm provides an improvement of the performance compared with the IC or AINV or even the diagonal as initial preconditioners, and this is particularly efficient for small values of the restart parameter $k_{\max}$. The proposed technique has a number of advantage on simply computing a preconditioner of $J(\boldsymbol{x}_k)$: (a) it reduces the number of iterations at least for small $k_{\max}$ values; and (b) it reduces the cost of forming the preconditioner. As a consequence, we expect that this technique, together with the one developed in [1], could be particularly effective e. g., in the interior point (IP) solution of constrained optimization problems, where linearized saddle-point Newton systems are very ill-conditioned toward the solution and the cost of the preconditioner computation may be prohibitive (see [2]). Finally, the update procedure is well suited to parallelization since it is based on scalar products and daxpy operations.

References

[1] L. Bergamaschi, R. Bru, A. Martínez, and A. Putti, Quasi-Newton preconditioners for the inexact Newton method, *Electronic Trans. Num. Anal.* 23 (2006) pp. 76-87.

[2] L. Bergamaschi, J. Gondzio, and G. Zilli, Preconditioning indefinite systems in interior point methods for optimization, *Comput. Optim. Appl.* 28 (2004) pp. 149-171.

[3] R. S. Dembo, S. C. Eisenstat, and T. Steihaug, Inexact Newton methods, *SIAM J. Num. Anal.* 19 (1982) pp. 400-408.

[4] J. E. Dennis, Jr. and J. J. Moré, Quasi-Newton methods, motivation and theory, *SIAM REv.* 19 (1977), pp. 46-89.

[5] C. T. Kelley, Iterative Methods for Linear and Nonlinear Equations, SIAM, Philadelphia, 1995.

[6] C. T. Kelley, Iterative methods for optimization, vol. 18 of Frontiers in Applied Mathematics, Society for Industrial and Applied Mathematics (SIAM), Philadelphia, PA, 1999.

[7] J. M. Martínez, An extension of the theory of secant preconditioners, *J. Comput. Appl. Math.* 60 (1995) pp. 115-125. Linear/nonlinear iterarive methods and verification of solution (Matsuyama, 1993).

Sector concentration risk: a model for estimating capital requirements

J. David Cabedo[*], and José Miguel Tirado

(*) Universidad Jaume I,

Departamento de Finanzas y Contabilidad

Av. Vicent Sos Baynat s/n E12071 Castellon (Spain).

October 10, 2010

1   Introduction

The Basel Committee on Banking Supervision issued in 2004 the Basel II Accord, containing a series of capital adequacy rules. Its first part (pillar one) contains the rules for determining the amount of regulatory capital required to banks for their exposure to credit risk. These rules do not consider the degree of concentration of the credit portfolio. That is why, according to pillar two, the supervisory authorities can fix a concentration surcharge for the credit risk capital requirements estimated in pillar one. There are two kinds of portfolio concentration ([1]): sectorial and name concentration, both stemming from the violation of the hypotheses assumed by the Asymptotically Single Risk Factor (ARSF) model. Therefore, some research has focused on introducing modifications into this model in order to estimate the concentration risk (see [2]). Other papers, [3], [4] and [5], simulate portfolios to estimate the economic capital within a concentration environment. Some papers, as [6] and [7], highlight the importance of sectorial concentration for calculating the economic capital needed to cover credit risk. For this, it is necessary not only to consider the degree of concentration in specific sectors but also the relationships between them. Finally, stemming from a different research path, [8] propose an index for quantifying name concentration in a credit portfolio. Our research follow a parallel path: we develop a sector concentration index that can be used for estimating the concentration surcharge for credit risk capital requirements.

---

[*]e-mail:cabedo@cofin.uji.es

2   The ASRF model

In accordance with the IRB method of pillar I, the minimum capital requirements for credit risk must be calculated as a function of a series of variables, of which the proportion of securities defaulted, is the key one. This must be estimated as follows:

$$x = N \left[\frac{\sqrt{\rho}}{\sqrt{1-\rho}} \cdot N^{-1}(0,999) + \frac{1}{\sqrt{1-\rho}} \cdot N^{-1}(PD) \right] \tag{1}$$

Where ρ denotes the constant coefficient of correlation between every pair of assets belonging to the credit portfolio; PD is the probability of default; and N represents de cumulative distribution function of a standard normal distribution. Expression (1) can be derived from the ARSF model, which is based on the Merton's model. Merton stated that a company attends its payment obligations when the value of its assets is higher than the value of its liabilities. If this is not the case, companies prefer to default. Therefore, for the company i, the probability of defaulting can be modelled as the probability of the value of its assets (AV_i) falling below that of its liabilities (LV_i).

$$PD = P[AV_i < LV_i] \tag{2}$$

Factor models use expression (2) as the starting point, modelling the value of the assets through a series of factors. One of these models is the ASRF model, which assumes the following hypothesis:

- Hypothesis 1: The value of a company's assets depends on a unique risk factor, which is the same for all firms. Furthermore, the model assumes that the correlation coefficient for every pair of exposures (ρ) remains constant.

- Hypothesis 2: The loss threshold is the same for all borrowers. Under this hypothesis, as we demonstrate, the conditional default probability is the same for all debtors.

- Hypothesis 3: Granularity. The number of debtors included in the bank portfolio is large enough for no single debtor to be able to affect significantly the value of the portfolio.

We demonstrate that when we predetermine a 99.9

3   Concentration risk: a supervisory approach

Concentration risk has traditionally been covered by limiting the amount of exposure to any single debtor. This is the approach stated in the Spanish banking regulation. However the Committee has not followed the path of limiting exposures to guarantee bank solvency. It has preferred to do so by requiring a minimum amount of capital for this aim. Nevertheless Basel II has not envisaged any minimum capital requirement for concentration risk. Why? Because of the hypotheses assumed by the model used for quantifying credit risk

capital requirements (which were highlighted in the preceding section). These hypotheses allow the use of the model by a wide range of entities. This is an advantage, but it also involves a drawback: the exclusion of concentration risk. That is why the Committee has envisaged additional capital requirements within Pillar two, and supervisory authorities are currently carrying out a series of analysis to determine the method for calculating the capital requirements for risk concentration. In Spain banks will choose between the following two possibilities:

- A general approach, with banks using their own methods for quantifying the capital surcharge for their portfolio concentration.

- A simplified approach, with surcharge calculated by means of two predetermined concentration indexes: one for name concentration and the other for the sectorial concentration.

Name concentration derives from large exposures to the same debtor. This was actually the only kind of concentration contemplated by the traditional approach when seeking to limit exposures. The need for a capital surcharge for this kind of concentration arises from the violation of one of the hypotheses of the ASRF model: the granularity one. The non-fulfilment of other hypothesis (default depending on a unique risk factor) brings about the need for an additional surcharge to deal with sectorial concentration . In this area and within the simplified approach, the Spanish supervisory authorities require the application of the Herfindahl Hirschman Index (HHI), a generic concentration measure.

4   Proposal of an index

The HHI measures suitably the level of concentration, but there is an important drawback: exposures to all sectors are equally weighted. This is not valid for a credit portfolio. Think in terms of economic sectors; some industries are riskier than other, and concentration in the riskiest sectors does not have the same implications as concentration in low risk sectors. The former, being worse, require a higher capital reserve for solvency purposes. Banks, therefore, need an index that weights exposures relative to each sector's risk. Furthermore, this index must also consider the relationship between every pair of sectors: the value of the index must be higher when portfolio concentration is greater in highly correlated sectors. Our proposal for a concentration index (CI) meets both requirements. It can be expressed as follows:

$$CI = SH^T \cdot VCM \cdot SH \tag{3}$$

Where SH represents the vector of the fractions of exposure to each sector and VCM is an adjusted variance-covariance matrix, where:

- Variance and covariance have been adjusted by the maximum variance.

- Negative covariances have been treated as null ones because we are not seeking a full quantification of portfolio risk, but rather, a quantification of risk weighted factors. To this end, positive correlations must not be compensated by negative ones.

CI has some properties, proved in the paper, that make it appropriate for portfolio concentration risk.

- Property 1: The maximum CI is reached when all the portfolio investments are located in the maximum variance sector.

- Property 2: When introducing exposures in a new sector into a portfolio, the index will decrease only when the risk (variance) of the new sector is lower than the portfolio's original variance.

- Property 3: CI has a lower boundary.

We must emphasize that we have defined CI in the context of concentration on economic sectors. But it can easily be extended to geographical concentration. We only need to introduce specific risk factors (sectors) for these areas and proceed with them as with the other sectors. Summarizing, the proposed index may be used by banks to determine their capital surcharges for concentration risk.

References

[1] Kalkbrener, M. An axiomatic approach to capital allocation *Mathematical Finance*, 15 (3): 425—437, 2005

[2] Garcia, J.C., de Juan, J.A., Kreinin, A., and Rosen, D., A Simple Multi-Factor Factor Adjustment for the Treatment of Diversification in Credit Capital Rules. Workshop Concentration Risk in Credit Portfolios, Frankfurt/Eltville, 2005.

[3] Düllmann, K. Measuring business sector concentration by an infection model *Deutsche Bundesbank Discussion Paper Series 2: Banking and Financial Studies* No 3, 2006.

[4] Pykhtin, M. Multi-factor adjustment *Risk Magazine*, March: 85—90, 2004

[5] Düllmann, K., and Masschelein, N. A Tractable Model to Measure Sector Concentration Risk in Credit Portfolios *Journal of Financial Services Research* 32 (1-2): 55—79, 2007

[6] Düllmann, K., and Masschelein, N. The impact of sector concentration risk in loan portfolios on economic capital *Financial Stability Review. National Bank of Belgium*, 2006: 175—186, 2006.

[7] Bonti, G., Kalkbrener, M., Lotz, C., and Stahl, G. Credit risk concentrations under stress Workshop 'Concentration Risk in Credit Portfolios': Frankfurt/Eltville, 18-19 November 2005.

[8] Uberti, P., and Figini, S. How to measure single-name credit risk concentrations *European Journal of Operational Research* 202: 232—238, 2010.

Mathematical Model for shape voids optimization in precast breakwater structures

Esteban Camacho[a], Maria Luisa Pérez[a], Javier Camacho[b]

[a] ICITECH, Edificio Caminos II – [b] Instituto de Matemática Multidisciplinar.
Universidad Politécnica de Valencia, Camino de Vera s/n – 46071 – Valencia (Spain)

October 10, 2010

1. Introduction

Vertical breakwaters are offshore structures used to protect harbors or coastal areas against the wave effect. These are made out of concrete tetrahedral blocks which are aligned longitudinally. Each block is casted on structures over the sea and transported floating over the water thanks to voids (rectangular or circular) that confer relative density lower than 1. This also entails a positive saving of concrete, used in massive volumes. In the sinking process the voids are filled with water, and for the definitive placing with low quality soils. This procedure requires specific offshore platform structure for different block dimension and results tricky and slow.

Here precast concrete elements are proposed to compose vertical breakwaters. With this system, the construction process is more flexible and the concrete is so far better controlled. The shape of the pieces can be more variable than in situ breakwaters.

It's useful to deduce the shape that provides the higher stiffness with the same volume of concrete used. This is the query which this paper tries to answer, analyzing four structure geometries and their slenderness variation submitted to different loads. The strain energy will be used to establish a comparison between the global work developed.

1.1 The direct stiffness Method

In the 30's Collar & Duncan presented the matrix systems which are the base of the called Direct Stiffness Method (DSM). Forces in the nodes of an isotropic beam[i] can be related with their displacements using a matrix equation K, called stiffness matrix (1).

$$[f^{(i)}] = [k^{(i)}] \cdot [u], \qquad [u] = [k^{(i)}]^{-1} \cdot [f^{(i)}]$$

(1), (2)

The matrix K is a function of the mechanical/geometrical properties of the element. The displacements can be expressed depending on the forces applied (2). This can be condensed in blocks of 3x3 elements, in terms of the nodes where the loads and displacements are produced. The matrix K is a 2nd order tensor, and it can be expressed in different covariant bases ($\overline{e_i}$ and $\overline{e_{i'}}$), which depends on the coordinate system chosen, which can be changed with the rotation matrix.

In 1954, J. H. Argyris systemized a method assembling elemental components of a structure, each one with its own stiffness matrix $k^{(i)}$, into a system of equations. This means to build a global stiffness matrix adding the matrices of the single elements. The resultant $[K]_{aNxaN}$ matrix governs the behavior of the entire idealized structure. The force-displacement

expression is similar than (1). The global load vector, as the K global matrix, has to be assembled, adding the appropriated values in the correct locations of the vector $[f]$. $[K]$ has the same properties than $[K]^{(i)}$.

[K] must be reduced to consider the boundary conditions, solving the matrix equation with the unknown displacements. When this is obtained, the reactions of the nodes are obtained direct because all the displacements are known.

The evaluation of the stiffness of the elements was made through of the strain energy, which is obtained using the DSM. This is useful because by means of the single value of strain energy, the total deformability of the elements against a load is quantified. This was expressed by Clayperion with (14). Energy is expressed such a quadratic function of the nodes displacements.

$$U_{ab} = \frac{1}{2} \cdot [f']^T \cdot [u'] = \frac{1}{2} \cdot [u']^T \cdot [K'] \cdot [u']$$

(14)

2. Process developed

In this document is analyzed the effect of the concrete block geometry in the global work capacity developed by a load. The displacements of the nodes are obtained with the DSM. The Strain energy is obtained with Clayperion formula and used to evaluate the global stiffness for the different sea loads. The evolution of this value is analyzed when the slenderness (a/b) of the structures is modified for four different geometries. With this, it is possible to obtain the geometry with higher stiffness, fact that imply important costs saving of the structure.

2.1 Variables modified

Four main simple geometries are proposed with rigid unions and divided by a number of elements between 8 and 14, remaining constant the parameters of the table. The values used for this study were the common dimensions for a conventional dike block.

$V = 40\ m^3$	$a \cdot b = 37.5\ m^2$	$Depth = 1\ m$	$E_c = 40000\ MPa$	$h \propto L$

The thickness of the bars has been distributed proportionally to the length of each bar. The slenderness of the elements (a/b) has been modified adopting the values 0.125, 0.25, 0.5, 0.75, 1, 2, 3, 4, 5, 6, 8, 10, 15 and 20, and the thickness of the bars for every slenderness value was obtained modifying a factor **c** and conditioning to the constant volume of concrete.

The loads applied were punctual symmetric and asymmetric (1 N), hydrostatic distributed for 1 m of depth (0.0098 N/m^2) and wave distributed in the side where it impacts
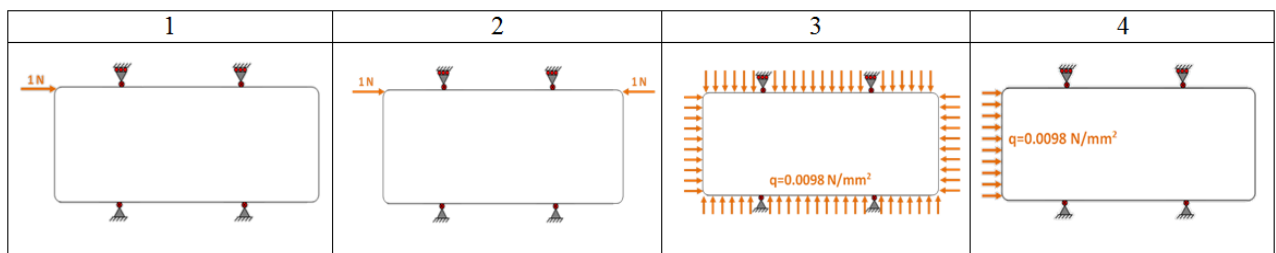
(0.0098 N/m^2).

The strain energy obtained for this last case load has been divided by the length of the bar where is acting (the value of b), because the load applied is proportional to this length. The magnitude of the loads doesn't affect to the final conclusions, because the strain energy has a quadratic relation with this value, and the differences between values of the studied elements remain proportional.

All this process was developed in four Excel files, where the strain energy was obtained immediately for every change. The four geometries proposed were: Triangular model; proposed in order to take the full advantage of the triangle, which constitutes the only polygon stable articulated at all the nodes. Rectangular model; this shape has been considered as the one which represents the most common void scheme used actually at in-situ breakwaters. Saint Andrew Cross model; the element has diagonal bars connecting corner nodes, which create four triangular dispositions that could increase the stiffness. Mixed model; this shape takes the diagonal concept from the previous one, but reducing the length thanks to the angle of the
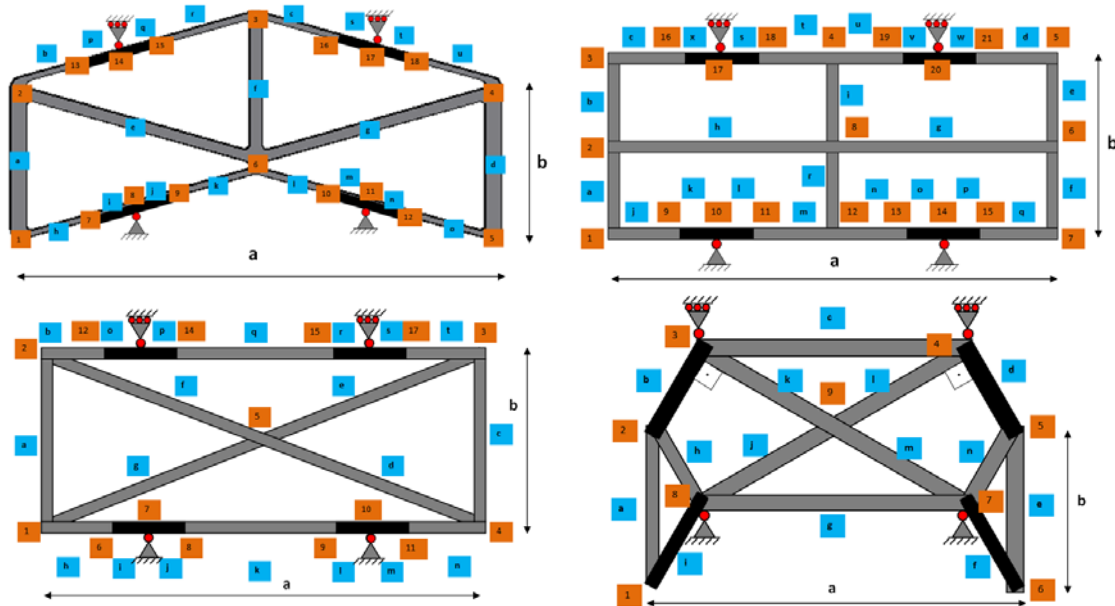
lateral bars.

It has to be considered that the concrete is distributed in length and thickness, so the shorter the total length of the bars, the higher the thickness, and a priori the higher the stiffness. If the total sum of the bars is studied modifying the slenderness, it can be observed that the rectangular model is the one that provides the lower values. This means that we could expect that the highest stiffness is provided by the rectangular shape with slenderness 1.

3. Analysis of the results

In the graphs 1 to 4 can be seen the results for 1 N asym. load, 1 N sym. load, hydrostatic and wave distributed load respectively. It shows the variation of the strain energy (Y axis) when the slenderness is modified for the different geometries and different loads. It's remarkable that the suitability of the bar geometries proposed, changes with the type of the load applied (symmetric or asymmetric, punctual or distributed). For the 1 N asymmetric load the lower strain energies are provided by triangular and mixed models, with optimum slenderness of 3 and 2 respectively. The rectangular seems to be more sensible to the slenderness variation due to the distortion created in the absence of triangular connections. On the other hand, for the 1 N symmetric loads, the absence of distortion generates for all the models almost the same strain energy evolution.

With regard to hydrostatic distributed load, which is symmetric, the rectangular geometry provides the slower value of strain energy. This is because in the absence of distortion, the geometry with thicker walls provides higher stiffness. For wave distributed load (asymmetric), the best geometry is the triangular, with an optimum slenderness for values higher than 3. Mixed model is suitable for slenderness=2, but has a big sensibility to change this parameter.
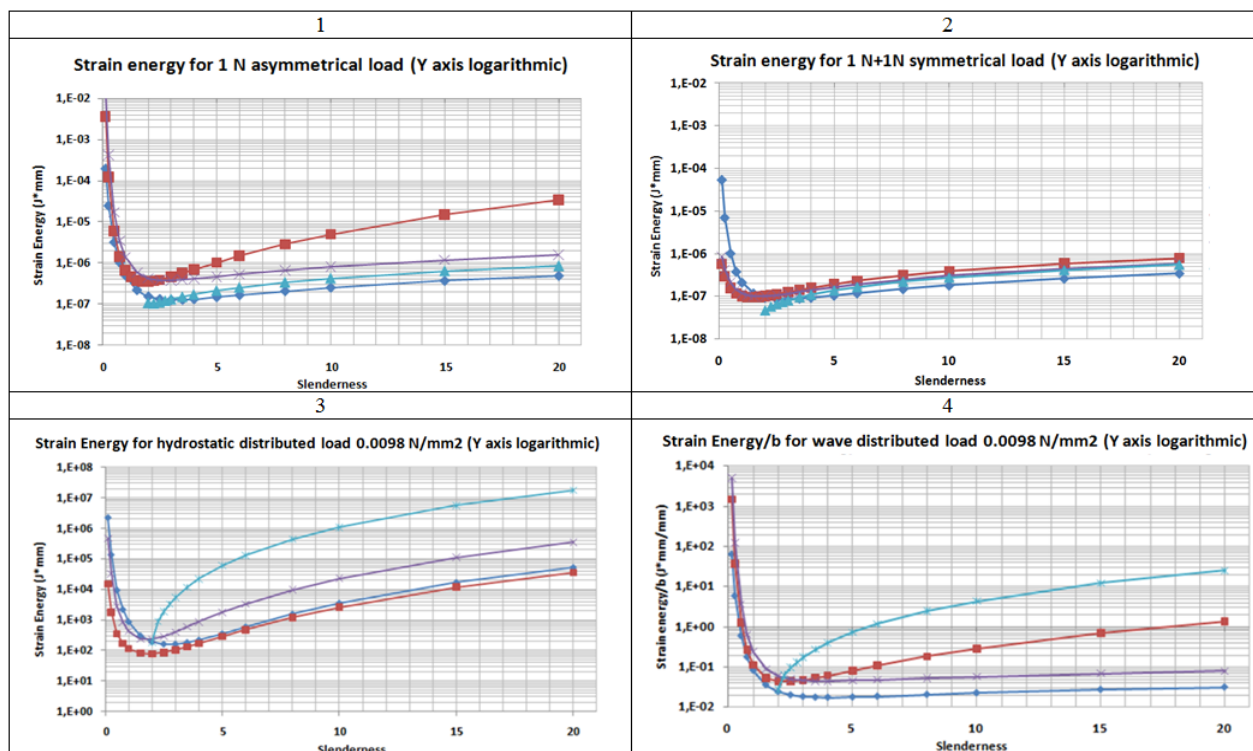
Global results show that geometries with triangulations, mainly the triangular, are very suitable for asymmetric loads. The rectangular geometry provides the best structural behavior with symmetric loads, like the hydrostatic pressure of the water. For the coasts with high waves comparing with the water depth, the triangular elements will be more suitable, while for the coasts with high depth and calm sea the most suitable shape is the rectangular. To deduce this, the strain energy can be obtained for different depths with the combination of all the sea loads. The autors studied cases for different seas, approaching the most cost-saving geometry.
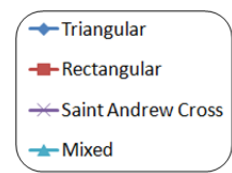
4. Conclusions

The optimum geometry and slenderness of these elements against different loads can be obtained with the Direct Stiffness Method. The most adequate precast elements for calmed sea will be the rectangular, with a slenderness $\cong$ 2. For regions with high waves comparing to the depth of the sea the best geometry is the triangular, with slenderness higher than 3. The mixed model is also suitable for all the loads, but only with slenderness 2.

References

[1]   Puertos del Estado. Manual para el diseño y la ejecución de cajones flotantes de hormigón armado para obras portuarias, 1999.
[2]   E. L. Wislon. Static & Dynamic analysis of Structures, Fourth Edition, Professor Emeritus of Civil Engineering, University of California, Berkeley.

[3]   G. Cuomo. Breaking wave loads at vertical seawalls & breakwaters. Coastal Engineering 57.

[4]   Marti Montrull, Pascual. Análisis de estructuras: Métodos clásicos y matriciales, 2003.

Mathematical model to determine Geometric Consistency in order to evaluate road safety

Camacho Torregrosa, Francisco Javier* *, Perez Zuriaga, Ana Maria†,
and Garcia Garcia, Alfredo‡

(*)Universidad Politecnica de Valencia, Spain,

fracator@posgrado.upv.es,

(†) Universidad Politecnica de Valencia, Spain,

anpezu@tra.upv.es,

(‡) Universidad Politecnica de Valencia, Spain,

agarciag@tra.upv.es.

October 10, 2010

1   Introduction

Road fatalities are one of the most important problems in our society, causing thousands of victims every year in the entire world. Three items may have influence in the appearance of a road accident: human factor, vehicle and the road. In fact, it is estimated that the road is behind over the 30% of the total amount of crashes. Note that if road wasnt a factor involving accidents, they would tend to spread in a random way along the road network. Road geometric consistency can be defined as how drivers expectancies and road behavior fit. Thus, a road with a good consistency level is the one in which its behavior and what drivers expect are very similar, so they wont be surprised while driving along them. A poor consistency means bad fitting, lots of surprises while driving and also high speed variability along different road segments and among different drivers. This concept is important because road consistency is highly related to crash rates. In order to make a road safer, we can improve its geometric consistency.

But, how do we measure road design consistency? There are several methods, most of them based on measuring the operating speed behavior along the road segment. Then, a road inconsistency can be detected if vehicles suddenly decelerate at some point, or if their speed is very variable along the road segment. Then, to examine the design consistency of

---

*e-mail: fracator@posgrado.upv.es

a road it will necessary to know the operating speed (speed not exceeded by the 85
In this research, a global consistency model, developed by Polus et al. {3}, is adapted to
Valencias two-lane rural roads. A computer program has been created in order to allow
users to get the geometry of the road, calculate the empirical operating speeds and to
estimate operating speeds by means of different models. These models also have been
calibrated in this research. Finally, a relationship between consistency and road crash
rates is presented. In all regressions it has been used a large amount of data collected from
real drivers on the Valencian Community.

2 Global Consistency Model

The global consistency model, adapted from Polus et al (2004), is defined as:

$$C = 2.808 \cdot e^{-0.278(R_a \frac{\sigma}{3.6})}$$

Where:

$$R_a = \frac{\sum a_i}{L}$$

$$\sigma = \sqrt{\frac{1}{N} \sum (v_i - \bar{v})^2}$$

Where:

a_i: Area between the operating speed of each geometric element and the average operating speed of the s

N :Number of geometric elements

v_i: Operating speed of each geometric element

$\bar{v}$: Average operating speed

If the consistency measurement is lower than 1, the design consistency is poor, while a
value higher than 2 means good consistency.

3 Geometry Restitution

If we want to calculate the design consistency for a planned road, there is no problem,
because the construction project is available. But what happens when the road to be
studied is already constructed and we have no access to its construction project? We will
have to restitute its geometry.

A methodology to obtain the road geometry by using GPS devices was developed. The GPS devices used in this research were so small. One device has to be placed on the vehicles roof, and the road has to be travelled at least one time forward and backward (more than one travel in each direction is recommended, in order to improve the accuracy of the result).

After downloading data, the results are stored in an Excel file. The user selects the road segment to study, and the program obtains an average path considering all the individual paths stored.

Any road geometry is composed by several road geometric elements: tangents, circular curves and transition curves. Thus, a list with all these geometric elements is enough to plot the road's horizontal alignment. The road geometry can be plotted in a graphical way, by means of the Curvature diagram. The horizontal axis means distance from the origin, and the vertical axis means curvature (inverse of the radius). Tangents have null curvature, a constant curvature value is for circular curves, and transition curves are represented by a linear transition of the curvature.

Thus, after obtaining the average path it is necessary to develop the curvature diagram. A local curvature can be obtained considering three successive points. This process has not enough accuracy, so it has been enhanced. The user can introduce the number of points he wants the program to consider in each side of the middle point (it is recommended to use from 3 to 6 points in each side). Then, by combining all possible groups of three points, the curvature whith best fitting is selected. This process gives a very good result, and an initial solution of the curvature diagram is obtained.

A further step has been programmed in order to improve this result. By means of genetic algorithms, several generations of 100 sons are created and mutated, by means of adding or deleting geometric elements, changing their characteristics, or varying the initial compass bearing of the solution. Finally, the curvature diagram is obtained by this method.

4   Operating Speed Observation

The computer program created also allows the user the possibility of calculating the speed at which each path has been done. Then, in order to evaluate the operating speed of an existing road, its easy to give a GPS device to normal drivers at one point and remove it at other point. Then, with several drivers (recommended not less than 80), the operating speed of the road segment can be characterized.

But, what happens when the road segment has not been built yet? In such case we cannot directly analyze the real speeds of the different drivers, but it is possible to estimate them for the different geometric elements.

Several investigations have demonstrated that the operating speed of a road geometric element is highly dependent on its geometric features. For example, for horizontal curves the most important variable for drivers to choose their speed is the radius.

In this research, a very important field study was carried out in order to obtain valid expressions for circular curves and tangents for two-lane rural highways in the Valencian

Community.

The data consisted of a total of 3683.9 vehicles-km. The following expressions for horizontal curves (v85c) and tangents (v85t) were obtained, with correlation coefficients of 76% and 52%, respectively:

$$v_{85c} = 97.4254 - \frac{3310.94}{R}$$

$$v_{85t} = v_{85c} + (1 - e^{-\lambda L})(v_{des} - v_{85c})$$

Where:

$$\lambda = 0.00135 + (R - 100) \cdot 7.00625 \cdot 10^{-6}$$

$$R: \text{Radius (m)}$$

$$v_{des}: \text{Desired speed (110 km/h)}$$

5   Relationship between Consistency and Safety

Finally, the relationship between consistency and safety was examined. To do it, 70 two-lane rural road segments between 3 and 10 km long of all the Valencian Community were chosen. As the vertical alignment was not examined, the longitudinal grade was limited between -4% and +4%.

For all sites, and considering a 5-year period, the average annual daily traffic and all crashes were analyzed, in order to obtain their crash rate. With the computer program, the geometry and the operating speed of each road segment was obtained, allowing the calculus of the consistency.

The relationship between consistency (C) and crash rates (ECR, Estimated Crash Rate, in accidents by million veh-km) was calibrated in a logarithmical way, with a correlation coefficient of 27.87%:

$$ECR = 0.36107848 \cdot e^{-0.33628257 \cdot C}$$

6   Conclusions

Several expressions have been obtained in order to allow engineers to analyze the crash rate likelihood for two-lane rural highway segments. A computer program has been generated, which has been useful to determine those callibrations, but also allows engineers to analyze both existing and planned roads in order to identify their safety lacks.

A true relationship between consistency and crash rates has been obtained, confirming that making the consistency better will deal to a lower crash rate index.

References

[1] Fitzpatrick, K., Anderson, I.B., Bauer, K.M., Collins, J.M., Elefteriadou, L., Green, P. et al Evaluation of Design Consistency Methods for Two-Lane Rural Highways, Executive Summary *Texas: Federal Highway Administration*, USA, 2000.

[2] Lamm, R., Psarianos, B., and Mailaender, T., Highway Design and Traffic Safety Engineering Handbook. McGraw-Hill, 1999.

[3] Polus, A., and Mattar-Habib, C. New Consistency Model for Rural Highways and Its Relationship to Safety *Journal of the Transportation Engineering ASCE*, 286-293, 2004.

[4] Polus, A., Fitzpatrick, K. and Fambro, D.B. Predicting Operating Speeds on Tangent Sections of Two-Lane Rural Highways *Transportation Research Record 1737*, 50-57, 2000.

Model to study the effect of worforce in a safety equipment maintenance plan and its optimization

S. Carlos* *, A. Sanchez†, and S. Martorell*

(*) Departamento de Ingeniería Química y Nuclear,

Universidad Politécncia de Valencia. Camino de Vera, 14. 46022 Valencia. Spain.

(†) Departamento de Estadístia e Investigación Operativa Aplicadas y Calidad,

Universidad Politécncia de Valencia. Camino de Vera, 14. 46022 Valencia. Spain.

October 10, 2010

1   Introduction

Traditionally, maintenance planning in complex systems such as Nuclear Power Plants (NPPs) is focused on achieving high levels of reliability, availability, maintainability and a minimum cost. To find the best planning only surveillance tests and maintenance task intervals are, usually, taken into consideration [1]. However the appropriate development of each maintenance strategy depends not only on the maintenance intervals but also on the human resources available. Recent studies concluded that the implementation of a given maintenance plan adopting adequate test surveillance and maintenance frequencies and workforce can suppose in large deviations from the availability, maintainability, reliability and cost goals obtained when only surveillance test and maintenance frequencies are considered [2]. Therefore, the consideration of workforce to perform a surveillance test or maintenance activity becomes an important variable to design an optimum maintenance plan.

2   Unavailability and Cost models

The total unavailability of a safety equipment is obtained by quantifying the following contributions:

$$u_r = \left(1 - \frac{1}{\lambda I} \left(1 - e^{-\lambda I} \right) \right) \approx \rho + \frac{1}{2} \lambda I \, , \tag{1}$$

*e-mail: scarlos@iqn.upv.es

$$u_S = f_S d_S , \tag{2}$$
$$u_N = f_N d_N , \tag{3}$$

where Eqn. (1) represents the unavailability associated with an undetected failure corresponding to the particular sort of failure cause being considered and, I is the interval to perform a scheduled maintenance task that is intended or supposed to detect the occurrence of such failure. Eqn. (2) represents the unavailability contribution associated with a scheduled testing or maintenance task, where f_S is the scheduled activity frequency, given by $f_S = 1/I$, and d_S is the duration of such activity. Eqn. (3) represents the unavailability contribution associated with a non-planned maintenance task, where f_N and d_N represent the frequency and downtime of the activity, respectively. Regarding the cost, the yearly cost contribution of performing planned testing or maintenance, and non-planned maintenance can be evaluated as:

$$c_S = 8760 \, f_S \, c_{1S} , \tag{4}$$
$$c_N = 8760 \, f_N \, c_{1N} , \tag{5}$$

Where c_{1S} and c_{1N} represent the unitary cost as a consequence of performing one single task, scheduled or non-planed, respectively, which can be formulated using the following relationship:

$$c_{1i} = N_P c_{HP} T_P + N_E c_{HE} T_E , \tag{6}$$

where T_P and T_E, represent the time spent by the N_P own and N_E external personnel, respectively. In addition, c_{HE} is the hourly cost for external personnel and c_{HP} is the hourly cost for own personnel.

To consider the effect of human resources in the analytical models, it is necessary to extend the existing models to include the workforce [1], i.e. the number of workers involved in a maintenance task and theirs skills to perform such maintenance [3] influences the unavailability and cost criteria. Thus, more skilled workers will result in less time to perform an activity and this will influence the equipment unavailability level. On the other hand, as more workers are assigned to perform a maintenance task, its duration will decrease until a certain value, what improves the equipment unavailability but increases the cost. So, the effect of the workforce assigned to perform a surveillance or maintenance task results in a different duration of the activity depending on the human resources available. In a similar way, as it is done in production systems to quantify this effect, the real duration of the activity, d, i.e. d_S and d_N in equations (2) and (3), can be calculated using the following expression:

$$d = d' \left(c + (1 - c) \left(\eta_P N_P + \eta_E N_E \right)^{ra} \right) , \tag{7}$$

where d', is the scheduled time to perform an activity, c is the percentage of the scheduled time that cannot be reduced regardless the number of workforce assigned to that activity, N_P and N_E are the number of own and external personnel involved in a task, respectively. And η_P and η_E, represent the efficiency of own personnel and external workforce to perform a task. Finally, ra in equation (7) represents the reduction in time due to the total amount of workforce involved in such activity.

3   Problem formulation

The extended models can be used as objective functions in a multi-objective optimization process to obtain a set of solutions corresponding to optimum maintenance plan. This work, transforms the multi-objective into a Single-objective optimization problem (SOP) using the concept of effectiveness:

$$y = f(\mathbf{x}) = 1 - (\omega e_u (\mathbf{x}) + (1 - \omega) e_c (\mathbf{x})) \ , \tag{8}$$

where $e_u (\mathbf{x})$ and $e_c (\mathbf{x})$ are the unavailability and cost effectiveness, defined as:

$$e_u (\mathbf{x}) = \frac{U_r - U}{U_r - U_m} \ , \quad e_c (\mathbf{x}) = \frac{C_r - C}{C_r - C_m} \ , \tag{9}$$

where U_r represents the equipment unavailability for the initial maintenance plan, and C_r is the associated cost. And U_m and C_m are the optima values obtained from solving to SOPs corresponding to the unavailability and cost optimization, respectively. ω, in Eqn. (8) is the weighting coefficient that range in the interval $[0, 1]$.

4   Case of application

The case of application is focused on optimizing the maintenance plan of a set of motor-driven pumps, which is a Nuclear Power Plant safety equipment, considering as decision criteria the equipment unavailability and cost and as decision variables the maintenance and test frequency, the number of own personnel and external workforce. The optimization has been undertaken using an algorithm based on Particle Swarm Optimization (PSO). This method is a member of the wide category of Swarm Intelligence methods. It was originally proposed by J. Kennedy as a simulation of social behavior, and it was initially introduced as an optimization method in 1995 [4]. This optimization technique has been proved to obtain good results in constrained optimization problems. Figure 1 shows a set of non dominated solutions considering in the optimization process the maintenance and test intervals c ompared with the result obtained when workforce is considered as a variable. In this figure it can be observed that the optimization result is quite different and that inclusion of workforce provides better solutions for the region of the Pareto Front where unavailability and cost have similar importance in the objective function.

5   Conclusions

An adequate maintenance plan depends not only on the maintenance and test intervals, but also on the human resources available to perform such maintenance. The analytical models developed have been extended to take into consideration this effect. Particle Swarm has succeeded in finding an adequate set of non-dominated solutions of the maintenance
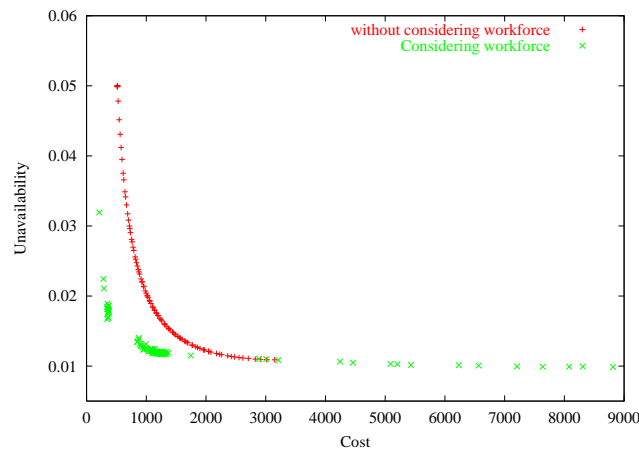
Figure 1: Comparison of non dominated solutions

optimization, and the comparison of the results obtained in the optimization process considering workforce with the results obtained by simply considering the surveillance test and maintenance frequencies, show the importance of including human resources as a variable in the optimization procedure.

References

[1] Martorell, S., Carlos, S., Sánchez, A., Serradell, V. Simltaneous and multi-criteria optimization of TS requirements and maintenance at NPPs. *Annals of Nuclear Energy*, 29: 147–168, 2001.

[2] Martorell, S., Villamizar, M., Sánchez, A. Maintenance modelling integrating human and material resources. *European Safety and Reliability Conference (ESREL)/17th Annual Meeting of the Society-for-Risk-Analysis-Europe (SRA-Europe)*, Valencia, Spain, September 2008.

[3] McCreery, J., Krajewski, L. Improving performance using workforce flexibility in an assembly environment with learning and forgetting effects. *International Journal of Production Research*, 37(9):2031-2058, 1999.

[4] Eberhart, R.C., Kennedy, J. A new optimizer using particle swarm theory. *Proceeding sixth symposium on Micro Machine and Human Science. IEEE Service Center*, Piscataway, NJ, pp 39-43, 1995.

Biofilm Growth on Medical Implants with Randomness

B. M. Chen-Charpentier* and Dan Stanescu†

(*) Department of Mathematics, University of Texas at Arlington,

Arlington, TX 76019-0408, USA,

(†) Department of Mathematics, University of Wyoming,

Laramie, WY 82071-3036.

October 10, 2010

1   Introduction

Device-centered infections are devastating complications associated with implanted medical devices [1]. Even under the most aseptic conditions some bacteria will be present on the device at the time of the implant. If during the approximately first 18 hours after the implant, the body's white cells and the antibiotic therapies have not succeeded in eliminating the bacteria, these will start attaching to the surface, producing extra-cellular polymers, and colonizing, forming biofilms. These are very difficult to combat, and usually the only effective treatment is removal of the implant. Mathematical models can help solve the problem by promoting understanding. One such model is described by reaction-diffusion partial differential equations which are obtained by averaging and perturbation techniques from conservation laws [2].

The objective of our research work is to develop a model of biofilm growth on a medical implant incorporating randomness. The growth of the microbes is given by a logistic growth model with competition for resources as the limiting growth factor. The microbes are attached to the surface of the implant and we assume that they can only move by diffusion. The model of the microbes is, therefore, given by a diffusion-reaction equation. The growth rate parameter as well as the diffusion coefficient will be considered random variables and the concentration of microbes will therefore be an stochastic process depending on position and time. Randomness in the growth rate coefficient may arise because of errors in the observed or measured microbial data, variability of the microbial populations, uncertainties like missing data, or plainly because of lack of knowledge. Lack of knowledge on how microbes move in a biofilm is the main reason to consider randomness in the diffusion coefficient.

---

*e-mail: bmchen@uta.edu

In this paper we use the polynomial chaos approach ([3, 4]) to study the time evolution of a partial differential equation for microbial biofilm growth in porous media. Equations for the time evolution of the polynomial chaos expansion coefficients are obtained and solved numerically. From these coefficients, means and higher-order statistics can

In the following sections we briefly describe the mathematical model for microbial growth on an implant, we present the polynomial chaos approach, show some numerical results and give some conclusions.

2 Microbial Growth on Medical Implants

Consider a microbial biofilm attached to the surface of an implant. We assume that there is a limited amount of nutrients that restricts the growth of the microbes as given by a logistic term. The growth and diffusion of the biofilm microbes is governed by the partial differential equation [2]:

$$\frac{\partial}{\partial t}(c) - \frac{\partial}{\partial x}\left(D\frac{\partial c}{\partial x}\right) = r\left(1 - \frac{c}{M}\right)c \tag{1}$$

Here c represents the mass concentration of microbes per unit volume, r is the growth rate and M is the saturation value. The diffusion coefficient $D(x,t)$ takes into account that the microbes displace if their concentration is high in a manner similar to dispersion of a chemical species.

We normalize the variables so x and c go from 0 to 1. Then equation (1) has the same form but with $M = 1$. We will consider that r and D are random variables with a specified uniform or normal distribution, but independent of time and position.

3 Random Coefficients and Polynomial Chaos

The expansion of the random variables and the stochastic process appearing in equation (1) can be arranged in a sequence of polynomial chaoses $\Phi_i(\boldsymbol{\xi}(\omega))$:

$$r(\omega) = \sum_{j=0}^{\infty} r_j \Phi_j(\boldsymbol{\xi}(\omega)); D(\omega) = \sum_{j=0}^{\infty} d_j \Phi_j(\boldsymbol{\xi}(\omega)); c(t,x;\omega) = \sum_{i=0}^{\infty} c_i(t,x)\Phi_i(\boldsymbol{\xi}(\omega)),$$

where the Φ_i are properly chosen polynomial basis functions of the random variable vector $\boldsymbol{\xi}$. The number of variables in $\boldsymbol{\xi}$ represents the dimension of the chaos. The sequences are then truncated to a finite number of terms. We have considered two types of expansions, in terms of Hermite and Lengendre polynomials.

Introducing the polynomial chaos expansions in the diffusion-reaction equation (1) leads

to

$$\sum_{i=0}^{P}\frac{\partial c_i}{\partial t}\Phi_i - \frac{\partial}{\partial x}\left(\left(\sum_{j=0}^{P}D_j\Phi_j\right)\sum_{i=0}^{P}\frac{\partial c_i}{\partial x}\Phi_i\right) =$$

$$= \left(\sum_{j=0}^{P}r_j\Phi_j\right)\left(\sum_{i=0}^{P}c_i\Phi_i\right)\left[1 - \left(\sum_{p=0}^{P}c_p\Phi_p\right)\right]. \quad (2)$$

Taking the inner product of the above equation with basis function Φ_L and using the orthogonality of the $\Phi_i's$ results in

$$\langle\Phi_L,\Phi_L\rangle\frac{\partial c_L}{\partial t} - \sum_{i=0}^{P}\sum_{j=0}^{P}D_j\frac{\partial^2 c_i}{\partial x^2}\langle\Phi_i\Phi_j,\Phi_L\rangle =$$

$$= \sum_{i=0}^{P}\sum_{j=0}^{P}c_i r_j\langle\Phi_i\Phi_j,\Phi_L\rangle - \sum_{i=0}^{P}\sum_{j=0}^{P}\sum_{l=0}^{P}c_i r_j c_p\langle\Phi_i\Phi_j\Phi_p,\Phi_L\rangle. \quad (3)$$

Equations (3) are a linear system of coupled partial differential equations in the $P+1$ unknowns $c_0,\ldots,c_P$. The system can be solved using, for example, a finite difference method explicit in time and centered in x.

4 Numerical Experiments

In the simulations presented here, we solve equation (1) with initial condition given by the highly localized discontinuous plume centered at x_0. The boundary conditions at $x = 0$ and $x = 1$ are $c(x,t) = 0$. We did calculations for several distributions of the parameters.

Case 1. Both parameters have uniform distributions. Legendre chaos expansion used. $r \sim U(.05, \frac{.05}{16})$, $D \sim U(.0002, \frac{.0002}{16})$. **Case 2.** Both r and D have normal distributions, $r \sim N(.05, \frac{.05}{16})$, $D \sim N(.0002, \frac{.0002}{16})$. Hermite chaos expansion has been used. **Case 3.** Same as Case 1. but with $r \sim U(.5, \frac{.5}{16})$. **Case 4.** Same as Case 2. but with $r \sim N(.5, \frac{.5}{16})$. The results show that there is very little difference between using normal and uniform distributions with the same mean and variance. The value of the variance grows with time as expected. Also, the solutions using polynomial chaos of orders 2 and 3 are very similar.

5 Conclusions

This paper is a first step in modeling biofilm growth on an implant. We have dealt only with the growth of microbes under logistic conditions and the only microbial movement is by diffusion. The randomness due to the variability in the populations and errors is dealt using polynomial chaos. We saw that there is little difference whether using normal or uniform distributions.

References

[1] J. W. Costerton, L. Montanaro and C. R. Arciola, *Biofilm in Implant Infections: Its Production and Regulation* ,Int. J. of Artificial Organs, **28:11** 2005, 1062–1068.

[2] A. O. Cai, K. A. Landman and B. D. Hughes, *Multi-scale Modeling of a Wound-healing Cell Migration Assay*, J. Theor. Biology **245** 2007, 576–594.

[3] D. Xiu and G. E. Karniadakis, *The Wiener-Askey polynomial chaos for stochastic differential equations*, SIAM J. Sci. Comput. **24** (2002), 619–664.

[4] D. Stanescu and B. Chen-Charpentier, *Random coefficient differential equation models for bacterial growth*, Mathematical and Computer Modelling **50** (2009), 885–895.

Numerical solution of differential models with uncertainty

J.-C. Cortés$^{(a)*}$, L. Jódar$^{(a)}$, L. Villafuerte$^{(b)}$, R. Company$^{(a)}$

(a)Instituto Universitario de Matemática Multidisciplinar

Universidad Politécnica de Valencia

Edificio 8G, 46022, Valencia, Spain

(b) CEFyMAP, Universidad Autónoma de Chiapas, México

Department of Mathematics, University of Texas at Arlington

Arlington, TX 76019, USA

October 20, 2010

1 Introduction

Random differential equations are powerful tools to model problems involving rates of changes of quantities representing variables under uncertainties or randomness, [1], [2]. Many of these models are based on random differential equations of the form

$$\dot{\mathbf{X}}(t) = F\left(\mathbf{X}(t), t\right), \ t_0 \leq t \leq t_e, \quad \mathbf{X}(t_0) = \mathbf{X}_0, \tag{1}$$

where $\mathbf{X}_0$ is a random vector and, the unknown, $\mathbf{X}(t)$, as well as, the right-hand side $F(\mathbf{X}(t), t)$ are vector stochastic processes. Reliable numerical solutions for problem (1) have been studied recently in [2], [3], [4]. In this paper, we present a random improved Euler method and we establish its mean square convergence in the fixed station sense. Moreover we take advantage of the improved Euler random numerical scheme for computing directly the expectation and variance of the mean square approximations. We are interested in second order real random variables (2-r.v.'s), $Y : \Omega \rightarrow \mathbb{R}$ having a density probability function, $f_Y(y)$, such that $E\left[Y^2\right] = \int_{-\infty}^{\infty} y^2 f_Y(y) dy < +\infty$, where $E\left[\cdot\right]$ denotes the expectation operator. The space of all 2-r.v.'s defined on $(\Omega, \mathcal{F}, P)$ and endowed with the norm $\|Y\| = \left(E\left[Y^2\right]\right)^{1/2}$, has a Banach space structure, denoted by L_2.

48

Let X^j, $j = 1, ...m$ be 2-r.v.'s, a m-dimensional second order random vector is given by $\mathbf{X}^T = (X^1, ..., X^m)$. The space of all m-dimensional random vectors of second order (2-r.v.v.'s) with the norm $\|\mathbf{X}\|_m = \max_{j=1,...,m} \|X^j\|$ is a Banach space and will be called the L_2^m-space.

Given an interval $T \subseteq \mathbb{R}$, a stochastic process $\{X(t), t \in T\}$ defined on $(\Omega, \mathcal{F}, P)$ is called a second order stochastic process (2-s.p.), if for each $t \in T$, $X(t)$ is a 2-r.v. In an analogous way, if for each $t \in T$, $\mathbf{X}(t)$ is a m-dimensional 2-r.v.v., then $\{\mathbf{X}(t), t \in T\}$ is a second order m-dimensional vector stochastic process (2-v.s.p.). We say that a sequence of 2-r.v.v.'s $\{\mathbf{X}_n\}_{n \geq 0}$ is mean square (m.s.) convergent to $\mathbf{X} \in L_2^m$, and it will be denoted by $\mathbf{X}_n \xrightarrow[n \to \infty]{m.s.} \mathbf{X}$, if $\lim_{n \to \infty} \|\mathbf{X}_n - \mathbf{X}\|_m = 0$. We say that a 2-v.s.p. $\{\mathbf{X}(t) : t \in T\}$ in L_2^m is m.s. differentiable at $t \in T$, if there exists a 2-v.s.p., denoted by $\left\{\dot{\mathbf{X}}(t) : t \in T\right\}$, such that $\lim_{\tau \to 0} \left\|\frac{\mathbf{X}(t+\tau) - \mathbf{X}(t)}{\tau} - \dot{\mathbf{X}}(t)\right\|_m = 0$, $t, t + \tau \in T$.

Definition 1.1 *Let S be a bounded set in L_2^m, an interval $T \subseteq \mathbb{R}$ and $h > 0$, we say that $F : S \times T \to L_2^m$ is m.s. randomly bounded time uniformly continuous in S if*

$$\lim_{h \to 0} \omega(S, h) = 0,$$

where $\omega(S, h) = \sup_{\mathbf{X} \in S \subset L_2^m} \sup_{|t-t'| \leq h} \|F(\mathbf{X}, t) - F(\mathbf{X}, t')\|_m$.

2   On the random improved Euler method

The goal of this section is to show the mean square convergence in the fixed station sense of the random Improved Euler method given by

$$\mathbf{X}_{n+1} = \mathbf{X}_n + \Phi(\mathbf{X}_n, t_n, h), \quad \mathbf{X}_0 = \mathbf{X}(t_0), \quad n \geq 0, \tag{2}$$

where $\Phi(\mathbf{X}_n, t_n, h) = \frac{h}{2}[F(\mathbf{X}_n, t_n) + F(\mathbf{X}_n + hF(\mathbf{X}_n, t_n), t_{n+1})]$, $F(\mathbf{X}_n, t_n)$, $\mathbf{X}_n$ are 2-r.v.v.'s, $h = t_{n+1} - t_n$, with $t_n = t_0 + nh$, for $n = 0, 1, 2, \ldots$, and $F : S \times T \to L_2^m$, with $S \subset L_2^m$ such that

- H1: $F(\mathbf{X}, t)$ is m.s. randomly bounded time uniformly continuous.

- H2: $F(\mathbf{X}, t)$ satisfies the m.s. Lipschitz condition
  $\|F(\mathbf{X}, t) - F(\mathbf{Y}, t)\|_m \leq k(t) \|\mathbf{X} - \mathbf{Y}\|_m$, $\int_{t_0}^{t_e} k(t)dt < +\infty$.

The following theorem gives conditions for the mean square convergence of the scheme (2). Due the limitation of space we omit the proof.

Theorem 2.1 *If F satisfies hypotheses H1 and H2, then the random improved Euler method (2) is m.s. convergent.*

points $t_n = nh$	Euler $h = 1/40$	improved Euler $h = 1/40$	Euler $h = 1/80$	improved Euler $h = 1/80$	theoretical value
0.2	0.244167	0.276526	0.261959	0.275337	0.274961
0.4	0.288691	0.210613	0.248255	0.213224	0.214190
0.6	-0.460131	-0.393853	-0.424472	-0.393106	-0.39308
0.8	0.022128	0.069489	0.445390	0.064280	0.062646
1.0	0.452318	0.331677	0.388030	0.335071	0.336368

Table 1: Approximations for the mean of Example 3.1

3 Numerical results and conclusions

In this section we show an application of the numerical method here presented and we compare its results with respect to an Euler method.

Example 3.1 *Let us consider the random differential equation given by*

$$L\ddot{Q}(t) + R\dot{Q}(t) + \frac{1}{C}Q(t) = G(t) + \alpha B(t), \quad Q(0) = Q_0, \quad \dot{Q}(0) = I_0, \qquad (3)$$

where $Q(t)$ is the charge at time t, L is the inductance, R is the resistance, C is the capacitance and $H(t) = G(t) + \alpha B(t)$ represents the potential source at time t being $B(t)$ a Brownian motion and $G(t) = 24\sin(10t)$. By introducing the vector $\mathbf{X}(t)^T = (X^1(t), X^2(t)) = \left(Q(t), \dot{Q}(t)\right)$, model (3) can be written as follows: $\dot{\mathbf{X}}(t) = F(\mathbf{X}(t), t) = \mathbf{A}\mathbf{X}(t) + \mathbf{C}(t)$, where $\mathbf{C}(t)$ and $\mathbf{A}$ are given by

$$\mathbf{C}(t) = \begin{pmatrix} 0 \\ \frac{G(t)+\alpha B(t)}{L} \end{pmatrix}, \qquad \mathbf{A} = \begin{pmatrix} 0 & 1 \\ -\frac{1}{CL} & \frac{-R}{L} \end{pmatrix}. \qquad (4)$$

Conditions H1 and H2 are easy to verify. So, by Theorem 2.1, the random improved Euler method is m.s. convergent and in this case it is given by

$$\mathbf{X}_n = (R_{\mathbf{A},h})^n \mathbf{X}_0 + \frac{1}{2}h \sum_{i=0}^{n-1} \left[(R_{\mathbf{A},h})^{n-1-i}\right] \left[(I + \mathbf{A}h)\mathbf{C}(t_i) + \mathbf{C}(t_{i+1})\right], \ n \geq 1, \qquad (5)$$

where $R_{\mathbf{A},h} := I + \mathbf{A}h + \frac{h^2}{2}\mathbf{A}^2$, being I the identity matrix of size 2. Henceforth we will assume that Q_0 and I_0 are 2-r.v.'s independent of $B(t)$ for each $t \geq 0$ such that $\mathrm{E}[Q_0] = 0.1$, $\mathrm{E}\left[(Q_0)^2\right] = 0.5$, $\mathrm{E}[I_0] = 0$, $\mathrm{E}\left[(I_0)^2\right] = 0.05$. Taking into account these data, by (5), one obtains the approximations for the mean and variance of the charge $Q(t)$. We compare our results with respect to the Euler approximations, see [3], and the theoretical ones, see [1, p. 154]. Tables 1 and 2 show our results by taking $\alpha = 0.5$, $C = 0.02$, $R = 6$, $L = 0.5$. Clearly the improved Euler method provides better approximations as h goes to zero.

References

[1] T.T. Soong, Random Differential Equations in Science and Engeneering, Academic Press, New York, 1973.

points $t_n = nh$	Euler $h = 1/40$	improved Euler $h = 1/40$	Euler $h = 1/80$	improved Euler $h = 1/80$	theoretical value
0.2	0.011265	0.022419	0.017010	0.023005	0.023149
0.4	0.009948	0.003969	0.004293	0.004403	0.004403
0.6	0.000090	0.000192	0.000074	0.000203	0.000206
0.8	0.000172	0.000097	0.000141	0.000103	0.000105
1.0	0.000094	0.000087	0.000087	0.000087	0.000087

Table 2: Approximations of the variance of Example 3.1

[2] J.C. Cortés, L. Jódar, L. Villafuerte, Mean square numerical solution of random differential equations: facts and possibilities, Comput. Math. Appl. 53 (2007) 1098–1106.

[3] J.C. Cortés, L. Jódar, L. Villafuerte, R.J. Villanueva, Mean square convergent numerical methods for nonlinear random differential equations, Transactions on Computational Science 5890 (2010) 1–21.

[4] J.C. Cortés, L. Jódar, L. Villafuerte, Numerical solution of random differential initial value problems: Multistep methods, Math. Meth. Appl. Sci., (in press, doi:10.1002/mma.1331) (2010).

Application of neural networks to the study of the influence of diet and lifestyle on the value of bone mineral density in post-menopausal women

F. J. de Cos Juez[**], M. A. Suárez-Suárez[†],
F. Sánchez Lasheras[‡] [*]and A. Murcia-Mazón[†]

(**) Project Management Area, Mining Department, University of Oviedo, 33004 Oviedo, Spain

(†) Orthopaedic Surgery Department, University of Oviedo, Cabueñes Hospital, 33203 Gijn, Spain

(‡) Research Department, Tecniproject SL, Marqués de Pidal 7, 33004 Oviedo, Spain

October 10, 2010

1   Introduction

Osteoporosis is characterized by a low bone mass and a structural deterioration of the bone tissue, leading to an increased risk of fractures. Since factors as diet and lifestyle are associated with osteoporosis [1]-[3], this work tries to develop a mathematical method able to calculate the value of BMD in post-menopausal women only from their diet and lifestyle habits.

2   Material and methods

2.1   Genetic algorithms

It is considered that the use of genetic algorithms (GA) started with the work performed by Holland in 1975 [4]. The aim of his research was to mimic the natural evolution of a population by allowing solutions to reproduce chromosomes, to create new offspring, and to compete for survival in the next generation. In each generation, the fitter elements are selected and processed by three basic genetic operators in order to obtain new offspring. These three basic operations are [4]: reproduction, crossover and mutation.

[*]e-mail: fsanchez@tecniproject.com

2.2   Multilayer perceptron neural network

A multilayer perceptron (MLP) is a feedforward artificial neural network model that maps sets of input data onto a set of appropriate output [4]. A multilayer perceptron consists of a linear activation function in all neurons. What makes a multilayer perceptron different is that each neuron uses a nonlinear activation function which was developed to model the frequency of action potentials, or firing, of biological neurons in the brain.

2.3   Design of experiments

In order to study the influence of some neural networks parameters on the RMSE of the predictive model of the BMD of the patients, a design optimization based on design of experiments (DOE) was carried out [5]. In a design optimization based on DOE (used in the deterministic method), each change of the value of any input variable requires a new multilayer perceptron analysis. A response surface is generated that is an explicit approximation function of the RMSE of the multilayer perceptron results expressed as a function of all the selected input variables.

2.4   The sample

The women in this study were members of a random healthy population. The examinations were performed between the months of September 2004 and February 2009. The questionnaire was offered to post-menopausal women between 50 and 69 years old.

3   Results and conclusions

In order to detect the influence of the 38 variables on the BMD and discard the least relevant, it was decided to apply genetic algorithms for the selection of variables. The procedure consisted in using as input variables the 38 obtained from the survey having the BMD as the output variable. The variables considered of importance by the genetic algorithms were as follows: BMI (body mass index), the intake of calcium, cholesterol, carbohydrates, fats, folates and vitamin D, the amount of weekly physical activities performed, the number of pregnancies that the patient had, and the level of sun exposure. All these variables were used as input neurons for a multilayer perceptron neural network model whose output variable is the BMD of the patients. This model was performed with the package AMORE [6] of the free software environment for statistical computing called R [6]. In order to optimize the multilayer perceptron neural network model, the design of experiments (DOE) methodology was employed. The DOE process applied was equivalent to that performed in a previous research by Snchez Lasheras et al. [6]. The optimum values achieved are: number of neurons intermediate layer (7); momentum (0.501); learning rate (10-4); and activation function (sigmoid function). The model with the final artificial neural networks parameters was trained using 80% of the patients of data base chosen at random. The other 20% of the information was used for the validation of the results. Fig.
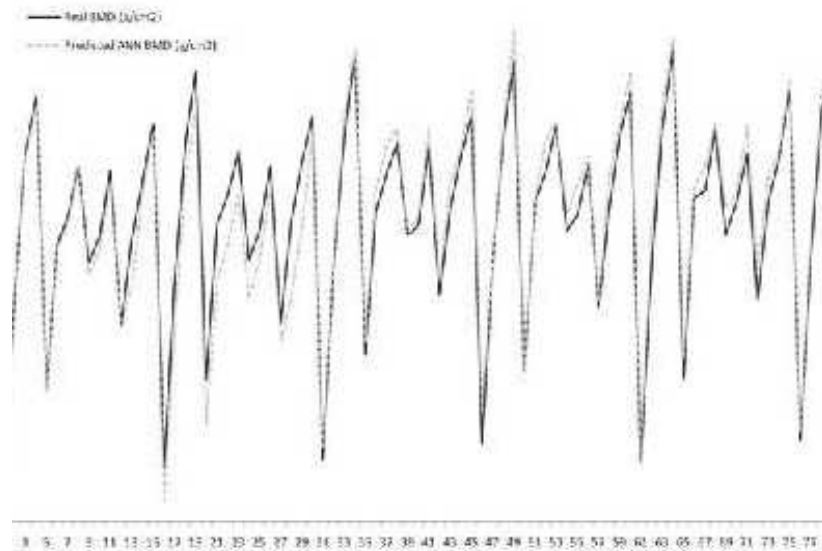
Figure 1: Real BMD versus predicted ANN BMD of the patients used for the validation.

1 shows the real BMD values of the women of the validation sample together with those predicted by the neural networks model. The average mean absolute error of these patients was 2.09%. The research described in this article demonstrates the usefulness of machine learning methods such as artificial neural networks and genetic algorithms for studying the relationship between BMD in women and a series of factors associated with diet and lifestyle. Genetic algorithms were used as dimensional reductor and artificial neural networks to construct a mathematical model that determined the relationship between the input variables and the BMD. It has been proved to be possible to build a neural network model able to forecast the BMD of the post-menopausal women according to their responses to the questionnaire.

References

[1] R. Marcus, D. Feldman, D. Nelson, C.J. Rosen, Osteoporosis. Academic Press, New York, 2007.

[2] S. Haykin, Neural Networks and Learning Machines. Englewood Cliffs, Prentice Hall, New Jersey, 2008.

[3] A.M. Dean, D. Voss, Design and Analysis of Experiments. Springer, New York, 2000.

[4] F.J. De Cos Juez, F. Sánchez Lasheras, P.J. García Nieto, M. A. Suárez Suárez, A new data mining methodology applied to the modelling of the influence of diet and lifestyle

on the value of bone mineral density in post-menopausal women, *International Journal of Computer Mathematics* 86(10-11): 1878–1887, 2009.

[5] F. Sánchez Lasheras, J.A. Vilán Vilán, P.J. García Nieto, J.J. del Coz Díaz, The use of design of experiments to improve a neural network model in order to predict the thickness of the chromium layer in a hard chromium plating process, *Mathematical and Computer Modelling* 52(7-8): 1169–1176, 2010.

[6] C. Ordóñez, J.M. Matías, F.J. de Cos Juez, P.J. García Nieto, Machine learning techniques applied to the determination of osteoporosis incidence in post-menopausal women, *Mathematical and Computer Modelling* 50(5-6): 673–679, 2009.

Balancing consistency and expert judgment in AHP*

J. Benítez, X. Delgado-Galván†, J. Izquierdo and R. Pérez-García

FluIng-IMM, Universidad Politécnica de Valencia,

Camino de Vera S/N 46022 Valencia.

October 10, 2010

1 Introduction

One of the well established, and at the same time up-to-date, human models of decision-making is AHP (Analytic Hierarchy Process) [1][2]. In this model, the input format for decision-makers to express their preferences derives from pair-wise comparisons to build the comparison matrices using, for instance, a scale of 1-9 to represent equal importance to extreme importance [2]. When judgment is completely consistent, the Perron theory provides suitable priority vectors that are used in the process of decision making. In general, however, only estimates of the comparison values are known through numerical judgment, and consistency is not achieved. The problem to solve is the eigenvalue problem $Aw = \lambda_{max}w$, where λ_{max} is, the unique largest eigenvalue of a comparison matrix A, which also gives the so-called Perron eigenvector, that is an estimate of the priority vector.

2 Consistent matrices

Saaty proposed a method to check the consistency of the comparison matrix [2]; and [3] states that additional artificial manipulation to increase the consistency will improve, on average, the reliability of the analysis. In [4] we have shown different methods to achieve consistency. In facing the problem of how to overcome inconsistency in AHP while still taking into account the experts' know-how, the authors propose a model to balance the latter with the former. Our integrated model incorporates an extended version of the linearization procedure described in [4]. As a result an algorithm is developed that following an iterative feedback process achieves an acceptable level of consistency while complying to some degree with experts' preferences.

3 Extension of the linearization process [4] for judgment modification

The main result in [4] states that the closest consistent matrix to an $n \times n$ comparison matrix A is given by the orthogonal projection of $L(A)$ onto a linear subspace of $M_{n,m}$ of dimension $n-1$, $L(A)$ being the matrix of the logarithms of the entries of A, and is given by a suitable Fourier expansion (see theorem 9 in [4]). The extension of this linearization process is given by the following results. Let's change judgment (r,s) of A to get matrix B defined by

$$L(B) = L(A) + \log \alpha (\mathbf{e}_r \mathbf{e}_s^{\mathrm{T}} - \mathbf{e}_s \mathbf{e}_r^{\mathrm{T}}). \tag{1}$$

Theorem 1 *Let $A \in M_{n,n}^+$ and let Y_A be the consistent matrix closest to A. If B is defined by (1) and Y_B is the consistent matrix closest to B, then $[Y_B]_{r,s} = \alpha^{2/n}[Y_A]_{r,s}$, $[Y_B]_{s,r} = \alpha^{-2/n}[Y_A]_{s,r}$; if $j \notin \{r,s\}$, then $[Y_B]_{r,j} = \alpha^{1/n}[Y_A]_{r,j}$, $[Y_B]_{j,r} = \alpha^{-1/n}[Y_A]_{j,r}$, $[Y_B]_{s,j} = \alpha^{-1/n}[Y_A]_{s,j}$, $[Y_B]_{j,s} = \alpha^{1/n}[Y_A]_{j,s}$; and in the remaining cases, $[Y_B]_{i,j} = [Y_A]_{i,j}$.*

Using the Hadamard product, Theorem 1 can be rewritten in a more compact form.

Theorem 2 *Let $A \in M_{n,n}^+$ and let Y_A be the consistent matrix closest to A. If B is defined by (1) and Y_B is the consistent matrix closest to B, then*

$$Y_B = Y_A \odot (\mathbf{x}\mathbf{y}^{\mathrm{T}}),$$

where $\mathbf{x} = [x_1 \cdots x_n]^{\mathrm{T}}$, $\mathbf{y} = [y_1 \cdots y_n]$, $x_r = y_s = \alpha^{1/n}$, $x_s = y_r = \alpha^{-1/n}$, and $x_i = y_i$ when $i \notin \{r,s\}$.

The idea of our algorithm is to start with the matrix in $M_{n,n}$ all of whose components are 1, and then, step by step, to modify this starting matrix and use Theorem 2. The MatLab code is

```
function [w,X] = aprox(A)
[n,m] = size(A);
if n == m
    w = ones(n,1);
    for i=1:n
        for j=i+1:n
            w(i)=w(i)*A(i,j)^(1/n);
            w(j)=w(j)*A(i,j)^(-1/n);
        end
    end
X = w*(w.^(-1))';
else error('Matrix must be square')
end
```

4 Application to leakage policy in a Water Distribution System

We consider here the minimization of water losses. For the sake of simplicity, we consider only two management alternatives: active leakage control (ALC) is the alternative that involves taking actions in distribution systems to identify and repair leaks that have not been reported, and passive leakage control (PLC) that boils down to just repairing reported or evident leaks. The criteria used to decide on the alternatives are seven: planning development cost; damage to properties; supply disruptions; closed streets; water extractions; construction reservoirs; and CO_2 emissions. We use the point of view of the management department of a supply company -OOAPAS (Public Water Company) in Morelia, Michoacn (Mexico)-. The matrix of criteria (7×7) is not consistent. After launching the process and analyzing the results with the experts, a negotiation process started. Finally, the main target is accomplished by aggregating these scores to determine the best decision to make. In this specific problem there is a clear preference for the ALC policy over PLC.

5 Conclusions

By extending a linearization process already described by the authors [4], and describing an efficient implementation for the calculations, an algorithm is developed that following an iterative feedback process achieves an acceptable level of consistency while complying to some degree with experts' preferences. Our ultimate objective was to devise a method and integrate it into a suitable DSS (Decision Support System) tool, to help practitioners build comparison matrices that, at the same time, rely on their judgment and are efficient and reliable in deriving priorities. This will help reap optimal benefits from decisions regarding task selection of alternatives, and will result in decisions well aligned with personal, social, or company's strategic direction.

References

[1] T.L. Saaty. A scaling method for priorities in hierarchical structures. *Journal of Mathematical Psychology*, 15 (234-281), 1977.

[2] T.L. Saaty. Relative measurement and its generalization in decision making. Why pairwise comparisons are central in mathematics for the measurement of intangible factors. The analytic hierarchy/network process. *Revista de la Real Academia de Ciencias Serie A: Matemáticas* 102(2) 251-318, 2008.

[3] J.S. Finan, W.J. Hurley. The analytic hierarchy process: does adjusting a pairwise comparison matrix to improve the consistency ratio help? *Computers & Operations Research* Volume 24, Issue 8, 749-755, 1997.

[4] J. Benítez, X. Delgado-Galván, M. Herrera, J. Izquierdo, R. Pérez-García. Consistent matrices and consistency retrieval through linearization. *2nd Meeting on Linear Algebra. Matrix Analysis and Applications, ALAMA2010.* Valencia, Spain, 2010.

Towards a development of a Mathematical model of workaholism

Mario Del Líbano*, Susana Llorens*,
Marisa Salanova*, and Wilmar Schaufeli‡

(*) Universitat Jaume I,

Departamento de Psicologa Evolutiva, Educativa, Social y Metodología;

Campus Riu Sec s/n, 12071 Castellón, Spain,

(‡) Utrecht University,

Department of Social and Organizational Psychology, Research Institute Psychology & Health,

P.O Box 80.140, 3508 TC Utrecht, The Netherlands

October 10, 2010

1 Introduction

Although workaholism is a common topic in the popular press and it is a concept with special relevance in Work and Organizational Psychology, scientific understanding of it is still quite limited. The concept can be generally considered as a negative psychological state characterized by two main dimensions: working excessively and working compulsively (Del Líbano, Llorens, Salanova, & Schaufeli, 2010). Many studies have tried to establish a theoretical model in order to explain the workaholism antecedents, but any of them have been successful. In all these studies the antecedents included are not derived in a systematically way, but it seems rather haphazard, whereby workaholism is often differently operationalized. With the present preliminary study we have the aim to begin the study of workaholism in a mathematical way analysing some relevant antecedents, i.e., work self-efficacy, job autonomy, emotional competence and mental competence.

Self-efficacy can be defined as the beliefs in one's capabilities to organize and execute the courses of action required to produce given attainments (Bandura, 1997), and according to the Resources, Experiences and Demands (RED) model (Salanova, Cifre, Llorens, & Martnez, 2007), job autonomy, emotional compentence and mental competence are related to experiences at work in a different way depending on self-efficacy. Thus employees perceive more or less personal and job resources depending on their levels of self-efficacy.

In order to achieve our aim we propose two hypotheses. The first one proposes that work self-efficay will be positively related to workaholism, whereas the second one proposes that job autonomy, and mental and emotional competence will mediate the relationship between work self-efficacy and workaholism.

2 Method

Participants and procedure
The sample consisted of 386 university administrative staff. Employees had work experience ranging from 1 to 45 years and the mean number of years worked was 14 (SD = 7.2). They answered an on-line questionnaire drawn up in order to implement an evaluation of psychosocial risks. Firstly, we met with the stakeholders of employees in order to explain the phases of the evaluation (e.g., objectives, procedure, diagnosis, etc.). Secondly, we generated several user-identifications and passwords that were confidentially and anonymously distributed among employees. Finally, we informed the stakeholders of the results by means of a professional report and they explained the main conclusions to the rest of the employees. *Measures*

Work self-efficacy. We measured work self-efficacy using 4 items from RED.es (Salanova et al., 2007). An example of the item is: '*I can do my job well although I have to solve difficult problems*'. Workers were asked to indicate the extent to which they agreed with each sentence on a seven-point rating scale ranging from 0 ('never') to 6 ('always/everyday')

Autonomy. We measured autonomy using 4 items from RED.es. An example of the item is: '*I can do my work tasks as I consider that it's better*?. Scores ranged from 0 ('never') to 6 ('always/everyday').

Mental competence. We measured mental competence using 3 items from RED.es. An example of the item is: '*In my job, I can work with many information and data*'.

Emotional competence. We measured emotional competence using 4 items from RED.es. An example of the item is: '*In my job, I can solve problems with the people in an objective way*'.

Workaholism. We measured workaholism by the short Spanish version (10 items) (Del Lbano, et al., 2010) of the DUWAS (DUtch Work Addiction Scale; Schaufeli, Shimazu, & Taris, 2009), which includes two dimensions: working excessively (5 items; e.g., '*I stay busy and keep my irons in the fire*?) and working compulsively (5 items; e.g., '*I often feel that there's something inside me that drives me to work hard*'). Scores ranged from 1 ('almost never') to 4 ('almost always').

Data analyses Firstly, we computed the internal consistencies (Cronbach's alpha), descriptive analyses, and intercorrelations among the variables with the PASW 18.0 program. Secondly, we computed Harman's single factor test with Confirmatory Factor Analyses (CFA) (e.g. Iverson & Maguire, 2000; cf. Podsakoff, MacKenzie, Lee, & Podsakoff, 2003) using the AMOS (Analysis of MOment Structures) software package (v. 18.0) for the study variables in order to test for bias due to common method variance. Thirdly, the AMOS was employed to implement Structural Equation Modeling (SEM) methods by using Maximum
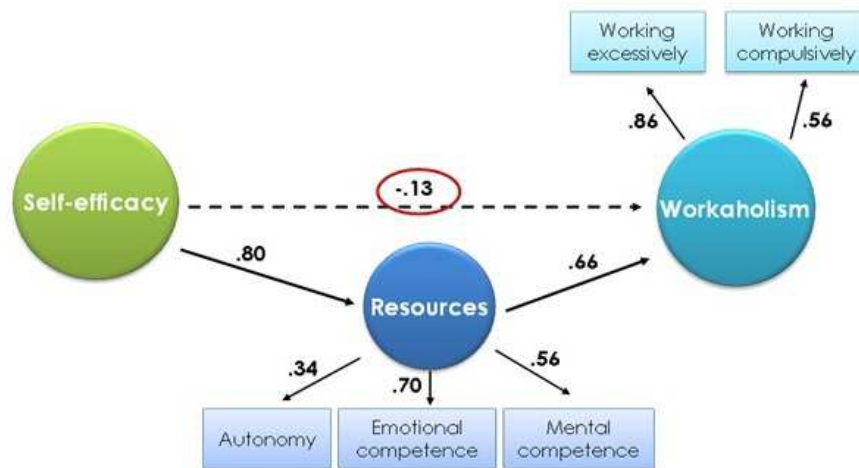
Figure 1:

Likelihood Estimation methods to establish the relationships between the model variables (Byrne, 2001).

3   Results

On the one hand, Table 1 displays the results of the descriptive analyses; that is, means, standard deviations, internal consistencies (Cronbach's alpha) and intercorrelations of the scales. All alphas meet the .70 criterion (Nunnally & Bernstein, 1994), As expected, the pattern of correlations shows that variables correlate significantly with each other.

On the other hand, four different structural models were fitted to the data to test the weight of the antecedents considered. Following the Baron and Kenny (1986) methodology, first (M1) we tested the direct relationship between self-efficacy and workaholism. The model fitted well to the data, the relationship between both variables was positive and significant.In the second model (M2) we tested the relationship between self-efficacy and autonomy, mental competence and emotional competence, and the model also fitted well to the data. Subsequently, we tested the third model (M3) in which autonomy, mental competence and emotional competence fully mediated workaholism. The model also fitted well to the data, with all the relationships positive and siginificant. Finally, as in the fourth model (M4) the direct relationship between self-efficacy and workaholism was not significant, we can conclude that, as we expected, autonomy, mental competence and emo-

Table 1

Means (M), Standard Deviations (SD), Internal Consistencies (Cronbach's α on the diagonal) and zero-order correlations in the sample (N = 386).

Dimension	University Staff		Correlations					
	M	SD	(1)	(2)	(3)	(4)	(5)	(6)
1. Self-efficacy	4.48	.91	.94	.28**	.45**	.53**	.20**	.04
2. Job autonomy	4.51	1.01	-	.86	.18**	.26**	.06	-.17**
3. Mental competence	4.59	0.85	-	-	.75	.38**	.15**	.11*
4. Emotional competence	4.07	1.09	-	-	-	.87	.32**	.09
5. Working Excessively	2.28	.62	-	-	-	-	.73	.50**
6. Working Compulsively	3.6	1.8	-	-	-	-	-	.74

Notes. * $p < .05$, ** $p < .01$

Figure 2: Table 1

Table 2

Structural Equation models (Baron & Kenny, 1986) (N = 386)

Model	χ^2	df	GFI	RMSEA	TLI	CFI
1. M1	9.89	3	.99	.07	.98	.99
2. M2	4.65	5	.99	.00	.99	.99
3. M3	56.01	14	.96	.08	.93	.95
4. M4	51.31	13	.96	.09	.93	.96

Notes. χ^2 = Chi-square; df = degrees of freedom; GFI = Goodness-of-Fit Index;

RMSEA = Root Mean Square Error of Approximation; TLI = Tucker-Lewis Index; CFI

= Comparative Fit Index.

Figure 3: Table 2

tional competence fully mediated the relationship between self-efficacy and workaholism (see table 2 for more information).

4   Discussion

This study constitutes the first step to build a mathematical model of workaholism. According to the results obtained, we can identify four antecedents that are important to its development, i.e., work self-efficacy, autonomy, mental competence and emotional competence. The higher self-efficacy is, the higher autonomy, mental competence and emotional competence employees will probably have, and more opportunities to develop workaholism they will have. Therefore, these four antecedents are possible candidates to be included in the hypothetical mathematical model of workaholism.

References

[1] Baron, R. M., and Kenny, D. A. The moderator-mediator variable distinction in social psychological research: Conceptual, strategic and statistical considerations *Journal of Personality and Social Psychology*, 51:1173–1182, 1986

[2] Del Líbano, M., Llorens, S., Salanova, M. and Schaufeli, W. B. Validity of a brief workaholism scale *Psicothema*, 22:143–150, 2010.

[3] Iverson, R. D., and Maguire, C. The relationship between job and life satisfaction: evidence from a remote mining community *Human Relations*, 53:807–839, 2000.

[4] Podsakoff, P. M., MacKenzie, S. B., Lee, J. Y., and Podsakoff, N. P. Common method biases in behavioral research: a critical review of the literature and recommended remedies *Journal of Applied Psychology*, 88:879–903, 2003.

[5] Schaufeli, W. B., Shimazu, A., and Taris, T. W. Being driven to work excessively hard: The evaluation of a two-factor measure of workaholism in the Netherlands and Japan *Cross-Cultural Research*, 43:320–348, 2009.

[6] Bandura, A., and AutorB NameB. Title of the paper *Name of the Journal*, 50(5-6):765–776, 2010.

[7] Bandura, A., Self-efficacy: the exercise of control. New York, NY: Freeman, 1997.

[8] Byrne, B. M.,Structural equation modeling with AMOS: Basic concepts, applications and programming. Mahway, New Jersey (London): Lawrence Erlbaum Associates, Publishers, 2001

[9] Nunnally, J. C., and Bernstein, I. H., Psychometric theory New York: McGraw-Hill, 1994

[10] Salanova, M., Cifre, E., Martínez, I., and Llorens, S., Caso a caso en la prevención de riesgos psicosociales. Metodología WONT para una organización saludable. Bilbao: Lettera Publicaciones, 2007.

Exact and analytic-numerical solutions of bidimensional lagging models of heat conduction

J. Escolano, F. Rodríguez, M.A. Castro, F. Vives, and J.A. Martín*

Dep. Matemática Aplicada, Universidad de Alicante,

Apdo. 99, 03080 Alicante, Spain.

October 10, 2010

1 Introduction

The classical model for describing heat conduction and other transport phenomena is the diffusion equation, the parabolic partial differential equation

$$T_t(\mathbf{r}, t) = \alpha \Delta T(\mathbf{r}, t), \tag{1}$$

where $\alpha > 0$ is the thermal diffusivity, t is time, $\mathbf{r}$ denotes a point in the space domain, Δ is the Laplacian, T the temperature, and T_t denotes partial differentiation with respect to t. It is based on the Fourier law

$$\mathbf{q}(\mathbf{r}, t) = -k \nabla T(\mathbf{r}, t), \tag{2}$$

where $\mathbf{q}$ is the heat flux vector and $k > 0$ the thermal conductivity, combined with the energy conservation equation

$$-\nabla \cdot \mathbf{q}(\mathbf{r}, t) + Q(\mathbf{r}, t) = C_p T_t(\mathbf{r}, t), \tag{3}$$

where C_p is the volumetric heat capacity and Q the volumetric heat source. In the absence of heat sources, Eq. 1 is obtained, where $\alpha = k/C_p$.

This classical model can be successfully applied to conventional technical problems, as it gives accurate macroscopic descriptions for the long time behavior of systems with large spatial dimensions. However, it implies an infinite speed of propagation, which has no physical meaning, and does not explain phenomena as thermal "inertia", heat waves and delayed responses to thermal disturbances, which appear in transient responses at the microscale level (see [1, 2]).

---

*e-mail: jose.martin@ua.es

66

Non-Fourier models of heat conduction have attracted much attention in recent years. Models incorporating time lags, as the single-phase-lagging, SPL, model [3] or the dual-phase-lagging, DPL, model [2, 4, 5], lead to heat conduction equations in the form of partial differential equations with delays or to partial differential equations of hyperbolic type. These models account for finite speeds of propagations and non-classical behaviors, and have been considered to model microscale heat transfer, as in short-pulse laser processing of thin-film engineering structures [6, 7], or heat transfer in nanofluids [8], and also to model bio-heat transfer during thermal therapy or laser irradiation of biological tissues in medical treatments [9, 10].

In this work we give explicit solutions for bidimensional lagging models of heat conduction, with different types of boundary conditions, in the form of infinite series solutions, allowing the construction of analytic-numerical solutions with prescribed accuracy in bounded domains.

2   Non-Fourier models

In the DPL model, Fourier law is replaced by

$$\mathbf{q}(\mathbf{r}, t + \tau_q) = -k\nabla T(\mathbf{r}, t + \tau_T), \tag{4}$$

where τ_q and τ_T are the phase lags of the heat flux and the temperature gradient, respectively. For $\tau_T = 0$, it reduces to the SPL model.

It is common in the applications of the DPL model to use first-order approximations in (4),

$$\mathbf{q}(\mathbf{r}, t) + \tau_q \frac{\partial \mathbf{q}}{\partial t}(\mathbf{r}, t) \cong -k\{\nabla T(\mathbf{r}, t) + \tau_T \frac{\partial}{\partial t}\nabla T(\mathbf{r}, t)\}, \tag{5}$$

and to refer to the equation derived from this approximation as the DPL model [4], which we will denote DPL(1,1),

$$T_t(\mathbf{r}, t) + \tau_q T_{tt}(\mathbf{r}, t) = \alpha\{\Delta T(\mathbf{r}, t) + \tau_T \Delta T_t(\mathbf{r}, t)\}, \tag{6}$$

For $\tau_T = 0$, (6) reduces to the well-known Cattaneo-Vernotte model [11, 12].

Higher order approximations, up to order two in τ_q and/or τ_T, have also been considered [13, 14]. Corresponding models will be denoted as DPL(2,1),

$$T_t(\mathbf{r}, t) + \tau_q T_{tt}(\mathbf{r}, t) + \frac{\tau_q^2}{2}T_{ttt}(\mathbf{r}, t) = \alpha\{\Delta T(\mathbf{r}, t) + \tau_T \Delta T_t(\mathbf{r}, t)\},$$

and DPL(2,2),

$$T_t(\mathbf{r}, t) + \tau_q T_{tt}(\mathbf{r}, t) + \frac{\tau_q^2}{2}T_{ttt}(\mathbf{r}, t) = \alpha\{\Delta T(\mathbf{r}, t) + \tau_T \Delta T_t(\mathbf{r}, t) + \frac{\tau_T^2}{2}\Delta T_{tt}(\mathbf{r}, t)\}.$$

However, retaining the original formulation of the DPL model, as given in (4), combined with the energy conservation equation, for $\tau = \tau_q - \tau_T > 0$ the DPL heat conduction model leads to the retarded partial differential equation

$$T_{t'}(\mathbf{r}, t') = \alpha \Delta T(\mathbf{r}, t' - \tau), \tag{7}$$

where $t' = t + \tau_q$, referred to as the delayed heat conduction model (DH).

3 Solutions of bidimensional models

Consider heat conduction in a rectangular plate, with boundary Dirichlet conditions, for $t \geq 0$,

$$T(0, y, t) = T(l_1, y, t) = T(x, 0, t) = T(x, l_2, t) = 0, \; 0 \leq y \leq l_2, \; 0 \leq x \leq l_1,$$

or Neumann conditions

$$T_x(0, y, t) = T_x(l_1, y, t) = T_y(x, 0, t) = T_y(x, l_2, t) = 0, \; 0 \leq y \leq l_2, \; 0 \leq x \leq l_1.$$

Appropriate initial conditions have to be given for the different models, specifying initial values for temperature, $T(x, y, 0) = \varphi(x, y, 0)$, and its time derivative, $T_t(x, y, 0) = \phi(x, y, 0)$, for DPL(1,1), and also its second derivative, $T_{tt}(x, y, 0) = \psi(x, y, 0)$, for DPL(2,1) and DPL(2,2). For the DH model, initial temperature has to be known for an initial interval of τ amplitude, $T(x, y, t) = \varphi(x, y, t)$, for $0 \leq t \leq \tau$.

Using the method of separation of variables, exact solutions can be obtained in the form of infinite double series of sine functions of the spatial variables, for Dirichlet conditions, or cosine functions, for Neumann conditions, with coefficients $\Phi_{n,m}(t)$ the solutions of the separate temporal problems for each of the eigenvalues $\lambda_{n,m} = n^2\pi^2/l_1^2 + m^2\pi^2/l_2^2$. These problems, for the DPL approximations, are initial value problems for linear differential equations with constant coefficients, and thus can be readily solved. For the DH model, they are initial value problems for delay differential equations with general initial functions, and to develop constructive solutions we applied a combination of the steps method and a convolution integral [15], obtaining, for $t \in [m\tau, (m+1)\tau]$,

$$\Phi_{n,m}(t) = B_{n,m}(\tau) + B_{n,m}(0) \sum_{k=1}^{m} \frac{\beta^k (t - k\tau)^k}{k!}$$
$$+ \sum_{k=1}^{m-1} \frac{\beta^k}{k!} \int_0^\tau (t - k\tau - s)^k B'_{n,m}(s) \, ds + \frac{\beta^m}{m!} \int_0^{t-m\tau} (t - m\tau - s)^m B'_{n,m}(s) \, ds,$$

where $\beta = -\alpha\lambda_{n,m}$, and $B_{n,m}(t)$ are the Fourier coefficients in sine or cosine series, accordingly to the type of boundary conditions, of the initial function $\varphi(x, y, t)$.

The infinite series solutions obtained with the method of separation of variables can be shown to converge and provide exact solutions under adequate regularity conditions

on the initial functions. Hence, by truncating these series, they allow the construction of analytic-numerical solutions with controlled errors.

Numerical explorations show that, for $\tau_T = 0$ and values of τ_q similar to those experimentally found in metals, the DPL approximations differ slightly from each other and from the classical diffusion model, but differ significantly from the behavior of the DH model. However, for different values of τ_T and τ_q such that $\tau = \tau_q - \tau_T > 0$ is kept constant, variations can be observed in the DPL approximate models, but not in the DH model. Our results also suggest that establishing appropriate initial conditions is a key point when comparing the different models.

References

[1] Joseph D.D., and Preziosi L. Heat waves. *Rev. Mod. Phys.*, 61: 41–73, 1989.

[2] Tzou D.Y. Macro- to Microscale Heat Transfer: The Lagging Behavior. Washington, Taylor & Francis, 1996.

[3] Tzou D.Y. On the thermal shock wave induced by a moving heat source. *J. Heat Transfer*, 111: 232–238, 1989.

[4] Tzou D.Y. The generalized lagging response in small-scale and high-rate heating. *Int. J. Heat Mass Transfer*, 38: 3231–3240, 1995.

[5] Tzou D.Y. Experimental support for the lagging behavior in heat propagation. *AIAA J. Termophys. Heat Transfer*, 9: 686–693, 1995.

[6] Qiu T. Q., and Tien C. L. Short-pulse laser heating on metals, *Int. J. Heat Mass Transfer*, 35: 719-726, 1992.

[7] Qiu T. Q., and Tien C. L. Heat transfer mechanisms during short-pulse laser heating of metals, *ASME J. Heat Transfer*, 115: 835-841, 1993.

[8] Wang L., and Wei X. Heat conduction in nanofluids. *Chaos Solitons Fractals* 39: 22112215, 2009.

[9] Xu F., Seffen K.A., and Liu T.J. Non-Fourier analysis of skin biothermomechanics. *Int. J. Heat Mass Transfer*, 51: 22372259, 2008.

[10] Zhou J., Zhang Y., and Chen J.K. An axisymmetric dual-phase-lag bioheat model for laser heating of living tissues. *Int. J. Thermal Sci.*, 48: 14771485, 2009.

[11] Cattaneo C. Sur une forme de l'équation de la chaleur éliminant le paradoxe d'une propagation instantanée. *C. R. Acad. Sci.*, 247: 431–433, 1958.

[12] Vernotte P. Les paradoxes de la théorie continue de l'équation de la chaleur. *C. R. Acad. Sci.*, 246: 3154–3155, 1958.

[13] Tzou D.Y. A unified approach for heat conduction from macro to micro-scales. *ASME J. Heat Transfer*, 117: 8–16, 1995.

[14] Quintanilla R., and Racke R. A note on stability in dual-phase-lag heat conduction. *Int. J. Heat Mass Transfer*, 49: 1209–1213, 2006.

[15] Reyes E., Rodríguez F., and Martín J.A. Analytic-numerical solutions of diffusion mathematical models with delays. *Comput. Math. Appl.*, 56: 743–753, 2008.

Coupling methodology of 1D finite difference and 3D finite volumes CFD codes based on the Method of Characteristics

J. Galindo, A. Tiseira, P. Fajardo[*] and R. Navarro [†]

CMT-Motores Térmicos,

Universidad Politécnica de Valencia

October 10, 2010

1 Introduction

CFD simulations allow researchers to understand flow behavior and quantify important flow parameters such as mass flow rates or pressure drops. In this way, CFD simulations have become a valuable tool in helping both the analysis and design of the intake and exhaust systems of internal combustion engines.

These kind of systems are mainly composed of ducts, which can be accurately simulated by means of one-dimensional, non-viscous codes. However, there are several components that manifest a complex three-dimensional flow behavior, such as turbomachinery or manifolds. These components cannot be simulated properly by 1D codes, and thus requiring viscous, 3D codes.

Hence, it is a right choice to save computational time by simulating the complex components by means of a 3D code and modeling with a 1D code the rest of the system, i.e. the ducts. In this way, a coupling methodology between the own-developed 1D code Open-WAM [1] and the 3D commercial code Fluent by means of the Method of Characteristics has been developed and validated.

2 Coupling methodology

The well-known Method of Characteristics (MoC) [2] has been used as a means of solving the coupling problem. Some references [3] performed the coupling directly transferring the

---

[*]Corresponding author

[†]galindo, anti1, pabfape, ronagar1@mot.upv.es

flow field variables, or by means of a Riemann solver [4]. In contrast of these, the use of the MoC is a physically-based methodology that will give the exact solution provided that its hypotheses are satisfied.

3   Implementation

In order to update the boundary condition in the interface of the two domains in each time step, the Riemann invariants must be extracted from the two regions to allow the transfer of information between the codes. The way in which these variables are obtained depends on the software considered.

OpenWAM previously had a function to connect two ducts by means of the MoC [5].

In the case of FLUENT, the impossibility to modify this code required a particular approach to obtain the desired invariants. First of all, a so-called *custom field function* is defined indicating the position that the information (Riemann invariant) of a given flow particle will reach in the considered time (Δt_{MoC}). Then, one must create an *isosurface* of the fluid particles whose information will reach the boundary condition of the considered domain for each one of the Characteristic lines.

FLUENT manages *isosurfaces* in a dynamic way, so that the values of the *isosurface* are the corresponding to the current time step. This approach allows to obtain the invariants which will arrive to the boundary condition after a Δt_{MoC}. Since the *isosurface* holds the proper position of the corresponding characteristic, one only needs to write with a *monitor* the involved variables at the *isosurface* to obtain the value of the invariant.

Finally, a *User Defined Function*(UDF) has been written to manage all the information.

4   Validation

In order to validate the coupling procedure, it has been applied to two different problems.

4.1   Sod's Problem

The Sod's problem [6] is a shock tube test problem commonly used to test the accuracy of computational fluid codes. In our case, the simulation consisted in a 2 meters tube divided into two computational domains. The first one is a 1D domain computed with OpenWAM, whereas the second one is simulated with FLUENT.

This problem is interesting assuming inviscid flow and neglecting the heat transfer through the walls, since it has analytical solution. The results obtained using the two codes coupled and the analytical solution are quite correlated, meaning that the coupling methodology transfers the information properly.

4.2   Impulse test rig

An impulse test rig is a device used for measuring the acoustic response of a system [7]. Mainly, it consists of two long ducts (each one about 20 meters long) at the inlet and outlet of the element whose acoustic response is meant to be measured. Simulating an impulse test rig exploits the main utility that this coupling BC has: reducing the size of a 3D computational domain and therefore its computational cost. This is performed by computing an important and geometrically simpler part of a domain, i.e. the ducts, with a 1D code and using the 3D code to simulate just the complex section of the domain.

In particular, the inlet duct of the impulse test rig was modeled. The performed simulation consists of a 20.1 m long duct in which the first 19.9 m are simulated with OpenWAM and the last 0.2 m with FLUENT, as shown in figure 1.

Figure 1: Computational domain of the impulse test rig

A pressure pulse is set at the inlet. The incident pressure arriving at a measuring section set at 20 m is monitorized in order to compare with the available experimental data. The solution obtained using the 1D-3D simulation is quite similar to the measured incident pressure. Moreover, if this simulation is performed entirely with the 3D solver, it takes 20 times more than the coupled one.

5   Conclusions

A methodology to perform a combined 1D & 3D simulation has been developed. The main advantage of this kind of modeling is that it allows to achieve good geometric resolution (3D) where required, but with reduced computational cost if compared to a 3D simulation of the whole domain.

The procedure of interchanging information between the two codes is done by means of the Method of Characteristic. It has been implemented for a 3D commercial software, with the difficulties inherent to this process due to the lack of accessibility of those kind of codes.

Finally, two different validation procedures have been performed, noticing a good agreement in the solution. Also, it can be stated that the coupling saves up to 1-2 orders of magnitude in time, although the time reduction is problem-dependent.

References

[1] OpenWAM Web Page.

[2] R.S. Benson, JH Horlock, and DE Winterbone. *The thermodynamics and gas dynamics of internal combustion engines*, volume 1. Oxford University Press, 1982.

[3] M. Brück, B. Michaelis, M. Awasthi, and R. Reinelt. 1D/3D-Coupling GT-POWER/FLUENT to Predict Species Transport in Exhaust Oxygen Sensors at Engine Operating Conditions. In *European Automotive CFD Conference*, 2007.

[4] A. Onorati, G. Montenegro, and G. D'Errico. Prediction of the Attenuation Characteristics of IC Engine Silencers by 1-D and Multi-D Simulation Models. Technical Report 2006-01-1541, SAE TECHNICAL PAPER SERIES, 2006.

[5] JR Serrano, FJ Arnau, P. Piqueras, A. Onorati, and G. Montenegro. 1D gas dynamic modelling of mass conservation in engine duct systems with thermal contact discontinuities. *Mathematical and Computer Modelling*, 49(5-6):1078–1088, 2009.

[6] G.A. Sod. A survey of several finite difference methods for systems of nonlinear hyperbolic conservation laws. *Journal of Computational Physics*, 27(1):1–31, 1978.

[7] A. Broatch, X. Margot, A. Gil, and F. D. Denia. A CFD Approach to the Computation of the Acoustic Response of Exhaust Mufflers. *Journal of Computational Acoustic*, 13(2):301–316, June 2005.

The curvature of the tracking error frontier: a new criterion for the partial index tracking problem

Fernando García,[*] Francisco Guijarro and Ismael Moya

Facultad de Administración de Empresas,

Universidad Politécnica de Valencia

Camí de Vera, s/n, 46022, Valencia, Spain

October 10, 2010

1   Introduction and Objectives

The analysis of the efficiency of investment funds remains a major area for research in the field of portfolio theory. Jensen (1968) was among the first to point out the need to critically evaluate the performance of investment funds. The proliferation of work in this area has advanced in parallel with the growth in the number of managed funds and assets. Comparisons are often made between active and passive management funds.

These studies demonstrate how difficult it is for investment funds to outperform a benchmark. In the United States, the Standard & Poor's 500 Index has been between 65% and 85% more profitable than the funds analyzed over a long time window. Similar conclusions have been reached after adjusting the results for variable risks.

The questionable efficacy of many actively managed investment funds in attempting to outperform the benchmark has helped ensure that index replication is currently among the most popular techniques used by investment fund managers (Coleman et al., 2006). This technique has become even more popular after the appearance of exchange traded funds (ETFs).

Index replication seeks to minimize the unsystematic risk component by imitating the movements of a reference benchmark – a stock index. Faced with active management techniques that endeavor to beat the underlying index, replica portfolios in general and replica indices in particular, are configured as a powerful passive strategy. In following this strategy, the manager does not necessarily pursue efficiency in the sense of mean-variance, but instead replicates the behavior of the market from a more conservative approach. Mixed approaches that search for consensus solutions between the two models can also be found in the literature (Burmeister et al., 2005).

---

[*]Corresponding author. Email: fergarga@esp.upv.es

Replicated indices can be full or partial – depending on the number of stocks that are included.

In the case of full replication, the portfolio includes the same stocks as the stock index, and a perfect replication is produced if these stocks are weighted in the same proportion as the index. It is also possible to generate other combinations of risk and return by varying the weights of the stocks in the replica portfolio. However, in this case, the imitation of the stock index is not accurate, and it does not necessarily outperform the index in the mean-variance sense; while the greater or lesser required returns may lead to an increase or decrease in the proportional risk of the position (Roll, 1992). The disadvantages of full replication include excessive portfolio management and transaction costs, as well as the need to invest in all the stocks in the index. Another disadvantage is the cost associated with realigning the portfolio if the composition of the underlying index changes. This situation is particularly critical for stocks with low weighting in the index, and which often have little impact on the movement of the index. It is also critical for stocks with little liquidity, while various other drawbacks are mentioned in the literature (Ruiz-Torrubiano and Suarez, 2009). A restrictive view of the costs associated with replica portfolios has also been discussed in numerous academic papers like Canakgoz and Beasley (2008) and the drawbacks are usually addressed through mathematical programming models.

In partial replication, which is the subject of our research, a manager builds a portfolio from a subset of stocks contained in the underlying index and this process removes some of drawbacks listed above. The counterpart is that an exact replica of the stock index cannot be built. However, this does not necessarily imply a decline in the risk-return relationship – as will become evident later.

Three issues must be resolved when building a partial replica.

Firstly, the number of stocks in the replica must be chosen. An evaluation can be made using sensitivity analysis on the results of the desirability of increasing or decreasing the cardinality of the portfolio (Tabata and Takeda, 1995).

After setting the number of stocks, the second question involves selecting from among the available stocks. This is the most complex problem when building a partial replica. The simplest approach is to assess each potential stock, measure the error in the replication of the index, and then select those stocks that minimize this deviation. Unfortunately this approach is computationally difficult because it represents an NP-hard problem (Ruiz-Torrubiano and Suarez, 2009). For example, some 17,310,309,456,440 portfolios must be evaluated if the aim is to replicate the S&P 100 with a portfolio of ten stocks.

Finally, the third question involves the precise weight to be given to each stock in the replication portfolio, depending on the desired return and the replication error the manager is willing to assume.

The second issue of stock selection has received special attention from researchers and many methods for finding the local problem optimums have been proposed. These methods can be grouped into two broad families: those that make use of mathematical programming; and those using multivariate analysis techniques.

Without wish being exhaustive, authors using mathematical programming models for optimal local searches include: Tabata and Takeda (1995), whose approach is employed in

our research and discussed in a later section; Beasley et al. (2003), whose approach uses a population heuristic in which the cardinality of the portfolio is made explicit through the restriction $i = 1, N$, $zi = n$, n being the number of stocks in the replica portfolio, and zi a binary variable that indicates if the i-th stock is to be included in the portfolio. This approach supposes that the found local optimum is conditioned by the whole problem resolution method being used; Derigs and Nickel (2004) use a procedure of *Simulated Annealing*; Ruiz-Torrubiano and Suárez (2009) combine a genetic algorithm with a model of quadratic programming in a more general formulation of the problem; Gaivoronoski et al. (2005) use different measures of risk in mathematical programming models, such as return variance, semi-variance, replica error variance, or value at risk.

Works that make use of multivariate analysis techniques include Dose and Cincotti (2005), who use cluster analysis on return time series so that the cardinality of the replica portfolio is established from the number of clusters obtained – preferably by choosing a single stock as representative of each cluster in each replica portfolio. Corielli and Marcellino (2006) propose the use of factor analysis so that stocks are grouped around various factors depending on their past returns, and the replica portfolio contains those stocks that that best explain the variability of these factors. In their results, several stocks are used as representatives of each factor, so that the replica portfolio can include stocks that explain the same parts of the variability in the performance of the index.

All these works are characterized by the search for a single portfolio, characterized by a maximum of three possible parameters (Chow, 1995): replication error variance, returns in excess of the index; and volatility of returns. The stocks in the replica portfolio are identified during this process and the given weighting complies with the constraints imposed on those parameters. If, for example, an investor does not wish to accept a level of returns in excess of the replica, he should look for another portfolio with different stocks and different weightings given to the stocks. The same applies if any of the other two parameters is unacceptable. In other words, the replica portfolio is optimal for just a few specific parameters, and these were used to determine the optimality. If these parameters vary then the selection of stocks also varies. An important problem to note is that if a manager wishes to cover a wide range of investment profiles, he will need to build many portfolios. This implies that the manager will eventually invest in a broad range of stocks, which reduces the previously mentioned advantages of a partially replicated portfolio in comparison with a fully replicated portfolio.

It is noteworthy how this analysis has not pursued a parallel strategy to that followed in Markowitz's classical mean-variance model of 1952, in which the goal is the generation of a so-called efficient frontier – rather than the identification of a specific portfolio with a fixed risk and return.

Our work proposes the addition of a new parameter: the curvature of the frontier. This criterion is not defined for a given portfolio, but for the set of portfolios that define the replicated frontier. The main advantage is that a fund manager can satisfy different investment profiles using the same subset of stocks – with all the portfolios on the frontier containing the same stocks and so reducing transaction costs.

For the joint consideration of these criteria we propose the use of multiobjective math-

ematicaL programming. In this way the solution can generate a new frontier as a consensus between the frontiers obtained by separately considering each criterion. Besides, the inclusion of the curvature of the tracking frontier as a new criterion enables us to contemplate a wider range of investment profiles. With this criterion, it is possible to go beyond the objective of building a single tracking portfolio and to aim for a more general goal: to obtain a tracking frontier that satisfies a larger number of investors by using the same subset of stocks.

References

[1] Beasley J.E., Meade N., and Chang T.J., An evolutionary heuristic for the index tracking problem, *European Journal of Operational Research* 148 (2003) pp. 621–643.

[2] Burmeister C., Mausser H., and Mendoza R., Actively managing tracking error, *Journal of Asset Management* 5(6) (2005) pp. 410–422.

[3] Canakgoz N.A. and Beasley J.E., Mixed-integer programming approaches for index tracking and enhanced indexation, *European Journal of Operational Research* 196 (2008) pp. 384–399.

[4] Chow, G. Portfolio selection based on return, risk, and relative performance, *Financial Analysts Journal* Mar-Apr 1995: pp. 54–60.

[5] Coleman, T.F., Li, Y., and Henniger, J., Minimizing tracking error while restricting the number of assets, *Journal of Risk* 8 (2006) pp. 33–56.

[6] Corielli, F. and Marcellino, M., Factor based index tracking, *Journal of Banking & Finance* 30(8) (2006) pp. 2215–2233.

[7] Derigs U. and Nickel N.H., On a local-search heuristic for a class of tracking error minimization problems in portfolio management, *Annals of Operations Research* 131 (2006) pp. 45–77.

[8] Dose C. and Cincotti S., Clustering of financial time series with application to index and enhanced index tracking portfolio, *Physica A* 335 (2005) pp. 145–151.

[9] Gaivoronoski A.A., Krylov S., and van der Wijst N.., Optimal portfolio selection and dynamic benchmark tracking, *European Journal of Operational Research* 163 (2005) pp. 115–131.

[10] Markowitz, H.M., Portfolio Selection, *Journal of Finance* 7 (1952) pp. 77–91.

[11] Roll. R., A mean/variance analysis of tracking error, *The Journal of Portfolio Management* 18 (1992) pp. 13–22.

[12] Ruiz-Torrubiano, R. and Suárez, A., A hybrid optimization approach to index tracking, *Annals of Operations Research* 166 (2009) pp. 57–71.

[13] Tabata, Y. and Takeda, E., Bicriteria optimization problem of designing an index fund, *Journal of the Operational Research Society* 46 (1995) pp. 1023–1032.

Coupling Methodology of One-dimensional and Multi-dimensional Computational Fluid Dynamics (CFD) Models for the Simulation of Diesel Sprays*

J.M. García-Oliver †, X. Margot, M. Chávez, A. Karlsson‡

CMT - Motores Térmicos,

Universidad Politécnica de Valencia,

Edificio 6D,46022, Valencia, Spain.

(‡) Volvo Technology Corp.,

Dept. 6100, Sven Hultins Gata 9 A,

Chalmers Science Park, 41288, Göteborg, Sweden.

October 10, 2010

1   Introduction

The 3D-CFD Eulerian-Lagrangian two-phase spray model has been formulated for the simulation of highly dispersed sprays originally. Nevertheless, it is commonly used for simulating Diesel sprays in different conditions inside the combustion chamber, though these sprays are characterised by presenting a dense liquid core in the region near the injector hole. A highly dispersed spray numerically means that the ratio between of the total volume of liquid inside a cell and the volume of the cell can not be high. This ratio called void fraction restricts the use of meshes with small cell size. However, performing spray simulations with coarse meshes leads to poor estimations of the numerical spray evolution. Specifically, the calculation of the momentum transfer is highly affected.

As Diesel sprays in engine conditions are experimentally demonstrated to be mixing-controlled, they can be analysed from a point of view of the gas jet theory [1]. In this sense, 1D-Eulerian models based on the gas jet analogy, can be used to simulate this two-phase problem with accuracy and with less numerical parameters dependencies. Some authors have proposed 1D3D Eulerian-Lagrangian models in order to combine the advantages of

†Correspondig author e-mail: jgarciao@mot.upv.es

both approaches and to obtain less grid dependent solution of the spray dynamics, as example [2-7], when coarse meshes are used.

In this work , the equations and strategies for obtaining a coupled 1D3D-CFD spray model are presented, which aims to improve the calculation predictions and reduce mesh dependency of the 3D-CFD standard model. The contribution of this research is based on the methodology for the implementation in the commercial *STAR-CD* CFD code. The coupling is achieved by modifying the standard momentum transfer calculation in the 3D-CFD code with the introduction of gas turbulent components and, self-similar radial velocity profiles determined by the 1D in home approach proposed by [1]. The gas jet axial velocity is only imposed in the near nozzle region.

2 1D3D-CFD spray model

The conservation equations for the gas/droplets phases developed by [9, 10] are solved in the 3D-CFD Eulerian-Lagrangian framework in the *STAR-CD* code [8]. In the Eulerian gas conservation equations, the source interaction terms and the void fraction permit to take into account the droplets presence in the flow. In the Lagrangian formulation, the droplets are statistically grouped in computational parcels depending on their properties. The movement of the droplets are determined in every calculation time step and the velocity change is based on the Newton's law. Different forces can act on the droplets. In this case only the drag force $\vec{F}_D$ will be considered. This latter force is caused by the relative velocity of the droplet to the surrounding gas phase, being the magnitude of the relative velocity (U_r) given by:

$$U_r = \sqrt{\left(U_x + U'_x - U_{x,d}\right)^2 + \left(U_y + U'_y - U_{y,d}\right)^2 + \left(U_z + U'_z - U_{z,d}\right)^2} \qquad (1)$$

where subscripts x, y, z denote the axis coordinate directions, U_x, U_y, U_z are gas mean, U'_x, U'_y, U'_z gas fluctuating and $U_{x,d}$, $U'_{y,d}$, $U'_{z,d}$ droplet velocity components. The momentum loss/gain of the total parcels traversing a given cell is hereafter calculated in order to obtain the momentum source interaction term, that transfers this information from the discrete to the continuous phase. Spray sub-models are used in order to simulate different spray phenomenons, such as the Huh-Gosman primary atomization model [11], Hsiang-Faeth secondary atomization model [12] with the methodology presented in [13], the drag coefficient proposed by [14] and droplets turbulent dispersion numerical algorithm developed by [15]. The gas phase turbulence is modelled with the RANS approach. The $k - \epsilon$ for High Reynolds Numbers model [16] has been used with the modification proposed by [17].

The coupling between the 1D and 3D model has been achieved in the calculation of phases relative velocity (eq. 1). The CFD gas axial velocity component in the vicinity of a droplet (U_z in eq. 1) has been substituted by the 1D gas jet velocity. The substitution is applied in the near nozzle region only.

The gas jet velocity is obtained with the 1D formulation proposed by [1] particularised for the simulation of non-vaporasing, non-isodense, inert sprays and for uniform injection

velocity profiles. This model allows to represent the 3D two-phase transient spray problem in a 2D single-phase steady spray problem (see Fig.1). Two zones are considered by the 1D model:
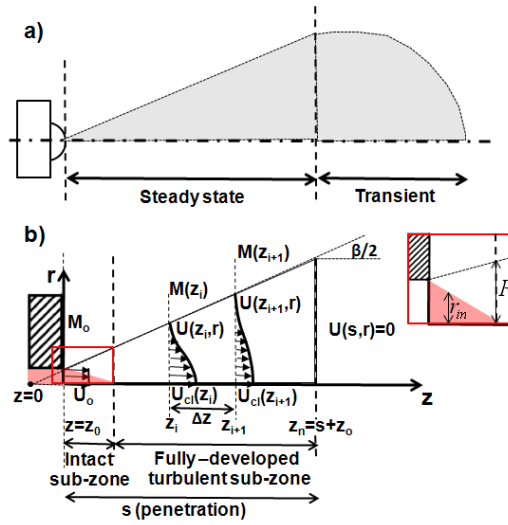
Figure 1: (a) Example of a spray and its regions, (b) schematic of a spray modelled as a turbulent gas jet.

- In the fully-developed turbulent zone the axial velocity distribution can be Gaussian and it is described as:

$$U(z,r) = U_{cl}(z) \exp\left[-\frac{4.6052}{\tan^2(\beta/2)}\left(\frac{r}{z}\right)^2\right] \tag{2}$$

where z is the axial position corresponding to the spray axis, r is any radial position, $U_{cl}(z)$ is the gas velocity on the spray axis (centerline), and β is the spray cone angle.

- In the intact sub-zone a constant and Semi-Gaussian radial profiles for the gas velocity has been used:

$$U(z,r) = \begin{array}{ll} U_0, & r \le r_{in} \\ U_0 \exp\left[-\frac{4.6052}{\tan^2(\beta/2)}\left(\frac{r-r_{in}}{R-r_{in}}\right)^2\right], & r > r_{in} \end{array} \tag{3}$$

where r_{in} is the inner radius and R is the external radius defining the intact core region and the spray limit, respectively (see the zoom of the sub-zone in Fig. 1-b). U_0 is equal to the effective injection velocity. In the 1D model development, a constant injection velocity is assumed in this sub-zone, instead.

The implementation of these profiles depends on the CFD spray penetration respecting to the length of a defined 1D3D-CFD zone or limit which is fixed during the total calculation

time. The intact-subzone length is also fixed. In a spray with lower penetration than this zone, U_z is calculated using eq. 3 for the intact-sub-zone region, calculated by eq. 2 for the turbulent-developed sub-zone and zero for the region between the 1D spray penetration and the 3D-CFD spray penetration. In a spray with larger penetration than this zone, U_z is calculated using eq. 3 for the intact-sub-zone region, calculated by eq. 2 for the turbulent-developed sub-zone and calculated by the default CFD after the corrected zone.

3 Simulated cases

For the spray simulations, four different 3D meshes has been used in the calculations. The specifications of the meshes are presented in Table 1. The non-vaporising set of

Table 1: Specification of the 3D meshes.

Meshes	Cells number	Cell size near the injection point (mm)
M1	144500	0.5x0.5x1.0
M2	75480	0.75x0.75x1.5
M3	36328	1.0x1.0x2.0
M4	29184	2.0x2.0x2.0

experimental data from the work published by Naber and Siebers [18] has been used for the model validation. The simulated cases are shown in Table 2 and they have been classified in A cases and B cases depending on two air density values considered. The whole matrix have been simulated with the 3D-CFD standard spray model, the 1D3D-CFD spray model and with the 1D spray model, the latter used as reference in the next section.

Table 2: Calculation matrix.

Cases	Meshes	ρ_a (Kg/m^3)
1A	M1	
2A	M2	14.8
3A	M3	
4A	M4	
1B	M1	
2B	M2	30.0
3B	M3	
4B	M4	

4   Results

The model validation using the calculation matrix described above is presented in this section for the spray penetration. The spray cases simulated with the 1D3D approach present a corrected zone of five times the intact sub-zone length (*5IL*). In Figure 2 the Diesel spray tip penetrations as a function of time are shown for B cases of Table ($\rho_a = 30.0$ Kg/m^3). The solid and dashed lines correspond to the simulated spray penetrations and the symbols represent the experiments. In both figures, the 3D-CFD standard spray simulations (left) are compared with the 1D3D-CFD spray simulations (right).
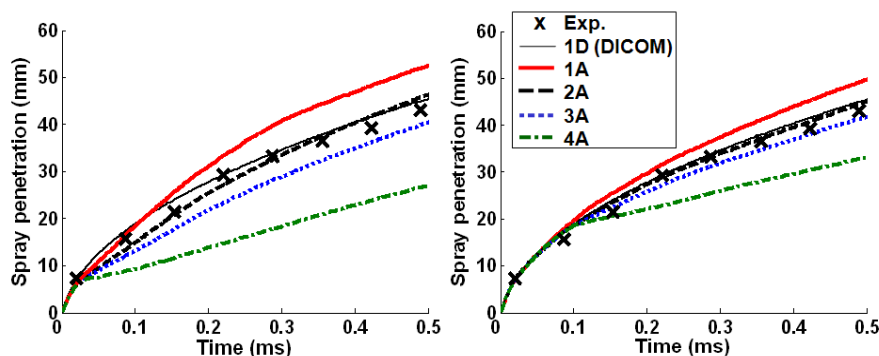
Figure 2: Spray tip penetration for B cases ($\rho_a = 30.0$ Kg/m^3): with the 3D-CFD standard spray model (left) and with the 1D3D-CFD spray model (right).

It can be observed that the 1D3D penetrations are overlapped independently on the mesh size used and until they reach the corrected zone limits (5IL=18.06 mm for $\rho_a = 30.0$ Kg/m^3). In the non-corrected zone of the spray, the 1D3D penetration curves tend to diverge as 3D standard penetrations. However, the differences between M1 and M4 penetrations calculated with the 1D3D model have been reduced considerably compared with the differences observed between M1 and M4 penetrations obtained with the 3D standard model. Moreover, the spray penetrations obtained with the 1D3D model show an evolution closer to the typical spray penetration with the square root of time. Finally, additional results have shown that the calculation of the droplets and gas on axis velocities have been improved with the 1D3D spray model.

5   Conclusions

A 1D-Eulerian spray model based on the turbulent gas jet analogy has been coupled successfully with the 3D-CFD Eulerian-Lagrangian spray model implemented in *STAR-CD* CFD commercial code. The model has been developed for simulating Diesel sprays in non-vaporising conditions and constant injection velocity profiles. The main assumptions and description of the general droplets/gas equations, spray sub-models, and gas jet axial velocity profiles have been presented. The coupling achieved in the calculation of the phases

relative velocity has been also described in the methodology. Spray simulations carried out with the proposed approach has been compared with those obtained with the 3D-CFD standard model, 1D spray model and experimental data. The results have shown that this methodology is valid in order to obtain more a more mesh-independent spray evolution.

References

[1] José V. Pastor, J. Javier López, José M. García and José M. Pastor. A 1D model for the description of mixing-controlled inert Diesel sprays, Fuel 87, 2871-2885, 2008.

[2] X. Yang, Y. Takamoto and A. Okajima. Improvement of Three-Dimensional Diesel Spray Modeling in Near Region with Coarse Mesh, SAE Paper 2000-01-0274, 2000.

[3] N. Abani and R.D. Reitz. A Model to Predict Spray-tip Penetration for Time-varying Injection Profiles. ILASS Americas, 20th Annual Conference on Liquid Atomization and Spray Systems, Chicago, May, 2007.

[4] N. Abani and R.D. Reitz. Unsteady turbulent round jets and vortex motion. *Physics of Fluids* 19(1), 125102, 2007, doi: 10.1063/1.2821910.

[5] N. Abani, A. Munnannur and R.D. Reitz. Reduction of Numerical Parameter Dependencies in Diesel Sprays Models. *Journal of Engineering for Gas Turbines and Power* 130, 032809-1, May, 2008, doi: 10.1115/1.2830867.

[6] N. Abani, S. Kokjohn, S.W. Park, M. Bergin, A. Munnannur, W. Ning, Y. Sun and R.D. Reitz. An Improved Spray Model for Reducing Numerical Parameter Dependencies in Diesel Engine CFD Simulations. SAE Paper 2008-01-0970, 2008.

[7] S.W. Park, H.K. Suh, C.S. Lee, N. Abani and R.D. Reitz. Modeling of Group-Hole Nozzle Sprays using Grid-size-hole-location, and Time-step-independent Models. *Atomization and Sprays* 19(6): 567-582, 2009.

[8] Computational Dynamics Ltd., STAR-CD Version 3.26 - Methodology, 2005.

[9] J.K. Dukowicz. A Particle-Fluid Numerical Model for Liquid Sprays. *Journal of Computational Physics* 35, 229-253, 1980.

[10] P.J. O'Rourke and F.V. Bracco. Modeling of Drop Interaction in Thick Sprays and a Comparison with Experiments. IME Stratified Charge Automotive Engines Conference, London, 1980.

[11] K.Y. Huh and A.D. Gosman. A Phenomenological Model of Diesel Spray Atomization, Proc. Int. Conf. on Multiphase Flow, Japan, September 24-27, 1991

[12] L.P Hsiang and G.M. Faeth. Near-limit Drop Deformation and Secondary Breakup, *Int. J. Multiphase Flow* 18(5), 635-652, 1992.

[13] X. Margot, R. Payri, A. Gil, M.Chávez and A. Pinzello. Combined CFD-Phenomenological Approach to the Analysis of Diesel Sprays Under Non-evaporative conditions. SAE Paper 2008-01-0962.

[14] G.B. Wallis. One Dimensional and Two Phase Flow, New York, McGraw-Hill Book Co., 1969.

[15] P.J. O'Rourke. Statistical Properties and Numerical Implementation of a Model for Droplet Dispersion in a Turbulent Gas. *Journal of Computational Physics* 83, 345-360, 1989.

[16] B.E. Launder and D.B. Spalding. Mathematical Models of Turbulence, London, Academic Press, 1972.

[17] B.B. Dally, D.F. Fletcher. and A.R. Masri. Flow and Mixing Fields of Turbulent Bluff-Body Jets and Flames, *Combust. Theory Modelling*, 2, 193-219, 1998.

[18] J.D. Naber and D.L. Siebers. Effects of Gas density and Vaporization on Penetration and Dispersion of Diesel Sprays. SAE Paper 960034, 1996.

On the boundary condition setup of Large Eddy Simulation of Diesel sprays.*

S. Hoyas,† A. Gil, J. M. Mompó-Laborda, D. Khuong-Anh

CMT - Motores Térmicos,

Universidad Politécnica de Valencia,

Edificio 6D,46022, Valencia, Spain.

October 10, 2010

1 Introduction

For engine designers insight in the behaviour of an evaporating fuel spray is of great importance. Improvements in injection equipment reduce emissions and increase power by a more effective combustion process. Therefore, a deep understanding of the physics of Diesel spray will provide some fundamental knowledge for the design of more efficient, less consuming and cleaner engines.

During the last years great advances on the comprehension of several physical phenomena in liquid jets and sprays have been achieved, both by means of diagnosis experimental tests and CFD techniques mainly based on RANS (Reynolds Averaged Navier-Stokes) to simulate turbulence. These computational methods are very useful to study the averaged flow, but they do not provide any information neither about the turbulent fluctuations nor about the flow on the jet boundary. In this paper we present an implementation of a LES (Large Eddy Simulations) method in an non-reactive sprays. LES methods are computationally more expensive than RANS, but modelling required by RANS is reduced, and therefore they are more accurate. Furthermore, a detailed study of the flow characteristics in zones where turbulent fluctuations are significant is allowed by means of LES, while RANS, by definition, cannot model these features. For a comprehensive description of both methods, the book of Pope [1] is an excellent starting point.

Regarding Diesel spray injection, the most commonly used codes in the automotive industry, until very recently, are based on the RANS approach because of their reasonably accurate results and relatively lower computational cost. However as the RANS approach

---

†Correspondig author.

has the highest level of modelling it can be seen as a successful interpolation between experimental data sets. On the contrary, direct numerical simulation (DNS) methods solve all the significative scales of the flow, so no modelling is require and it provides the highest level of description of the flow. Since the smallest structures of the flow have to be solved, the computational cost increases as $Re^{9/4}$ and the resources required for most practical cases are above current computer hardware limitations (and will probably be in the next 20 years). While the use of LES increases the computational cost, these methods are able to consistently simulate the complex structures related with turbulent mixing, which is decisive in the injection and combustion processes and invisible for RANS solvers ([2], and [3]).

The main goal of this work is to numerically investigate the influence of the inlet boundary conditions on a LES of the flow in a Diesel fuel spray evaporation system. This is the first part of a research project where the idea is to obtain a LES solver able to reproduce the different turbulent patterns that appear in the free shear flow of Diesel sprays, as well as the velocities profiles. In this paper we limited ourselves to the numerical simulation of Diesel spray with the isothermal, isodense and non-vaporizing conditions. Following the characteristic features of this congress, the paper concentrates on the mathematical aspects of the simulation. Thus, the chemical and physical analysis have also not discussed in this article and will be published elsewhere. The results are compared with the classical numerical RANS method with both Eulerian-Eulerian and Lagrangian-Eulerian approaches and are simultaneously validated with experimental data. Our algorithm has been implemented in the free all-purposes CFD code OpenFOAM © 2004-2010 OpenSource Ltd.

2   Numerical Technique

As mentioned above, the RANS approach has been traditionally used in order to model Diesel spray injections[4]. The RNG (Renormalization Group Theory) k-epsilon turbulence model with the default coefficients for the turbulent dissipation rate equation and turbulent viscosity is used for both Euler – Euler and Lagrangian – Euler spray calculations. Previous works [5] showed that RANS accurately predicts average velocity profiles and average spray's shape (i.e. dispersion rate, penetration), since the mean velocity profile and the spreading rate are independent of Re. Nevertheless, RANS is not valid if higher level of turbulence structure description is required during the calculations [3]. Table 1 resume the main characteristics of RANS models compared to LES formulation. Differences are based on the statistical treatment of the turbulence (RANS) and the use of the self-similarity theory of Kolmogorov (LES). Also differences can be found on the time-averaging of the Navier-Stokes equations and the spatial filtering for the RANS and LES respectively, see Table 2.

Application of the filtering operation to the continuity and momentum equations [1] yields:

Table 1: Comparison between RANS and LES.

RANS	LES
Reynolds-averaged Navier-Stokes	Large Eddy Simulation
Statistical phenomena	Kolmogorov theory of self similarity [1]
Time-averaged NS [2]	Spatial filtered NS
k - ϵ model (Jones and Launder, 1972)	Smagorinsky (Smagorinsky, 1963)
RNG k - ϵ model (Yakhot, 1992)	One Equation model (Yoshizawa,1985)
Less computationally demanding	Predict transient flows better

[1]Large eddies of the flow are dependent on the flow geometry, while smaller
eddies are self similar and have a universal character.

[2]NS: Navier-Stokes Equations

$$\nabla \cdot \overline{u} = 0 \tag{1}$$

$$\frac{\partial \overline{u}}{\partial t} + \nabla \cdot \overline{uu} = -\frac{1}{\rho}\nabla \overline{p} + \nu \nabla^2 \overline{u} - \nabla \tau \tag{2}$$

where $\overline{u}$ is the filtered velocity field, t is the time, $\overline{p}$ is the filtered pressure, ρ is the fuel density, ν is the uniform kinematic viscosity and τ is the stress-like tensor ($\tau = \overline{uu} - \overline{u}\,\overline{u}$). Eqs. (1) and (2) govern the evolution of the large (energy-carrying) scales of motion and the modelled stress term is τ . Also, this SGS stress tensor provides the communication between the resolved scales and the dissipation scales [6].

Closure is obtained by modelling the residual-stress tensor. The Smagorinsky [7] model is used for the sub-grid scale tensor:

$$\tau_{ij}^d = -2\mu_{SGS}S_{ij} \tag{3}$$

where τ_{ij}^d is the deviatoric SGS stress with $\mu_{SGS} = \overline{\rho}\left(C_S\Delta^2\right)\left\|\widetilde{S_{ij}}\right\|$. C_S is the Smagorinsky constant, a theoretical value (0.065–0.2) and $\left\|\widetilde{S_{ij}}\right\|$ is the Frobenious norm $\left\|\widetilde{S_{ij}}\right\| = \sqrt{2\widetilde{S_{ij}}\widetilde{S_{ij}}}$ of the filtered strain tensor, $\widetilde{S_{ij}} = \frac{1}{2}\left(\frac{\partial \overline{u_i}}{\partial x_j} + \frac{\partial \overline{u_j}}{\partial x_i}\right)$. Δ is the filter width, here assigned to be the cube root of the local cell volume.

3   Boundary conditions

Experimental results have confirmed the hypothesis that spray evolution is controlled by fuel-air mixing rates and thus they can be analysed in the same way as a gas jets [5]. Besides

Table 2: Time Averaging vs. Spatial Filtering.

Instantaneous = Average + Fluctuations ($u = \overline{u} + u'$)	
Averaging or filtering of NS equations gives identical equations for the	
averaged/filtered variables plus averaged fluctuation terms.	
Time Averaging	Spatial Filtering
$u_i\left(x\right) = \frac{1}{T}\int_t^{t+T} \overline{u_j}\left(x,s\right)ds.$	$u\left(x_0\right) = \int_\Omega u\left(x,t\right)G\left(x_0,x,\Delta\right)\,{}^{\llcorner 3}dx.$
$\overline{u_i'} = 0$, and $\overline{\overline{u_i}} = \overline{u_i}$.	$\overline{u_i'} \neq 0$, and $\overline{\overline{u_i}} \neq \overline{u_i}$.
Reynolds Stress Tensor	SGS$^{\llcorner 4}$ Stress Tensor
$\tau_{ij}^R = \overline{u_j'u_i'}$	$\tau_{ij}^S = -\left(\overline{\overline{u_i}u_j'} + \overline{u_i'\overline{u_j}} + \overline{u_i'u_j'}\right) = \overline{u_iu_j} - \overline{u_i}\,\overline{u_j}$

---

[3]Spatial filter $G\left(x_0,x,\Delta\right)$ with filter size Δ

[4]Subgrid Scale

the simplifications brought by the experimental researches, CFD still remains limitations in term of the modelling of the atomisation process of the nearby zone which is not the goal of the present study. In addition, the present work can be seen as a previous approach to the inclusion of droplets (Lagrangian term) as a source of mass and momentum. Hence, to keep the same computational domain will provide a better application of present conclusions to future Lagrangian-Eulerian LES calculation and a more suitable framework for further comparison between them. Consequently, the simplification of the computational domain presented by Vuorinen [8] is also assumed. In his work the inlet boundary condition is set far enough from the nozzle avoiding the problems of the void fraction limits which grid resolution required by LES makes it more restrictive. As presented below, turbulent gas jet theory will be applied to set the fields in the inlet boundary conditions of the domain.

Studies show how under certain conditions, for any section perpendicular to the spray axis in the steady region of the gas jet or diesel spray, momentum flux is conservative, and thus equal to that existing at the nozzle exit ([9], [10]). Therefore, a proper implementation of the inlet boundary condition would perform the same spray development independent of where it would be placed. Consequently, the inlet boundary condition must be perpendicular to the spray axis, contain the whole spray and the same momentum flux as at the nozzle exit and in order to ensure a more realistic development of the flow the boundary inlet has to reproduce the same profile of the fields as in a steady spray.

Since momentum flux can be obtained from experimental data, the unknown factors to set up the BC. can be identified by integrating momentum over the whole spray section:

$$\dot{M_0} = \frac{\pi}{2\alpha} \cdot \rho_a \cdot \tan^2\left(\frac{\theta_u}{2}\right)$$

$$\cdot x^2 \cdot U_{axis}^2 \cdot \sum_{i=0}^{\infty} \frac{1}{\left(1 + i\frac{S_C}{2}\right)}$$

$$\cdot \left[\left(\frac{U_{axis}}{U_0}\right)\left(\frac{1 + S_C}{2}\right)\left(\frac{\rho_f - \rho_a}{\rho_f}\right)\right]^i \tag{4}$$

Desantes et al. obtain the previous expression for the spray momentum [11] assuming a Gaussian radial profile [12] for fuel concentration and axial velocity. Here the Schmidt number (S_C) represents the relative rate of momentum and mass transport and θ_u is the spray cone angle. The point of interest for the present work can be seen in Figure 1 where the axis velocity equals the injected velocity $(U_{axis} = U_0)$ and a Gaussian radial profile can be assumed. The spray injected under the physical conditions shown in Table 3 has been simulated [13]. In these conditions the end of the non-perturbed zone for the isodense case is located at 4.073mm, approximately $8d_{eq}$ from the nozzle exit (with $d_{eq} = d_0\sqrt{\rho_f/\rho_a}$) and the spray diameter is 2.07mm which is set as the inlet boundary condition diameter. Since LES calculation requires perturbed inlet boundary conditions, the velocity and concentration reference profiles at the inlet boundary condition are Gaussian profiles randomly perturbed a 10% as a first simplify approximation. The discussion of the convenience of this hypothesis will be discussed in the followings sections.

Table 3: Definition of experimental and gas jet CFD simulation $\dot{M} = 1.11N$.

	reference[13]	simulation
Fuel	$C_{13}H_{28}(l)$	fuel (N_2)
Air	N_2	N_2
P_{inj} (MPa)	73.995	-
$P_{a,\infty}$ (MPa)	3.5	3.55
$T_{f,0}$ (K)	307.58	307.58
$T_{a,\infty}$	307.58	307.58
$\rho_{f,0}/\rho_{a,\infty}$	21.26	1
U_0 m/s	373.27	373.27
d_{inlet} μm	112	2070
d_{eq} μm	516	516

The computational domain is a cylindrical volume (d = 40mm, L = 70mm) that represents the shape of the injection test rig chamber. The meshing methodology is fairly the same for the RANS and LES calculations, with different grid densities depending on
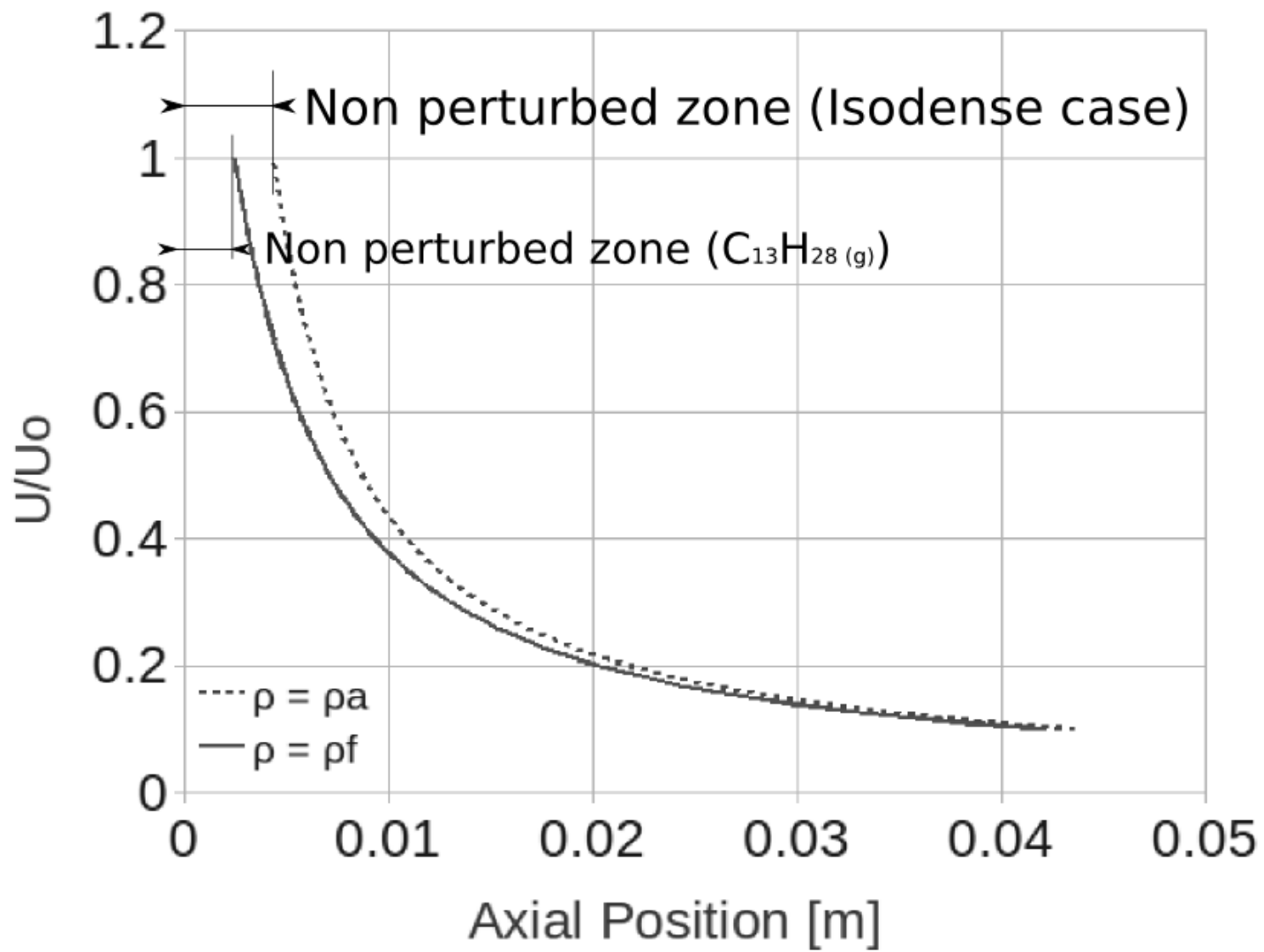
Figure 1: Axis velocity. Red line: Isodense case, Blue line: $C_{13}H_{28}(g)$ case

Table 4: Definition of gas jet CFD boundary conditions.

Surface	Boundary type	Defining variables
Spray inlet diameter	Velocity turbulent inlet	$U_0(r) \& C(r)$, T_f
Wall	rigid wall, non-slip condition	–
outlet	constant pressure,	$P_{a,\infty}$;
	wave Transmissive boundary	$T_{a,\infty}$

the turbulence formulation. Hexahedral cells have been preferred for the grid generation, since they provide better accuracy and stability than tetrahedral cells. The computational domain has been decomposed into hexahedral subparts in order to get a semi-structured topology mesh, as shown in Figure 2(a). Cells are concentrated around the spray diameter (d = 2.07mm) to get a cell size of 60 μm and 20 μm for the RANS and LES meshes respectively. Downstream the nozzle the mesh is progressively adapted to the shape of the computational domain in order to obtain a homogeneous cell size at sections located downstream the inlet boundary condition, see circular sections on the right of Figure 2(a) &(b). The number of cells is around $4\text{x}10^5$ and $5.5\text{x}10^6$ for the RANS and LES formulation respectively. Also, an evolution on the LES mesh has been performed in order to optimize skewness, uniformity and number of cells (reduced to $4.9\text{x}10^6$ elements) of the mesh along the fluid zone occupied by the spray. Previous studies performed on RANS Euler – Euler [14] in similar spray conditions show that the structure of the mesh and cell size are enough to get a grid independent solution. Also, the meshes used for the LES formulation have comparable and also smaller cell sizes than recent LES studies [8] for sprays characterization where the grid independence is proved. Finally, three boundary conditions are assigned in the computational domain as depicted in Table 4.

4   Numerical results

The obtained numerical results are contrasted with those predicted by classical RANS models and compared with experimental data. Experimental results have been obtained from previously published data from the authors' research group [10], [15], [13].

Temporal evolution of the axial velocity at 25mm of the virtual nozzle has been used to justify the beginning for the statistical measurements. In Figure 3 (first of temp ev.) the criteria of a constant spray angle was used to set the radial position range of the probes. It is also shown the velocity value imposed in the center of the inlet boundary condition (4.073mm from the virtual nozzle under the isodense conditions). The difference in both the frequency content and the width of the velocity signals in the inlet boundary condition and the axis velocity at 25mm show a lack of precision of the spray fields simulated at the inlet boundary condition and justify the transient period needed for the turbulent
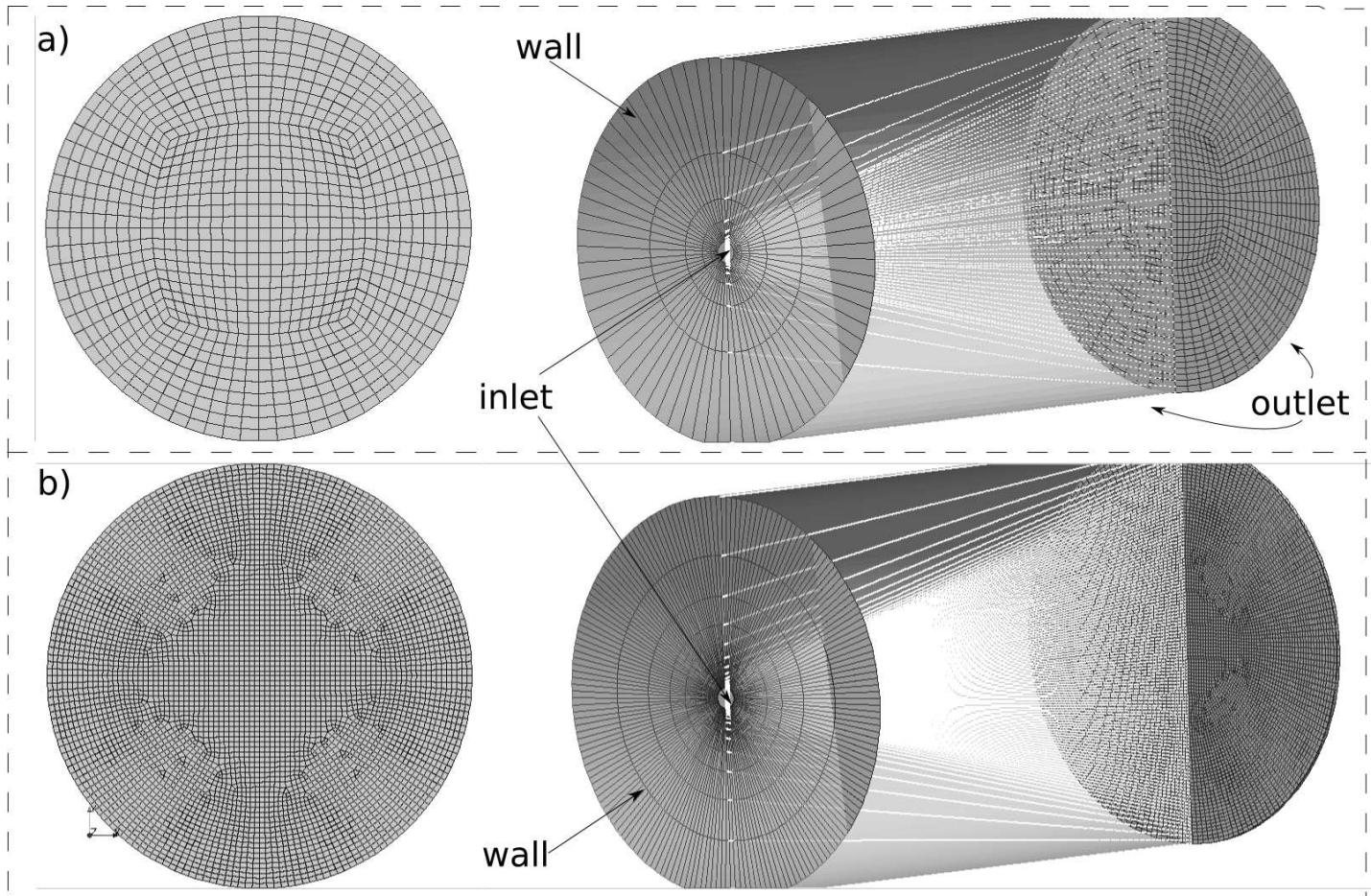
Figure 2: Calculation domain and boundary conditions. a) RANS case, b) LES case
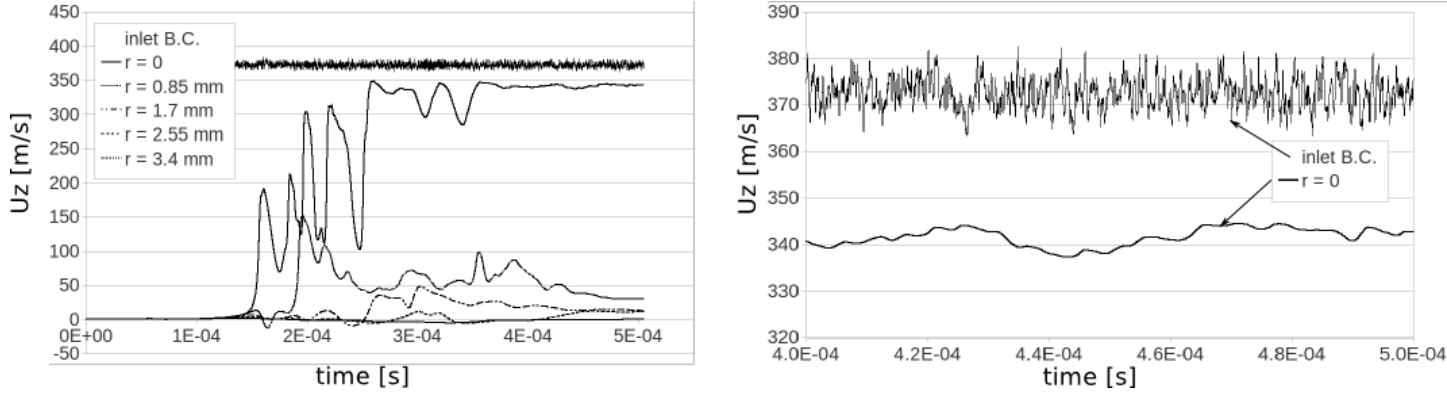
Figure 3: Measurements of radial probes (x=25mm)

evolution. Its effect in LES in terms of the classical parameters to characterize the spray is decisive as shown in Figures 4 and 5

The maximum axial distance for a 1% fuel concentration is the criteria used to define the penetration at Figures 4. Notice that this distance is located at the edge of the spray for theoretical and RANS calculations but not necessarily for LES simulations as shown in Figures 5. RANS and LES (E-E) calculations correspond to isodense cases detailed in previous sections and to obtain the RANS (L-E) penetration a Lagrangian formulation is coupled with an Eulerian one to track the particle dispersion and solve the gas phase variables.

The over prediction of both the RANS and LES Eulerian-Eulerian penetration at is affected by: the different injection mass flow rate shape, the fact that spray is more effective in transferring injection momentum to the ambient than the gas jet [16] and the non-fulfilment of the isodense hypothesis up to $30d_{eq}$. Furthermore, for the LES calculation, the first 5mm can be seen as a length required to develop turbulence Figure 5. Thus, the first assumption of a 1% of velocity fluctuation at the inlet boundary condition is not a good enough turbulent initialization of the flow. Although the inlet is placed at the end of an not well-known zone, authors think a more realistic turbulent conditions can be achieved by applying more realistic measured or calculated profiles of velocity variation [17], [18]. The Figure 5 show iso-surfaces of fuel concentration for the LES simulation at 0.3ms. The red line and the green line mark the stoichiometric iso-surface for LES and RANS (E-E) simulations respectively. These areas have a relevant importance in combustion processes. The upper part of the figure plots the radial distance of these surfaces where detached surfaces far from the jet can be found.

A comparison with the Gaussian radial profiles is shown in Figure 6. In both the axial velocity has been normalized with the axis velocity. In Figure 6(left) the radial distance is normalized with the jet's half-width as defined by Pope [1] where in Figure 6(right) is normalized with the axial distance. A spatial average at 25mm of the nozzle of the axial velocity (t= 0.5ms) shows a good agreement with the theoretical Gaussian profile from the edge to the 30% of the axis speed Figure 6(left). Differences in simulated profiles at 20
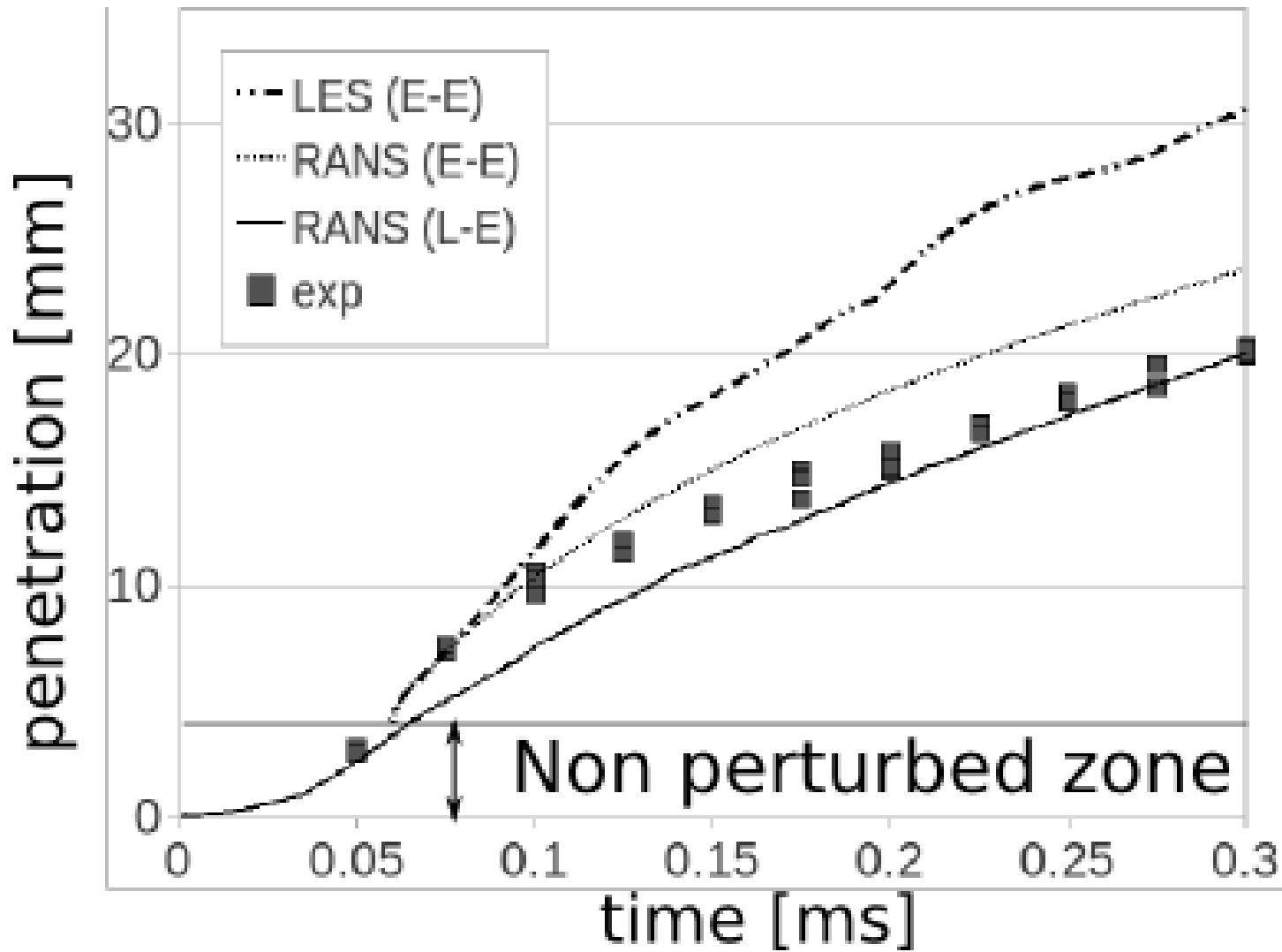
Figure 4: Comparison between experimental spray tip penetration (symbols) and CFD simulations (lines). The time axis is referred to the start of injection.
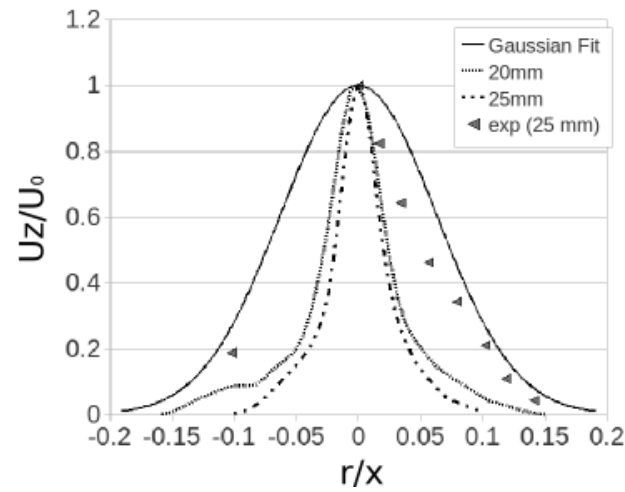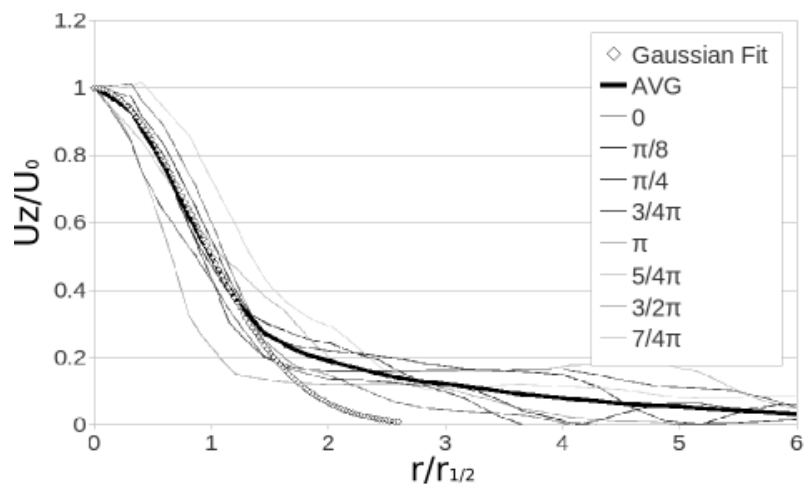
Figure 6: Radial velocity profiles (t=0.5ms). Left: Spatial average of eight different angles, Right: Time-averaged.

and 25 mm in Figure 6(right) can be affected by the amount of statistics for each location (around 0.05ms of data less at 25mm). Experimental data is close to LES simulated profile near the edge of the spray but moves to the Gaussian one as r increases.

5   Conclusions

Using the OpenFOAM code, the authors have performed a completed simulation of diesel spray in LES. Even the results do not match completely with the experimental results and RANS simulation, however; it performs a correct trend of spray simulation. These depict the complicate of modelling of spray processes with many direct or indirect parameters involved. Some specific needs are presented in our paper as challenges to overcome. The future research is now focusing on identifying the important parameters that affect the model and on improving the stability and accuracy of algorithms within OpenFOAM code. By so doing, the better spray simulation will be performed and a reliable tool will be used in modelling the spray simulation in the near future. Hence, LES modelling can become the practical tool in both industry and academic in the design process of combustion systems.

References

[1] Pope S. B., Turbulent Flows, Cambridge University Press, 2000. 771 pp.

[2] J.J. Riley, Review of large-eddy simulation of non-premixed turbulent combustion, J Fluids Eng 128 (2006), pp. 209-215.

[3] Pitsch, H., Large-Eddy Simulation of Turbulent Combustion, Annual Review of Fluid Mechanics, Vol. 38, No. 1, 2006, pp. 453-482.

[4] Fabian Peng-Krrholm, Numerical modelling of diesel spray injection, turbulence and combustion, Ph.D. Thesis, Chalmers Uni. of Technology, 2008.

[5] J.M. Desantes and J.V. Pastor and J.M. García-Oliver and J.M. Pastor, A 1D model for the description of mixing-controlled reacting diesel spray, Combustion and Flame, 2009, 156, pp 234 - 249.

[6] R. Payri and B. Tormos and J. Gimeno and G. Bracho, The potential of Large Eddy Simulation (LES) code for the modeling of flow in diesel injectors, Mathematical and Computer Modelling, Volume 52, Issues 7-8, 2010, Pages 1151-1160.

[7] J.S. Smagorinsky, General circulation experiments with the primitive equations. I. The basic experiment, Mon. Weather Rev. 91 (1963), pp. 99–164.

[8] Ville Vuorinen, LES of Certain Droplet Size Effects in Fuel Sprays, PhD Thesis, the Aalto University School of Science and Technology, 2010.

[9] Desantes JM, Payri R, Salvador FJ, Gimeno J. Measurements of spray momentum for the study of cavitation in diesel injection nozzles. SAE Paper 2003-01-0703; 2003.

[10] R. Payri, J.M. García, F.J. Salvador and J. Gimeno, Using spray momentum flux measurements to understand the influence of Diesel nozzle geometry on spray characteristics, Fuel 84 (2005), pp. 551–561.

[11] J.M. Desantes, R. Payri, J.M. Garcí

a and F.J. Salvador, A contribution to the understanding of isothermal diesel spray dynamics, Fuel 86 (2007), pp. 1093–1101.

[12] Correas D. Theoretical and experimental study of isothermal Diesel free sprays (In Spanish), PhD Thesis, Universidad Politcnica de Valencia; 1998.

[13] D. Jaime Gimeno Garca, Desarrollo y aplicacin de la medida del flujo de cantidad de movimiento de un chorro diesel, PhD thesis, Universidad Politécnica de Valencia, 2008.

[14] Abraham J, What is Adequate Resolution in the Numerical Computations of Transient Jets? SAE 970051 pp 81-95

[15] L. Araneo, V. Soare, R. Payri, J. Shakal, Setting up PDPA system for measurement in a diesel spray, Journal of Physics, 45, 2006, 85-93.

[16] Abraham J, Magi V, Macinnes J, Bracco FV. Gas versus Spray Injection: Which Mixes Faster? SAE paper 940895; 1994, pp163-177

[17] Hussein HJ, Capp and George WK. Velocity measurements in a high-Reynolds-number, momentum-conserving, axisymetric, turbulent jet, J Fluid Mech (1994). 258, 31-75.

[18] Levy Y, Lockwood FC, Combust. Flame 40, 333 (1981)

Numerical approximation of the term structure models with different risk-neutral drifts

L. Gómez-Valle [*]and J. Martínez-Rodríguez [†]

Departamento de Economía Aplicada,

Facultad de Ciencias Económicas y Empresariales, Universidad de Valladolid,

Avenida del Valle de Esgueva 6, 47011 Valladolid, Spain.[‡]

October 10, 2010

1 Introduction

An understanding of the stochastic behavior of interest rates is important for the conduct of the monetary policy, the financial of public debt, the expectations of the real economy activity and inflation, the risk management of a portfolio of securities, and the valuation of interest rate derivatives, [4].

In this paper we consider the possible dependence of the market price of risk on time and interest rates. This fact gives as a result that the risk-neutral drift, which is one of the coefficients of the pricing equation, also depends on time and interest rates. Then, we estimate the risk-neutral drift directly from the slope of the yield curve. This approach is very accurate as we show with a numerical experiment. In order to obtain the term structure we also propose a suitable finite difference method, which converges to the true solution. Finally, we obtain and compare the yield curves by means of US Treasury Bill data.

2 The model

In this study, we focus on a Markov model with only one state variable, the instantaneous interest rate, which follows this process $dr_t = \mu(r_t)dt + \sigma(r_t)dz_t$, where z_t is the standard Wiener process, $\mu(r_t)$ is the instantaneous drift and $\sigma(r_t)$ is the instantaneous volatility.

Let $P(t, r; T)$ denote the price at time t of a zero-coupon bond maturing at time T, with $t \leq T$. The bond is assumed to have a maturity value of one unit, i.e. $P(T, r; T) = 1$. By means of the risk-neutral pricing approach a zero-coupon bond price, is a martingale under probability measure Q, [4]. Therefore:

$$P(t, r; T) = E_t^Q \left[\exp \left(-\int_t^T r_u du \right) P(T, r; T) \right], \tag{1}$$

where $dr_t = (\mu(r_t) - \sigma(r_t)\lambda(t, r_t))dt + \sigma(r_t)dz_t$, is the interest rate under Q or the risk-neutral interest rate and $\lambda(t, r)$ is the market price of risk. Furthermore by means of the Feynman-Kac theorem, [6], it can be easily proved that (1) is the solution of the following partial differential equation:

$$\frac{\partial P}{\partial t} + (\mu(r) - \sigma(r)\lambda(t, r))\frac{\partial P}{\partial r} + \frac{1}{2}\sigma^2(r)\frac{\partial^2 P}{\partial r^2} - rP = 0, \tag{2}$$

which is the same for all interest rate derivatives, [5].

In the literature of the term structure, there are different models depending on the different assumptions about the interest rates and the market price of risk. In this paper, we focus on CIR and CKLS models proposed by [1] and [2], respectively.

One of the goals of this paper consists of considering the possible dependence of the market price of risk on time and interest rates. Thus, we propose the following functions: $\lambda(t, r) = (\lambda_1 + \lambda_2 t)\sqrt{r}$ in the CIR model; and $\lambda(t, r) = (\lambda_1 + \lambda_2 t)r^{1-\gamma}$ when $0 \leq \gamma < 1$ in the CKLS model. This assumption gives as a result two models with the same functional form for the risk-neutral drift $g(t, r) = \alpha_1 + (\alpha_2 + \alpha_3 t)r$, with $\alpha_1, \alpha_2, \alpha_3 \in R$, but different volatilities, which we will call MODCIR and MODCKLS, respectively.

3   Estimation methodology

In the pricing equation (2), the coefficient of $\dfrac{\partial P}{\partial r}$ is the drift of the risk-neutral interest rate $g(t, r) = \mu(r) - \sigma(r)\lambda(t, r)$. Therefore, in order to obtain the term structure it is not necessary to estimate either the interest rate drift or the market price of risk, as usually in the literature. It is enough to estimate the risk-neutral drift of the short rate. As this coefficient is not observable we propose to use the following result,

$$\frac{\partial R}{\partial T}\Big|_{T=t} = \frac{1}{2}(\mu(r) - \sigma(r)\lambda(t, r)), \tag{3}$$

proposed by [7] for estimating the market price of risk. As a consequence, we reduce the number of functions to estimate and the computational cost of the model. Moreover, it can be shown that this approach prevents arbitrage opportunities, see [3]. The efficiency of this approach is showed by means of a numerical experiment.

4   Empirical evidence

In this section we compare the yield curves obtained with the models we propose (MODCIR and MODCKLS) with those proposed by [1] and [2]. We have chosen the most actual data available from the Federal Reserve h.15 database at the moment of the study, from January 2000 to February 2010.

In order to obtain the yield curves we estimate all the parameters in the pricing equation (2) and we solve it. Then we compare them by means of the RMSE. We see that the RMSE of the models we propose are lower than the RMSE of the traditional models. Moreover, we think that analyzing these errors for the different maturities through the time gives some extra information. For exemple the errors of the models we propose (MODCIR and MODCKLS), which have the same risk-neutral drift, are very similar. Therefore, the risk-neutral drift seems to have more effect than the volatility in the pricing equation.

On the other hand the traditional models, where the possible dependence on time is not taken into account, provide low errors for the short term. However, for higher maturities (such as 2 or 3 years) when interest rates are slightly higher (2006-2008) the errors increase considerably. Furthermore, in these years the models we propose provide more accurate yields curves.

5   Conclusions

The main conclusions that we can draw from this paper are the following. First it is not necessary to estimate either the drift of the interest rate or the market price of risk; it is enough to estimate the risk-neutral drift. This approach allows us to reduce the errors and the computational cost as we showed by means of a numerical experiment. Secondly, it is not necessary to choose the functions of the model in order to know a closed-form solution for the pricing equation. Finally from the empirical analysis of some recent US Treasury data, we show that the market price of risk dependence on time as well as interest rates provides more accurate yield curves when interest rates are not too low. Furthermore, we also show that the risk-neutral drift of the instantaneous interest rates has a higher influence than the volatility in the pricing equation.

References

[1] Cox J.C., Ingersoll J.E., Ross S.A., A theory of the term structure of interest rates, *Econometrica*, 53: 385–407, 1985.

[2] Chan J.C., Karoly G.A., Longstaff F.A., Sanders A.B., An empirical comparision of alternative models of the short-term interset rates, *Journal of Finance*, 47: 1209–1228, 1992.

[3] Gómez-Valle L. and Martínez-Rodríguez J., Modelling the term structure of interest rates: An efficient nonparametric approach, *Journal of Banking and Finance*, 32: 614–623, 2008.

[4] K. Maes, Modeling the term structure of interest rates: where do we stand?, National Bank of Belgium Research Series, 200402 (2004).

[5] S.K. Nawalkha, N.A. Beliaeva and G.M. Soto, Dynamic Term Structure Modeling. John Wiley and Sons, Inc., New Jersey, (2007).

[6] S.E. Shreve, Stochastic Calculus for Finance II. Continuous-Time Models. Springer Finance, New York, (2004).

[7] O. Vasiceck, An equilibrium characterization of the term structure, Journal of Financial Economics, 5, No. 2 (1977) 177-188.

Modeling AH1N1/09 in selected regions

G. González-Parra*and A. J. Arenas‡

(*) Grupo Matemática Multidisciplinar, Universidad de los Andes, Mérida, Venezuela,

gcarlos@ula.ve,

(†) Departamento Matemáticas y Estadística, Universidad de Córdoba, Montería, Colombia,

aarenas@sinu.unicordoba.edu.co

October 10, 2010

1   Introduction

There are more than 14,000 confirmed deaths worldwide by the AH1N1/09 virus. Therefore, it is important to understand the dynamics regarding the evolution of the AH1N1/09 virus. The classical SIR epidemiological model has been used to model the influenza AH1N1/09 virus spread in the United States population, where the authors use a seasonal forced function in order to generate two waves. However, the classical SEIR model has been used to predict the infected individuals, hospital bed shortage and effectiveness of vaccination for a city of Japan [1].

Discussions of the the pandemic virus AH1N1/09 in human populations are present all around the world and its seasonality is still under debate. The appearance of waves of infection have been documented in various regions of the world for influenza during a relatively short period of time in between seasons [2]. However, it is not clear yet which are the mechanisms responsible for the generation of multiple pandemic influenza waves. A mathematical model for two-strain of influenza and with a two peaks pandemic profile has been presented in [2].

We propose several mathematical models to study the dynamics of H1N1 influenza virus spread in selected regions around the world. Since each region have different waves we rely on different SEIR models in order to explain the dynamics of each region. It is important to remark that the classical SEIR model has some inconveniences to reproduce the dynamics of H1N1 virus in some regions. We use time series notifications of individuals with virus AH1N1/09 to estimate some of the parameters of the models. Simulations of the models were made in order to analyze different dynamics of the pandemic virus AH1N1/09 during year 2009. We find that, in order to reproduce the time series data and the spread of the

---

*gcarlos@ula.ve

disease, it is convenient to suggest spatio-temporal models. Regions with only one wave are modelled with the classical SEIR and regions with multiple waves using spatio-temporal characteristics.

2   SEIR epidemiological model for AH1N1/09 virus transmission dynamics

This model consider that once an individual is recovered, acquires permanent immunity. Since we use the model for a short time period we assume constant population size. The only parameter to be estimated in the SEIR model is the transmission. The fitting process is performed by least squares method and using Nelder-Mead algorithm. In Figure 1 it is shown the suitability of the SEIR model to reproduce one wave series data of confirmed cases of pandemic AH1N1/09 influenza for Bogotá D.C. and the Venezuelan Nueva Esparta state. Next section is devoted to modeling series data of confirmed cases of pandemic AH1N1/09 influenza of other regions where a two wave profile is clear.
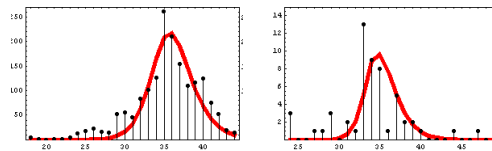
Figure 1: Model fitting for Bogotá D.C. (left) and for Venezuelan Nueva Esparta state (right) with the classical SEIR model.
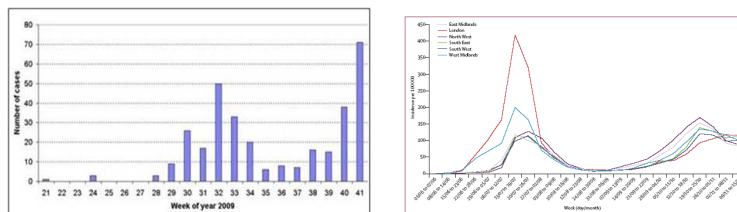
Figure 2: Confirmed cases by week during year 2009 in Iceland (left) and incidence of AH1N1 by week in different United Kingdom provinces [3].

3   Two community SEIR models

In some cases the SEIR epidemiological model is not suitable to reproduce dynamics of individuals with virus AH1N1/09. In this Section we introduce two community SEIR models that are more suitable to time series where there are two peaks. The first proposed model considers two isolated community SEIR model that include both delay and social

distancing hypotheses. In Figure 2 we show two peak time series data regarding virus AH1N1/09 in Iceland and United Kingdom provinces. The model include the possibility of a delay in the second community in regard to the introduction of the AH1N1/09 virus. In Figure 4 it can be seen the suitability of the proposed two community SEIR model to reproduce series data for Venezuela and for Venezuelan Mérida state. One hypothesis of these two peaks behaviour is that since total data come from different municipalities, it is possible that there are outbreaks in each village in different times. The other model considers two related community SEIR model. In this model it is necessary to introduce two additionally parameters for the transmission between communities. In Figure 4 it can be seen the suitability of this model to reproduce series data of confirmed cases of AH1N1/09 influenza for Venezuela and Venezuelan Mérida state.
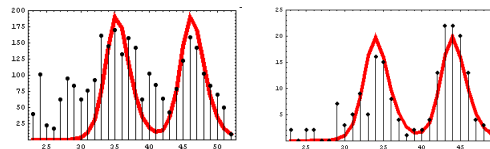
Figure 3: Model fitting for Venezuela (left) and for Venezuelan Mérida state (right) with the two community SEIR model.
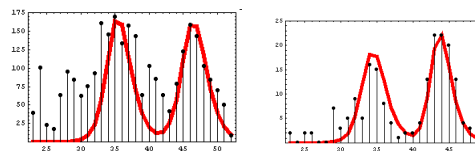
Figure 4: Model fitting for Venezuela (left) and for Venezuelan Mérida state (right) with the two related community SEIR model.

4 Conclusions

We proposed several epidemiological mathematical models applied to the spread of the pandemic virus AH1N1/09. The models were fitted and compared to time series notifications of individuals with virus AH1N1/09 from selected regions around the world. We find that for some regions the classical SEIR model was able to reproduce approximately the time series with one wave. However, for two waves series it is necessary to include two community models. It is important to remark that other models including networks, patches or stochasticity may also fit well to time series notifications of AH1N1/09 virus but may require more unknown parameters. The proposed models do not predict the appearance of new outbreaks. Nevertheless, since it is possible that some communities are still free of the AH1N1/09 virus some new outbreak may come. In this way, if social network or spatial structure is known, new outbreaks may be forecasted.

References

[1] S. Takeuchi and Y. Kuroda. Predicting spread of new pandemic swine-origin influenza A(H1N1) in local mid-size city: evaluation of hospital bed shortage and effectiveness of vaccination. *Nippon Eiseigaku Zasshi*, 65(1):48–52, 2010.

[2] D. Rios-Doria and G. Chowell. Qualitative analysis of the level of cross-protection between epidemic waves of the $1918 - 1919$ influenza pandemic. *Journal of Theoretical Biology*, 261(4):584 – 592, 2009.

[3] E. Miller, K. Hoschler, P. Hardelid, E. Stanford, N. Andrews, and M. Zambon. Incidence of 2009 pandemic influenza A H1N1 infection in England. *The Lancet*, 375(9720):1100 – 1108, 2010.

Updating the Lambda Modes of a nuclear power reactor

S. González-Pintor[†], D. Ginestar[‡], and G. Verdú[†]

(†) Instituto de Seguridad Industrial, Radiofísica y Medioambiental,

(‡) Instituto de Matemática Multidisciplinar,

Universidad Politécnica de Valencia, Camino de Vera, 14. 4602 Valencia, Spain

October 10, 2010

1   Introduction

An important problem in Nuclear Reactor Physics is the generalized eigenvalue problem,

$$\mathcal{L}\Phi_i = \frac{1}{k_i}\mathcal{M}\Phi_i \, , \tag{1}$$

where

$$\mathcal{L} = \left[\begin{array}{cc} -\vec{\nabla} \cdot (D_1 \vec{\nabla}) + \Sigma_{a1} + \Sigma_{12} & 0 \\ -\Sigma_{12} & -\vec{\nabla} \cdot (D_2 \vec{\nabla}) + \Sigma_{a2} \end{array} \right] \, ,$$

and

$$\mathcal{M} = \left[\begin{array}{cc} \nu\Sigma_{f1} & \nu\Sigma_{f2} \\ 0 & 0 \end{array} \right] \, , \quad \Phi = \left[\begin{array}{c} \Phi_1 \\ \Phi_2 \end{array} \right] \, .$$

This problem is known as the Lambda Modes problem. The fundamental eigenvalue (the largest one) is called the effective multiplication, k-effective, of the reactor core. This eigenvalue and its corresponding eigenfunction describe the steady state neutron distribution in the core.

On the other hand, to compute the dominant modes of the reactor core is useful to develop modal methods [2] to integrate the time dependent neutron diffusion equation and also for perturbative calculations.

2   Updating Modes problem

To solve the Lambda modes problem a spatial discretization of the equations has to be selected. We have used either a nodal collocation method or a high order finite element method, ending up

with an algebraic problem of the form

$$
\begin{bmatrix} L_{11} & 0 \\ -L_{21} & L_{22} \end{bmatrix} \begin{bmatrix} \psi_1 \\ \psi_2 \end{bmatrix} = \frac{1}{k} \begin{bmatrix} M_{11} & M_{12} \\ 0 & 0 \end{bmatrix} \begin{bmatrix} \psi_1 \\ \psi_2 \end{bmatrix} ,
\tag{2}
$$

This problem is reduced to the ordinary eigenvalue problem

$$
A\psi_1 = k\psi_1 ,
\tag{3}
$$

where the matrix A is defined as

$$
A = L_{11}^{-1} \left(M_{11} + M_{12} L_{22}^{-1} L_{21} \right) .
\tag{4}
$$

For perturbative calculations, we start from a known set of dominant modes for the problem

$$
\mathcal{L}_0 \Phi_i^0 = \frac{1}{k_i^0} \mathcal{M}_0 \Phi_i^0 , i = 1, \dots, p,
\tag{5}
$$

for a given configuration of the reactor, $\mathcal{L}_0$, $\mathcal{M}_0$, and we want to compute a new set of dominant modes

$$
\mathcal{L}_1 \Phi_i^1 = \frac{1}{k_i^1} \mathcal{M}_1 \Phi_i^1 , i = 1, \dots, p,
\tag{6}
$$

for a new configuration of the reactor core, $\mathcal{L}_1$, $\mathcal{M}_1$, that is close to the previous one.

3   Subspace tracking problem

The updating modes problem can be formulated as a subspace tracking problem. We have to compute a set of dominant eigenvalues and their corresponding eigenvectors of the problem

$$
Av_i^1 = k_i^1 v_i^1 , \quad i = 1, \dots, p
\tag{7}
$$

using as initial guess the eigenvectors $\{v_1^0, \dots, v_p^0\}$ of a matrix, which is 'close' to matrix A.

The Lambda modes problem is usually solved for the dominant eigenvalues and their corresponding eigenvectors using, for example, the Implicit Restarted Arnoldi method. To update the modes along a transient it is interesting to take into account that the space spanning the new modes should be close to the space spanning the previous ones.

We will consider different 'Newton-like' methods, [1], for the subspace tracking problem and we will compare their performance for the Lambda modes problem. These methods are a Modified Block Newton Method (MBNM), a One Sided Block Newton Method (OSBNM), and a Two Sided Block Newton Method (TSBNM).

4 Numerical Results

Starting from a steady state configuration of a nuclear power reactor some situations arise in which the reactor configuration is perturbed. Different events justify the study of these perturbations: poisoning by Xenon, insertion of control rods, subcooling of the entry, study of Doppler effect of a nuclear core by means of a uniform perturbation of the core, etc. An interesting transient of this kind is found in the BWR reactors when the SLCS (standby liquid control system) injects water with a high proportion of boron dissolved [3].

We consider three different configurations for the reactor core: the first one with 0 ppm of boron, the second one with 750 ppm of boron, and the third one with 1500 ppm of boron. The first 3 eigenvalues for the three configurations are shown in Table 1.

Table 1: Eigenvalues along the transient.

	λ_k		
k	0 ppm	750 ppm	1500 ppm
1	1.000487	0.964937	0.937197
2	0.989396	0.948851	0.919146
3	0.989536	0.948736	0.919430

Results for updates of these eigenvalues using the different Block Newton type methods are summarized in tables 2 and 3, where we can see the good convergerce properties of the methods. Also, the dependence of the convergence on the initial guess can be orserved, because of the local behaviour of the method.

Table 2: Iterations to converge and final relative residual from 0 to 1500 ppm

	$k = 1$	$k = 2$	$k = 3$
MBNM	11 (0.504 E-6)	14 (0.640 E-6)	14 (0.558 E-6)
OSBNM	7 (0.864 E-6)	9 (0.892 E-6)	9 (0.663 E-6)
TSBNM	7 (0.916 E-6)	9 (0.818 E-6)	9 (0.747 E-6)

Table 3: Iterations to converge and final relative residual from 750 to 1500 ppm

	$k = 1$	$k = 2$	$k = 3$
MBNM	8 (0.557 E-6)	9 (0.603 E-6)	9 (0.576 E-6)
OSBNM	7 (0.320 E-6)	7 (0.661 E-6)	7 (0.641 E-6)
TSBNM	7 (0.321 E-6)	7 (0.666 E-6)	7 (0.647 E-6)

5 Conclusions

The updating of Lambda Modes process is interesting for several applications as the development of modal methods and perturbative computations. Different methods for this process based on

the block Newton method have been proposed and their performance has been tested using a Boron injection transient.

One sided and Two sided Block Newton methods have shown the best performance regarding the number of iterations. Since the cost per iteration, is cheaper in the One Sided Block Newton method, this is the best method for this application.

References

[1] Ralf Lösche, Hubert Schwetlick, and Gisela Timmermann. A Modified Block Newton Iteration for approximating an invariant subspace of a symmetric matrix, *Linear Algebra and its Applications*, 275-276:381–400, 1998.

[2] Rafael Miró, Damián Ginestar, Gumersindo Verdú, and Dieter Hennig. A nodal modal method for the neutron diffusion equation. Application to BWR instabilities analysis, *Annals of Nuclear Energy*, 29:1171–1194, 2002.

[3] Hernan Tinoco, Przemyslaw Buchwald, and Wiktor Frid. Numerical simulation of boron injection in a BWR, *Nuclear Engineering and Design*, 240(2):221–234, 2010.

Modelling behaviour in relation to the use of potentially addictive drugs

Natividad Guadalajara Olmeda, Isabel Barrachina Martínez, Elena De la Poza Plaza and David Vivas Consuelo

Universidad Politécnica de Valencia, Departamento de Economía y Ciencias Sociales, Centro de Investigación en Economía y Gestión de la Salud, Spain

1. Introduction

Psychotropic drugs are used as a long-term symptomatic treatment in several patient types.

Of all the above drugs, the most widely used are anxiolytics (AX) belonging to the benzodiazepine group (BZN) [1] defined by the ATC N05B code (Anatomical, Therapeutic Chemical Classification System) [2].

In Spain, BZN use has considerably increased since the 1990's. Specifically between 1995 and 2002 [5], a mean increase from 39.71 to 62.02 DDD (defined daily doses) has been observed per 1000 inhabitants in the prescriptions doctors prescribed in primary health care centres. Besides, the use of such drugs is potentially chronic for periods longer than 2 years [6]. Prolonged use may lead to tolerance and addiction [4,7], withdrawal symptoms if discontinued [8], possible osteoporosis-related fractures [9] and to other adverse reactions, most of which are never notified [10].

Several studies have demonstrated a higher number of prescriptions for female subjects and at more advanced ages [3, 6, 11]. AX use is also associated with comorbidity [12, 13, 14], presence of chronic conditions [15] and with other social, economic and demographic variables [16].

This study aims to obtain mathematical models to identify different behaviours in AX prescriptions according to age, gender and the continuous prescription of other drugs associated with chronic conditions to specifically define the exact factors that determine their level of prescription and the likelihood of them occurring at different DDD levels.

2. Material and methods

2.1. Information sources and explanatory variables

The study population in this work is made up of subjects who have received a prescription of any N05B group AX in the Primary Health Care Centres in the province of Castellón (Spain) from November 2008 til 2009. This province was selected because information about electronic prescriptions provided by the DGF (the Regional Valencian Government's General Pharmacy Management) was available.

The DGF offers information for each SIP code in the province of Castellón about: the health district, the basic health area, the patient's age and gender, whether drugs are freely prescribed or subsidised[1], the price and date of each prescription, the drug type prescribed, and the number of DDD prescribed.

Consequently of the 504,224 SIP-registered inhabitants who were initially considered, approximately half (254,722) were prescribed drugs associated with the 24 chronic diseases determined. Of these, 84,394 (33.13%) had been prescribed some N05B group drug. Finally, we eliminated 8,616 SIP-registered inhabitants who did not correspond to the 4 health districts in the province under study. The number of the analysed SIP-registered inhabitants was 75,778.

The explanatory variables for AX prescriptions were: age, gender, freely prescribed drugs and being prescribed more than 5 drugs per year other than AX which are associated with any of the chronic diseases determined.

2.2. Mathematical models

We firstly did a descriptive study into AX use with the aforementioned explanatory variables. Then we obtained the mathematical models by firstly using the multivariate linear regression model [1], and the logistic regression model [11, 12, 15, 16].

With the linear regression model, we attempted to explain the number of prescribed DDD for AX (regressor variables, Y) in terms of each considered explanatory variable (regressor Xi).

The logistic regression model quantified the joint influence of the explanatory variables, which were considered predictive, on the likelihood (l) of prescribing a certain number of DDD of AX (dependent variable)

3. Results

3.1. Regression model

We obtained a multivariate logarithm regression model to explain the number of DDD of prescribed AX.

---

[1] Pensioners obtain drugs free of charge, most are retired; the remaining inhabitants pay 40% of the cost.

Few differences, in prescriptions were observed in relation to gender; thus male subjects received fewer prescriptions than female subjects. On the other hand, the older the patient, the higher the number of prescribed DDD.

The continuous use of 10 of the 24 drugs associated with chronic diseases also contributed to the increased number of DDD prescribed for AX. The free-of-charge prescription condition did not appear in the model as it correlates highly with age.

3.2. Logistic model

The results obtained with the logistic regression analyses for the 4 prescribed DDD groups (< 30, 31-90, 91-180 and >181).
The effect of age, gender and the continuous use of the drugs associated with chronic diseases on the likelihood of prescribing AX of a DDD under 30 was virtually null.

The prescription of higher DDD was virtually not due to gender differences. Male patients showed a slightly higher risk (1.094 times) of receiving prescriptions of below 30 DDD, and a slightly lower risk (0.929 times) of receiving prescriptions of 91-180 DDD. No significant gender differences were found for the other dose levels.

Also the risk of receiving prescriptions of between 31-90 DDD for the 15-29 age group was 15 times greater than for the under 14-year-old age group, and was almost 29 times greater for the over 79-year-old age group.

4. Discussion

The results of this study coincide with the findings reported by other authors in Spain [6] and in other countries [1, 10, 15]**.** The strong point of this study lies in its large study sample size as it includes the whole population of a given geographical area.

Gender differences in AX use and prolonged use have also been reported by other authors [11, 15]; Our descriptive results reveal that this higher prescription frequency in females is more noticeable as from the age of 45. The mathematical models obtained indicate that the number of DDD prescribed to females scarcely increases; The probability of higher DDD being prescribed is practically null for the medium and high DDD.

Evidently, the use of group N05B drugs to treat anxiety is associated with the use of those drugs to treat other mental pathologies, a scenario which has also been reflected by other authors [8].

5. Conclusions

This study demonstrates that the prevalence of AX use in the general population who go to the primary health care centres in the province of Castellón is over 16%.

These results provide very relevant information for Health Authorities' policy making in relation to the rational use of AX drugs and for preventing the risk of addiction and adverse effects.

5. References

[1] A. Bocquier, K. Bezzou, S. Nauleau, P. Verger, Dispensing of anxiolytics and hypnotics in southeastern France: demographic factors and determinants of geographic variations, Fundamental & Clinical Pharmacology 22 (2008) 323-333.

[2] WHO Collaborating Centre for Drugs Statistics Methodology. Anatomical Therapeutic Chemical (ATC) classification index. Oslo: WHO Collaborating Centre for Drug Statistics Methodology; 1999

[3] C. Vedia, S.Bonet, C. Forcada, N.Parellada, Estudio de utilización de psicofármacos en atención primaria, Atención Primaria 36 (5) (2005) 239-247.

[4] B. Baltheme, Y. Poirot. Anxiety level and addition to fist-time prescriptions of anxiolytics: a psychometric study. Presse Medicale, 37. (11) (2008):1555-1560.

 [5] J. García del Pozo, F.J. de Abajo Iglesias, A. Carvajal García Pando, D. Montero Corominas, M. Madurga Sanz, V. García del Pozo, Utilización de ansiolíticos e hipnóticos en España (1995-2002), Revista Española de Salud Pública 78 (2004) 379-387.

[6] C. De las Cuevas, E. Sanz, J.A. De la Fuente, C. Cabrera, Prescribed Daily Doses and "Risk Factors" Associated with the Use of Benzodiazepines in Primary Care, Pharmacoepidemiology and Drug Safety 8 (1999) 207-216.

[7] S. Marriott, P. Tyrer, Benzodiazepine dependence. Avoidance and withdrawal, Drug Safety 9 (2) (1993) 93-103.

[8] N. Cardoner, J. Segalàs, Fármacos Ansiolíticos, Medicine 8 (104) (2003) 5612-5619.

[9] B.M. Verdel, P.C. Souverein, T.C.G. Egberts, T.P. van Staa, H.G.M. Leufkens, F. De Vries, Use of antidepressant drugs and risk of osteoporotic and non-osteoporotic fractures, Bone (2010) forthcoming. Doi: 10.1016/j.bone.2010.06.006

[10] S. Antich, V. Rodilla, L. Moreno, Estudio de la utilización de ansiolíticos, hipnóticos y antidepresivos desde farmacias comunitarias, Farmacia de Atención Primaria 6 (2008) 11-14.

[11] J.H.A. Van der Heyden, L. Gisle, E. Hesse, S. Demarest, S. Driekskens, J. Tafforeau, Gender differences in the use of anxiolytics and antidepressants: a population based study, Pharmacoepidemiology and Drug Safety, 18 (2009) 1101-1110.

[12] S. Sihvo, J. Hämäläinen, O. Kiviruusu, S. Pirkola, E. Isometsä, Treatment of anxiety disorders in the Finnish general population, Journal of Affective Disorders 96 (2006) 31-38.

[13] J. Hämäläinen, E. Isometsä, S. Sihvo, S. Pirkola, O. Kiviruusu, Use of Health Services for Major Depressive and Anxiety Disorders in Finland, Depression and Anxiety 25 (2008) 27-37.

[14] J. Hämäläinen, E. Isometsä, S. Sihvo, S. Pirkola, O. Kiviruusu, J. Lönnqvist, Treatment of Major Depressive Disorders in the Finnish general population, Depression and Anxiety 26 (2009) 1049-1059.

[15] F. Empereur, M. Baumann, F. Alla, S. Briançon, Factors associated with the consumption of psychotropic drugs in a cohort of men and women aged 50 and over, Journal of Clinical Pharmacy and Therapeutics 28 (2003) 61-68.

[16] M.T. Gónzalez, R. Landero, Variables asociadas a la depresión: un modelo de regresión logística, Revista Electrónica de Metodología Aplicada 11(1) (2006) 16-30.

A performance study of the Multidynamics Algorithm for Global Optimization

J. A. Hernández[1] *, J. D. Ospina[2]†, and D. Villada[3]

‡(1) Universidad Nacional de Colombia

Cra. 80 No. 65 - 223, Of. M8-302, Medellín, Antioquia, Colombia

(2) Universidad Nacional de Colombia

Calle 59A No 63-20 - Ncleo El Volador, Medellín, Antioquia, Colombia ,

(3) Universidad Nacional de Colombia,

Cra. 80 No. 65 - 223,Of M3-206, Medellín, Antioquia, Colombia.

October 10, 2010

1   Introduction

The MAGO (Multi Global Optimization Algorithm) is an algorithm developed for optimization problems using a scheme of evolution by dynamics, where the population, separated in subsets, is guided around the search space trying to find the global optimum. Through a novel combination of techniques such as: Selection, Elitism and Statistical Population Distribution, individuals are able to evolve from generation to generation within the guided groups in search of an optimum. Recently, in the evolutionary algorithms field there is a movement to combine them with probability theory, an arrangement that has shown successful results. The MAGO algorithm belongs to this paradigm of optimization algorithms. However, is necessary to have precise criteria for determining the performance of the MAGO. This paper presents an experiment to determine in what conditions the MAGO could not find the global optimum of a problem. The experiment also determines, when increasing the objective function dimension, which dynamics can be improved or changed so the MAGO more likely do not have convergence problems with complexity.

*jahernan@unal.edu.co

†jdospina@unal.edu.co

‡jdvillad@unal.edu.co

2 The MAGO

The MAGO algorithm [1] uses three different dynamics to produce the new individuals at each generation. As most of the evolutionary algorithms it starts with a uniform randomly distributed population over the whole searching space. Then, the exploration is performed through the creation of new individuals from three subgroups.

In [2], an evolution strategy that consists of fitting a Gaussian distribution for exploring the searching space was reviewed. New individuals are created sampling from the Gaussian distribution with the covariance matrix adapted to explore, with a major intensity, inside the promising regions of the searching space. Here, in MAGO, the idea of using the covariance matrix to set an exploring distribution is also found, but a simpler distribution, the uniform one, is used instead of the Gaussian distribution.

3 The Experiment

The MAGO depends on two parameters: the population size, called n, and the number of iterations, named ng. The experiment consisting on varying both, the population size and the number of iterations while increasing the dimension of the test function, was designed. The idea behind this experiment is to check out in what conditions the MAGO algorithm has a reasonable good approximation to the optimal solution.

For each one of the standard test functions the following procedure was done:

- Fifty runs of the algorithm for each combination of the levels of the population size and number of iterations were performed.

- For each combination of levels the final solution was classified as correct or incorrect, depending on how close it is from the theoretical solution in terms of the Euclidean distance.

- With the above information the successful rate is calculated.

4 Results

This section shows the results obtained after testing the algorithm on the functions: Rastrigin, Schwefel, Griewangk, Goldstein and Camel, looking for global minimum. Each table displays the combination of different values of the n and ng parameters, while the MAGO algorithm performs on each test function but increasing their respective dimension.

4.1 Rastrigin's function

In Table 1 start to be an obvious fact that, as it increases the ability of the algorithm, in this case by increasing the parameters n and ng the MAGO converges to the global optimum of the function. But note that in the table for some operating points are recorded letters

Succesful Rate	ng								
n	100	200	300	400	500	600	100	5000	10000
10	0,08	0,38	0,54	0,56	0,64	0,76	0,98	1	1
25	0,1	0,42	0,58	0,76	0,82	0,82	0,98	1	1
50	0,46	0,64	0,76	0,84	0,92	1	1	1	1
100	0,48	0,74	0,76	0,92	0,94	0,96	1	1	1
500	0,98	0,92	0,96	1	0,96	0,98	1	NA	NA
1000	0,98	1	1	1	0,98	1	1	NA	NA

Table 1: Results For Rastrigin's Function In Two Variables

Succesful Rate	ng								
n	100	200	300	400	500	600	1000	5000	10000
10	0,02	0,04	0,06	0	0,06	0,04	0	0,04	0
25	0,04	1	1	1	1	1	1	1	1
50	0,48	1	1	1	1	1	1	1	1
100	1	1	1	1	1	1	1	1	NA
500	1	1	1	1	1	1	1	NA	NA
1000	1	1	1	1	1	1	NA	NA	NA

Table 2: Results For Goldstein's Function In Four Variables

NA: Not Applicable, ie computationally not possible that the MAGO perform iterations under these conditions, since MATLAB does not have enough capacity to store as much data in virtual memory.

4.2 Schwefel's function

In Schwefel's function you can observe a similar behavior to that seen in Rastrigin function, in the sense that, as it increases the ability of the algorithm by means of the parameters, the probability of convergence is increased to a value of one.

4.3 Goldstein-Price's function

Table 2, there is a clear evidence of the fact that as increases the ability of the algorithm, it is in better conditions to ensure convergence to the global optimum of the function. The algorithm on the Goldstein's function shows a great performance regardless of the level of complexity to that subject. Although some very small values of n, it is not possible to find the global optimum even though the number of generations varies significantly.

4.4 Griewank's function

It can be said until now that the algorithm shows a progressive increase on the probability of convergence in the optimal search. It is then appropriate to launch the idea of the future

Succesful Rate	ng								
n	100	200	300	400	500	600	1000	5000	10000
10	0	0,2	0	0	0	0	0	0	NA
25	1	1	1	1	1	1	1	1	1
50	1	1	1	1	1	1	1	1	1
100	1	1	1	1	1	1	1	1	NA
500	1	1	1	1	1	1	1	NA	NA
1000	1	1	1	1	1	NA	NA	NA	NA

Table 3: Results For Camel's Function In Two Variables

a change in the dynamics of the MAGO, so that if the function is very large limits, as is the case Griewangk, the dynamics of the algorithm is in top condition to go all the search space, by means of a control Crowd Dynamics, which distributes many individuals in new areas that have not been explored before, and so ensure that covers the entire space at different times.

4.5   Six-hump camel back function

MAGO success in finding the global optimum Camel function is evident by the data shown in table 3. At this point we can conclude that in fact, if you increase the ability of the algorithm increases the likelihood of converging to a global optimum in a function that will submit the MAGO.

5   Conclusions

The MAGO study permitted to know the causes of the divergence of the algorithm, given the different dynamics that occurring in it. These dynamics can in principle provide clues about the cause of non convergence in a problem, because the dynamics are just the performance relationships between individuals of the population.

The MAGO algorithm can be efficient in finding global optima, under some conditions, as mentioned. But it is evident that much work has to be doing, since the MAGO in some levels of complexity cases is not able to respond as it should.

It is expected that in future, the dynamics of MAGO can be reformulated so that the dynamics of crowd has a control over the search space through a function that can be called: Crowd Dynamics to Reciprocity Distance, and so ensuring that for all generations the algorithm is executed, the whole search space is explored without leaving maxima o minima unknown.

References

[1] Hernández, J. A. and Ospina, J. D. A multi dynamics algorithm for global optimization *Mathematical and Computer Modelling*, 52(7-8):1271-1278, 2010.

[2] Lozano, Jose A. and Larrañaga, Pedro and Inza, Iñaqui and Bengoetxea, Endika, Towards a new evolutionary computation. Springer, 2006.

Mathematical Morphology for Design and Manufacturing

A. Jimeno[†] *, R. Molina[‡], and J.L. Sanchez[†]

(†) Department of Computing Technology and Data Processing, University of Alicante

Carretera de San Vicente s/n, 03690, Alicante (Spain)

(‡) Department of Computing Sciences and Artificial Intelligence, University of Alicante

Carretera de San Vicente s/n, Ap. Correos 99, E-03080, Alicante (Spain)

October 10, 2010

1   Introduction

A geometric model is a set of information, data structures, operations and tools for designing geometric objects. The features of a CAD/CAM system are largely determined by the underlying geometric model. At present, there are several types of representations with interesating features, but they also have some major drawback: limited number of primitives, difficult modification and adjustment of the surfaces, and the need of additional superficial models to display the objects. Moreover, they completely separate the design process from the manufacturing one, so additional complex operations are needed (offset calculation, machining strategies [1]-[3]) and the quality of the manufactured pieces is usually affected. The mathematical morphology framework [4] is related for first time in [5] to the description of machining processes in two dimensions. The major advantage is that mathematical morphology is not subject to any spatial restrictions [6],[7]. Another approach for describing objects directly through manufacturing operations is the Surface-Trajectory model [8]. In this paper, a new specialized morphological model of representation is presented, integrating the process of machining with the display of machined objects using mathematical morphology.

2   Morphological model of representation

Mathematical morphology is based on set theory, describing geometric shapes from simpler ones. Sets represent object shapes in a n-dimensional space and morphological operations

---

*e-mail: jimeno@dtic.ua.es

represent geometric relationships between points. An analogy between the design and the machining processes can be established. The classical morphological model has a non-deterministic nature, defined over elements of a set without order restrictions. For machining purposes, a redefinition of the morphologic operations is needed to support an order, so that it will represent the tool trajectory. Moreover, only the boundary of operations are needed. Let $E \equiv \Re^n$ be the domain where the sets are defined. Let $X \subseteq E$ be a subset of E (X is an object). The erosion operation is defined as the place of centre positions y of the structuring element B when it is forced to be inside an X set. For solid objects, the contour of the erosion is defined as the centers of B when it touches the inner frontier of the object (function $Fr(\mathrm{X})$ obtains the object contour).

$$X \odot B = \{y \in E, B_y \subseteq X\}; Fr(X \odot B) = \{y \in E, B_y \subseteq X \;\wedge\; B_y \cap Fr(X) \neq \emptyset\} \quad (1)$$

Our new morphological operations are divided into an ordered sequence of unitary or *instant basic operations* (they correspond to a particular position of a tool along a trajectory, at a time instant). Let us define the instant basic operator $\odot_{\Gamma(k)}$ for instant k as follows:

$$X \odot_{\Gamma(k)} B = y \in E : y = dist_{\vec{v}}(B, X \bullet \Gamma(k)) \cdot \vec{v} \wedge B_y \cap X \neq \emptyset \quad (2)$$

where X is the target object, B the structuring element, $\Gamma(k)$ is a homogeneous transformation matrix in $\Re^{n+1} \times \Re^{n+1}$ for a particular $k \in [0, 2\pi)$ real value; and $dist_{\vec{v}}$ is the Euclidean distance B and X once transformed in the direction of vector $\vec{v}$. The concept is illustrated in figure 1, where object X is tranformed applying a 2D rotation over its center c. The only geometric calculations are a homogeneous transformation and the Euclidean distance. From the instant basic operation, a new operation can be defined, so that it
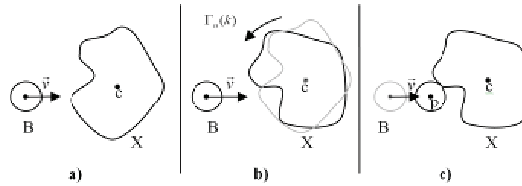
Figure 1: Instant basic dilation. a) Initial Position. b) X Transformation c) Distance computing

fulfills the condition of the structuring element to be included in the target set X. Erosion with trajectory is defined as the set of points obtained by repeated application of the instant erosion $\odot_{\Gamma(k)}$ for the real domain $[0, 1]$.

$$X \odot_{\Gamma} B = \bigcup_{k \in [0,1]} (X \odot_{\Gamma(k)} B)) = \{y \in E : B_y \cap Fr(X) \neq \emptyset \;\wedge\; B_y \subseteq X\} \quad (3)$$

The transformation Γ guarantees an ordered path placed inside X in the normalized space $[0, 1]$. From this process, it follows that the boundary of the morphological erosion and the erosion with trajectory will coincide:

$$X \odot_{\Gamma} B = Fr(X \odot B) \subseteq X \odot B \quad (4)$$

The process of removing material in a milling operation can be interpreted as a morphological operation of erosion. However, it is necessary to broaden the definition of the complete morphological erosion to adapt it to manufacturing purposes.

2.1 Regularized partial erosion

The partial erosion partially covers the parametric space k, constituting a subset of the complete erosion:

$$X \odot_{P\Gamma} B \subseteq X \odot \Gamma B \tag{5}$$

However, the partial erosion has not a direct equivalent in the machining process. While the result of (5) is formally correct, the solution is not valid in the context of a machining system. In this case, it is necessary to redefine it as a *partial regularized operation*. The operation of morphological dilation $X \oplus B$ is defined as the place of the positions of the centre of the structuring element B when it touches the set X. From the machining point of view, the regularized partial erosion of an object X is now defined as the subtraction of the dilated trajectory T from the object to erode (figure 2).

$$X \ominus_\Gamma B = X \odot (T \oplus_\Gamma B); T \subseteq Fr(X) \tag{6}$$
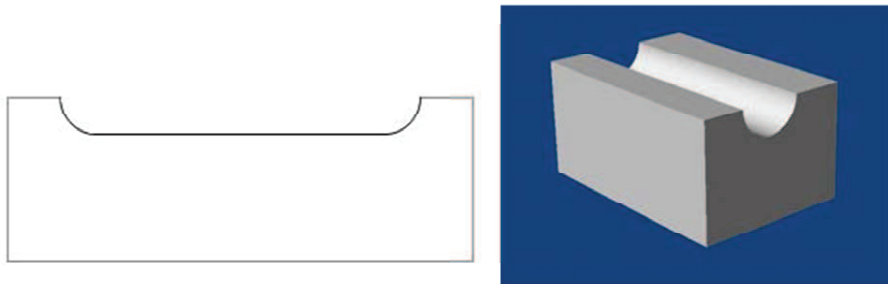
Figure 2: 2D and 3D views of the result of the regularized partial erosion of a trajectory

3 Secondary model of representation

The definition of the model is made on the continuous field, so it is necessary to provide a discrete model of representation for displaying the result of regularized partial erosions on screen. The calculation of the subtraction of the dilation from the object is immediate, since this solution is based on set theory. Nevertheless, the result of the regularized erosion is an infinite set of points, so a discretization (meshing) is needed to represent it on screen. The representation of a dilation consists in discretizing the set X in *nseg* segments and calculating every point P in the parallel of each polygon. There is a singularity at the end points of the segments, where two senses of rotational sweeping are needed at the path

extremes, side and front. The lateral sweep produces perpendicular arches to the segment and the frontal sweep produces hemispheres (figure 3). The final dilation is defined as the union of the points set of the parallel and the points set of the sweeping. Finally, the partial erosion is obtained as the subtraction of the obtained dilation from the object to be eroded. The last step is the generation of the erosion surface from the arches of
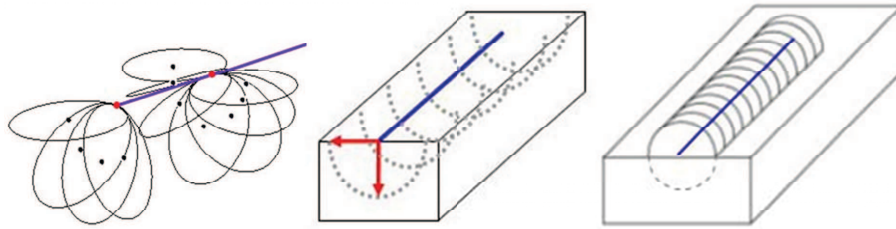
Figure 3: Dilation of a three-dimensional trajectory

dilation. As the arches are generated in an ordered manner, the erosion surface is obtained triangulating point to point the consecutives arches. This calculation is accurate and fast (figure 4).
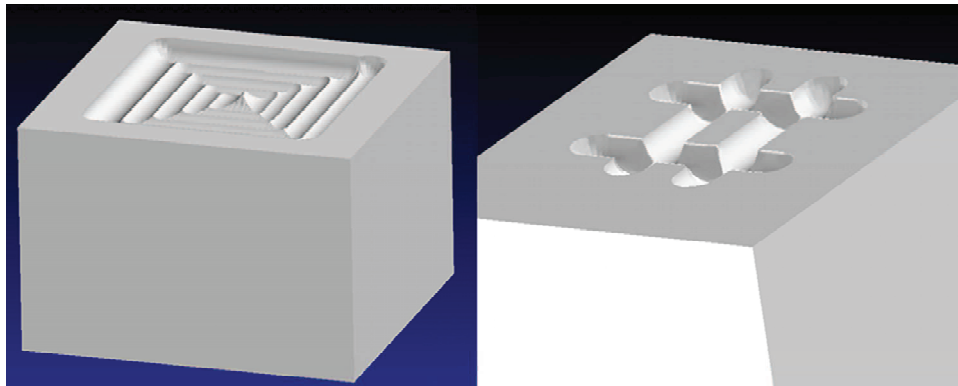
Figure 4: Examples of regularized partial erosion in three dimensions

4   Conclusions

The morphological model gives solution to the design of complex objects and an arithmetic support to the generation of manufacturing trajectories, one of the most complex problems in the CAD/CAM. It establishes an analogy between the design process and the craft work of a sculptor. The proposed model is generic and robust. It is generic, because there are no constraints in the shape of the structuring element or tool. The model can be extended to other tool shapes (squared-end, corner radius, toroidal tools, or conical tools). The model is robust because the internal representation is based on set theory so no complex

geometric calculation is needed. Moreover, the display is done by a simple triangulation method that avoids special cases, numerical errors and degenerated triangles. In a future research, it is planned to deal with the use of more complex structuring elements and the application of the proposed model on current CAD/CAM systems.

References

[1] B.K. Choi, Surface Modeling for CAD/CAM. Amsterdam, Elsevier Science Publishers, 1991.

[2] A. Iglesias, A. Galvez, and J. Puig-Pey. Computational Methods for Geometric Processing. Applications to Industry. *Lecture Notes in Computer Science*, 2073, 698–707, 2001.

[3] T. Maekawa. An overview of offset curves and surfaces. *Computer-Aided Design*, 31(3), 165–173, 1999.

[4] J. Serra, Image Analysis and Mathematical Morphology. London, Academic Press, 1982.

[5] A. Jimeno, F. Macia, and J.M. Garcia. Trajectory-based morphological operators: a morphological model for tool path computation. *Proceedings of the international conference on algorithmic mathematics & computer science, AMCS 2004*, 2004.

[6] R. Molina, A. Jimeno, and R. Rizo. Morphological offset computing for contour pocketing. *Journal of Manufacturing Science and Engineering Transactions of the ASME*, 129(2), 400–406, 2007.

[7] R. Molina, A. Jimeno, and M. Davia. Contour pocketing computation using mathematical morphology. *Int J. Adv. Manuf. Technol.*, 36(3-4), 334–342, 2008.

[8] R. Molina, Modelo Superficie - Trayectoria. Un modelo geometrico para el diseno y la fabricacion de objetos tridimensionales, PhD Thesis. University of Alicante, Alicante (Spain), 2002.

An application of graph theory to colour image processing

C. Jordán[†] [*], S. Morillas[‡], and E. Sanabria-Codesal[‡]

(†) Instituto Universitario de Matemática Multidisciplinar,

Universidad Politécnica de Valencia, Camino de Vera s/n 46022 Valencia, Spain,

Universidad Politécnica de Valencia, Camino de Vera s/n 46022 Valencia, Spain,

(‡) Instituto Universitario de Matemática Pura y Aplicada,

Universidad Politécnica de Valencia, Camino de Vera s/n 46022 Valencia, Spain.

October 10, 2010

1   Introduction

Colour image denoising is a topic which has been extensively studied in the fields of computer vision and digital image processing. The denoising (or filtering) step is essential for almost every computer vision system because noise can significantly affect the visual quality of the images as well as the performance of most automatic image processing tasks. Among the different sources of noise in digital imaging, probably the most common is modeled as additive white Gaussian noise [1].

The earliest approaches for Gaussian noise smoothing were based on a linear approach. These methods, such as the *Arithmetic Mean Filter* (AMF) [1], are able to suppress noise, because they take advantage of its zero-mean property, but they blur edges and texture significantly. This fact motivated the development of many nonlinear methods that try to overcome this drawback, among them we can find families of filters based on different approaches, for example fuzzy logic or soft switching [2, 3].

Recent nonlinear methods exhibit an improved performance with respect to the linear approaches, above all, from the edge and detail preservation point of view, since they try to detect and preserve these features.

In this paper we propose how to improve the performance of these filters by overcoming this drawback. We propose a robust method based on graph theory to classify image pixels into two classes: homogeneous regions and edge-detail regions. Specifically, we combine

---

[*]e-mail:cjordan@mat.upv.es

127

the AMF, to process image homogeneous regions, and the recent nonlinear method called *Fuzzy Noise Reduction Method* (FNRM) [2] to process the rest of the image.

The proposed filter follows the idea presented in [3] but including a new graph-based classification criteria that allows to achieve high level performance. Also, notice that although we have used the FNRM, any other nonlinear method can be used within the same structure and similar improvements are expected.

2 Proposed method of soft-switching filtering

We consider a weighted complete graph G associated to the image which set of vertices is defined by the pixels and the weight of each edge is given by the Euclidean distance between their ends. By using Kruskal algorithm [4] we determine the minimum and maximum spanning trees of G which we denote by K_m and K_M, respectively. Considering the weights of K_m and K_M we define the following coefficients, which will be used to perform the desired classification:

$$C_1 = \frac{\log w(K_m)}{w(K_M)}, C_2 = \frac{w(K_M)^2 - w(K_m)}{W}, \text{ where } W = \sum_{e \in E(G)} w(e).$$

The reasoning behind these coefficients is that their values will be very different in homogeneous and edge-detail regions of the image even in the presence of noise. Indeed, $w(K_M)$ and $w(K_m)$ will be quite similar in homogeneous regions since all edges will have similar weights and the global weight of the minimum and maximum spanning trees will be similar. In the presence of noise, some edge weights may be larger and others may be smaller, but since all pixels (vertices) are involved in the computation of the spanning trees, no large differences are expected between $w(K_M)$ and $w(K_m)$. On the other hand, $w(K_M)$ and $w(K_m)$ will be pretty different in edge-detail regions since in these regions there exist some edges with large weights and others with low weights, expressions to determine C_1 and C_2 exploit these facts, making used of logarithms and squares to enhance the difference between $w(K_M)$ and $w(K_m)$ when appropriate. For C_1, larger values are associated to homogeneous regions whereas lower values correspond to edge-detail regions. The converse situation is observed for C_2.

The proposed denoising method called *Soft-Switching Graph Denoising Method* (SSGD) uses the AMF to process homogeneous regions, whereas the FNRM is employed to filter pixels in edge-detail regions. The switching between these two methods is done in a soft fashion. So, the output of the proposed method, will be obtained as $SSGD_{out} = \alpha AMF_{out} + (1 - \alpha)FNRM_{out}$, for each image pixel. Thus, the value of α should depend on the nature of the pixel under processing; if it belongs to an homogeneous region α should be large (closer to 1), otherwise, α should be lower (closer to 0). To decide whether the particular pixel belongs to one type of region or the other we can use the coefficients C_1 and C_2. If using C_1, we know that "if C_1 is large, then the pixel belongs to an homogeneous region". Since "C_1 is large" is a vague statement, it can be modeled using fuzzy theory [5].

Specifically, we define α as a membership function which depends on two parameters: a, b that provides a value in $[0, 1]$ that represents the certainty degree of the vague statement.

Table 1: Suggested parameter setting obtained through experimental evaluation for different noise densities

Coefficient	C_1			C_2		
	$s = 10$	$s = 20$	$s = 30$	$s = 10$	$s = 20$	$s = 30$
a	0.10	0.10	0.10	0.90	0.75	0.55
b	0.85	0.75	0.60	1.00	1.00	1.00

Table 2: Performance comparison in terms of PSNR using the images contaminated with different standard deviation of Gaussian noise

Filter	PillsD			ParrotsD2			LennaD		
	10	20	30	10	20	30	10	20	30
None	28.40	22.59	19.21	19.16	22.44	19.16	19.17	22.54	19.17
AMF	25.90	25.21	24.14	23.36	22.91	22.33	27.69	26.61	25.28
FNRM	32.28	28.14	25.13	30.84	27.36	24.66	32.53	28.14	25.20
SSGD C_1F	32.40	**28.90**	26.13	30.91	**28.94**	**25.45**	32.82	29.04	26.50
SSGD C_2F	**32.48**	28.89	**26.17**	**30.94**	27.92	25.26	**32.86**	**29.12**	**26.55**

In the experimental section we have used images that have been corrupted with noise using the classical white additive Gaussian model [1]. To assess the performance of the filtering process, we use the *Peak Signal to Noise Ratio* (PSNR) as defined in [1]. We have observed that optimal parameter setting depends on both noise density and the image to be processed. However, we have seen that the settings in Table 1 are able to provide sub-optimal performance in different conditions. Notice that the standard deviation of the corrupting Gaussian noise s can be estimated using the method in [6], so the information in this table can be used to set the parameters for processing any input image. Now, using the suggested parameter setting, the test images contaminated with different densities of noise have been processed using the AMF, FNRM and the proposed SSGD method with the coefficients C_1 and C_2. As above, the quality of the filtered images has been evaluated using the PSNR quality measure. These numerical results are given in Table 2. We can see that the AMF is below the rest of the methods and the SSGD method is able to provide improved performance with respect to the FNRM.

The filter SSGD is able to smooth the noise in the homogeneous regions of the image better than FNRM, specially as the noise is high, and while keeping the same quality in edge-detail regions, which explains the PSNR improvement. This also confirms the good classification performed by the graph theory based method. It is interesting to point out that, as this filtering structure has been used to improve the performance of the FNRM, it can be also used to improve the performance of other colour image smoothing methods.

References

[1] K.N. Plataniotis, A.N. Venetsanopoulos, *Color Image processing and applications* (Springer-Verlag, Berlin, 2000).

[2] S. Schulte, V. De Witte, E.E. Kerre, A fuzzy noise reduction method for colour images, *IEEE Transactions on Image Processing*, **16** (2007) 1425-1436.

[3] S. Morillas, S. Schulte, T. Mélange, E.E. Kerre, V. Gregori, A soft-switching approach to improve visual quality of colour image smoothing filters, *in Proceedings of Advanced Concepts for Intelligent Vision Systems ACIVS07,Lecture Notes in Computer Science*, **4678** (2007) 254-261.

[4] J.L. Gross, J. Yellen *Graph Theory and its applications* (Chapman&Hall CRC, Second ed., 2006).

[5] E.E. Kerre, *Fuzzy Sets and Approximate Reasoning* (Xian Jiaotong University Press, 1998).

[6] J. Immerkaer, Fast noise variance estimation, *Computer Vision and Image Understanding*, **64** (1996) 300-302.

Spatial Season Queries in a Multidimensional Model

Francisco Moreno, Ph.D.(c),[*] Fernando Arango, Ph.D.[†]

and Jaime Echeverri, MS.c.[‡]

(*) School of Systems, University National of Colombia,

Cr 80 # 65 - 223, Medellín, Antioquia, Phone: (094) 425 5376,

(†) School of Systems, University National of Colombia,

Cr 80 # 65 - 223, Medellín, Antioquia, Phone: (094) 425 5376,

(‡) School of Systems, University of Medellín,

Cr 87 # 30 - 65, Medellín, Antioquia, Phone: (094) 340 5555

October 10, 2010

Abstract

A data warehouse is a specialized database designed to support decision–making and is usually modeled using a multidimensional view of data. A multidimensional model includes dimensions that are composed of levels. The levels of a dimension are organized in a hierarchy,e.g., salespersons are grouped into stores. Throughout its lifespan a member (instance) of a level can be associated with several members of a higher level of the hierarchy, e.g., the salespersons can rotate between the stores. This succession of associations enables the formulation of queries such as "How much did a salesperson sell in his n–th season (stay) in the store X?" In this paper, we enrich this type of query, known as season queries, with spatial features. This enhancement enables the formulation of queries such as: "How much did a salesperson sell in his n–th season in a given geographic region?" (A region that covers a set of stores.) In order to facilitate the formulation of this type of query, we propose an operator called Spatial Season and present its formal specification.

Keywords: Temporal data warehouses, spatial data warehouses, OLAP, members reclassification, season queries.

A data warehouse is a specialized database designed to support decision making and is usually modeled using a multidimensional view of data. A multidimensional model is a model of business activities in terms of dimensions and facts. A dimension is a categorizing

---

[*]e-mail: fjmoreno@unal.edu.co

[†]e-mail: farango@unal.edu.co

[‡]e-mail: jaecheverri@udem.edu.co

structure by which factual data can be classified for analysis purposes [1]. A fact represents a subject of analysis and is associated with dimensions. For example, a fact sale can be associated with SALESPERSON, TIME, PRODUCT, and CUSTOMER dimensions. A fact has measures, i.e., business metrics that analysts want to evaluate and report on, e.g., number of units of a product sold and sale value, are measures of a sale. A multidimensional collection of data arrange din this way is commonly referred to as a data cube. A dimension is organized in a hierarchy of levels to enable factual data analysis at various levels of detail according to the analysis needs [2].

The hierarchical relationship between the levels captures their full containment. A member (instance) of a level can be associated with several members of a higher hierarchical level throughout its lifespan,i.e., a member can be reclassified. These reclassifications originate the concept of season. Informally, a season is a maximum interval during which a member of a level is associated with a member of a higher level.

In this paper we proposed an operator to facilitate the formulation of spatial season queries within the context of a multidimensional model, i.e., queries such as "What were the total sales of cosmetics made by a salesperson to middle–aged women in his first season in the stores of a given geographic region?" This type of query can help evaluate the performance of the salespersons in the wake of their rotation between the stores. Furthermore, these queries can be useful in other domains too, where several phenomena are involved in a recurring manner in a geographic scenario, e.g., analyze both the material and human losses caused by a hurricane in its n–th season in acity, state, or country. This can help not only to take preventive measures but also to evaluate their effectiveness [3].

As future work, we plan to incorporate our operator in a multidimensional query language such as MDX, a language which in recent years has become a de facto standard to query multidimensional data. However, in principle there are two drawbacks that ought to be considered: first MDX has no spatial features and second MDX does not support temporal relationships between levels.

On the other hand, the temporality that exists between two levels can generate a complex data type: a trajectory. For example, a salesperson rotation between the stores defines a trajectory. We believe that the management of a trajectory as a first–class concept in a data warehouse can similarly generate interesting queries, e.g., to analyze the performance of the salespersons that have followed similar trajectories, where the notion of similarity of trajectories should be defined. For example, two salesperson trajectories could be considered similar if they have in common at least 75% of stores visited.Finally, we plan to experiment with real data in several domains and analyze the results in order to discover trends that may be associated with spatial seasons.

The table 1 presents formulations to some spatial season queries using our spatial season operator. We use the multidimensional query language of Datta [4], which operates with cubes as the basic unit of input and output for all operators. This language includes typical multidimensional operators such as selection and aggregation, allows us to select values from dimensions.

Spatial_Season sqw, gc, al$(C) = C'$
Input: Cube C **Ouput:** C'
Procedure
Step 1. Let *highest_level* be the highest level of GC. Identify the members of *highest_level*, which is a spatial level, that are contained in the spatial query window SQW.
Step 2. Let *lowest_level* be the lowest level of GC. For each member of *lowest_level* compute its seasons with regard to the region SQW and considering the members identified in the Step 1. For this purpose, consider the periods of association between the members of *lowest_level* and *highest_level*. The results make up a SEASON dimension with a level Season and attributes SStart, SEnd, and SNumber.
Step 3. Insert the SEASON dimension, generated in Step 2, into the cube C. Each fact instance $f \in C$ is associated with a member of Season level as follows. Let SM be the set of members of Season level corresponding to the member f.lowest_level. The member $sm \in SM$ associated with the fact instance f is $\{sm \mid sm \in SM AND sm@SeasonStart <= f.\text{time\_level} <= sm@SeasonEnd\}$, where f.time_level refers to the member of the bottom level of the TIME dimension associated with f. We use the symbol @ to access the attributes of a level.
Step 4. Remove the TIME dimension from C and aggregate the measures, according to the aggregate list AL, for the rest of dimensions. The output is a cube C'.

Table 1. Spatial_Season operator algorithm

Notation

- $P(Cube_1) = Cube_2$, where P is a predicate. applies aggregate functions to measures with one or more levels of a dimension specified as grouping elements.
- $[AL, GDL](Cube_1) = Cube_2$. AL is a list of elements $af_i(m_i)$ where af_i is an aggregate function applied to measure m_i, and GDL is a set of grouping dimensions levels.

References

[1] Kimball R., Ross M., Thornthwaite W., Mundy J., and Becker B., "*The Data Warehouse Lifecycle Toolkit*", Wiley, New York, 2008.

[2] Jensen C. S., Kligys A., Pedersen T. B., and Timko I., "*Multidimensional data modeling for location–based services*", 10th GIS 2002, McLean (2002) 55-61.

[3] Moreno F., Arango F., and Fileto R., "*Season queries on a temporal multidimensional model*", 11th IM2, Valencia (2009) to appear.

[4] Spaccapietra S., Parent C., Damiani M. L., Fernandes de Macêdo J. A., Porto F., and Vangenot C., "*A conceptual view on trajectories*", Data & Knowledge Engineering, Vol. 65, No. 1 (2008), 126-146.

Analysis of the influence of forest environments on the accuracy of GPS measurements by using genetic algorithms

C. Ordóñez Galán**, J. R. Rodríguez-Pérez†,
J. Martínez Torres‡ and P. J. García Nieto *

(**) Department of the Natural Resources and Environment

University of Vigo, 36310 Vigo, Spain

(†) ESTIA,University of León, 24400 Ponferrada, León, Spain

(‡) Centro Universitario de la Defensa, Academia General Militar,

Universidad de Zaragoza, 50090 Zaragoza, Spain

(*) Department of Mathematics

University of Oviedo, 33007 Oviedo, Spain

October 10, 2010

Abstract

The present paper analyzes the influence of the forest canopy on the accuracy of the measurements performed by global positioning systems (GPS) receivers using genetic algorithms technique. The influence on the accuracy of the measurements of other variables related to the GPS signal, such as the Position Dilution of Precision (PDOP), the signal-to-noise ratio and the number of satellites was also studied. The results obtained show that the variables that have the highest influence on the accuracy of the GPS measurements are those related with the forest canopy, that is, the forest stand variables. Finally, conclusions of this study are exposed.

Keywords: Forest environments; GPS measurements; Machine learning; Genetic algorithms; Multivariate adaptive regression splines (MARS)

1   Introduction

Initially The global positioning system (GPS) was developed to be employed primarily in the open spaces [1]. However, in practice many users have to operate GPS

---

*e-mail: lato@orion.ciencias.uniovi.es

receivers in less favourable conditions such as the forest cover on GPS data collection. In this way, the occurrence of canopy overhead may degrade the positional precision by one order of magnitude [2]. This research paper studies the impact of forest canopy on quality and accuracy of GPS measurements by means of the genetic algorithms (GA) technique [3] in combination with the multivariate adaptive regression splines (MARS) method [4] with success. As input variables, the dasometric characteristics of the fields together with the GPS signal variables are taken into account. As output variables, horizontal and vertical accuracies were calculated for each sample through the following expressions [2]:

$$H_{acc} = \sqrt{(E_i - E_{true})^2 + (N_i - N_{true})^2} \tag{1}$$

$$V_{acc} = |Z_i - Z_{true}| \tag{2}$$

where H_{acc} and V_{acc} indicate horizontal and vertical accuracies, respectively. E_i, Z_i and Z_i are the measured positions at the i second, and E_{true}, N_{true} and Z_{true} are the true positions along the easting, northing and ellipsoidal height directions, respectively. In this sense, the aim of the present work is to find by means of genetic algorithms those variables that have a higher influence over H_{acc} and V_{acc}. The goodness of the variables selected will be evaluated by means of R^2 the of a multivariate adaptive regression splines (MARS) model [4, 5]

2   Mathematical model

2.1   Genetic algorithms

Holland [3] in 1975 was the first who proposed the use of genetic algorithms (GAs) for problem solving. The GA uses the current population of strings to create a new population such that the strings in the new generation are on average better than those in current population (the selection depends on their fitness value). The selection process determines which string in the current set will be used to create the next generation. The crossover process determines the actual form of the string in the next generation. Weak individuals are discarded and only the strongest survive.

2.2   Multivariate adaptive regression spline

Multivariate adaptive regression splines (MARS) is a form of regression analysis introduced by Jerome Friedman in 1991 [4]. Its main purpose is to predict the values of a continuous dependent variable, from a set of independent explanatory variables. MARS builds models of the form:

$$\hat{f}(x) = \sum_{i=1}^{M} c_i B_i(x) \tag{3}$$

The model is a weighted sum of basis functions $B_i(x)$. Each c_i is a constant coefficient. Each basis function $B_i(x)$ takes one of the following three forms: (1) a

constant 1. There is just one such term, the *intercept*; (2) a *hinge* function. A hinge function has the form max(0,*x-const*) or max(0,*const-x*). MARS automatically selects variables and values of those variables for knots of the hinge functions; and (3) a product of two or more hinge functions. In this sense, the following parameters are important in this technique [4]: (1) Nsubsets: this criterion counts the number of model subsets in which each variable is included. Variables that take part in more subsets are considered more important; (2) Generalized cross validation (GCV): the GCV is the mean squared residual error divided by a penalty dependent on the model complexity; and (3) Residual sum of squares (RSS): is the residual sum of squares measured on the training data.

3   Results and conclusions

The input variables employed in the present research could be outlined as [2, 5]:

- In order to characterize each tree mass, the trees in each parcel in a radius of 10 metres around the observation point were measured and the following dasometric parameters were calculated: arithmetic mean diameter (d_m), mean height (h_m), slenderness coefficient (SLC), crown height (h_c), dominant height (H_0), treetop height (T_{t_h}), tree density (N), basal area (G), quadratic mean diameter (d_g), Hart-Becking index (HBI), wood volume (V) and biomass (W).

- In addition to parameters reflecting plant cover, a number of variables were recorded in each second measurement so that the accuracy of observation was conditioned independently of the plant cover (GPS signal variables). These variables are the following ones: (1) $PDOP_p$ (position dilution of precision for each point ($PDOP$) under the forest canopy); (2) $PDOP_r$ (PDOP for the reference point); (3) $DLLSNCA_p$ (indicator of the signal-noise ratio in CA code (in dB*Hz) for a point under the forest canopy); (4) $DLLSNL1_p$ (indicator of the signal-noise ratio in P code for $L1$ (in dB*Hz) for a point under the forest canopy); (5) $nL2_r$(number of satellites receiving code in the $L2$ carrier for the reference point), etc.

In order to find those input variables with a greater influence over $H_{acc}$and V_{acc}, a variable selection by means of GA was performed. The input variables used for the GA model are: size of the population (2,000 individuals); probability of mutation (10%); probability of crossover (50%); percentage of each population kept (20%); cardinality of the smallest subset (1); cardinality of the largest subset (20); and generations of the optimum (237 for H_{acc} and 274 for V_{acc}). In our case, the stop criterion causing the finalization of the iterations of the models was that the mean of the R^2 of the best 10 models of a generation does not improve more than a 0.05% the R^2 of any of the 10 previous generations. Table 1 shows the summarized information of the best model of the last iteration for the output variable H_{acc}. The R^2 of the MARS model performed using as input variables the corresponding variables of this individual of the population was 0.8024. In the same way, a similar table would represent the information of the best model of the last iteration for the output variable V_{acc}. The R^2 of this MARS model carried out using as input variables the

Table 1: Classification of importance of those variables that have influence over the output variable H_{acc} by means of the parameters Nsubsets, *GCV* and *RSS*.

Variables	Nsubsets	GCV	RSS
SLC	34	100.0000	100.0000
HBI	32	100.0000	21.0223
V	32	20.9356	21.0223
H_0	32	20.9356	21.0223
N	32	20.9356	19.5735
G	29	19.4836	10.8318
W	25	7.3603	6.6852
d_g	15	6.6084	1.5564
h_c	12	1.5064	0.7243
d_m	8	0.6828	0.6898
$PDOP_p$	8	0.6801	0.6566
$DLLSNL1_p$	8	0.6614	0.6233
$nL2_r$	8	0.6573	0.6146
$DLLSNCA_p$	7	0.3777	0.5965

corresponding variables of this individual of the population was 0.6739. Finally, to fix ideas, the results of this research proved that for both parameters the most important variables are in these order: *SLC*, *HBI*, *V*, d_m, H_0, *N* and *G*.

References

[1] A. El-Rabbany, Introduction to GPS: The Global Positioning System, Artech House Publishers, New York, 2006.

[2] P. Sigrist, P. Coppin, M. Hermy, Impact of forest canopy on quality and accuracy of GPS measurements, *International Journal of Remote Sensing* 20(18): 3595–3610, 1999.

[3] J.H. Holland, Adaptation in Natural and Artificial Systems, University of Michigan Press, Ann Arbor, 1975.

[4] J.H. Friedman, Multivariate adaptive regression splines, *Annals of Statistics* 19(1):1–141, 1991.

[5] J.C. Gegout, C. Piedallu, Effects of forest environment and survey protocol on GPS accuracy, *Photogrammetric Engineering and Remote Sensing* 71(9):1071–1078, 2005.

Growth impact of hydrodynamic dispersion in Couette-Taylor bioreactor

Š. Papáček[†] [*], V. Štumbauer[†], D. Štys[†], K. Petera[§], and C. Matonoha[‡]

(†) Institute of Physical Biology, University of South Bohemia,

Zámek 136, 373 33 Nové Hrady, Czech Republic,

(§) Czech Technical University in Prague, Faculty of Mechanical Engineering,

Technická 4, 166 07 Praha 6, Czech Republic,

(‡) Institute of Computer Science, Academy of Sciences of the Czech Republic,

Pod Vodárenskou věží 2, 182 07 Prague 8, Czech Republic

October 10, 2010

1 Introduction

Biotechnology with microalgae and photo-bioreactor (PBR) design is nowadays regaining attention thanks to emerging projects of CO_2 sequestration and algae biofuels. Nevertheless, there neither exist reliable methods nor software for modelling, simulation and control of PBR [10]. Modelling in a predictive way the photosynthetic response in the three-dimensional flow field seems today unrealistic, because the global response depends on numerous interacting intracellular reactions, with various time-scales.

In our previous works [7, 9, 8] we examined an adequate multi-scale lumped parameter model, describing well the principal physiological mechanisms in microalgae: photosynthetic light-dark reactions and photoinhibition. Now is our main goal the development, implementation, and validation of a mathematical model of microalgae growth in a general gas-liquid-solid PBR as tool in PBR design and optimization of its performance.

2 Development of a distributed parameter model of microalgae growth in a PBR

Leaving apart the inherently non-reliable scale-up methodology for PBR design [10], two main approaches for transport and bioreaction processes modelling are usually chosen

---

[*]e-mail: papacek@alga.cz

[11]: (i) Eulerian, and (ii) Lagrangian. While the Eulerian approach, resulting in partial differential equations, is an usual way to describe transport and reaction phenomena in bioreactors, the Lagrangian approach, leading either to a stochastic ordinary differential equations, or a technique based on random walk simulation of transport by turbulent diffusion (hydrodynamic dispersion), is an interesting alternative to PBR models.

Till nowadays, the most important information about the photosynthetic production of some microalgae species resides in the measurement of the coupling between photosynthesis and irradiance (being a controlled input), in form of the steady-state light response curve (so-called *P–I curve*), which represents the microbial kinetics, see e.g. *Monod* or more general *Haldane* type kinetics [11]. However, PBR operating under high irradiance, permitting large non-homogeneities of irradiance and allowing the photoinhibition of the cell culture and the photolimitation as well, belong to intensively studied topics of microalgal biotechnology, see e.g. [4] and references within there.

Hence, we need such a model of microalgal growth, which can describe both the steady state and dynamic phenomena, i.e. it has to fulfill the following experimental observations: (i) the steady state kinetics is of *Haldane* type or *Substrate inhibition kinetics* [6]; (ii) the microalgal culture in suspension has the so-called *light integration* property [12, 6], i.e. as the light/dark cycle frequency is going to infinity, the value of the resulting production rate (e.g. oxygen evolution rate) goes to a certain limit value, which depends on the average irradiance only [7]. These features are best comprised by the mechanistic **model of photosynthetic factory** - PSF model [2, 13, 7].

PSF model has the following form of bilinear controlled system:

$$\dot{y} = [\mathcal{A} + u(t)\mathcal{B}]y, \tag{1}$$

where the state vector has three components and it holds: $y_R + y_A + y_B = 1$. Eq. (1) has to be completed by an equation connecting the hypothetical states of PSF model with the specific growth rate μ.[1] According to [2, 13], the rate of photosynthetic production is proportional to the value of activated state: $\frac{d}{dt}c_x = \kappa \, y_A(t) \, c_x$. Considering that the value of κ is of order 10^{-4} s^{-1}, cf. [13], and $y_A(t)$ is periodic with period h, cf. [7] for more details, we have the following relation for the specific growth rate μ, according to [3]:

$$\mu = \frac{\kappa}{h} \int_0^h y_A(t) \mathrm{d}t \ . \tag{2}$$

Eq. (2) reveals why PSF model can successfully simulate the growth in high-frequency fluctuating light conditions: the growth is described through the "fast" state y_A, hence we reach the sensitivity to high-frequency inputs, see e.g. flashing light experiments [6] or light/dark cycles induced by hydrodynamic mixing. As we know, this highly required sensitivity is not reached in any other model describing microalgae growth in a PBR, cf. [5].

---

[1] $\mu := \dot{c}_x/c_x$, c_x stands for microbial cell concentration. The notation used is the most usual in biotechnological literature, cf. [11].

Eq. (1), for a given model parameters and a constant input signal u, is a stiff system and its system matrix $\mathcal{A} + u\mathcal{B}$ has three distinct eigenvalues. Two eigenvalues are negative (λ_F, λ_S), and the third is zero (its corresponding eigenvector $y_{ss} = (y_{Rss}, y_{Ass}, y_{Bss})^\top$, is the globally stable steady state solution of (1)). Introducing a new "faster" time scale $\tau = \varepsilon^{-1}t$, and eliminating state y_R $(y_R = 1 - y_A - y_B)$, (1) takes the standard form of the singularly perturbed system [3] with respect to the small parameter ε:

$$\varepsilon \frac{\mathrm{d}}{\mathrm{d}\tau} y_A = g(y_A, y_B, u(t), \varepsilon), \quad \frac{\mathrm{d}}{\mathrm{d}\tau} y_B = f(y_A, y_B, u(t), \varepsilon), \tag{3}$$

where ε is further allowed to be decreasing until zero.[2] The above (3), completed by (2), represents for some known input signal $u(t)$ the Lagrangian model of PBR. However, it should be stressed that $u(t)$ is a random variable, depending on the fluid flow in PBR. For a single microalgae cell, it can be either simulated (knowing the dispersion coefficient $D(\vec{r})$) or measured a sufficient number of trajectories $\vec{r}(t)$, and thereafter identify $u(\vec{r}(t))$.

Using Eulerian modelling approach, the stationary solution[3] in generally three dimensional domain Ω can be directly calculated from:

$$-\nabla \cdot (D(\vec{r})\nabla y) = [\mathcal{A} + u(r)\mathcal{B}]y \ \text{ in } \Omega, \nabla y = 0 \text{ on } \partial\Omega. \tag{4}$$

3   Case study: Couette-Taylor bioreactor

The main benefit of this paper resides in an extension of a lumped parameter model of photosynthetic microorganism growth to the domain with heterogeneously distributed relevant parameters; in our case these parameters are the exponential irradiance profile inside PBR, and space dependent hydrodynamic dispersion (turbulent diffusion). For a special laboratory bioreactor based on Couette-Taylor flow, so-called Couette-Taylor bioreactor (CTBR), in order to validate our approach we reached the similar simulation results using both modelling frameworks, Lagrangian and Eulerian. Moreover, our simulation results of microalgae growth in CTBR were sensitive to all relevant phenomena, including it of hydrodynamic dispersion (depending on inner cylinder angular velocity ω), i.e. we extended our conclusion about *light integration* property of PSF model to CTBR: the resulting photosynthetic production rate, for growing ω, goes to a certain limit value, which depends on the average irradiance only.

To speed up the calculation, we used the fast reduction of system (1), for more details

---

[2]Notice that the parameter ε quantifies, roughly speaking, the separation between the fast and slow dynamics; $\varepsilon \approx 10^{-3}$, based on [13].

[3]Taking advantage from the fact that only the long term cultivation in continuous PBR operation mode is of biotechnological importance and the quasi-steady state is reached.

see [8].[4] Then for the axisymmetrycal case of CTBR, (4) takes the form:

$$-\frac{1}{r}\frac{\partial}{\partial r}\left[rD(r)\frac{\partial y_A}{\partial r}\right] + q(x)\,y_A = f(x), \quad \frac{\partial y_A}{\partial r}(r_i) = 0, \; \frac{\partial y_A}{\partial r}(r_e) = 0 \; . \qquad (5)$$

References

[1] Čelikovský S., Papáček Š., Cervantes-Herrera A., and Ruiz-León J. Singular Perturbation Based Solution to Optimal Microalgal Growth Problem and its Infinite Time Horizon Analysis. *TAC IEEE*, 55 (3): 767–772, 2010.

[2] Eilers, P.H.C., and Peeters, J.C.H. Dynamic behaviour of a model for photosynthesis and photoinhibition. *Ecological Modelling*, 69: 113–133, 1993.

[3] H. K. Khalil, Nonlinear systems. Prentice Hall, 2002.

[4] Masojídek J., Papáček Š., Jirka V., Červený J., Kunc J., Korečko J., Sergejevová M., Verbovikova O., Kopecký J., Štys D, and Torzillo G. A Closed Solar Photobioreactor for Cultivation of Microalgae under Supra-High Irradiances: Basic Design and Performance of Pilot Plant. *J. Appl. Phycol.*, 15: 239–248, 2003.

[5] Muller-Feuga A., Le Guédes R., and Pruvost J. Benefits and limitations of modeling for optimization of *Porphyridium cruentum* cultures in an annular photobioreactor. *Journal of Biotechnology*, 103: 153–163, 2003.

[6] Nedbal L., Tichý V., Xiong F., and Grobbelaar J.U. Microscopic green algae and cyanobacteria in high-frequency intermittent light. *J. Appl. Phycol.*, 8: 325–333, 1996.

[7] Papáček Š., Čelikovský S., Štys D., and Ruiz-León J. Bilinear System as Modelling Framework for Analysis of Microalgal Growth. *Kybernetika*, 43: 1–20, 2007.

[8] Papáček Š., Čelikovský S., Rehák B., and Štys D. Experimental design for parameter estimation of two time-scale model of photosynthesis and photoinhibition in microalgae, *Math. Comput. Simul.*, 80: 1302–1309, 2010.

[9] Rehák B., Čelikovský S., and Papáček Š. Model for Photosynthesis and Photoinhibition: Parameter Identification Based on the Harmonic Irradiation O_2 Response Measurement. Joint Special Issue of *TAC IEEE* and *TCAS IEEE*: 101–108, 2008.

[10] A. Richmond (Ed), Handbook of Microalgal Culture: Biotechnology and Applied Phycology. Blackwell Publishing, 2004.

---

[4]The slow reduction was considered in [1]. Nevertheless, in the presence of high-frequency inputs due to the hydrodynamic mixing, and for the constant amount of light radiant energy (i.e. for a constant u_{av}), this approach leads to rather unsatisfactorily results because the inhibited state is nearly constant across the PBR and holds: $y_B = y_{B_{ss}}(u_{av})$.

[11] K. Schugerl, K.-H. Bellgardt (Eds), Bioreaction Engineering, Modeling and Control. Berlin, Heidelberg, Springer-Verlag, 2000.

[12] Terry K. L. Photosynthesis in Modulated Light: Quantitative Dependence of Photosynthetic Enhancement on Flashing Rate. *Biotechnology and Bioengineering*, 28: 988-995, 1986.

[13] Wu X., Merchuk J.C. A model integrating fluid dynamics in photosynthesis and photoinhibition processes. *Chemical Engineering Science*, 56 (11): 3527-3538, 2001.

Fuzzy control for handling occlusion in stereo sequences

E. Parrilla [*], J.R. Torregrosa, J. Riera, and J.L. Hueso

Instituto de Matemática Multidisciplinar, Camino de Vera s/n, 46022 Valencia, Spain.

October 10, 2010

1 Introduction

One of the most important problems in 3D tracking is the occlusion effect produced by obstacles.To solve this problem,we have developed a tracking system based on optical flow [1] and stereovision [2], combined with adaptive filters or neural networks to predict the expected 3D velocities of the objects [3].The critical point of the system is the coupling between tracking and predictive algorithms. We propose the use of a fuzzy control system [4] to solve this coupling problem between the different velocities. This technique has been previously tested in 2D videosequences [5], providing great robustness to the tracking algorithm.

2 Handling occlusion

In order to predict the velocities of the objects, we follow the next steps:

1. We calculate velocities for N_{in} frames of each sequence by using Lucas and Kanade algorithm and stereo vision, and we use this samples to inicialize the filter coefficients or train the neural network.

2. For the N-th frame, we calculate the velocities v_{LN} and v_{RN} in the following way:

   a. We calculate v_{LN}^{of} and v_{RN}^{of} by using optical flow and stereo vision.

   b. We estimate v_{LN}^{es} and v_{RN}^{es} by using an adaptive filter or a neural network.

   c. If $|v_{L,RN}^{of} - v_{L,RN}^{es}| < tol_{L,RN}$, then $v_{L,RN} = v_{L,RN}^{of}$. Else $v_{L,RN} = v_{L,RN}^{es}$

3. We use $v_{L,RN}$ and $N_{in} - 1$ previous samples to update the filter coefficients.

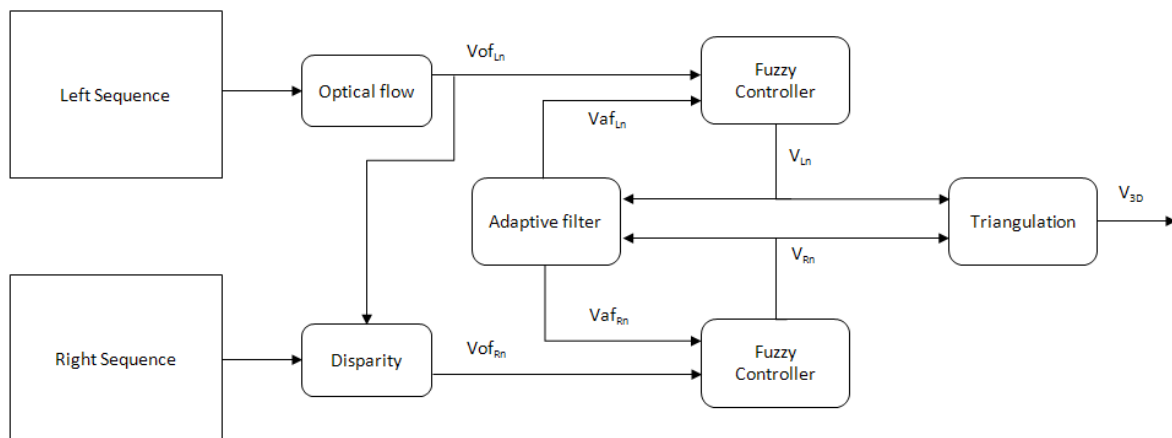---

[*]e-mail: edparber@teleco.upv.es

143

Figure 1: Tracking system diagram

It can be demonstrated that an optimum value of tolerance is

$$tol_{L,RN} = k \left| v_{L,RN-1} \right| . \tag{1}$$

3   Fuzzy controller

Tolerance values are a critical factor for the correct operation of the proposed algorithms. A very small value of the tolerance will cause the methods to select predicted velocities when there is no obstacle. On the other hand, a large value of the tolerance will make that the methods can not detect any occlusion. For this reason, the choice of parameter k is very critical. In this paper, we propose to use a variable value for parameter k controlled by a fuzzy system, instead of selecting its value a priori.

In our system, we want the value of *tol* to be small when there is an obstacle and large in any other case. The value of *tol* can be controlled by the variable k. In this way, we have designed a fuzzy system to control the value of k.

4   3D tracking system

In Figure 1, we can see a diagram of the entire system. An optical flow algorithm is applied to the left sequence in order to perform a 2D tracking of the object. From the obtained results, by calculating the disparity, we track the object in the right sequence. Moreover, the velocity values are predicted by using the adaptive filter. The velocity values calculated using optical flow and the predicted values are the inputs of two identical fuzzy controllers that are responsible for deciding which velocities are selected according to whether there is occlusion. These selected velocities will also be the inputs of the adaptive filter that will
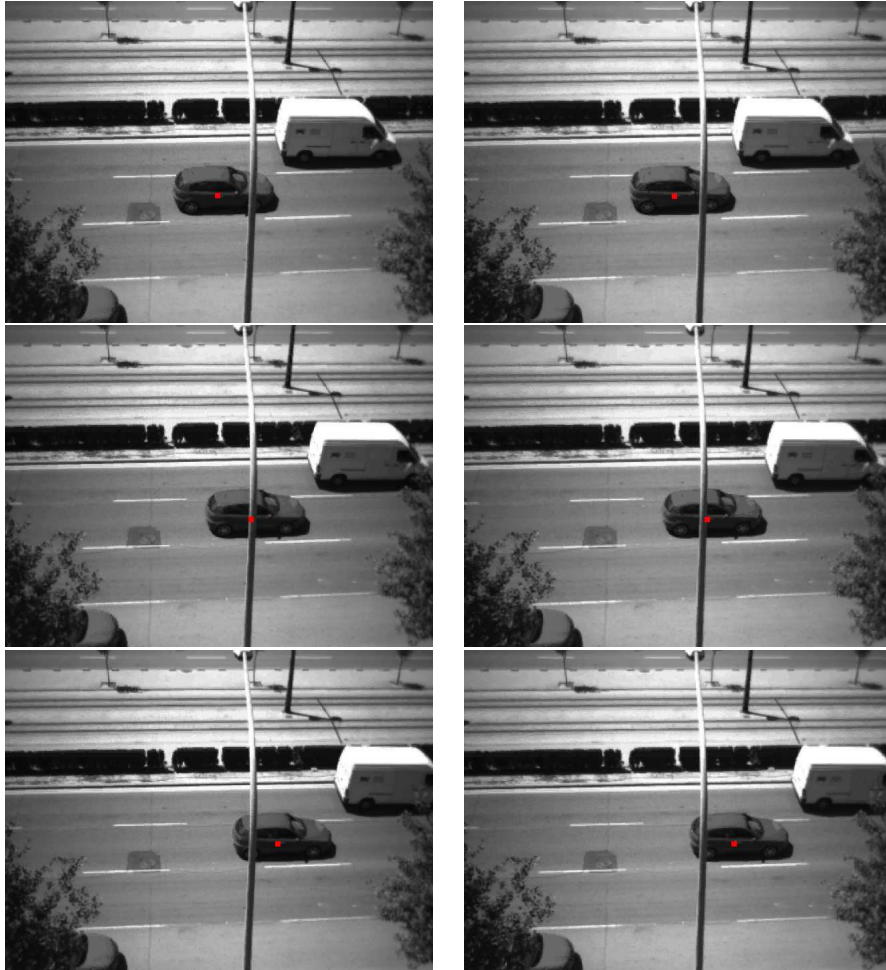
Figure 2: RLS tracking in a real sequence

update the coefficients in order to make the prediction in the next frame. Once the object has been tracked in both sequences, using the triangulation principle, we can obtain the 3D velocity of the object.

5   Numerical results

The two methods explained above have been used to analyze synthetic and real video sequences. The result has been satisfactory, since the algorithms have allowed to track the objects along the whole sequence.

An example is shown in Figure 2. We can see an urban route where there is a partial vehicle occlusion because of a street light.

As we can observe in the images, objects are successfully tracked along all the frames, there is not any error when they disappear behind the obstacles and their trajectory is predicted correctly.

6   Conclusions

In this article, we have studied a system to track objects in the three-dimensional space by combining optical flow and stereo vision.

We have proposed the use of a fuzzy controller to combine the velocities calculated by the optical flow algorithm and the ones estimated by the adaptive filter in order to predict the target movement and approximate its trajectory when the target disappears.

We have studied the effect that parameters values produce in the performance of the method, obtaining an optimal system to control the tolerance value. This fuzzy system provides a great robustness and a low computational cost.

Finally, we have shown some examples that verify the efficiency of the algorithms, proving that this technique also can detect and correct errors in the object tracking.

References

[1] E. Trucco, and K. Plakas. Video Tracking: A Concise Survey. *IEEE Journal of Oceanic Engineering*, 31(2):520–529, 2006.

[2] S.D. Cochran, and G. Medioni. 3-D Surface Description from Binocular Stereo. *IEEE Transactions on Pattern Analysis and Machine Intelligence*, 14(10):981–994, 1992.

[3] E. Parrilla, J. Riera, J.R. Torregrosa, and J.L. Hueso. Handling occlusion in object tracking in stereoscopic video sequences. *Mathematical and Computer Modelling*, 50(5-6):823–830, 2009.

[4] L.A. Zadeh. Fuzzy sets. *Inf. Control*, 8:338–353, 1965.

[5] E. Parrilla, J. Riera, and J.R. Torregrosa. Fuzzy control for obstacle detection in object tracking. *Mathematical and Computer Modelling*, 52(7-8):1228–1236, 2010.

Improvement of a LES solver for calculation of compressible liquid flows in high pressure conditions

R. Payri* [†], B. Tormos[†], J. Gimeno[†] and G. Bracho[†]

(*) CMT Motores Térmicos,

Universidad Politécnica de Valencia, Edificio D, 46022 Valencia, España,

October 10, 2010

1 Introduction

The modelling of turbulent compressible flows is an important aspect for calculations of many problems of practical engineering interest, such as aerodynamics, combustion and acoustics. Flows that involve significant changes in density are called *compressible flows*, and they frequently involve flow at very high speeds [1]. Many authors have confirmed that density is a property that increases with the pressure, then, density will increase when pressure is high [2]. Nevertheless, most of the times, in the modelling of liquid flows at high pressure conditions the effect of variable density is not considered.

So Far, any Large Eddy Simulation (LES) software is not able to resolve this problem for turbulent liquids at compressible conditions (for moderate Mach numbers). The aim of this work is to improve a LES solver, extending the mathematical description of high pressure processes in liquids, considering density as a variable.

For validating the code improvement, the LES solver is applied to a specific industrial process, such as modern common-rail nozzle injector used in diesel engines. Flow in diesel injection nozzles is characterized by high pressure drops that produce very high velocities. Therefore, because of the elevated pressure drop, density variations inside the domain could be very important, and this variation could modify the flow velocity and discharge coefficients. Results have been compared against other calculations that assumed constant properties, and simultaneously validated with experimental data.

2 Model Description

The modeling technique used is the Large Eddy Simulation, since it is able to reproduce the turbulence behaviour of the studied flow with high confidence and accuracy [3]. The basics

---

*e-mail: rpayri@mot.upv.es

148

of the LES Technique has been reported in several previous studies [4, 5]. Specifically, in this work the filtered continuity equations is written as:

$$\frac{\partial \rho}{\partial t} + \nabla \cdot (\rho \bar{u}) = 0 \tag{1}$$

where ρ is density, t is time and u is the velocity field. Commonly in liquid flows, when density is considered constant, the first term is neglected. But in this study since density is not constant, it should be taken into account. The same operation is applied to Momentum equation (Eq. 2). Again, density cannot be neglected in the right side of the expression. And should be resolved.

$$\frac{\partial (\rho \bar{u})}{\partial t} + \nabla \cdot (\rho \bar{u} \bar{u}) = -\nabla \bar{p} + \mu \nabla^2 \bar{u} - \nabla \tau \tag{2}$$

In Eq. 2 μ is the dynamic viscosity of the fluid and τ is the Sub Grid Scale Stress. In order to estimate the Sub-grid scale-stress the Smagorinsky model has been used. This is one of the most convenient and widely used model in channels and internal flows [4, 6]. Moreover, in this study the PISO (pressure Implicit with Splitting of Opperators) procedure is used to couple the pressure to the velocity via flux conservation. The PISO algorithm employed is the typical of any incompressible solver, but two more steps have been added: The first one solves the continuity equation (with the density as a variable) at the beginning of the loop, and the second one updates the density value at the end of the loop, using the final pressure values.

In order to describe the effect of pressure on liquid density, appropriate equations of state had to be considered. For the current study the equation of state derived by Payri et al. has been used [2]. They measured the variation of density for a wide range of pressures and many temperatures T, obtaining the following expression:

$$\rho = k_1 + k_2 T + k_3 p + k_4 p^2 + k_5 T^2 + k_6 pT \tag{3}$$

In Eq. 3 density is calculated using a 2nd order polynomial function of p, T and fitting constants k_n reported in [2], where the first three terms are the most significant.

3   Test Case

As was commented before, for validating the code improvement, the modified LES solver is applied to a specific industrial process, such as modern common-rail nozzle injector used in diesel engines. That particular flow is under high pressure condition. Additionally, inside the nozzle the liquid experiences an expansion, producing significant gradients of the fuel properties. The study is dedicated only to the liquid phase inside the nozzle, and the main goal is to predict the flow pattern at the hole exit (velocity and Discharge Coefficients).

The orifice has an outlet diameter of 112 μm and 1 mm of length. The geometry corresponds to an axi-symmetric nozzle manufactured specially for research purposes. The orifice has a convergent shape, thus cavitation is avoided, so the simulation only involves

incompressible liquid. The simulation conditions are characterized by a pressure inlet of 120 MPa and a pressure outlet of 5 MPa. This operating condition is selected due to the existence of previous experimental data [7], so comparison and validations can be made. The fluid is winter diesel fuel, used in previous experimental works. The fluid physical viscosity used in the simulations is 2.68e-3 Kg/m.s, whereas the density has been calculated from pressure values, according the state equation presented before (Eq. 3). In
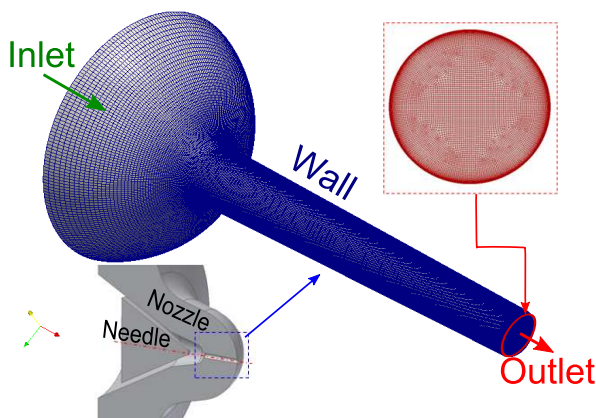

Figure 1: Geometry used for the simulations

Figure 1, it can be seen the characteristics of the mesh constructed for testing the new LES solver ability. The mesh near the wall has been refined obtaining a mesh resolution of 0.05 μm at the hole exit section; also, the mesh size is around 1.5 million cells. Moreover, previous grid study has been presented in [8].

The CFD code used for performing the simulations is OpenFOAM [9]. The case is solved twice: the first case has been calculated with the improved LES solver, named in this study as *rhoLES*. The second case has been calculated with the standard incompressible LES solver, available in [9] and described in [3], and named in this work as *stdLES*. Both cases were performed at same conditions.

4   Results and Validation

In this section the main results for the simulated cases are presented and analysed. Specifically, the results presented are Velocity trend along the nozzle domain, comparing *stdLES* solver versus *rhoLES*, analysing instantaneous and time-averaged velocity. These results will be validated using experimental data, comparing discharge Coefficient values.

In Figure 2 it can be seen a comparison between the *stdLES* solver and the improved solver *rhoLES* cases, where both cases are not exactly the same. The case solved with *stdLES* solver has slightly higher maximum velocities. This implies an over-prediction of the averaged velocities as will be demonstrated later on. On the other hand, the time averaged velocity at the hole exit is depicted. The exit velocity profiles have very similar trend, but higher value for the standard case (green color).
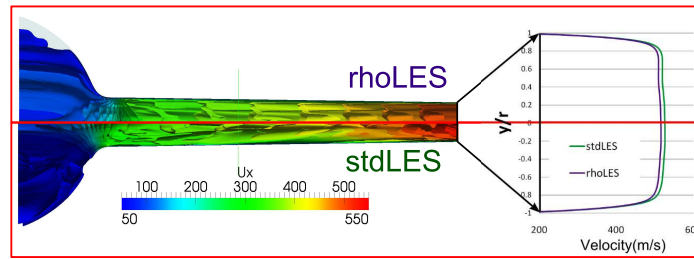
Figure 2: Velocity trend comparison. Instantaneous velocity is shown in the Left Side: *rhoLES* solution is depicted in the upper part, *stdLES* solution is depicted in bottom part. The right side shows the Averaged Velocity profile in the exit section

Since the improved solver could calculate the density changes along the geometry, it is possible to visualise the density variation through the nozzle, depicted in Figure 3. Also a interesting phenomena is captured by the calculation, smaller density values in the hole inlet radius (zones with very high pressure drops) where cavitation usually appears in non convergent nozzles.
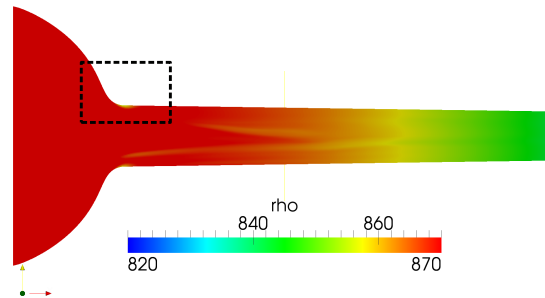

Figure 3: Instantaneous density contours. Smaller density values are observed in the hole inlet (zone inside the dashed line rectangle)

As was commented before, simulated cases are validated against equivalent experimental results reported in [7]. Specifically, the experimental data available is the mass flow at the exit of the hole. With this parameter is possible to calculate the discharge coefficient C_d dividing the obtained mass flow $\dot{m}_o$ by the theoretical mass flow $\dot{m}_t$, as states Equation 4:

$$C_d = \frac{\dot{m}_o}{\dot{m}_t} \tag{4}$$

Figure 4 plotted the experimental C_d in red line and the C_d calculated with both solvers. The result obtained with *rhoLES* solver is closer to the experimental value, whereas the standard incompressible solver case over-predicts the result. This is in agreement with

Benedict [10], who states that C_d of compressible flows is smaller than C_d of compressible flows for the same Reynolds number. This demonstrates that the flow is somehow in compressible state for the tested pressures, and that compressibility causes additional losses that reduces the discharge coefficient.
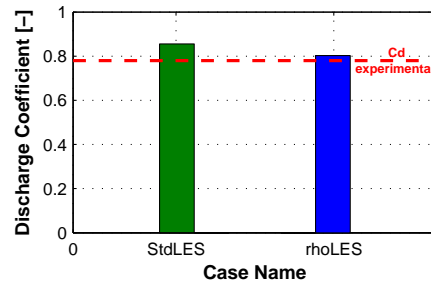

Figure 4: Discharge Coefficient Comparison: CFD values vs Experimental.

5   Conclusions

The present study gives a general outline for the fluid-dynamic calculation of liquid flows at high pressure conditions. This is achieved improving an existent incompressible LES solver. The new solver is capable for perform calculations at variable density conditions. Density is considered as a variable in all the equations, then improved solver determines density changes along the domain. Better prediction of velocity values at the hole exit is achieved, also there is an improvement in discharge coefficients determination (adapted to compressible conditions). Nevertheless, compressible Solver is more expensive than the Standard one, but it is capable to reproduce the flow pattern with enhanced precision.

References

[1] Marzougui H., Khlifi H., and Lili B. Extension of the Launder, Reece and Rodi model on compressible homogeneous shear flow. *The European Physical Journal B*, 45:147–154, 2005.

[2] Payri R., Salvador F.J., Gimeno J. and Bracho G. The effect of temperature and pressure on thermodynamic properties of diesel and biodiesel fuels. *FUEL Elsevier*, JFUE-D-10-00350R1 under revision, 2010.

[3] Payri R., Tormos B., Gimeno J. and Bracho G. The potential of large Eddy Simulation (LES) code for the modeling of flow in diesel injectors. *Mathematical and Computer Modelling*, 52:1151–1160 , 2010.

[4] Piomelli U., Large-eddy simulation: achievements and challenges, *Progress in Aerospace Sciences*, 335-362, 1999.

[5] Sagaut P., Large Eddy Simulation for incompressible flows. Springer, Berlin, 2001.

[6] Roop J.P. Numerical comparison of nonlinear subgridscale model via adaptative mesh refinement. *Mathematical and Computer Modelling*, 46:1487-1506, 2007.

[7] Payri R., Salvador F.J., Gimeno J. and Bracho G., Understanding diesel injection characteristics in winter conditions. *SAE paper 2009-01-0836*, 2009.

[8] Payri R., Tormos B., Gimeno J. and Bracho G. Internal flow modeling in diesel nozzles using Large Eddy Simulation. *Congress: Modelling for Medicine, Business and Engineering*, 2009.

[9] *OpenCFD Ltd., FOAM - The complete Guide, http://www.opencfd.co.uk*

[10] R. Benedict, Fundamentals of Temperature, pressure, and flow measurements. New York, Editorial John Wiley & Sons, 1984.

Tips for a mathematical model of Facebook

F. Pedroche*

Instituto de Matemática Multidisciplinar,

Universidad Politécnica de Valencia,

Edificio 8G, Piso 2, 46022 Valencia, España.

E-mail: pedroche@imm.upv.es

October 10, 2010

1   Introduction

From statistics of Facebook [1] we know that Facebook has more than 500 million active users, and that 50% of the active users use Facebook in any given day. The average user of Facebook has 130 friends. This great popularity of the Online Social Networking has attracted companies and researchers. In fact, some have claimed that a new discipline is established. This discipline is called Computational Social Science [2]. There are some works that handle the details of this vast field of research from the point of view of *Complex Networks*. See, for example [3], [4], [5].

2   A review of papers on Facebook

Focusing on Facebook some recent papers deal with some interesting topics. In [6] the authors analyze five Facebook networks corresponding to five American universities. The study uses data from 2005. They consider only ties between students at the same institution. Thereafter they compare the resulting community structure of each network. The method they used to identify communities is based on a modularity quality function; high values of this function correspond to groups with more intra-community links than expected at random. Then they correlate the belonging to a community with some features of the users such as residence, career, class year and high school. In [7] the authors show an interesting comparison between presence relationships (i.e., face-to-face relationships, also called spatial relationships) and online relationships (also called transpatial). The technique to make such an investigation is based on using Bluetooth technology to monitoring

---

spatial relationships, while using Facebook to measure transpatial relationships. The authors remark that there exist very similar structural features between online and physical social networks. In [8] the authors claim they have produced a method to sample users of Facebook obtaining a uniformly distributed random sample of nodes. With this unbiased sample they obtain a sample of nearly 1 million users. They claim that Facebook has a power-law degree distribution[1] separated in two zones, one using an exponent $\gamma = 1.32$, for $1 \leq k \leq 300$, and the other with an exponent $\gamma = 3.38$, for $300 \leq k \leq 5000$. The authors announce they plan to make publicly available this sample. In [9] the authors analyzed the messages sent by 4 million of users of Facebook. They conclude that messages are mostly sent to friends, but most friends do not receive messages. They propose that messaging is a more reliable measure of Facebook activity than friends links, since it is easy to have Facebook friends but you have to invest time to send messages. They also show that college student do not use Facebook as much on weekends. They obtained that the curve relating the number of messages sent in function of the number of users sending that amount of messages is of the form $n^{-\alpha n^{\beta}}$, i.e., only a small number of users send a big number of messages. In [10] the authors present a community assignment algorithm which is valid for overlapping communities. They apply this algorithm to some synthetic networks and also to the Facebook network given in [6]. They claim the usual network Facebook has overlapping communities. In [11] the authors study the reasons people have to use Facebook. The study include 423 Facebook users from 5 countries. They found that one of the main reasons to use Facebook is *social searching*: finding out what friends are doing, reconnecting with people, finding and contacting people, etc. They also remark that Facebook help people connect to their offline social networks. *Social browsing* (viewing other people's friends, looking at other profiles, browsing your friends' friends, etc.) occurs at higher level in French and Italian users than in US users. In [12] a study from 10 public and private US universities is analyzed. The data are from Facebook users, in 2005. The authors are interested in the motivations of tie strength [13]. They use data from Facebook and from administrative sources. Features such similar characteristics of students, same political orientations, same race, make the formation of a friendship more likely. They obtained that very few friendships appear to be only online friendships. They also present a model of social network formation. In [14] the authors study seven dimensions related to tie strength: intensity, intimacy, duration, reciprocal services, structural, emotional support and social distance. They recruited 35 participants to rate the strength of their Facebook friends, obtaining data over 2000 ties. They relate the dimensions with 74 Facebook variables. They conclude that the dimensions that most affect the tie strength are intimacy (32.8 %) and intensity (19.7%), follow by duration (16.5 %). As a result of the study, they present a model to predict tie strength. In [15] the authors present a network dataset based of Facebook users from universities. The population is of 1640 students. The authors claim this is the first dataset of its kind to be made publicly available[2] but the data are not available since 10/2/09 until present time. They obtain that people that connect

---

[1]The probability of having k friends is given by $P(k) \sim k^{-\gamma}$.
[2]http://dvn.iq.harvard.edu/dvn/dv/t3

with one another share some sociodemographic traits. They also obtain that Facebook is used to maintain or reinforce existing offline relationships. In [16] an study based on 24 Facebook users is done. They collect 4989 newsfeed ratings and 4238 friends ratings. One of objectives is to predict tie strength using as predictive variables some information displayed on, or associated with, newsfeed posts. The results showed a significant correlation between newsfeed rating and friend rating. In [17] the authors relate some properties of a message thread to obtain insight about the tie strength. They use 1783 postings and 2575 comments from 281 Facebook users. As a result of the study they propose a model to extract social relations from message threads. The studies on Facebook are no limited to human to human relationships. For example, in [18] the authors claim they have created the first robot that uses Facebook to socialize. The robot can take information of the profiles of the users to construct conversations. The robot can give news about mutual friends, change of status, BBC news online, etc.

3   Tips for a mathematical model

We think there are mainly three ways of classifying people in an SNS like Facebook:

- One can attend to the structure (or topology) of the network.

- One can attend to the type, quality or *tie strength* of the links.

- One can focus on particular issues of the users.

In this communication we present a model to classify the users of an SNS based on the PageRank [19] algorithm. The PageRank is a centrality measure and therefore, is a measure of the importance of a user taking into account the structure of the network.

The basis of the presented model can be found in [20]. In detail, we use the so-called *personalization vector*. Our main idea consists in using the personalization vector to bias the PageRank to users that are important according some specific features of the SNS, such as number of friends or activity. This idea also enables to introduce dimensions associated to the *tie strength* using the personalization vector.

References

[1] http://www.facebook.com/press/info.php?statistics

[2] D. Lazer, A. Pentland, L. Adamic, S. Aral, A-L Barabasi, D. Brewer, N. Christakis, N. Contractor, J. Fowler, M. Gutmann, T. Jebara, G. King, M. Macy, D. Roy, M. Van Alstyne Computational Social Science, *Science* **323** (2009), 721.

[3] D. Easley, J. Kleinberg, "Networks, Crowds, and Markets: Reasoning about a Highly Connected World," Cambridge University Press, New York, 2010.

[4] S. N. Dorogovtsev "Lectures on Complex networks," Oxford University Press, New York, 2010.

[5] M. E. J. Newman "Networks. An introduction," Oxford University Press, New York, 2010.

[6] A. L. Traud, E. D. Kelsic, P. J. Mucha, and M. A. Porter, Community structure in online collegiate social networks, submitted to *SIAM Review*, preprint, arXiv.0809.0690. 2008.

[7] V. Kostakos. An empirical study of spatial and transpatial social networks using Bluetooth and Facebook. Submitted on 22 Oct 2009. arXiv:0910.4292v1.

[8] M. Gjoka, M. Kurant, C. T. Butts, and A. Markopoulou. Unbiased Sampling of Facebook. Last revised 30 Jun 2009. arXiv:0906.0060.

[9] S. Golder, D. M. Wilkinson, and B. A. Huberman. Rhythms of social interaction: messaging within a massive online network. In *Steinfield, Pentland, Ackerman, and Contractor (eds.), Communities and Technologies 2007: Proceedings of the Third Communities and Technologies Conference, Michigan State University, London. Springer, 41-66.*

[10] C. Lee, F. Reid, A. McDaid, and N. Hurleyar. Detecting highly overlapping community structure by greedy clique expansion. Last revised 15 Jun 2010. arXiv:1002.1827v2.

[11] A. Vasalou, A. N. Joinson, and D. Courvoisier. Cultural differences, experience with social networks and the nature of true commitment in Facebook. *Int. J.Human-Computer Studies* 68 (2010) 719-728.

[12] A. Mayer, and S. L. Puller, The old boy (and girl) network: Social network formation on university campuses, *Journal of Public Economics*, 92 (2008), pp. 329347.

[13] M. S. Granovetter. The strength of weak ties. *American Journal of Sociology*, 78(6), 1973.

[14] E. Gilbert, and K. Karahalios. Predicting tie strength with social media, *Proc. Conf. on Human Factors in Computing Systems (CHI09).* 2009.

[15] K. Lewis, J. Kaufman, M. Gonzalez, A. Wimmer, N. Christakis. Tastes, ties, and time: A new social network dataset using facebook.com, *Social Networks*, 30 (2008), pp. 330342.

[16] T. Paek, M. Gamon, S. Counts, D. M. Chickering, and A. Dhesi. Predicting the Importance of Newsfeed Posts and Social Network Friends. *Proceedings of the Twenty-Fourth AAAI Conference on Artificial Intelligence (AAAI-10).* 2010. 1419–1424.

[17] M. Song, W. Lee and J. Kim. Extraction and Visualization of Implicit Social Relations on Social Networking Services. *Proceedings of the Twenty-Fourth AAAI Conference on Artificial Intelligence (AAAI-10)*. 2010. 1425–1430.

[18] N. Mavridis, S. Emami, C. Datta, W. Kamzi, C. BenAbdelkader, P. Toulis, A.Tanoto, T. Rabie. FaceBots: Steps Towards Enhanced Long-Term Human-Robot Interaction by Utilizing and Publishing Online Social Information. Submitted on 30 Apr 2009. arXiv:0904.4836v1.

[19] L. Page, S. Brin, R. Motwani, T. Winograd, The PageRank Citation Ranking: Bringing Order to the Web, Stanford Digital Library Technologies Project, 1999.

[20] Pedroche, F. "Competitivity groups on Social Network Sites," *Mathematical and Computer Modelling* **52**, (2010) 1052–1057.

Non linear multi-dimensional acoustic simulation of silencers for Internal Combustion Engines

F. Piscaglia,[*] A. Montorfano, and G. Montenegro

Dipartimento di Energia, Politecnico di Milano

via Lambruschini 4, I-20156 Milano (Italy)

October 10, 2010

1   Abstract

The level and quality of noise radiated from the open end of an internal combustion engine can be controlled by different arrangements of pipe systems and silencers, to achieve the required vehicle sound characteristic. Multi-dimensional CFD codes are effective tools to predict attenuation features of simple and complex acoustic filters. To optimize a multi-dimensional acoustic simulation, in terms of quality and accuracy of the results, it is necessary to pay attention to:

  - the case setup: combination of boundary conditions, numerical methods, discretization and interpolation schemes used

  - the minimum simulation time required to reach the convergence of the simulation

In this paper, authors test central schemes for solving non linear convection-diffusion equations together with ad-hoc developed boundary conditions for the generation of different acoustic perturbations (white noise, sweep, impulse) to perform acoustic simulation of silencers of internal combustion engines. Central schemes are not tied to the specific eigenstructure of the problem and they show low numerical viscosity even for small time steps. The temporal solution, carried out by a first-order integration of the conservation laws by the explicit Euler's method, has been first transferred into the frequency domain using FFT and then it has been processed to evaluate the transfer function of different geometries of silencers for internal combustion engines. The results obtained from the simulations have been compared with experimental data available from the literature.

2   Case setup

In order to reduce the time required by the simulations to converge, authors decided to set an impulse perturbation instead of a white noise acoustic perturbation at the inlet end of the computational domain. The formulation of the impulse is:

$$p(t) = p_0 + \sum_{n=1}^{N} \Delta P \sin(n\omega t + \phi) \tag{1}$$

where phase ϕ is constant; this allows to make the simulation time independent by the amplitude of the frequency range of the perturbation, so the time period to simulate should be given by the

---

[*]Corresponding author. Tel. (+39) 02 2399 8620, e-mail: federico.piscaglia@polimi.it

time required by the pressure impulse to travel through the computational domain. In authors' experience, by this approach two periods are needed to reach full convergence in the simulation.

The timestep of the simulation has been chosen according to the CFL criterion:

$$\frac{(v+c)\Delta t}{\Delta x} \leq \frac{1}{2} \qquad (2)$$

to ensure a maximum Courant number of 0.4.

At the inlet section a pressure impulse having frequency content between 20 to 2000 Hz (with step of 20 Hz) has been set. At the outlet section a pure reflecting boundary condition has been used.

The period of the function representing the acoustic perturbation has been assumed as $T = 1/\min(f_{min}, f_{step})$; the simulation time has been set as multiple of the period T. Since simulations were performed with no mean flow velocity, no turbulence terms were included in the governing equations.

The fluid was considered as inviscid, thus homogeneous Euler equations (**??**) were solved. Two different discretization schemes for face-interpolation of the the cell-centered quantities to compute fluxes have been tested and compared in the cases studied: the former scheme was the first-second order limited scheme of Van Leer (4), combined with a flux limiter for vector fields developed by Greenshields et al. (2). The latter was an intrinsically-limited pure-upwind differencing scheme, with first order accuracy in space.

3 Results

Noise reduction $TF(f_n)$ in ICE is defined as the ratio of Sound Pressure Level spectrums (L_p) between points A and B of the experimental apparatus of Fig. 1 described in (3):

$$TF(f_n) = -\frac{L_{p,B}(f_n)}{L_{p,A}(f_n)} = -\frac{20log\frac{p_{B,n(rms)}}{p_{ref}}}{20log\frac{p_{A,n(rms)}}{p_{ref}}} \qquad (3)$$

where p_{ref} is the reference pressure and it is set to $2 \cdot 10^{-5}$ Pa. In the simulations performed in this work, the location of microphone B is not included in the computational domain.
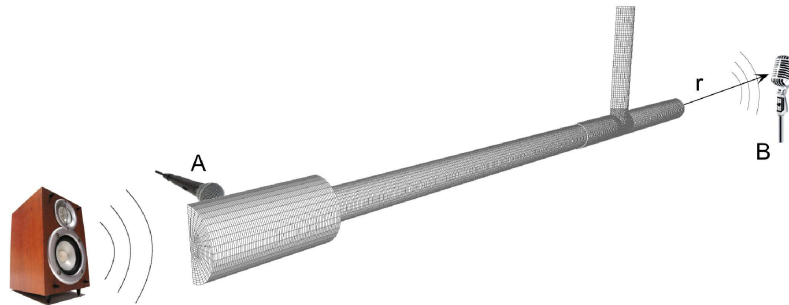

Figure 1: Experimental apparatus for the calculation of the transfer function of a silencer for internal combustion engines.

Since perturbations at the inlet are sufficiently small, the outlet end may be assumed as a monopole source radiating spherical waves (Lifshitz formula):

$$p(r,t) = \frac{\rho_0 S_{end}}{4\pi r}\frac{d}{dt}\left[U_{end}\left(t - \frac{r}{a_0}\right)\right]$$

where U_{end} is the predicted trace of flow velocity at the outlet patch.

Simulations were performed on the fully 3D dimensional geometries, as shown in Fig. 2. Comparisons between calculated and experimental transfer functions pubblished in (3) are presented in Fig. 3.
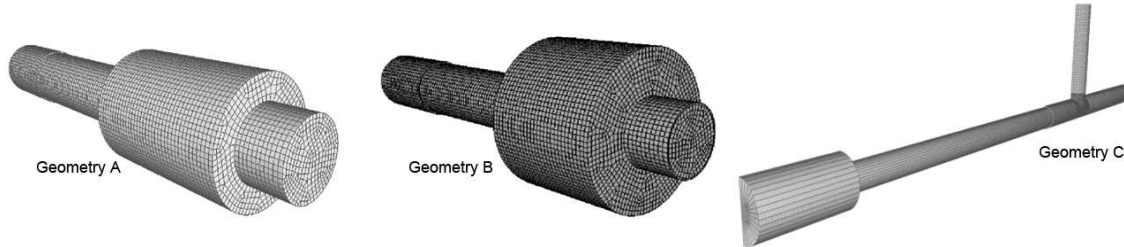

Figure 2: Three dimensional meshes of the three geometries tested.

In the simple expansion chambers (geometries 'A' and 'B' of Fig. 2), interpolation with the upwind scheme gives almost reliable predictions at medium-low frequency (below 1000 Hz), but at high frequency its high numerical dissipation does not make it suitable to capture the high frequency components of the waves (Fig. 3). Results obtained with the van Leer differencing scheme looks more satisfying. Small discrepancies occurs only at the highest frequencies of the spectrum (over 1800 Hz); in this region, however, uncertainty about experimental data have to be taken into account. In Fig. 3 (third row) the transfer function of the column resonator is also shown. Similarly to what happened for cases A and B, simulations carried out by the upwind discretization scheme are not able to predict the attenuation. When the van Leer scheme is used, results improve significantly: the fundamental frequency of the resonator is correctly captured, although a discrepancy on the second resonance frequency (at about 1200 Hz) still exists. This aspect is currently under investigation.
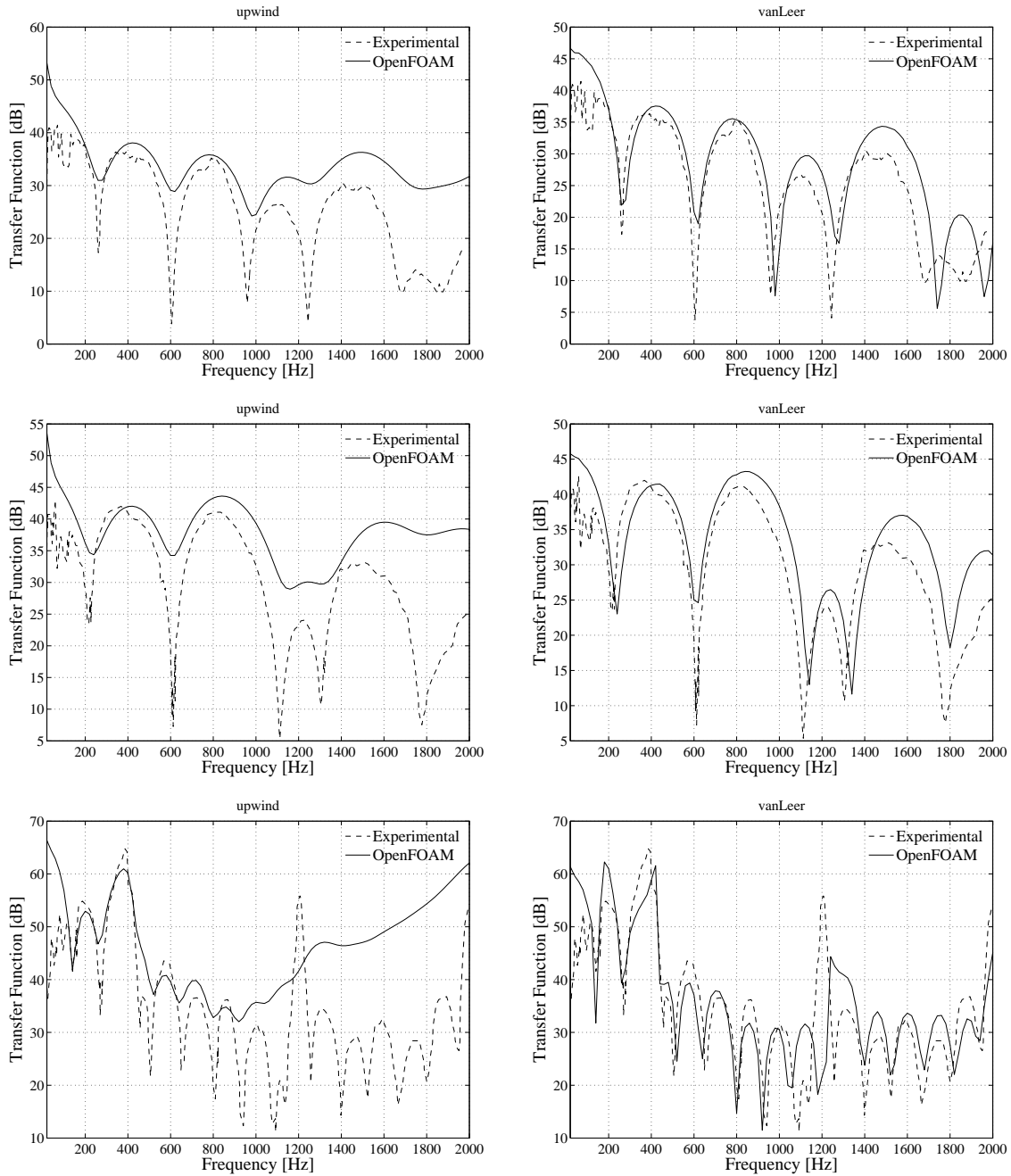
Figure 3: Simulation results on geometry A (first row), B (second row) and C (third row). Face-interpolation of the the cell-centered quantities to compute fluxes was performed by the upwind differencing scheme (left) and by the van Leer limiter differencing scheme (right).

4 Conclusions

The aim of this paper was to find a reliable methodology to use multi-dimensional non linear acoustic simulation to predict the performance and the attenuation of silencers for internal combustion engines applications. A newly developed boundary condition has been coupled with central scheme for compressible fluids, that is characterized by low numerical dissipation and high reso-

lution. Three different simple silencer geometries have been studied, in order to test and validate the code.
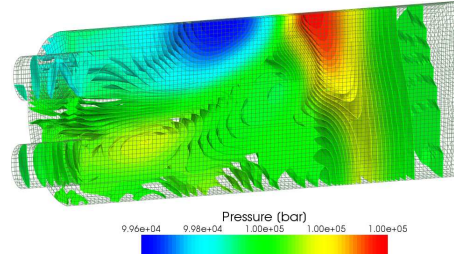

Figure 4: Code validation on a non symmetric reverse chamber.

Future work will be focused on the improvement of the results at high frequencies (1800-2000 Hz), on the further validation on different geometries (Fig. 4). The development of an implicit non-reflecting outlet boundary condition based on the Navier Stokes Characteristic Boundary Conditions in the OpenFOAM® technology, to extend the code to the calculation of the Transmission Loss (TL) of silencers, is under progress.

References

[1] A. Kurganov, S. Noelle, G. Petrova. "Semidiscrete Central-Upwind Schemes for Hyperbolic Conservation Laws and Hamilton–Jacobi Equations." *SIAM Journal on Scientific Computing*, 23(3):707-740, 2001.

[2] C. J. Greenshields, H. G. Weller, L. Gasparini, J. M. Reese. "Implementation of semi-discrete, non-staggered central schemes in a colocated, polyhedral, finite volume frameworsk for high-speed viscous flows." *International Journal for Numerical Methods in Fluids*, 2009.

[3] A. Onorati. "Numerical Simulation of Unsteady Flows in I.C. Engine Silencers and the Prediction of Tailpipe Noise". in: *"D. E. Winterbone and R. J. Pearson - Design Techniques for Engine Manifolds"*, Chapter 6. Professional Engineering Publishing, London, 1999.

[4] Bram van Leer. "Towards the ultimate conservative difference scheme. II. Monotonicity and conservation combined in a second-order scheme". *Journal of Computational Physics*, 14(4): 361-370, 1974.

New efficient numerical methods to describe the heat transfer in a solid medium

E. Ponsoda*, S. Blanes and P. Bader

Instituto Universitario de Matemática Multidisciplinar,

Universidad Politécnica de Valencia. Spain.

1   Introduction

The analysis of the spatial heat conduction through a solid with local areas of heat generation, leads to a linear matrix differential equation with separated boundary conditions. Indeed, let us denote by z the direction of the heat flow and by Z the total length of the solid medium. If we consider that the flow in other directions is much smaller, the problem can be approximated in one dimension. Then, we define a control volume of length Δz and cross sectional area A, where we can perform an energy balance in order to derive a conservation equation for thermal energy in terms of temperature. This analysis leads to a boundary value problem (BVP) which describes the temperature along the length of the body in the direction of the flow, see [5]. If we denote $t = z/Z$, the non autonomous and non homogeneous BVP is given by

$$\left.\begin{array}{c} T''(t) + p(t)\,T'(t) + q(t)T(t) = f(t); \\ K_{11}T(0) + K_{12}T'(0) = \gamma_1, \quad K_{21}T(1) + K_{22}T'(1) = \gamma_2\,; \end{array}\right\} \tag{1}$$

where $T(t)$ is the temperature, $f(t)$ is the heat generation, and $p(t)$, $q(t)$ are the advection and convection coefficients, respectively, that can be depending of the local position t and its cross section A at this point. The first term in the equation corresponds to the conduction on the direction flow. Whit appropriate coefficients and boundary conditions, the system (1) describes also a material processes in which a solid body is moving out of a hot region and the heat flow is mainly oriented in the direction of the motion of the body, like a long slab of steel emerging from a furnace or a metal rod undergoing continuous hardening, for example, see [2] for details.

It is also important to remark that non linear BVPs can be numerically solved by quasilinearization, and this is, in practice, the recommended approach of implementation because it leads to a modular program design. Once we have a program module to solve

---

*e-mail: eponsoda@imm.upv.es

linear problems with a given method, it can be invoked repeatedly for each iteration of a non linear problem by first linearizing it [1]. An additional remark to take into account is that in many cases, $p(t)$, $q(t)$ and $f(t)$ are functions which are only known on a given mesh.

2 The matrix boundary value problem

In order to addresses the problem (1), we consider the numerical integration of a general linear two point boundary value problem of the form

$$\mathbf{y}'(t) = M(t)\mathbf{y}(t) + \mathbf{h}(t); \quad B_0\mathbf{y}(0) = \gamma_1, \quad B_1\mathbf{y}(1) = \gamma_2; \quad 0 \le t \le 1.$$

Here $\mathbf{y}(t), \mathbf{h}(t) \in \mathbb{C}^n$, $M(t) \in \mathbb{C}^{n \times n}$, $B_0 \in \mathbb{C}^{p \times n}$, $B_1 \in \mathbb{C}^{q \times n}$, $\gamma_1 \in \mathbb{C}^p$, $\gamma_2 \in \mathbb{C}^q$, with $p + q = n$, and we assume that $\mathrm{rank}(B_0) = p$ and $\mathrm{rank}(B_1) = q$. We consider the case $q \le p$ because the case $p < q$ can be treated in a similar way. Notice that the limit cases $p = 0$ or $q = 0$ corresponds to initial and final value problems respectively. Let us denote

$$\mathbf{y}(t) = \begin{bmatrix} \mathbf{y}_1(t) \\ \mathbf{y}_2(t) \end{bmatrix}, \quad M(t) = \begin{bmatrix} A(t) & B(t) \\ C(t) & D(t) \end{bmatrix}, \quad \mathbf{h}(t) = \begin{bmatrix} \mathbf{f}_1(t) \\ \mathbf{f}_2(t) \end{bmatrix}.$$

Note that problem (1) corresponds to the particular scalar case when $y_1(t) = T(t)$, $y_2(t) = T'(t)$, $A(t) = 0$, $B(t) = 1$, $C(t) = -q(t)$, $D(t) = -p(t)$, $f_1(t) = 0$ and $f_2(t) = f(t)$, $B_0 = [\, K_{11} \quad K_{12} \,]$, $B_1 = [\, K_{21} \quad K_{22} \,]$. For stiff problems it is convenient to consider the imbedding formulation which we briefly introduce. Let us consider the change of variables

$$\mathbf{y}(t) = Z(t)\mathbf{w}(t) = \begin{bmatrix} I_p & X \\ 0 & I_q \end{bmatrix} \begin{bmatrix} \mathbf{w}_1(t) \\ \mathbf{w}_2(t) \end{bmatrix}. \tag{2}$$

By the imbedding formulation [4], the two-point boundary value problem can be replaced by a set of initial value problems (IVPs), and it is closely related to the shooting method. This procedure leads to a matrix Riccati differential equation (RDE) that is coupled with other equations. Thus, in the same way that in [4], the original BVP can be solved as follows:

(I) Solve, from $t = 0$ to $t = 1$, the IVPs

$$X'(t) = B(t) + A(t)X(t) - X(t)D(t) - X(t)C(t)X(t), \ X(0) = -K_{11}^{-1}K_{12}.$$

(II) Taking into account (2) and the initial condition of the step **I**, solve, from $t = 0$ to $t = 1$, the $\mathbf{w}_1$-equation

$$\mathbf{w_1}'(t) = [A(t) - X(t)C(t)]\mathbf{w}_1(t) - X(t)\mathbf{f}_2(t) + \mathbf{f}_1(t); \quad \mathbf{w}_1(0) = K_{11}^{-1}\gamma_1.$$

(III) Next, solve from $t = 1$ to $t = 0$, the $\mathbf{w}_2$-equation

$$\mathbf{w}_2'(t) = [D(t) + C(t)X(t)]\mathbf{w}_2(t) + C(t)\mathbf{w}_1(t) + \mathbf{f}_2(t),$$

with the starter final condition $[K_{21}X(1) + K_{22}]\mathbf{w}_2(1) + K_{21}\mathbf{w}_1(1) = \gamma_2$.

(IV) Finally, to recover $\mathbf{y}(t) = Z(t)\mathbf{w}(t)$, with $Z(t)$ given by (2).

3   Exponential Integrators for the Matrix RDE

From [6], in a simple way, the study of our matrix RDEs reduces to the study of the IVP

$$Y'(t) = \begin{bmatrix} V'(t) \\ W'(t) \end{bmatrix} = S(t)Y(t), \ Y(0) = \begin{bmatrix} X_0 \\ I_q \end{bmatrix}, \ S(t) = \begin{bmatrix} A(t) & B(t) \\ C(t) & D(t) \end{bmatrix} \tag{3}$$

with $Y \in \mathbb{C}^{n \times q}$ and $S \in \mathbb{C}^{n \times n}$. Then, the solution of RDE is given by $X(t) = V(t)W^{-1}(t)$, with $V \in \mathbb{C}^{p \times q}$, $W \in \mathbb{C}^{q \times q}$, in the region where $W(t)$ is invertible. If $W(t)$ has no inverse in some point of the interval $[0, 1]$, the error for $X(t)$ will cause large error in $\mathbf{w}_1$ and $\mathbf{w}_2$ which are then propagated, leading to large errors for the solutions $\mathbf{y}_1$ and $\mathbf{y}_2$, because the equations are coupled. However, this problem can be solved easily by covering the interval $[0, 1]$ by a finite set of intervals where the problem can be reformulated with appropriate permutation matrices, see Lemma 3.1 of [4] for more details. This multiple imbedding implies that at each interval one has to solve a different linear differential equation where the inverse of the matrix appearing in (3) is far from being singular.

Now, let us present an explicit symmetric second order Lie group integrator to solve numerically (3). If we denote by $\Phi(t, t_0)$ the fundamental solution of (3), then

$$\exp\left(\int_t^{t+h} S(t) \, dt\right) = \Phi(t+h, t) + \mathcal{O}(h^3),$$

corresponds to the first order approximation for most exponential methods like e.g. the Magnus, Fer or Wilcox expansions, see [3] and the references therein for details. Here, it suffices to approximate the integral by a second order symmetric rule, like the trapezoidal rule so

$$\Psi(t+h, t) \equiv \exp\left(\frac{h}{2}(S(t+h) + S(t))\right) = \Phi(t+h, t) + \mathcal{O}(h^3).$$

The non-homogeneous problem can be treated in a similar way.

4   Solving the thermal energy equation

Applying the exponential integrator method presented in the above section to our system of coupled IVPs presented at the end of section 2, we obtain

$$\begin{bmatrix} W_{n+1} \\ V_{n+1} \end{bmatrix} = \exp\left(\frac{h}{2}(S(t_{n+1}) + S(t_n))\right) \begin{bmatrix} W_n \\ V_n \end{bmatrix} \ \Rightarrow \ X_{n+1} = V_{n+1} W_{n+1}^{-1}$$

where $X_n = X(t_n) + \mathcal{O}(h^3)$, $t_n = nh$. In this way, the matrix functions $A(t_n)$, $B(t_n)$, $C(t_n)$, $D(t_n)$ are computed at the same mesh points as the approximations X_n to $X(t_n)$. The second step are the integration of the $\mathbf{w}_1$-equation by a symmetric second order exponential integrators for non homogeneous linear equations

$$\mathbf{w}_{1,n+1} = \exp\left(\frac{h}{2}\big(A_{n+1} + A_n - X_nC_n - X_{n+1}C_{n+1}\big)\right)\left(\mathbf{w}_{1,n} + \frac{h}{2}\mathbf{g}_n\right) + \frac{h}{2}\mathbf{g}_{n+1},$$

where $\mathbf{g}_n = -X_n \mathbf{f}_{2,n} + \mathbf{f}_{1,n}$. Next, we approximate the non-homogeneous $\mathbf{w}_2$-equation backward in time by

$$\mathbf{w}_{2,n} = \exp\left(\frac{-h}{2}\left(D_{n+1} + D_n + C_n X_n + C_{n+1} X_{n+1}\right)\right)\left(\mathbf{w}_{2,n+1} - \frac{h}{2}\mathbf{h}_{n+1}\right) - \frac{h}{2}\mathbf{h}_n,$$

where $\mathbf{h}_n = C_n \mathbf{w}_{1,n} + \mathbf{f}_{2,n}$. Finally, the solution given by $\mathbf{y}(t) = \left(\mathbf{w}_1(t) + X(t)\mathbf{w}_2(t), \mathbf{w}_2(t)\right)$, is approximated at the mesh points $t_i = t_0 + ih$, $i = 0, 1, \ldots, N$, by $\mathbf{y}_{1,n} = \mathbf{w}_{1,n} + X_n \mathbf{w}_{2,n}$, $\mathbf{y}_{2,n} = \mathbf{w}_{2,n}$, $n = 0, 1, \ldots, N$. A variable step procedure can also be used.

Acknowledgements

References

[1] U. M. Ascher, R. M. Mattheij, and R. D. Russell. Numerical solutions of BVPs for ODEs. Prentice-Hall. Englewood Cliffs, NJ, 1988.

[2] A. Bejan, Heat Transfer. New York, John Wiley and sons, 1993.

[3] S. Blanes, F. Casas, J. A. Oteo, and J. Ros. The Magnus expansion and some of its applications. *Physics Reports*, 470:151–238, 2009.

[4] H. B. Keller and M. Lentini. Invariant imbedding, the box scheme and an equivalence between them. *SIAM J. Numer. Anal.*, 19:942–962, 1982.

[5] T. Y. Na, Computational Methods in Engineering Boundary Value Problems. New York, Academic Press, 1079.

[6] W. T. Reid, Riccati Differential Equations. New York, Academic, 1972.

Consensus Networks as Agreement Mechanism for Autonomous Agents in Water Markets

M. Rebollo, A. Palomares and C. Carrascosa [*]

Universidad Politécnica de Valencia

Departamento de Sistemas Informáticos y Computación (DSIC)

Camino de Vera s/n – 46022 Valencia – Spain

October 10, 2010

1 Introduction

The aim of this paper is to present a way of share opinions in a decentralized way by a set of agents that try to achieve an agreement by means of a Consensus Network, allowing them to know beforehand if there is possibilities to achieve such an agreement or not. The interaction topology of the agents is represented using directed graphs and a *consensus* means to reach an agreement regarding a certain quantity of interest that depends on the state of all agents in the network. This value represents the variable of interest in our problem. The convergence of this method depends on the topology of the network and its convergence is usually exponential. But sometimes it not needed to reach a final agreement on a concrete value. This proposal uses consensus networks to determine if an agreement is possible among a set of entities. Agents can leave the agreement if its parameters are out of the expected bounds, so the consensus network can be used to detect the candidate agents to be members of the final agreement. All this process is solved in a self-organized way and each individual agent decides to belong or not to the final solution. To show the validity of the present approach, a water market is presented as case of study.

2 Consensus Networks for Water Rights

The theoretical framework for solving consensus problems in dynamic networks of agents was formally introduced by Olfati-Saber and Murray[1]. Suppose that the market consist

---

of n entities (agents) $E_i, i = 1, \ldots, n$ that have authorization to commerce in a water market. The initial state of the entity E_i is represented by the following parameters $E_i = \{R_i, \widetilde{R}_i, P_i, \widetilde{P}_i\}$ where R_i and $\widetilde{R}_i$ represent, respectively, the rights entity E_i owns and rights E_i would like to have (Optimal Rights), P_i is the initial Price entity E_i proposes for buying or selling rights in the market and $\widetilde{P}_i$ is the Limited Price entity E_i accepts for buying or selling rights in the market (private).

Suppose water rights price must be fixed in the market (a constraint) and some previous agreements, acceptable by the maximum number possible of agents, are required in order to establish this value. The average of the prices P_i is probably one the most acceptable agreement value for the price, and also can be calculated asymptotically using consensus algorithms. Dynamics of agents are defined by the following equations:

$$P_i^S(k+1) = P_i^S(k) + \varepsilon \sum_{j \in N_i} (B_j(P_j^B(k) - P_i^S(k) + C_i(k))), \tag{1}$$

$$P_i^B(k+1) = P_i^B(k) + \varepsilon \sum_{j \in N_i} (S_j(P_j^S(k) - P_i^B(k) + C_i(k))) \tag{2}$$

where k is the discrete time and the index S and B denotes seller and buyers respectively. the added term $C_i(k)$ is proportional to rights bought and sold by agents in each iteration, and is calculated as follows:

$$C_i(k) = \delta \cdot \frac{\sum_{j \in N_i} B_j}{\sum_{j \in N_i} S_j} \tag{3}$$

where $\delta > 0$.

Seller agents adapt iteratively prices in order to converge to the mean price of the connected buyer agents and simultaneously buyer agents adapt his price in order to converge to the mean price of the connected seller agents. In this iterative process non cooperative agents are disconnected of the network in order all others agents to have the possibility of asymptotically agree. The algorithm converges and stops when prices converge to the consensus value the mean prices of buyers and sellers are approximately equal.

3   Results

Some simulations have been chosen to show the behaviour of the network to achieve a decision. The algorithm converges and stops when the mean prices of buyers and sellers are approximately equal.

- The simplest case (Fig. 1, col. 1) is a full connected graph where all the agents are forced to stay and reach a consensus value. This experiment shows that the number of exchanged water rights remains constant (because no agents leave the system), but there is a difference between the desired rights and the offered rights. The modification of the basic algorithm solves this problem by introducing a second factor, represented by the $C_i(k)$ term (Eq. 2).

- In the second experiment (Fig. 1, col. 2), besides the adjustment between the involved water rights, agents are allowed to leave the system if the terms of the negotiation (the consensus value for the price of the water) is out of its bounds. In this case, the number of rights decreases while the consensus evolves. Nevertheless, the offer and the demand are biased (see how the lower lines matches in the upper graphic).

- Finally, the third experiment (Fig. 1, col. 3) a scale free network is used instead of the full connected graph. Furthermore, the initial price distribution is different too. In this case, the network does not converge to one unique value. The topology just affect to the speed of the convergence. But when an agent leaves theconsensus it can split the network apart. This fact prevents the hole group to reach a common consensus value, because each isolated group converges to their own consensus value and they never receive the vallues agreed by theother group. The result is that, instead an unique consensus value, there are as many as isolated groups. This can be seen in Fig. 1, where the prices do not converge. Anyway, the values of the prices stabilises. In this case, instead of a final agreed value, a range is found. This fact allows to identify which agents are interested in the agreement and the range of prices. After this process, some other techniques can be used to find an agreement. Then, the consensus network can be used at least to identify the subset of participants interested in reaching and agreement and the boundaries of such an agreement.
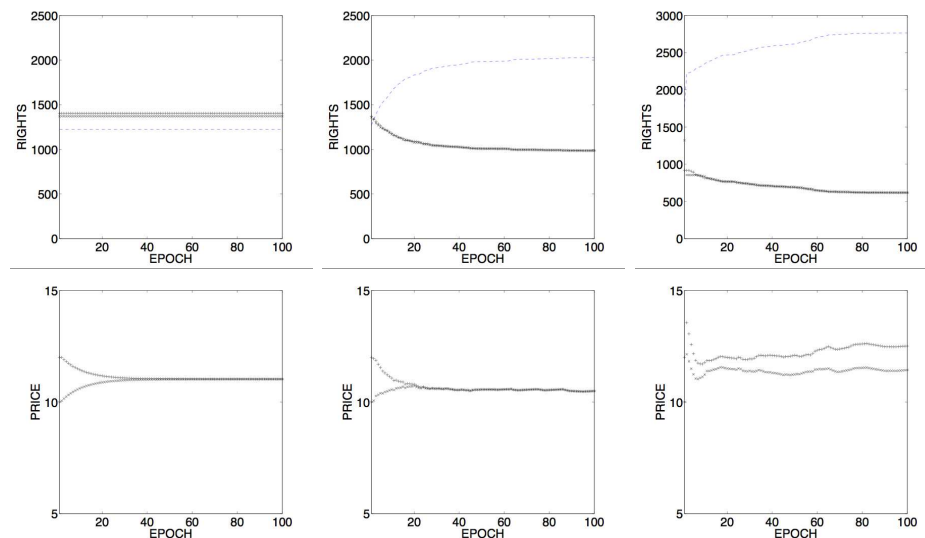

Figure 1: Consensus evolution. First row shows the evolution of the interchanged water rights. Second row shows the evolution of the average price (for sellers and buyers). In columns, left to right, full connected graph, fixed topology and unbiased rights // full connected, switching topology, biased rights // scale free topology ($\alpha = 2.5$) switching topology, biased rights

4   Conclusions

This paper shows the application of consensus networks to model agreement spaces for virtual organizations. The results obtained show that this approach seems to be valid and it has been applied to a water rights market in order to check its viability in real-world problems.

References

[1] R. Olfati-Saber and R. M. Murray, Consensus problems in networks of agents with switching topology and time-delays, *IEEE Trans. on Automatic Control*, 49(9):1520–1533 (2004).

Estimating hospital production functions through flexible regression models

Francisco Reyes Santías[§†] [*], Carmen Cadarso-Suárez[†‡],
and María Xosé Rodríguez-Álvarez[§†‡]

(§) Complexo Hospitalario Universitario de Santiago (CHUS).

(†) Universidade de Santiago de Compostela, Spain.

(‡) Instituto de Investigación Sanitaria de Santiago.

October 10, 2010

1 Background

Two models are commonly used in the estimation of hospital production function: the Cobb-Douglas and the transcendental logarithmic (Translog model). Using these models for estimation and prediction, the functional shape of continuous inputs is "forced" to follow a linear parametric form, which frequently does not fit the data closely. The relative lack of flexibility of parametric models has led to the development of non-parametric regression techniques based on the broad family of generalized additive models (GAMs; [?, ?]).

This paper studies the use of Additive Models (AMs) to calculate hospitals production functions. The results of this new approach are compared with the Cobb-Douglas and the Translog models.

2 Data description

The variables we use consist of inputs to hospital production in the form of capital and labour, and outputs from production.

We have chosen the output of Inpatient care measured as number of admissions standardized by means of complexity, obtaining homogeneous units of production (UPHs), calculated by multiplying the number of admissions by the complexity (weight) obtained from the Diagnostic Related Groups (DRGs) [?].

Following Ferrier and Valmanis [?] hospital inputs are measured as follows: in terms of capital we use the average number of beds (Beds) in each hospital. Labour inputs

---

[*]e-mail: Francisco.Reyes.Santias@sergas.es

are measured by the number of consultant full-time equivalents (FTEs) employed in each hospital.

Workload statistics were collected by hospital, as panel data, from the Regional Ministry's Information System, for the period 2002-2008. Hospitals have been classified within three clusters by Reyes [**?**] following their size: Cluster 1 (small; < 200 beds), Cluster 2 (medium; $200 - 650$ beds), and Cluster 3 (large; > 650 bedts).

3 The statistical models

The **Cobb-Douglas production function** proposed by Charles W. Cobb and Paul H. Douglas [**?**], takes the following form for our model:

$$\log UPHs = \beta_0 + \beta_1 \log FTEs + \beta_2 \log Beds + \beta_3 Year + \sum_{h=1}^{nH-1} \alpha_k Hospital_k + \varepsilon.$$

A standard procedure for introducing the possibility of technical change is to include a time trend (*Year*). This captures observed changes in the technology.

An alternative to the Cobb-Douglas production function is the **translog production function** [**?**]. The form of translog production function used is as follows:

$$\begin{aligned} \log UPHs &= \beta_0 + \beta_1 \log FTEs + \beta_2 \log Beds + + \beta_3 \log FTEs \log Beds \\ &+ \beta_4 Year + \sum_{h=1}^{nH-1} \alpha_k Hospital_k + \varepsilon. \end{aligned}$$

The **flexible model** considered was the following AM including a Beds-by-FTEs interaction:

$$\begin{aligned} \log UPHs &= \beta_0 + \beta_1 Year + f_1\left(\log FTEs\right) + f_2\left(\log Beds\right) \qquad (1) \\ &+ f_3\left(\log FTEs, \log Beds\right) + \sum_{h=1}^{nH-1} \alpha_k Hospital_k + \varepsilon. \end{aligned}$$

where f_1 and f_2 are unknown smooth functions of the number of beds (log scale) and the number of physicians (log scale) respectively, and f_3 is a unknown smooth function representing the possible interaction between the number of beds and the number of physicians (both in log scale).

It should be noted that the categorical covariate 'Hospital' was also included in the previous models. In these models, nH denotes the number of hospitals (in our study 10), and $Hospital_h$ is a dummy variable taking the value 1 for the hth hospital and 0 otherwise.

With regard to the estimation of the model (**??**), penalized thin plate splines were used to represent the smooth functions f_1, f_2 and f_3, and the optimal smoothing parameters were estimated via Restricted (or Residual) Maximum Likelihood (REML, see e.g. [**?**]).

All the statistical analysis was performed using R software, version 2.9.1 [**?**]. AMs were fitted using `mgcv` package [**?**].

4   Results

In this section, we describe the results of each estimated model, for the Regional Health Service hospitals as an overall and every hospital Cluster. We evaluated the models based on the AIC (Akaike Information Criterion; [**?**]) and the economic interpretation for an output change due to changes in input factors.

First of all, the models have been estimated for the Regional Health Service hospitals as an overall. Related to goodness of fit for the models, both the R^2 and the AIC indicate that the AM provides a better fit in comparison with the two classic models, CD and Translog.

Following the results for Cluster 1, AM regression model is the only one able to detect a significant interaction between Beds and FTEs inputs ($p = 0.041$). Paying attention to AIC (CD = 1073.084, Translog = 1072.302, AM = 875.337) and R^2 values (CD = 63.41, Translog = 63.54, AM = 78.50) we could observe a higher explanation power from the AM rather than for classic ones.

Paying attention to the results for Cluster 2, the effect of interaction between input factors is captured by models translog and flexible one ($p < 0.003$). Even more, the AM model, unlike the classic ones, is able to show that changes in production technology, captured by time trends, would affect the output ($p = 0.022$). The significant hospital effect for the three models ($p < 0.001$, in all cases) seems to reflect some variability related to the size of the hospitals included in Cluster 2. As in the previous results, not only the AIC estimates but also the R^2 (CD=77.68, Translog=78.32, AM=85.30) seem to show the advantage of AM behind the classic ones.

The estimation results for Cluster 3 show significant effects of Beds for the three models ($p < 0.001$) while at the same time there are not any significant effects related to FTEs, hospital and technical change (Years) variables for the CD and Translog, but the AM detects effect for the FTEs ($p = 0.037$). However, there is a significant interaction between Capital and Labour factors for the AM ($p = 0.022$) whereas there is not for the Translog ($p = 0.772$). The goodness-of-fit of the AM measured by the R^2 (CD=78.01, Translog=77.96, AM=86.50) as well as the AIC (CD=775.441, Translog=777.311, AM=619.218) have been more satisfactory for the AM compared with Cobb-Douglas and Translog.

Graphical output of the results for the AMs, for the overall sample and for each hospital cluster separately, are depicted in Figure **??**.

5   Discussion and Conclusions

The decision to measure production of hospitals by the AM made an attempt to improve flexibility for the functional form. The model proposed is certainly a simplified version of the complete econometric model specification (some other variables, in fact, can affect the analyzed phenomenon) but, also at this preliminary stage, the obtained results are really closed to the desirable hypotheses.

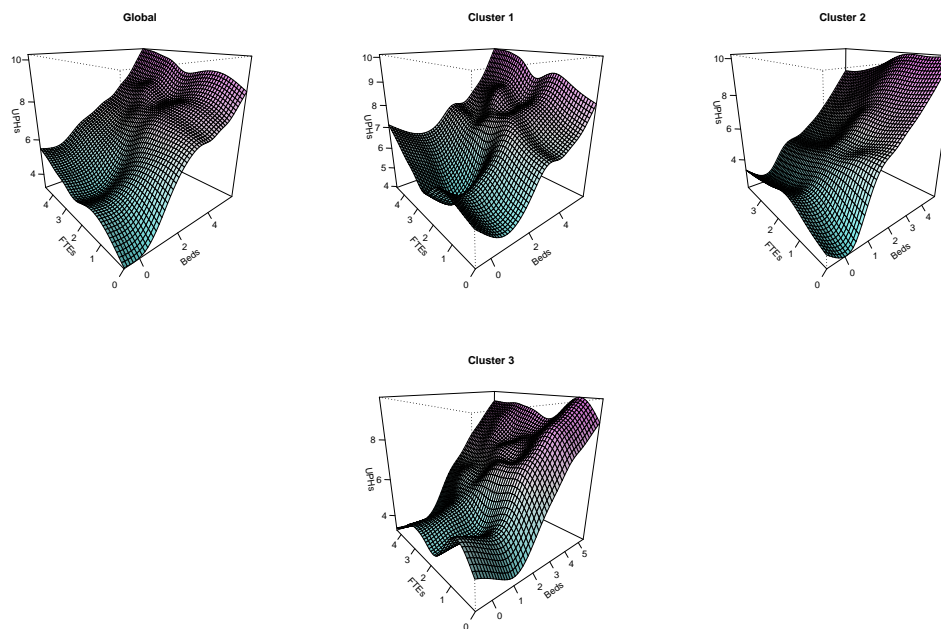A selected set of simple indicators of production has been analyzed. These indicators

Figure 1: Productivity growth as a result of increments in the inputs, based on the flexible model (AM). Variables (UPHs, FTEs, Beds) are expressed in logarithm scale. Global sample, Clusters 1, 2 and 3.

have been compared across different hospital typologies. This comparative analysis gives important insights to the different variations among hospitals.

As reported in Figure **??**, while medium size and small basic-care hospitals are almost homogenous in terms of bed productivity, large size hospitals presents a more complex bed productivity trend. Among hospital typologies, the AM presents a large variability for consultants' productivity. The interpretation of these results is surely an interesting instrument for decision makers in order to analyze the productive conditions of each hospital and the health care sector as an overall. Moreover, AMs may also be applied to check the classical models performance.

Results in this study suggest that AM is a promising technique for the research and application areas on health economics. Moreover, results allow to characterize the domains in which our approach may be effective like those related to demand, costs and utility functions in health care.

Acknowledgements

References

[1] Hastie T J, Tibshirani R J. Generalized Additive Models. London, Chapman and Hall, 1990.

[2] Wood S N. Generalized Additive Models: An Introduction with R. Chapman and Hall/CRC Press, 2006.

[3] López Rois F J, Mateo R, Gómez J R, Ramón C, Pereiras M. *Methodological criteria for drawing up a contract-programme or singular sector-based agreement of specialized care using HPUs*. Secretara Xeral SERGAS. Consellera de Sanidade e Servicios Sociais. Xunta de Galicia. Santiago de Compostela, 1999.

[4] Ferrier G, Valmanis V. Do mergers improve hospital productivity? *Journal of the Operational Research Society*, 55: 1071–1080, 2004.

[5] Reyes F. Adopción, difusión y utilización de la Alta Tecnologa Médica en Galicia. Tomografía Computerizada y Resonancia Magnética. Universidade de A Coruña, Servizo de Publicacións. A Coruña, 2009.

[6] Cobb C W, Douglas P H. A Theory of Production *The American Economic Review*, 18 (Supplement): 139–165, 1928.

[7] Christensen L R, Jorgenson D W, Lau L J. Transcendental Logarithmic Production Frontiers *The Review of Economics and Statistics*, 55: 28–45, 1973.

[8] Ruppert D, Wand M P, Carroll R J. Semiparametric Regression. Cambridge University Press, 2003.

[9] R Development Core Team. R: A language and environment for statistical computing (2009). R Foundation for Statistical Computing, Vienna, Austria. ISBN 3-900051-07-0, URL http://www.R-project.org

[10] Akaike H. A new look at the statistical model identification *IEEE Transactions on Automatic Control*, 19 (6): 716–723, 1974.

Polar Symmetries for Weight Matrix design in CT Imaging.*

M. J. Rodríguez-Alvarez, †F. Sánchez‡, A. Soriano ‡,
A. Iborra †, C. Mora ‡

(†) Instituto de Matemática Multidisciplinar, Universidad Politécnica de Valencia,

Edificio 8G, 2°,Camino de Vera, 46022 Valencia, (Spain)

(‡) Instituto de Física Corpuscular (IFIC), Centro Mixto CSIC-Univ. Valencia,

Edificio Institutos de Investigación, Paterna, Valencia E46071 (Spain)

October 10, 2010

1 Introduction

Algebraic Reconstruction Techniques (ART) produce higher image quality than Fourier-based methods, mainly with incomplete or noisy data [1]. However, these kind of techniques are not used in routine clinical computed tomography (CT) because of high computational requirements of ART. Since the system matrix (SM) is the core of the ART algorithms, the construction of the SM is crucial for providing an accurate reconstruction. Usually, more precise SMs have more computational cost and complexity which may become unfeasible in 3D. In order to decrease the computational complexity, a number of methods focused on exploiting the symmetries of SM have been proposed using polar pixels , blob grid. Furthermore, several approaches are based on polar pixel grid for Comptom-camera, and CT for medical imaging [2]. Following these ideas, four different ways to construct a SM are presented and compared for a fan-beam CT scanner geometry defined by an X-Ray source and a 1-D array pixellated detector. They are summarized in the following table:

Grid	Pixellation	Shape of pixels
Cartesian	Classical	Square (CART-SQ)
Polar	Relation Aspect Unitary	Polar (RAU-P)
		Circular (RAU-C)
	Constant Radius	Polar (CR-P)

†e-mail: mjrodri@imm.upv.es

178

In the following, we identify the pixellations with their corresponding pixel shapes and their SM by their acronyms, i.e., classical square pixels in a cartesian grid and the cartesian SM will be denoted by CART-SQ, polar pixels with relation aspect unitary in a polar grid and its SM will be denoted by RAU-P, the same for circular pixels will be called by RAU-C, and polar pixels with constant radius in a polar grid and its SM will be named by CR-P. The algorithm we use in all cases to reconstruct the CT images is Maximum Likelihood Emission Maximization (MLEM) [3]. This algorithm will be adapted for polar pixellations.

2 System matrix construction

The design of the grid has been tackled using the criteria described in Section 1: to preserve the intrinsic spatial resolution of the scanner and to take advantage of the symmetries of the system. The data obtained from the scanner can be considered as a sequence of measurements taken from each one of the v positions or views of the scanner. Therefore, the geometry of the scanner has v symmetric views which shape is a circular FOV. Each rotation of the scanner is used as a symmetry in the SM in order to reduce computation time. Only four symmetries can be implemented to reduce SM in cartesian grid.

2.1 Calculation of system matrix weights

The construction of the SM weights is crucial for providing an accurate reconstruction. Although SM approaches use different pixel weight calculations, the process to construct the SM is the same in all cases. Due to the polar grid symmetry, only one view has to be calculated and the remainder views can be obtained by means of the rotation of the first view. The numbering of the pixels is performed following the scanner rotation direction to make the calculations of the rotated positions easier. Furthermore, beams of each view are symmetric with respect to the line that goes from the focus to the center of the FOV. Therefore, only the first half of beams of the first view need to be calculated because the second half can be obtained by reflecting the SM data of the first one. In this way, the complete SM can be represented by one half of the first view of the scanner.

3 Data source

The four SM approaches (CART-SQ, RAU-P, RAU-C and CR-P) were compared by reconstructing simulated projections and real measurements supposing a 2-D scanner system of similar characteristics. The simulated projection was the 2-D Shepp-Logan head phantom [4]. Real measurements are also used to evaluate the reconstructions using the four SM. These measurements are provided from the Radiophysics and Radiological Protection Service of the *Hospital Clínico Universitario de Valencia* and are made using a CT-simulator.

4 Conclusions

Usually, SM is constructed only once, therefore it is not crucial the SM generation time. Due to the circular-pixel SM generation takes only a few seconds, it can be considerer in a near future to calculate the SM elements on-the-fly, only when they are necessary [5]. The effectiveness of this option depends on each measurement, but this is the most efficient option without loss of information and allow a flexible system in which the matrix will adapt to changes easily.

The polar grid allows us a reduction of 800 times in the SM size, but it needs a displaying procedure. Also a fast viewer procedure which provided quality images without polar artifacts is developed. These SM have been compared using different quality indicators with a simulated phantom and with real data. The previous discussion show that all SM provide a valid reconstruction of similar quality.

Nevertheless, SM generation is only 4s for RAU-C approach. Therefore, the RAU-C system matrix seems to be a better option than the RAU-P and CR-P because it provides a high reduction of the generation time with quite quality in the reconstructed images. The proposed RAU-C make feasible the calculation of the matrix elements "on-the-fly" without the storage of the matrix and the searching of these elements during reconstruction process. The satisfactory results of the SM implementation in a 2-D system, the implementation in a 3-D system and a reconstruction algorithm that takes more advantage of the symmetries of the matrix, will be part of future work in the future.

References

[1] H. Guan, R., Gordon: Computed tomography using algebraic reconstruction techniques (ARTs) with different projection access schemes: A comparison study under practical situations. Phys. Med. Biol, **41**,1727–1743, (1996)

[2] C. Mora, M.J. Rodríguez-Alvarez, J. V., Romero: New pixellation scheme for CT algebraic reconstruction to exploit matrix symmetries. Comput. Math. Appl. **56**(3), 715–726, (2008)

[3] L. A. Shepp, Y. Vardi, Y.: Maximun likelihood reconstruction for emission tomography. IEEE Trans. Med. Imaging, **1**(2), 113–122, (1982)

[4] L. A. Shepp, B. F. Logan, : The fourier reconstruction of a head section. IEEE Trans. Nucl. Sci, **21**(3), 21–43, (1974)

[5] H. Kudrolli, W. Worstell, V. Zavarzin: SS3D − Fast 3D PET iterative reconstruction using stochastic sampling. IEEE Trans. Nucl. Sci, **49**(1), 124 − 130, (2002)

Influence of biofuels on the internal flow in Diesel injector nozzles

F.J. Salvador[†] [*], J. Martínez-López[†], J.-V. Romero[‡]
and M.-D. Roselló[‡]

(†) CMT- Motores Térmicos,

Universidad Politécnica de Valencia,

Camino de Vera s/n, 46022, Valencia, Spain,

(‡) Instituto de Matemática Multidisciplinar,

Universidad Politécnica de Valencia,

Camino de Vera s/n, 46022, Valencia, Spain.

October 10, 2010

1 Introduction

It is well known that fossil fuels reserves will not provide energy eternally. That is why a lot of companies are interested in making the engines more efficient to reduce the fuel consumption. Another solution that seems to be a great alternative is the use of vegetable oils, animal fats and algae as carburant that should provide enough power to run the actual thermal engines as they do with fossil fuels. Up to now, biofuel studies have been focused only in the performance and emissions of the engine [1] treating the engine as a "black box", without study in depth how biodiesel influences on the injection process or what are the repercussions of its use on the air-fuel mixing process.

2 Description of the CFD approach

Under the injection conditions in modern Diesel engines (with pressures which can reach up 180 MPa) cavitation often occurs in fuel injection nozzles, whose length is about 1 mm and whose diameter ranges from about 0.1 mm to 0.2 mm. When a fluid of high velocity passes through a contraction like a nozzle and the pressure falls below the saturation pressure,

[*]e-mail: fsalvado@mot.upv.es, telephone: 34-963879659, fax: 34-963877659

the liquid will cavitate, and as a consequence a local change of state from liquid to vapour takes place.

Due to high pressures and velocities that occur in diesel injectors, the use of a homogeneous equilibrium model which assumes that liquid and vapour are always perfectly mixed in each cell, together with a barotropic equation of state is the most suitable method to model cavitation [2]. The code used in the present work is implemented in OpenFOAM 1.5 and was validated and optimized improving the convergence and the accuracy of the results and choosing the most suitable numerical schemes by Salvador et al. [3]. In addition, turbulence effects have been introduced using a RNG k-ε model.

3   Geometry and nozzle mesh description

The geometry simulated in this report is a multi-hole nozzle with six cylindrical orifices, whose inlet and outlet diameters have 170 μm. However, due to the nozzle symmetry and with the aim of speed up the calculations, the domain simulated has been reduced to 60º (one orifice), breaking up the geometry into 115252 hexahedral cells (Figure 1).
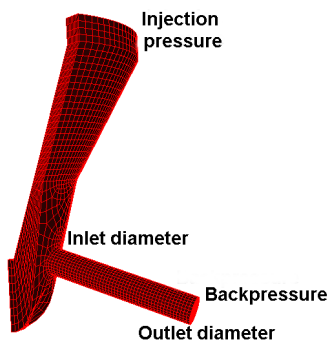

Figure 1: Nozzle mesh simulated.

The simulations calculated in the present study have been performed using two different injection pressures (30 and 80 MPa) and varying the back pressure between 1 and 29 MPa.

4   Results

The mass flow as a function of pressure drop squared, being the pressure drop the difference between the injection pressure and the backpressure, has been plotted in Figure 2 for two different injection pressures (30 and 80 MPa) and different backpressures. The large amount of backpressures simulated (indicated above of each point of the graph) allows studying in depth the behavior of both fuels at cavitating and no cavitating conditions. As expected, due to the highest value of density, biodiesel injects more fuel at the same pressure drop for all the points simulated. However the most important difference between

both fuels is related to critical cavitation conditions (CCC), characterized from the mass flow choking beginning. As can be seen, mass flow collapse is reached earlier for the diesel fuel, so it is possible to state that biodiesel inhibits cavitation compared to standard diesel fuel.
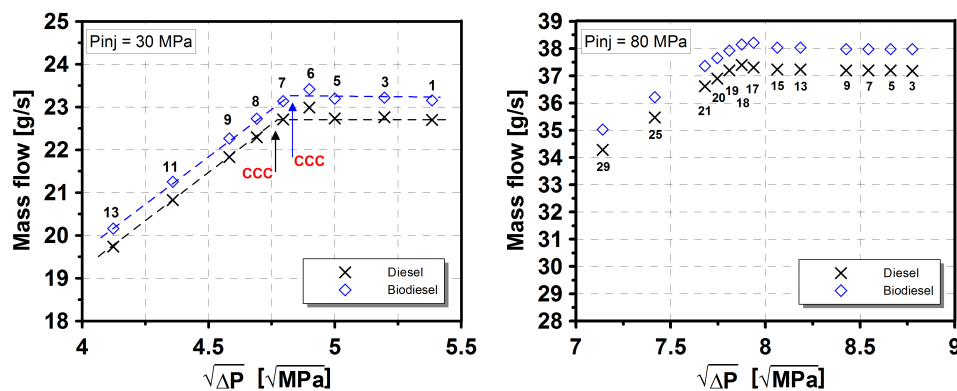

Figure 2: Comparison of both fuels in terms of mass flow.

Indeed, comparing the vapour field average in the middle plane of the orifice, diesel fuel cavitates more than biodiesel for the same pressure conditions. As an example, Figure 3 shows cavitation distribution for the injection pressure 80 MPa and the backpressure 18 MPa (red colour represents pure vapour and blue colour pure liquid).
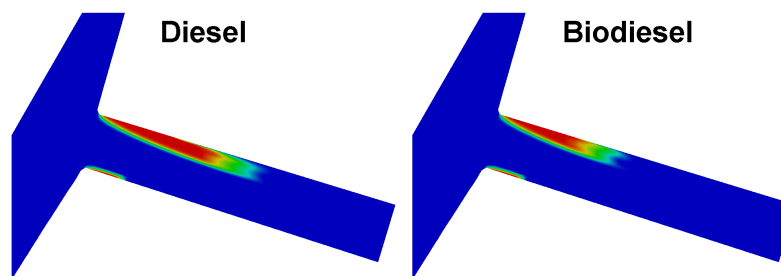

Figure 3: Comparison of vapour field average ($P_{\text{inj}} = 80$ MPa $- P_{\text{back}} = 18$ MPa).

Apart from mass flow and cavitation intensity, the comparison between standard diesel and the fuel made from soybean oil has been done also in terms of effective velocity at the nozzle exit. As shown Figure 4, the effective velocity for biodiesel fuel is lower than diesel for all pressure conditions.

It is well known that for the same geometry, the air-fuel mixing process in the combustion chamber depends on the injection effective velocity and the spray cone angle and both increase with cavitation intensity [4, 5].

As seen before, for a given pressure condition the effective velocity of biodiesel is lower. Furthermore, in cavitating conditions it presents less cavitation intensity, so, small spray

cone angle [4] is expected for biodiesel. As a conclusion, a worse air-fuel mixing process is expected for biodiesel leading to a worse combustion process.
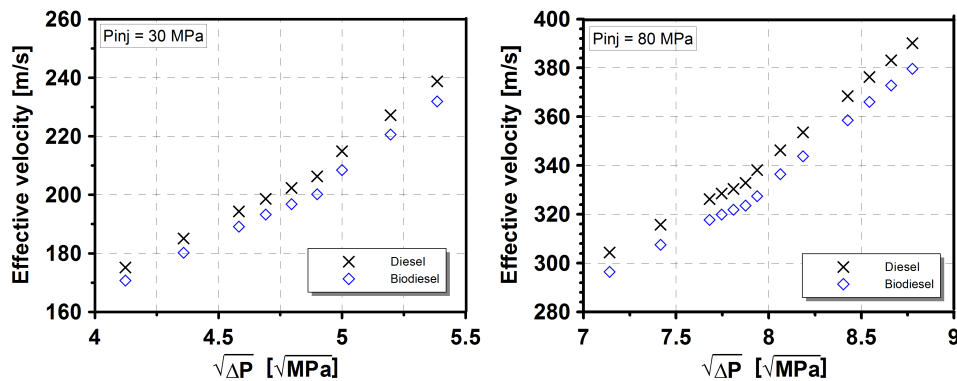

Figure 4: Comparison of both fuels in terms of effective velocity.

5   Conclusions

From the present study the following main conclusions can be drawn:

- A code to model cavitation phenomena taking into account the turbulence effects has been applied for compare the behavior of a conventional diesel fuel and a biodiesel one made from soybean oil.

- Biodiesel injects more fuel and reaches later critical cavitation conditions. As a consequence, cavitation intensity is lower for the same pressure conditions.

- As a consequence of the decrease of injection velocity and cavitation intensity for the biodiesel, the air-fuel mixing process gets worse.

Acknowledgments

Nomenclature

P_{back}: discharge back pressure
P_{inj}: injection pressure
Greek symbols:
ΔP: pressure drop, $\Delta P = P_{\text{inj}} - P_{\text{back}}$

References

[1] J.M. Luján, B. Tormos, F.J. Salvador and K. Gargar. Comparative analysis of a DI diesel engine fuelled with biodiesel blends during the European MVEG-A cycle: Preliminary study (I), *Biomass and bioenergy*, 33:941–947, 2009.

[2] F.P. Kärrholm, Numerical Modelling of Diesel Spray Injection, Turbulence Interaction and Combustion, PhD. Thesis, Chalmers University of Technology, 2008.

[3] F.J. Salvador, J.-V. Romero, M.-D. Roselló and J. Martínez-López. Validation of a code for modeling cavitation phenomena in Diesel injector nozzles, *Mathematical and Computer Modelling* 52:1123–1132, 2010 .

[4] F. Payri, V. Bermúdez, R. Payri and F.J. Salvador. The influence of cavitation on the internal flow and the spray characteristics in diesel injection nozzles, *Fuel* 83:419–431, 2004.

[5] R. Payri, F.J. Salvador, J. Gimeno and L.D. Zapata. Diesel nozzle geometry influence on spray liquid-phase fuel penetration in evaporative conditions, *Fuel* 87:1165–1176, 2008.

An analysis of the recurrence-progression process in bladder carcinoma by means of joint frailty models.

C. Santamaría* *,* B. García-Mora*, G. Rubio* and S. Luján[†]

(*) Instituto de Matemática Multidisciplinar. Universidad Politécnica de Valencia

(†) Departamento de Urología. Hospital Universitario La Fe de Valencia

1   Introduction

In recent years, there has been a growing interest in studying processes which generate events repeatedly over time. When the event of interest occurs repeatedly a correlation between the recurrent relapse times within the subject may exist due to either the *heterogeneity* among individuals and the *event dependence.* The *heterogeneity* is produced because some subjects have a higher (or lower) event rate than the other ones due to unknown or unmeasurable effects. The *event dependence* can be produced when the occurrence of a given event may make further relapses more or less likely. Furthermore, the repeated event process is associated with an elevated risk of a terminating event. This dependence must be accounted in a joint modelling so we use a non-parametric penalized likelihood method for estimating hazard functions in a general *joint frailty model* for recurrent events and terminal events [1]. This approach makes possible to deal with informative censoring for recurrent event data and a joint treatment of two processes.

The analysis we develop is motivated by a study of patients diagnosed with bladder carcinoma. This disease is characterized by a primary tumor which is managed with a transurethral resection (*TUR*), followed by superficial *recurrent tumors* in the bladder (more than 50%) or a muscle invasive *progression* (10–30%). Because of the association between *superficial recurrent tumors* and the *progression* we study them jointly by means of the *joint frailty model.* Then we can obtain the hazard and survival functions associated with both the *recurrence* and *progression* that would allow us to establish predictions of this carcinoma after the *TUR*.

2   The recurrence–progression processes

From the *TUR* each patient can undergo one or more recurrences (*recurring events*) that can be interrupted by a progression (*terminating event*). Those patients who don't expe-

---

*e-mail: crisanna@imm.upv.es

rience neither recurrence nor progression in the follow–up period are *censored*.

In the study of the recurrence process the follow-up period of a patient is completed by a progression event or by a censoring time. The Andersen and Gill [2] (AG model) propose to model the risk for the kth recurrence of the ith patient at time t conditionally on observed covariates X_{ik} by

$$\lambda_k(t; X_{ik}) = e^{\beta' X_{ik}(t)} \lambda_0(t) \tag{1}$$

where $\lambda_0(\cdot)$ is an unknown baseline hazard rate function and β is a vector of parameters associated with covariate effects that can be time-dependent. This model is suited to the situation of mutual independence of the observations within a subject. However, if we assume that after experiencing the first recurrence, the risk of the next recurrence may increase, it is necessary to introduce a time–dependent covariate to capture the dependence structure.

Another way to take into account the presence of the correlation between recurrences is by means of the introduction of a cluster-specific random effect: *the frailty*. The recurrence times are conditional independent, given the frailty. The hazard function of the ith subject for the kth event is defined by

$$\lambda_{ik}(t; X_{ik}, Z_i) = Z_i e^{\beta' X_{ik}(t)} \lambda_0(t)$$

where the correlation between recurrence times is modelled with Z_i which are unobserved frailties. Z_i follows a gamma distribution with mean 1 and unknown variance ξ and ξ determines the degree of association among recurrence measurements or heterogeneity.

In a second step it is studied the joint evolution of the recurrence process and the progression by means of the *joint frailty model*. That model establishes the hazard functions for recurrent event $r_i(\cdot)$ and terminal event $\lambda_i(\cdot)$ of the ith subject by

$$\begin{cases} r_i(t; X_i, Z_i) = Z_i e^{\beta_1' X_i(t)} r_0(t) \\ \lambda_i(t; X_i, Z_i) = Z_i^{\alpha} e^{\beta_2' X_i(t)} \lambda_0(t) \end{cases}$$

where $r_0(t)$ and $\lambda_0(t)$ are the recurrent and terminal event (progression) baseline hazard function respectively. The effect of the explanatory variables is assumed to be different for recurrent and progression times. Z_i is again the *frailty* term for the ith subject. α quantifies the association between the recurrence and the progression. $\alpha = 0$ means that $\lambda_i(t)$ does not depend on Z_i and thus the progression is not informative for the recurrence rate $r_i(t)$.

3   Application to Bladder Carcinoma

The transurethral resection database from La Fe University Hospital of Valencia (Spain) contains information on *superficial* TCC of bladder patients of 960 patients. The variables recorded are the following: the *stage* of the bladder tumors, classified in Ta, T1 and Tis

(according to TNM system classification); *Grade* categorized from G1 to G3 (from low aggressive to highly aggressive); *Number* classified in two levels: one and two or more tumors; *Size* with also two levels: less or equal to 3 cm and more than 3 cm; *Sex* and *Age*. The initial treatment is no treatment and chemotherapy after *TUR*.

In a first step we fit the AG model including age, grade, number, size and treatment which were significant at the 5% level. We define the time–dependent covariate *prior number* of recurrences in order to analyze the dependence among recurrences which was significant at the 1% level.

In a second step we introduce the *frailty term* in the AG model with estimated variance $\hat{\xi} = 1.29$ (s.e 0.19) which indicates that the frailty component is significant (p value from one-side Wald statistic 2.8×10^{-11}). Both models (AG model with *prior number* and AG model with *frailty term*) present close HR estimates, but the HR for model with the frailty component are slightly higher. The AG model allows us to estimate the average effect of accumulating recurrences, in fact for each new prior recurrence the risk is increased by 57% (HR= 1.57 95% CI (1.45-1.67)) which indicates a significant heterogeneity among individuals.

Finally we modelled jointly the recurrences and progression processes of this disease and obtain the same prognostic factors. Notice the grade is the only prognostic factor for progression. The value of $\alpha = 1.04$ indicates that incidence of recurrences is positively associated with progression; higher frailty will result in higher risk of recurrence and progression. Furthermore the variance of frailty term is significant at the 1% level.

Covariate	AG with prior number	AG with Frailty	Joint Frailty Model
For recurrences:			
Age	1.01 (1.01-1.02)	1.02 (1.01-1.03)	
Grade			
G1	1	1	1
G2	1.24 (1.01-1.51)	1.36 (1.06-1.74)	1.33 (1.05-1.69)
G3	1.01 (0.74-1.37)	1.05 (0.71-1.57)	0.87 (0.59-1.29)
Number of tumors			
One	1	1	1
Two or more	1.36 (1.09-1.70)	1.45 (1.08-1.95)	1.45 (1.09-1.92)
Size			
$\leq 3cm.$	1	1	1
$> 3cm.$	1.48 (1.14-1.91)	1.80 (1.29-2.51)	1.87 (1.35-2.59)
Treatment			
No treatment	1	1	1
Treatment	0.76 (0.63-0.92)	0.80 (0.63-1.02)	0.75 (0.60-0.94)
For progression:			
Grade			
G1			1
G2			1.97 (0.66-5.86)
G3			8.27 (2.95-23.19)
Prior number of recurrences	1.57 (1.45-1.67)		
ξ (s.e)	-	1.29 (0.193)	0.83 (0.09)
α	-	-	1.04

4   Concluding remarks

We have observed that the frailty term is not significant if we only model the recurrent process, but it becomes significant if we fit jointly recurrence and progression processes. The joint model shows that both processes are related, so they can not be modelled separately using traditional methods.

References

[1] Rondeau, V., Mathoulin-Pelissier, S., Jacqmin-Gadda, H., Brouste, V. and Soubeyran, P. (2007). Joint frailty models for recurring events and death using maximum penalized likelihood. *Biostatiscs*, 8:708–721.

[2] Andersen, P. K. and Gill, R. D. (1982). Cox's regression model for counting processes: a large sample study. *Ann. Stat.*, 10:1100–20.

Modelling the dynamic of addictive buying

F.-J. Santonja[*] [,] I. García[†], L. Jódar[‡], and P. Merello[‡]

(*) Departamento de Estadística e Investigación Operativa, Universidad de Valencia,

(†) Departamento de Comunicación Audiovisual y Publicidad, Universidad del País Vasco,

(‡) Instituto Universitario de Matemática Multidisciplinar, Universidad Politécnica de Valencia.

October 10, 2010

1 Introduction

Although addictive buying is not specifically described in DSM-IV [1], uncontrolled problematic buying behavior has been studied by the psychologists and the psychiatrists since the early 20th century [2]. For some people, shopping is a leisure activity, a way to manage emotions or a means of expressing the self-identity and brings about adverse consequences, including guilt, excessive debt, family conflict, illegal activities, and even suicide attemps.

Some cross-sectional studies have been performed to analyse the uncontrolled problematic buying behavior [2]. However, to the best of our knowledge, there are no studies that allow to predict the prevalence of this pathological behavior in the next few years. In this paper, we present a discrete mathematical model that allows us to do it. Taking into account [3] we build the model considering that social behaviors may spread from one person to another.

2 Method

Firstly, in order to know the addictive buying prevalence rate two surveys have been performed, the first one was in 2001 [4] and the second one has been performed in 2010. In both cases, to estimate the prevalence of addictive buying, we used the Compulsive Buying Scale proposed in [5].

Secondly, the mathematical model is built. The information contributed by the prevalence analyses allows us to estimate some of the parameters of the model.

3 Mathematical model

To build the mathematical model, population is divided into three subpopulations using the Compulsive Buying Scale proposed in [5]: N, rational buyers, S, excessive buyers and A, addictive buyers such that the total population size (P) at any given time n is given by:

$$P_n = N_n + S_n + A_n \tag{1}$$

The dynamic of the population can be described by the following system of equations (n, time in months):

---

[*]e-mail: francisco.santonja@uv.es

$$N_{n+1} - N_n \quad = \quad \mu P_n - dN_n - \beta_1 \frac{N_n A_n}{P_n} - \beta_2 N_n + \epsilon_2 A_n \tag{2}$$

$$S_{n+1} - S_n \quad = \quad \beta_1 \frac{N_n A_n}{P_n} + \beta_2 N_n - dS_n - \gamma_1 \frac{S_n A_n}{P_n} - \gamma_2 S_n + \epsilon_1 A_n \tag{3}$$

$$A_{n+1} - A_n \quad = \quad \gamma_1 \frac{S_n A_n}{P_n} + \gamma_2 S_n - \epsilon_2 A_n - dA_n - \epsilon_1 A_n \tag{4}$$

where the population state vector $PS_n = (N_n, S_n, A_n)$ gives the number of rational buyers, excessive buyers and addictive buyers at time n. See [6] (Section 2.2) for more details about the assumptions to build the mathematical model.

The parameters of the model are:

- μ, birth rate in Spain. We assume that the birth rate for Vizcaya is the Spanish birth rate.

- d, death rate in Spain. We assume that the death rate for Vizcaya is the Spanish death rate.

- β_1, transmission rate due to social contact with addictive buyers (rational buyers $\rightarrow$ excessive buyers).

- β_2, rate at which a rational buyer transits to excessive buyers subpopulation. We admit that this parameter is related to the economic situation.

- γ_1, transmission rate due to social contact with addictive buyers (excessive buyers $\rightarrow$ addictive buyers).

- γ_2, rate at which a excessive buyer transits to addictive buyers subpopulation. We consider that this parameter is also related to the economic situation.

- ϵ_1, rate at which an addictive buyer reduces his/her addictive behavior himself/herself and becomes an excessive buyer.

- ϵ_2, rate at which an addictive buyer goes to therapy and becomes a rational buyer.

4   Numerical simulations

Future short term addicted population (until year 2013) is computed assuming several future economic scenarios.

- Scenario V. The economic situation will finish in one year and half (fast economic recovery).

- Scenario U. The economic situation will finish in three years.

- Scenario W. The economic situation will experience recoveries and relapses in the next four years.

- Scenario L. The deteriorating economic situation will remain at least five years (long economic recovery).
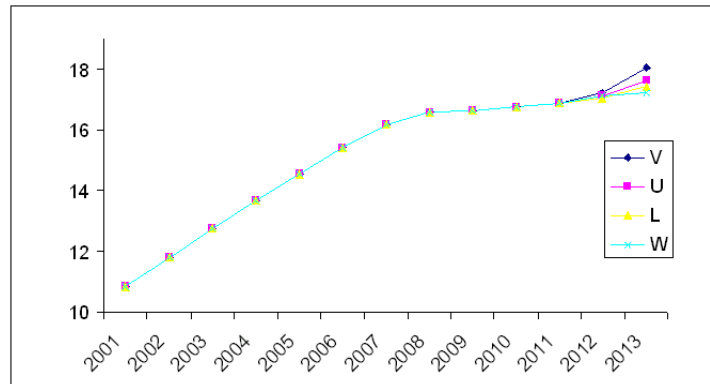
The results show a trend of increase in addictive buyers. The mathematical model predicts that around 17%-18% of the population of Vizcaya will present addictive buying behaviour at the end of 2013.

5 Conclusions

In this work, we present an approximation to the Spanish addictive buying prevalence for 2010 and some prediction for the next few years. According to the numerical simulations described, we can affirm that the addictive buying prevalence rate in Spain is increasing.

In this paper we also show how mathematical models can be an useful tool to understand social epidemics.

References

[1] American Psychiatric Association. Diagnostic and statistical manual of mental disorders, American Psychiatric Publishing, 2004.

[2] D.W. Black, A review of compulsive buying disorder, World Psychiatry, 6 (2007) 14-18.

[3] N.A. Christakis, J.H. Fowler, Connected: The Surprising Power of Our Social Networks and How They Shape Our Lives. Hachette Book Group, 2009.

[4] E. Olabarri, I. García, La compra por impulso y la adicción al consumo en el País Vasco (in Spanish), Estudios sobre consumo, 65 (2003) 86-109.

[5] G. Valence, A. D'Astous, L. Fortier, Compulsive buying: concept and measurement, Journal of Consumer Policy, 11 (1988) 419-433.

[6] F.J. Santonja, R.J. Villanueva, L. Jódar, G. González, Mathematical modelling of social obesity epidemic in the region of Valencia, Spain, Mathematical and Computer Modelling of Dynamical Systems, 16 (2010) 23-34.

Computing matrix exponential to solve coupled differential models in Engineering*

J. Sastre$^+$ † J. Javier Ibáñez^o, Emilio Defez‡ and Pedro Ruiz^o

(+) iTEAM, (o) I3M, (‡) IMM, Universidad Politécnica de Valencia.

October 10, 2010

1   Introduction

Many scientific and engineering processes are described by systems of linear first-order ordinary differential equations with constant coefficients, whose exact solution is given in terms of the matrix exponential, and a large number of methods for its computation have been proposed [1, 2]. This paper presents the key ideas for a competitive new scaling and squaring algorithm. Throughout this paper $\mathbb{C}^{n \times n}$ denotes the set of complex matrices of size $n \times n$, I denotes the identity matrix for this set, $\rho(A)$ is the spectral radius of matrix A, and $\mathbb{N}$ denotes the set of positive integers. The matrix norm $\|\cdot\|$ denotes any subordinate matrix norm, in particular $\|\cdot\|_1$ is the 1-norm. Next theorem will be used in next section to bound the norm of matrix power series.

Theorem 1.1 *Let $h_l(x) = \sum_{k \geq l} b_k x^k$ be a power series with radius of convergence w, and let $\tilde{h}_l(x) = \sum_{k \geq l} |b_k| x^k$. For any matrix $A \in \mathbb{C}^{n \times n}$ with $\rho(A) < w$, and $p \in \mathbb{N}$, $p \geq 1$, if a_k is an upper bound for $\|A^k\|$ ($\|A^k\| \leq a_k$), and $\alpha_p = \max\{(a_k)^{\frac{1}{k}}\,; k=p, l, l+1, \ldots, l+p-1\}$, then $\|h_l(A)\| \leq \tilde{h}_l(\alpha_p)$.*

Proof. $\|h_l(A)\| \leq \sum_{j \geq 0} \sum_{i=l}^{l+p-1} |b_{i+jp}| \|A^p\|^{|j|} \|A^i\| \leq \sum_{j \geq 0} \sum_{i=l}^{l+p-1} |b_{i+jp}| \alpha_p^{i+pj} = \sum_{k \geq l} |b_k| \alpha_p^k = \tilde{h}_l(\alpha_p)$.   □

2 Error analysis and algorithm

If we denote $T_m(A) = \sum_{i=0}^{n} A^i/i!$ the truncated matrix exponential Taylor series with Taylor remainder $R_m(A)$, for a scaled matrix $2^{-s}A$ we can write

$$\left(T_m(2^{-s}A)\right)^{2^s} = e^A \left(I + g_{m+1}(2^{-s}A)\right)^{2^s} = e^{A + 2^s h_{m+1}\left(2^{-s}A\right)}, \quad s \in \mathbb{N} \cup \{0\}, \tag{1}$$

$$g_{m+1}(2^{-s}A) = -e^{-2^{-s}A} R_m(2^{-s}A), \; h_{m+1}\left(2^{-s}A\right) = \log\left(I + g_{m+1}(2^{-s}A)\right), \tag{2}$$

see [4, sec. 3], where log denotes the principal logarithm and $h_{m+1}(X)$ is defined in the set $\Omega_m = \left\{X \in \mathbb{C}^{n \times n} : \rho\left(e^{-X}T_m(X) - I\right) < 1\right\}$. If we choose s so that $2^{-s}A \in \Omega_m$, then from (1) one gets that $\Delta A = 2^s h_{m+1}\left(2^{-s}A\right)$ and $\Delta E = e^A[(I + g_{m+1}\left(2^{-s}A\right))^{2^s} - I]$ represent the backward and forward errors in exact arithmetic from the approximation of e^A by Taylor series with scaling and squaring, respectively. If s is chosen so that

$$\left\|h_{m+1}\left(2^{-s}A\right)\right\| \leq \max\left\{1, \|2^{-s}A\|\right\} u, \tag{3}$$

where $u = 2^{-53}$ is the unit roundoff in IEEE double precision arithmetic, then: if $2^{-s}\|A\| \geq 1$, then $\Delta A \leq 2^{-s}\|A\| u$ and using (1) one gets $(T_m\left(2^{-s}A\right))^{2^s} = e^{A + \Delta A} \approx e^A$, and if $2^{-s}\|A\| < 1$, using (1),(2),(3) and Taylor series one gets

$$\left\|R_m\left(2^{-s}A\right)\right\| = \left\|e^{2^{-s}A} g_{m+1}\left(2^{-s}A\right)\right\| = \left\|e^{2^{-s}A}\left(e^{h_{m+1}\left(2^{-s}A\right)} - I\right)\right\|$$

$$= \left\|e^{2^{-s}A} \sum_{k\geq 1}\left(h_{m+1}\left(2^{-s}A\right)\right)^k/k!\right\| \leq \left\|e^{2^{-s}A}\right\| \sum_{k\geq 1} u^k/k!$$

$$\approx \left\|T_m\left(2^{-s}A\right)\right\| u \left(1 + u/2! + u^2/3! + \cdots\right) \approx \left\|T_m\left(2^{-s}A\right)\right\| u. \tag{4}$$

Hence, as we are evaluating explicitly $T_m\left(2^{-s}A\right)$, in IEEE double precision arithmetic $T_m\left(2^{-s}A\right) + R_m\left(2^{-s}A\right) \approx T_m\left(2^{-s}A\right)$, and there is no point in increasing m or the scaling to try to get better accuracy. From (2) one gets

$$h_{m+1}\left(2^{-s}A\right) = \sum_{k\geq m+1} b_k^{(m)}\left(2^{-s}A\right)^k, \tag{5}$$

and using MATLAB symbolic Math Toolbox, 200 terms, high precision arith. and a zero finder we obtained the maximal values $\Theta_m = \|2^{-s}A\|$ such that

$$\|h_{m+1}\left(2^{-s}A\right)\| \leq \tilde{h}_{m+1}\left(\|2^{-s}A\|\right) = \tilde{h}_{m+1}\left(\Theta_m\right) \leq \max\left\{1, \Theta_m\right\} u. \tag{6}$$

We have applied Horner's method to Paterson-Stockmeyer method for the evaluation of matrix polynomial $T_m\left(2^{-s}A\right)$ [2, p. 72-74], modifying it as

$$T_m\left(2^{-s}A\right) = \left(\left(\cdots\left(\frac{A_j}{2^s m} + A_{j-1}\right)/(2^s(m-1)) + A_{j-2}\right)/(2^s(m-2)) + \cdots + A_2\right)/(2^s(m-j+2))\right.$$

$$+ A + 2^s(m-j+1)I)\frac{A_j}{2^{2s}(m-j+1)(m-j)} + A_{j-1}\right)/\left(2^s(m-j-1)\right)$$

$$+ A_{j-2})/\left(2^s(m-j-2)\right) + \cdots + A_2)/\left(2^s(m-2j+2)\right) + A$$

$$+ 2^s(m-2j+1)I)\frac{A_j}{2^{2s}(m-2j+1)(m-2j)} + \cdots + A_2\right)/(2^s2) + A + 2^s I\right)/2^s, \tag{7}$$

where $A_i = A^i$ are computed as $A_2 = A^2$, $A_4 = A_2^2, \ldots, A_{2k+1} = A_{2k}A$, and we will use a subset of optimal values of m in terms of matrix products, see Table 4.1 of [2, p.74], $m = 4, 6, 9, 12, 16, 20, 25, 30$, with $j = 2, 3, 3, 4, 4, 5, 5, 5$ respectively. (7) saves $O(n^2)$ operations with respect to classic Paterson-Stockmeyer Horner's form and avoids factorials improving numerical results [5]. Similar floating point bounds to those in [5] are applied to the intermediate results in $T_m(2^{-s}A)$ to save matrix products. Then, the scaling algorithm will be as follows: Estimate $\|A^{m+1}\|_1$ using the $O(n^2)$ algorithm of [6]. Then, use Theorem 1.1 and (6), calculating the necessary bounds a_k for $\|A^k\|_1$ using the known matrix power norms, to obtain the initial maximum matrix scaling s_0. Then, try if (3) is satisfied using the bounds for $\|A^k\|_1 \leq a_k$ in

$$\left\|h_{m+1}\left(2^{-s}A\right)\right\|_1 \leq \sum_{k \geq m+1} |b_k^{(m)}| \frac{\|A^k\|_1}{2^{sk}} \approx \sum_{k=m+1}^{m+j+M} \left|b_k^{(m)}\right| \frac{\|A^k\|_1}{2^{sk}} \leq \sum_{k=m+1}^{m+j+M} \left|b_k^{(m)}\right| \frac{a_k}{2^{sk}}, \qquad (8)$$

with $s = s_0 - 1$, choosing $M \geq 1$. If it is not satisfied, try then

$$\left\|h_{m+1}\left(2^{-s}A\right)\right\|_1 \leq \left\| \frac{b_{m+1}^{(m)}}{b_{m+2}^{(m)}} 2^s I + A + \frac{b_{m+3}^{(m)}}{b_{m+2}^{(m)}} \frac{A_2}{2^s} + \frac{b_{m+4}^{(m)}}{b_{m+2}^{(m)}} \frac{A_3}{2^{2s}} + \cdots + \frac{b_{m+j}^{(m)}}{b_{m+2}^{(m)}} \frac{A_j}{2^{s(j-1)}} \right\|$$

$$\times \frac{\|A^{m+1}\|_1}{2^{s(m+2)}} \left|b_{m+2}^{(m)}\right| + \sum_{k=m+j+1}^{m+j+M} \left|b_k^{(m)}\right| \frac{\|A^k\|_1}{2^{sk}} \qquad (9)$$

(9) is lower or equal than (8) for normal matrices and low bounds for it can be obtained to avoid unnecessary evaluations. Repeat the process with $s = s_0 - 2, s_0 - 3, \ldots$ If the last scaling s where (8) or (9) satisfy (3) is $s \geq 1$ then try if s and previous optimal m also satisfy (3). Return s and the minimum m satisfying (3). The total algorithm consists of using Theorem 1.1, (8) and (9) to try if one of the orders $m = 4, 6, 9, \ldots, m_{max}$ satisfy (3) with $s = 0$, where m_{max} is the max. allowed order. If not, obtain the scaling s using previous algorithm and use (7) and squaring to evaluate $\left(T_m\left(2^{-s}A\right)\right)^{2^s}$.

3   Numerical experiments

133 matrices from [1, 3], MATLAB gallery, and others have been used to compare MATLAB functions `expm` [3] and `expm_new` [4] with an implementation of our algorithm, `dgeexftay`. Table 1 shows that `dgeexftay` average matrix product number is lower than `expm`'s, and slightly greater than `expm_new`, and that `dgeexftay` is more accurate in the majority of cases. Normwise and performance profile figures [3] have shown that all functions perform in a numerically stable way on this test and that `dgeexftay` has better precision performance than `expm` and `expm_new` even since maximum allowed Taylor order $m_{max} = 16$. Now we are applying the new algorithm to Padé method.

References

[1] C.B. Moler and C. Van Loan, Nineteen dubious ways to compute the exponential of a matrix, twenty-five years later, SIAM Rev 45:3-49, 2003.

Table 1: Relative error $E = ||e^A - \tilde{X}||_1/||e^A||_1$, and matrix product number (%) comparison between `dgeexftay`, `expm` and `expm_new`.

Maximum allowed Taylor order m_{max}	16	20	25	30
$E_{\texttt{dgeexftay}} < E_{\texttt{expm}}$	74.44	90.98	89.47	88.72
$(P_{\texttt{dgeexftay}} - P_{\texttt{expm}})/P_{\texttt{expm}}$	-15.47	-15.69	-14.95	-14.35
$E_{\texttt{dgeexftay}} < E_{\texttt{expm\_new}}$	66.17	87.22	87.22	86.47
$(P_{\texttt{dgeexftay}} - P_{\texttt{expm\_new}})/P_{\texttt{expm\_new}}$	1.31	1.04	1.94	2.65

[2] N.J. Higham. Functions of Matrices: Theory and Computation. Society for Industrial and Applied Mathematics, Philadelphia, PA, USA, 2008.

[3] N.J. Higham. The scaling and squaring method for the matrix exponential revisited. SIAM J. Matrix Anal. Appl., 26(4):1179-1193, 2005.

[4] A.H. Al-Mohy and N.J. Higham. A new scaling and squaring algorithm for the matrix exponential. SIAM J. Matrix Anal. Appl., 31(3):970-989, 2009.

[5] J. Sastre, J. Ibáñez, E. Defez and P. Ruiz. Efficient scaling-squaring Taylor method for computing matrix exponential. Accepted with modifications in SIAM J. on Scientific Computing.

[6] N.J. Higham and F. Tisseur, A block algorithm for matrix 1-norm estimation, with an application to 1-norm pseudospectra, SIAM J. Matrix Anal. Appl., 21:1185-1201, 2000.

Effects of the computational grid on the solution of boundary conditions in one-dimensional flow modeling

J. R. Serrano, F. J. Arnau*, P. Piqueras and M. A. Reyes-Belmonte

CMT-Motores Térmicos. Universidad Politécnica

Camino de Vera s/n, 46022 Valencia, Spain

Phone:+34 963877650; Fax: +34 963877659

October 10, 2010

1 Introduction

The work reported in the present paper deals with the solution of the boundary conditions in gas dynamics codes and how the way in which the sort of spatial mesh of the 1D-elements can affect the accuracy of the solution. Instead of the traditional mesh that introduces the calculation nodes uniformly distributed, the proposal of Corberán and Gascón [1] has been developed and implemented in OpenWAM™[2] [3]. According to this proposal the distance from the end nodes of a 1D-element to the neighboring ones is set to $\Delta x/2$ instead of Δx. The existance of contact dicontinuities has been analyzed as a validation that the proposed methodology has better accuracy in solution.

2 Methodology and Equations

The governing equations for one-dimensional unsteady compressible non-homentropic flow, i.e. the mass, momentum and energy conservation equations [4] [5], are represented in matrix form in equation 1.

$$\mathbf{W}(x,t) = \begin{bmatrix} \rho F \\ \rho u F \\ F\left(\rho\frac{u^2}{2} + \frac{p}{\gamma-1}\right) \end{bmatrix} \quad \mathbf{F}(\mathbf{W}) = \begin{bmatrix} \rho u F \\ \left(\rho u^2 + p\right) F \\ u F\left(\rho\frac{u^2}{2} + \frac{\gamma p}{\gamma-1}\right) \end{bmatrix}$$

$$\mathbf{C}(x,\mathbf{W}) = \begin{bmatrix} 0 \\ -p\frac{dF}{dx} + g\rho F \\ -q\rho F \end{bmatrix} \tag{1}$$

*e-mail: farnau@mot.upv.es

This system of equations is applied to the solution of flow advection through 1D-elements like ducts or channels. The solution of this problem requires the 1D-element to be discreticized into nodes of calculation where the conservation equations are solved. The flow properties at the internal nodes of the 1D-element are obtained applying a sock capturing numerical methods.
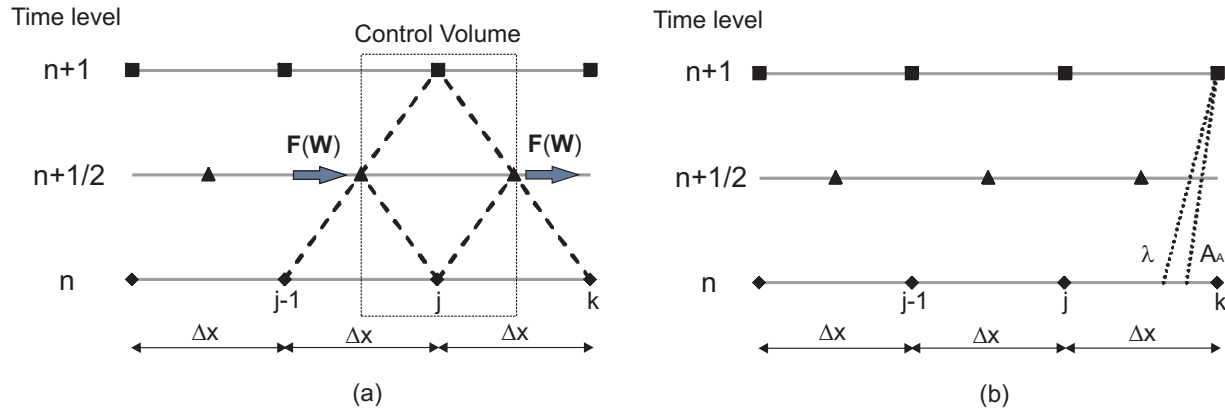

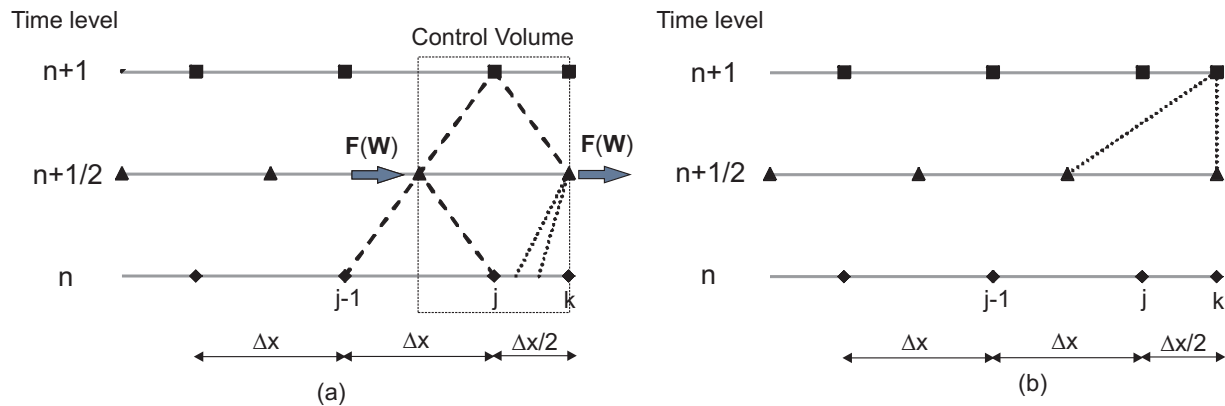Figure 1: Time marching with a homogeneously distributed spatial mesh:(a) solution of internal nodes; (b) solution of boundary nodes.

Figure 2: Time marching with the proposed extra-node grid: (a) solution of internal nodes; (b) solution of boundary nodes.

For the solution of an internal node j at instant time $n + 1$, point $(j, n + 1)$, these methods evaluate the fluxes entering and exiting to/from the control volume, as shown in Figure 1(a) for the case of the two-step Lax-Wendroff method [6]. Equation 4 is the second step of the method and equations 2 and 3 represent the first step [7]. At these equations Δt is the time-step obtained from the application of the CFL condition [8].

$$\mathbf{W}_{j-\frac{1}{2}}^{n+\frac{1}{2}} = \frac{1}{2}\left(\mathbf{W}_j^n + \mathbf{W}_{j-1}^n\right) - \frac{\Delta t}{2\Delta x}\left(\mathbf{F}_j^n - \mathbf{F}_{j-1}^n\right) - \frac{\Delta t}{4}\left(\mathbf{C}_j^n + \mathbf{C}_{j-1}^n\right) \qquad (2)$$

$$\mathbf{W}_{j+\frac{1}{2}}^{n+\frac{1}{2}} = \frac{1}{2}\left(\mathbf{W}_k^n + \mathbf{W}_j^n\right) - \frac{\Delta t}{2\Delta x}\left(\mathbf{F}_k^n - \mathbf{F}_j^n\right) - \frac{\Delta t}{4}\left(\mathbf{C}_k^n + \mathbf{C}_j^n\right) \tag{3}$$

$$\mathbf{W}_j^{n+1} = \mathbf{W}_j^n - \frac{\Delta t}{\Delta x}\left(\mathbf{F}_{j+\frac{1}{2}}^{n+\frac{1}{2}} - \mathbf{F}_{j-\frac{1}{2}}^{n+\frac{1}{2}}\right) - \frac{\Delta t}{2}\left(\mathbf{C}_{j+\frac{1}{2}}^{n+\frac{1}{2}} + \mathbf{C}_{j-\frac{1}{2}}^{n+\frac{1}{2}}\right) \tag{4}$$

If the 1D-element is discretized with a homogeneously distributed spatial mesh with size Δx, the end nodes can be solved by means of the Method of Characteristics [4]. The solution at the end node $(k, n+1)$ is obtained from the Riemman variables and the entropy level, being calculated their departure points at time level n, as it is shown in Figure 1(b).

The problem of this sort of solution arises on the high influence of the solution of the end node, of first order in time and space, on the solution of the neighboring nodes. To avoid that problem and to obtain a higher accuracy in conservation of the flow properties, it is proposed an alternative methodology to mesh the spatial domain. According to this proposal the neighboring nodes of the 1D-element boundaries are placed at a distance $\Delta x/2$ of the end, while the rest of the internal nodes are separated a distance of Δx, as it is shown in Figure 2.

The solution of the neighboring node to the end of the 1D-element is shown in Figure 2(a). The flow properties at node j at time level $n + 1$ are calculated again by applying the two-step Lax-Wendroff method, but now equation 3 is not necessary, due to the vector of fluxes is obtained by applying the method of characteristics. Once the vector of fluxes is known at nodes $(k, n + 1/2)$ and $(j - 1/2, n + 1/2)$ the solution of flow properties will be obtained applying the second step of the Lax-Wendroff method, equation 4.

The problem now is to obtain flow properties at the boundary node k at time level $n + 1$. A first order method has been used to solve that boundary node.

$$\mathbf{W}_k^{n+1} = \mathbf{W}_k^{n+\frac{1}{2}} - \frac{\Delta t}{2\Delta x}\left(\mathbf{F}_k^{n+\frac{1}{2}} - \mathbf{F}_{j-\frac{1}{2}}^{n+\frac{1}{2}}\right) + \frac{\Delta t}{2}\mathbf{C}_k^{n+\frac{1}{2}} \tag{5}$$

According to equation 5 and Figure 2(b) the flow properties at point $(k, n + 1)$ are calculated with the information of properties at point $(k, n + 1/2)$ (known from Method of Characteristics), and information at point $(k, n - 1/2)$ (known from first-step of the Lax-Wendroff method).

3   Results Analysis

The proposed extra-node methodology has been applied to simulate the behavior of the model shown in Figure 3. Sinusoidal pressure signals with phase-shift have been imposed at the inlet and outlet of the system to generate a thermal contact discontinuity at the inlet and outlet of the volume. That contact discontinuity causes a back flow through the system shown in Figure 3.

Figure 4(a) shows the obtained results when a coarse mesh is applied to both mesh methodologies. The traditional methodology does not work properly when few numbers of nodes are considered. Therefore the spatial mesh up to 1 cm has been necessary to obtain
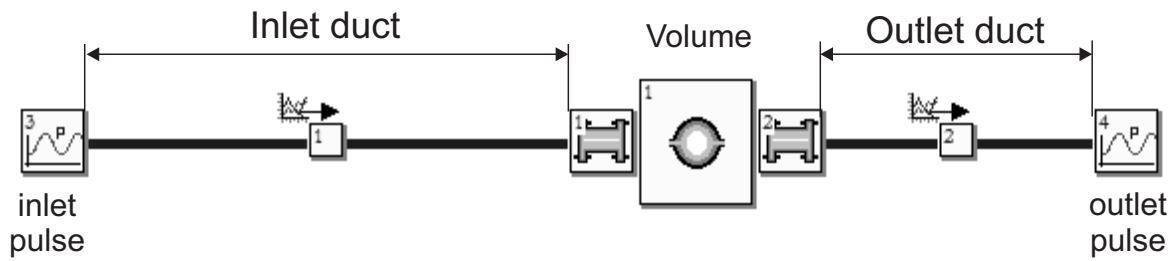
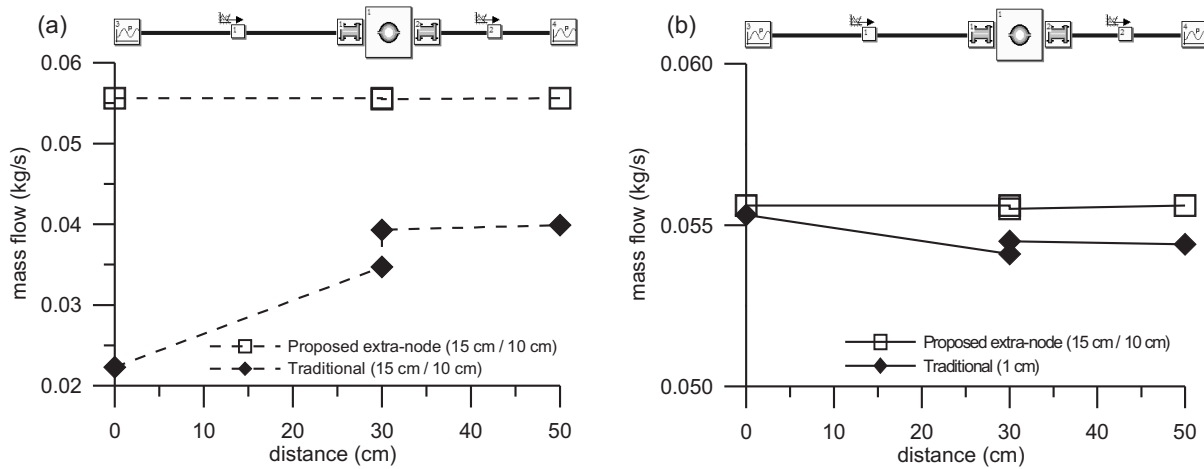Figure 3: Analyzed model represented by OpenWAM interface.

Figure 4: Mass flow conservation at boundary conditions:(a) coarse mesh; (b) thin mesh.

similar accuracy than the extra-node methodology working with a coarse mesh, as it is shown in Figure 4(b). In this case the artificial mass flow generation inside the volume is small for the traditional methodology although that mass conservation error is still lower with the extra-node mesh. In addition, the conservation of mass flow between the first and the last nodes of the model with the spatial mesh size of 1 cm using the traditional homogeneously distributed mesh is not as good as the obtained with the proposed methodology even with a more coarse mesh.

4   Conclusions

The solution of the governing equations for compressible flow in 1D-elements requires to divide the spatial domain into nodes where the conservation equations are solved. The traditional spatial mesh can provide lack of mass conservation at boundaries, mainly if thermal contact discontinuities appears. To avoid that phenomenon it has been proposed an extra-node mesh. This method consists on placing the neighboring nodes to the boundary ones at a distance $\Delta x/2$, while all the other internal nodes are separated a distance equal to Δx.It has been proved the better accuracy in mass conservation at pipe boundaries when the proposed extra-node mesh is used to simulate thermal contact discontinuities. To obtain a similar accuracy by using the traditional mesh it would be necessary to reduce dramatically the spatial mesh size, which would mean the need of higher computational effort.

References

[1] J. M. Corberán and L. Gascón, New method to calculate unsteady 1-D compressible flow in pipes with variable cross-section. Application to the calculation of the flow in intake and exhaust pipes of ic engines, Proceedings of the ASME Internal Combustion Engine Division Spring Meeting, *ICE Engine Modeling*, 23: 77–87,1995.

[2] J. Galindo, J. Serrano, F. Arnau and P. Piqueras, Description and analysis of a one-dimensional gas-dynamic model with Independent Time Discretization, Proceedings of the ASME Internal Combustion Engine Division 2008 Spring Technical Conference ICES2008, ICES2008-1610: 187–197, 2008.

[3] Openwam website. CMT-Motores Térmicos. Universidad Politécnica de Valencia. www.openwam.org.

[4] R. S. Benson, The thermodynamics and gas dynamics of internal combustion engines, Vol. 1, Oxford, Clarendon Press, 1982.

[5] D. E. Winterbone and R. J. Pearson, Theory of engine manifold design: wave action methods for IC engines. London, Professional Engineering Publishing, 2000.

[6] P. D. Lax and B. Wendroff, Systems of conservation laws, *Communications on Pure and Applied Mathematics*, 17: 381–398, 1964.

[7] R. D. Richtmyer and K. W. Morton, Difference methods for initial value problems, New York, Interscience Tracts in Pure and Applied Mathematics, 1967.

[8] R. Courant, K. O. Friedrichs and H. Lewy, Über die partiellen Differenzengleichungen der mathematischen Physik (Text in German), *Mathematische Annalen*, 100: 32–74, 1928.

Computational Framework based on Behavioural Modelling: Application to the matching of ECG recordings

María Teresa Signes * ,† Higinio Mora †, Juan Manuel García ‡

(*,†,‡) University of Alicante,

Address .

October 10, 2010

The electrocardiogram signal (ECG) is an important and commonly used aid in cardiovascular disease diagnosis because it provides key information about the electrical activity of the heart, which consists mainly in the alternation between polarization and depolarization caused by the blood that enters or exits the atrial or ventricular cavities. The 12-lead ECG provides information about the electrical activity in three approximately orthogonal directions: Right/Left, Superior/Inferior, Anterior/Posterior. Many disturbances in the heart performance show variations in the normal waveform shapes and can be used as cues to diagnose the disease. To detect the abnormal ECG signals continuous monitoring is required by the physicians. Several methods for automated arrhythmia detection have been developed to attempt simplify the huge monitoring task due to the large number of patients in intensive care units as well as to eliminate the inaccuracies of visual inspection and to improve diagnostic efficiencies. The most popular techniques are usually based on descriptive parameters of the wave shape, such as the segments and curves [1, 2, 3]; on frequency or time-frequency features, such as dynamic time warping, [4, 5] or the well known wavelet transform [6]. Other approaches are based on linear discriminants [7, 8, 9] or involve artificial intelligence techniques such as artificial neural networks or fuzzy logics [10, 11]. Finally, proposals combining different techniques succeed in improving classificaion results [5, 12, 13, 14, 15, 16, 17, 18, 19]. In this sense, intelligent agents can be mentioned because they provide a structure that can combine not only data types but also a variety of reasoning methodologies in the same decisionsupport system [20, 21].

The comparison between methods is sometimes difficult because published works differ in the results presentation. Whereas some papers lying in the classical artificial intelligence field use accuracy measures, others use as measures the sensitivity, and specificity that are more suitable for the classification in the medical field [10, 19]. While the accuracy gives an overall insight of the correctness of the methods, the sensitivity and the specificity evaluate

---

*teresa@dtic.ua.es

the methods from the clinical point of view and say how successful is the method in diagnosing healthy and ill people by means of detecting the proportions of true/false positive cases and true/false negative cases. As mentioned in [17], existing approaches generally present problems such as high sensitivity to noise included in the data, and unreliability in dealing with new or ambiguous patterns so, for clinical needs, it is necessary to develop new detection schemes in order to provide higher level of accuracy, or equivalently, lower false-positive and false-negative statistics.

In this paper we present a framework to model natural (living or not) systems behaviour. Generally these systems exhibit behaviours hard to model when we approach them by means of conventional mathematical formalism such as usual functions or ODEs. Our proposal consists on modelling the behaviours without relating them to the particular structure under study that is to say without having to depict or understand the physical phenomena that occur. The framework involves a set of elementary standard behaviours (shapes), see Fig.1, that can combine in order to emulate more complex behaviours, see Fig. 2. The algebraic formalization shown in equation 1 is based on a recursive weighted sum which carries out iteratively a sequence of values. It can be noticed that the seed value F_0, the couple (α, β) and the set $G = \{G_i\}$ are the crucial parameters involved in the generation of the values that define behaviour F. For the particular case ($\forall i \in N, G_i = 1$), the set of elementary standard behaviours is obtained. An exhaustive analysis has been done to study the stability intervals of these behaviours when the parameters F_0, (α, β) vary. The summary is shown in Fig. 3.
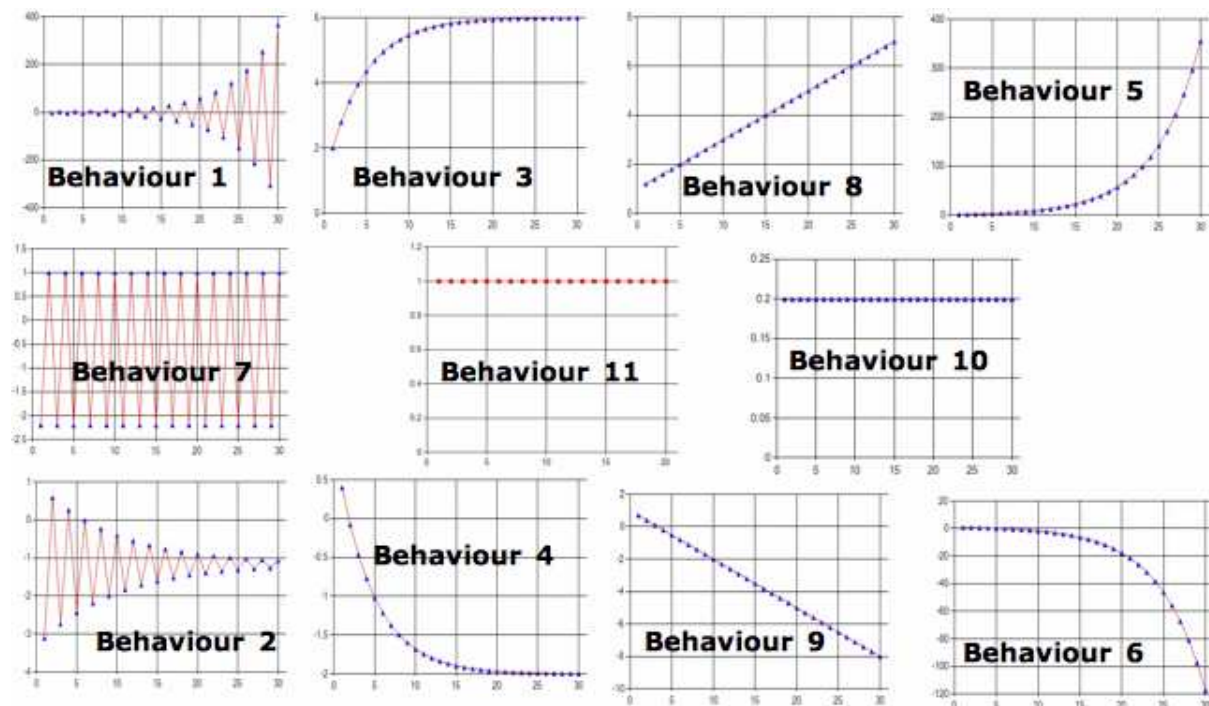

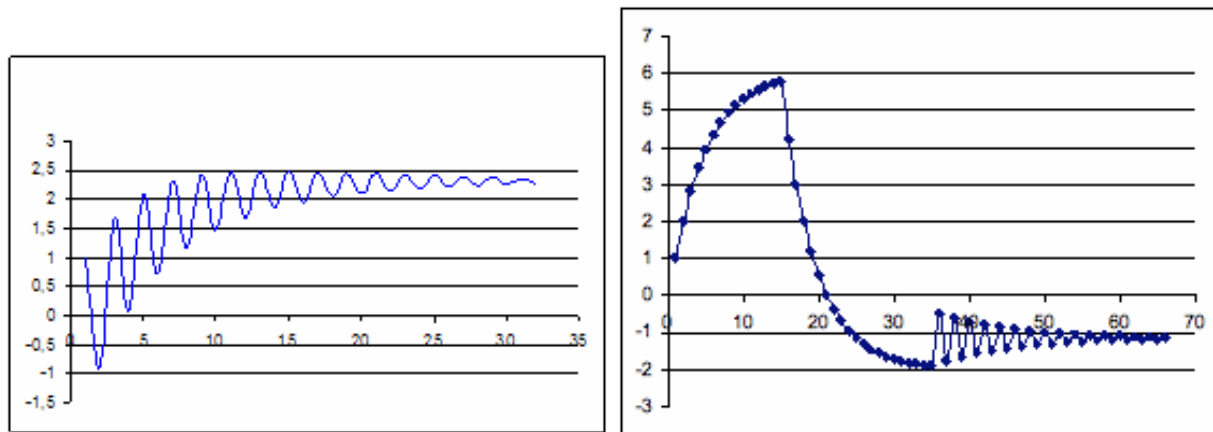Figure 1: Set of eleven elementary behaviours plotted vs. iteration number

Figure 2: Example of complex behaviours plotted vs. iteration number

$$F_0 \in R,$$
$$F_{i+1} = \alpha F_i + \beta G_i,$$
$$\forall i, i \in N, (F_i, G_i) \in R^2, (\alpha, \beta) \in R^2 \qquad (1)$$


Figure 3: Definition of the stability intervals of the elementary behaviours in function of F_0 and (α, β)

The capabilities of a behaviour F to match a given function Ψ can be understood as the equivalence of the respective sets of values $\{F_i\}$ and $\{\Psi(i)\}$, a sampling function of Ψ. The accomplishment of the mapping implies some conditions to be fulfilled. If the independent variable for function Ψ is denoted $x + ih$, (where x is the initial real value, $i \in N$ can take successive increasing values and h stands for the iteration step), the conditions are:

a x (initial Ψ value) is mapped to 0 (index of F), that is to say $\Psi(x) \equiv F_0$.

b the successive samples of function Ψ are mapped to successive F_i irrespectively to the value of h.

c the two previous assumptions allow not having to discern between i (index belonging to the independent variable of function Ψ) and i (iteration number for function F), that is to say, $\Psi(x + ih) \equiv \Psi(i) = F_i$.

A measure of accuracy must be set for the evaluation of the matching. It can be noticed that for a given function Ψ, the function F is not unique because different samplings of Ψ can be made. In this paper we focus the acute myocardial infarction (AMI) as the disease we are interested in and we pursue detecting the alterations it causes in the ECG in order to quantify and define them by the variation of the parameter values of our recursive formula related to a normal pattern. The behavioural approach has been applied first to match the normal ECG waveform shape and then the morphological variations in ECG shapes that occur. Concretely we have matched five abnormal ECGs as shown in the previous figure
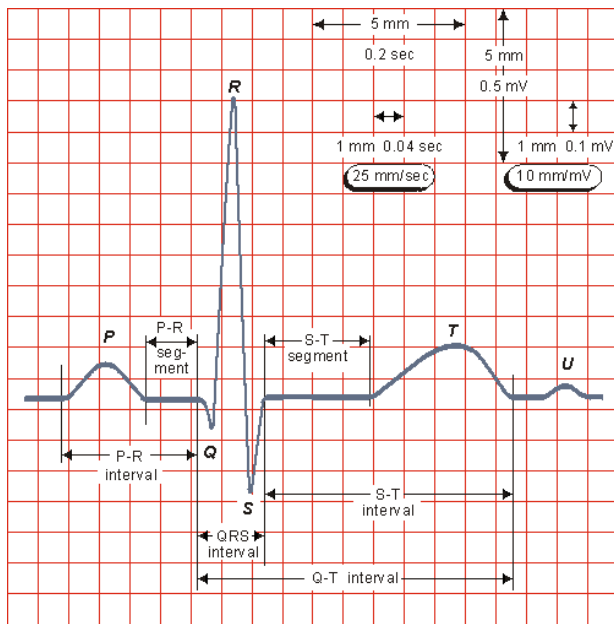
(a) A normal ECG (from University of Utah School of Medicine)
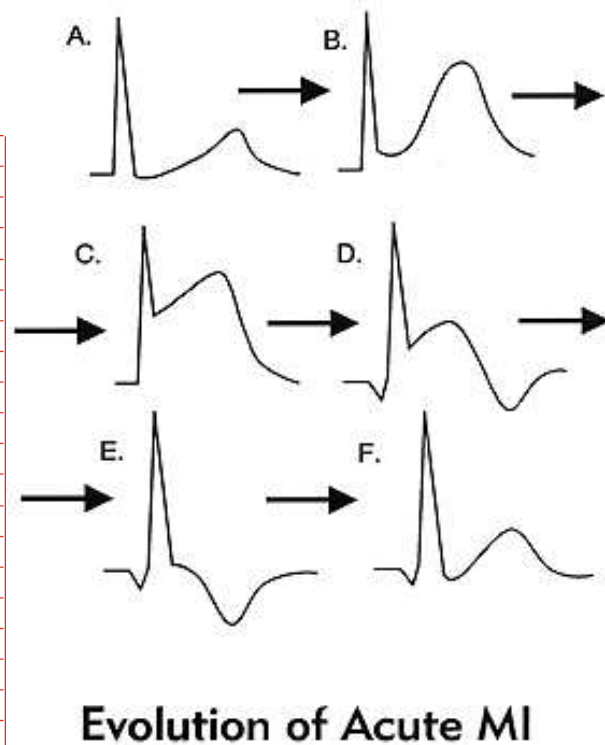
Evolution of Acute MI

A Normal ECG, prior to AMI

B Hyperacute T wave changes - increased T wave amplitude and width; may also see ST elevation

C Marked ST elevation with hyperacute T wave changes (transmural injury)

D Pathologic Q waves, less ST elevation, terminal T wave inversion (necrosis)

E Pathologic Q waves, T wave inversion (necrosis and fibrosis)

F Pathologic Q waves, upright T waves (fibrosis)

Our method provides a characteristic pattern for each ECG, defined by the partition performed by the matching. The partition reflects the changes of behaviour depending on the values of α, β and the interval between iterations it occurs. A pattern is represented as an ordered set of pairs (**behaviour**, *iteration interval*). As an example, see equation (1) which represents A, the pattern of the normal ECG. The first pair has a particular meaning: it only informs about the iteration number the pattern initializes so, "0" is not the associated behaviour, it only fills the space for homogeneity in the notation. The reason for initializing the matching at iteration 150 is that the abnormalities begin after this iteration, as shown in the previous figure.

$$Pattern(A) = \{(0, 150), (4, 20), (3, 30), (11, 110), (3, 100), (5, 80), (11, 80)\} \qquad (2)$$

This approach seems to be suitable to implement in the future a cardiac disease classifier we are developing. To perform a similarity test between the reference ECG and the unknown one in order to classify it, the pattern provides a compact representation which fixes the bounds between behaviours and allows local comparisons. The encouraging preliminary results available now allow to augur the behavioural modelling is a good tool to extract shape features.

References

[1] Syeda-Mahmood T, Beymer D,Wang F. Shape-based matching of ecg recordings, IEEE Conf on EMBC 2007.

[2] P. de Chazal, O. O, and R. B. Reilly. Automatic classification of heartbeats using ecg morp.heartbeat intervals features. IEEE Trans. on Biom. Eng., 51(7):11961206, 2004.

[3] D. Cuesta-Frau, J. C. Perez-Cortes, and G. Andreu-Garcia. Clustering of electrocardiograph signals in computer-aided holter analysis. Computer methods and programs in Biomedicine, 72:179196, 2003.

[4] Tuzcu V, Nas S. Dynamic time warping as a novel tool in pattern recognition of ecg changes in heart rhythm disturbances. IEEE Conf on SMC 2005;1:182–186.

[5] I. Christov, G. et al. Comparative study of morphological and time-frequency ecg descriptor for heartbeat classification. Medical Engineering & Physics, 28:876887, 2006.

[6] de Chazal P, Celler BG, Reilly RB. Using wavelet coefficients for the classification of the electrocardiogram. IEEE Conf on EMBS 2000;1:64–67.

[7] G. Moody and R. Mark. Qrs morphology representation and noise estimation using the Karhunen-Loeve transform. Computer Cardiology, 16:269272, 1989.

[8] M. Lagerholm, C. Peterson, L. Edenbrandt, and L. Sornmo. Clustering ecg complexes using Hermite functions and self-organizing maps. IEEE Trans. on Biom. Eng., 47:838848, 2000.

[9] K. I. Minami, H. Nakajima, and T. Toyoshima. Real-time discrimination of ventricular tachycardia with Fourier-transform neural network. IEEE Trans. Biomed. Eng. 1999; 46: 179–185.

[10] G. Bortolan, I. Jekova, and I. Christov. Comparison of four methods for premature ventricular contraction and normal beat clustering. Computers in Cardiology, 32:921924, 2005.

[11] Vclav Chudček et al. Comparison of Methods for Premature Ventricular Beat Detection Computers in Cardiology 2005.

[12] P. Frasconi, M. Gori, M. Maggini, and G. Soda. United integration of explicit knowledge and learning by example in recurrent networks. IEEE Trans. Knowl. Data Eng. 1995; 7: 340–346.

[13] Yang Wang et al. A Short-Time Multifractal Approach for Arrhythmia Detection Based on Fuzzy Neural Network. IEEE Trans Biomed. Eng. 2001; 48 (9): 989–995.

[14] Alim O, Hamdy N, El-Hanjouri M. Heart diseases diagnosis using heart sounds. Proc National Radio Science Conference 2002; 636 –640.

[15] Nasiri, J.A.; Naghibzadeh, M. Yazdi, H.S.; Naghibzadeh, B. ECG Arrhythmia Classification with Support Vector Machines and Genetic Algorithm Computer Modeling and Simulation, EMS'09.

[16] Wang, F. Syeda-Mahmood, T. Beymer, Finding disease similarity by combining ECG with heart auscultation sound D.;Computers in Cardiology, 2007.

[17] Dayong Gao, Michael Madden, Michael Schukat Arrhythmia Identification from ECG Signals with a Neural Network Classifier Based on a Bayesian Framework, Twenty-fourth SGAI International Conference on Innovative Techniques and Applications of Artificial Intelligence, December 2004.

[18] Kam, A. Cohen, A Detection of fetal ECG with IIR adaptive filtering and genetic algorithms. Acoustics, Speech, and Signal Processing, 1999. ICASSP '99. Proceedings.

[19] Miroslav Cepek, Vaclav Chudacek , Milan Petrik Comparison of Inductive Modeling Method to Other Classification Methods for Holter ECG, Proceedings internacional workshop on Inductive modelling IWIM 2007.

[20] Hudson, D.L. Cohen, M.E.; Use of intelligent agents in the diagnosis of cardiac disorders, California Univ., San Francisco, CA, USA. Computers in Cardiology, 2002

[21] M Kuttikrishnan and M. Dhanabanachandran, A novel approach of cardiac disease prediction and classification using intelligent agents. IJCSIS vol 8 n5 august 2010